University of Naples Federico II
Naples, Italy



Identification of Aerodynamic Force Sources for Next Generation Aircraft

Lorenzo Russo

Thesis for the degree of
Doctor of Philosophy
in Industrial Engineering
Cycle XXXII

Supervisor: Renato Tognaccini

Coordinator: Michele Grassi

March 2020

© 2020 - Lorenzo Russo
All rights reserved.

Identification of Aerodynamic Force Sources for Next Generation Aircraft

Abstract

Hot topic of modern Aerodynamics is the analysis of the aerodynamic force. Indeed, the growth in global air traffic passenger demand together with the ever more stringent regulations on environmental impact of commercial flight pushed the designers to advanced aircraft configurations.

The link between the flow structures and aerodynamic force generation became a fundamental point for the design of the next generation aircraft; just think of the joined-wing airplanes, which mount staggered interconnected non-planar wings, or the boundary-layer ingestion architectures, based on a strong integration of aerodynamic surfaces and propulsion systems. The aerodynamic analysis of these unconventional configurations revealed the necessity to deepen the understanding of new flow phenomena and their connection with the aerodynamic force.

In the last decades, a big jump forward has been taken thanks to the high-technological advances introduced in both Experimental Fluid Dynamics (EFD) and Computational Fluid Dynamics (CFD); they allowed aerodynamicists to have a profound insight in the flow-field features and develop unconventional techniques for the analysis of the aerodynamic force: the *far field methods*. These methods directly rely on the phenomena occurring in the flow and permit the decomposition of the aerodynamic drag in viscous, wave and lift-induced contributions, the ones which the aeronautical designers are interested in.

In the present dissertation a recently proposed unconventional method for the analysis and the breakdown of the aerodynamic force, based on the *vortex force theory*, is studied and new developments are introduced.

The vortical method will be compared with the more assessed thermodynamic methods stressing the link between the different drag definitions. The connection of the vortex force with the *reversible* flow phenomena will be definitively proven also in the compressible regime and a vortical method will be provided for dealing with the thrust computation in case of actuator disk.

Finally, two drag breakdown analyses will be proposed. An innovative turboprop wing-body configuration, mounting natural laminar flow and riblets drag reduction systems, will be analyzed with a standard thermodynamic method to compute the impact of each technology on the overall aerodynamic performance. In addition, a simple Box Wing configuration will be analyzed by the innovative vortical method for investigating if the compressibility effects degrade its low induced drag feature, that was showed only in inviscid incompressible flow so far.

The applications proposed have to be intended as a proof of the strong impact that the far field aerodynamic force analysis may have in the aerodynamic design of the next-future airplanes.

Contents

Abstract **iv**

Nomenclature **xii**

List of Figures **xxi**

List of Tables **xxiii**

Introduction **xxv**

1 The Aerodynamic Force **1**

1.1 Near Field and Far Field Formulae 1

1.2 Aerodynamic Force Breakdown 5

1.3 Far-field Methods 6

1.3.1 Betz: the Wing-section Drag (1925) 6

1.3.2 Jones: improved Betz's Method (1936) 7

1.3.3 Maskell: Induced Drag Formula (1972) 8

1.4 Thermodynamic Methods 9

1.4.1 Oswatitsch: entropy drag concept (1956) 9

1.4.2 Van Der Vooren & Destarac (2003-4) 10

1.4.3 Paparone & Tognaccini (2003-5) 15

1.4.4 Gariepy et al. (2011-13) 18

1.4.5 Thermodynamic Methods for Unsteady Flow 19

1.5 Vortical Methods 19

1.5.1 Noca et al. 1999 20

1.5.2 Wu et al. (2006-19) 22

1.5.3 Tognaccini et al. (2010-16) 24
1.5.4 Vortical Methods for Unsteady Aerodynamics 29
1.6 Modern Aerodynamics and Classical Theories 30
1.6.1 The Kutta-Joukowskij-Filon Theorem 31

2 A Recent Aerodynamic Force Decomposition **33**
2.1 A Lamb Vector Based Aerodynamic Force Formula 34
2.1.1 Analytical Derivation of Lamb Vector Based Formula 35
2.1.2 Extension of the Lamb Vector Theory to Turbulent Flow 38
2.2 Thermodynamic vs. Vortex-force Methods 40
2.2.1 Numerical Comparison of Drag Breakdown Methods 45
2.3 Extension of the Lamb Vector Theory to Inviscid Flow 49
2.3.1 Force Breakdown in Inviscid Flow: Numerical Verifications . . 54
2.3.2 Reversible and Irreversible Aerodynamic Forces 64
2.4 Towards a Vortical Thrust/Drag Bookkeeping 70
2.4.1 The Actuator Disk Model 70
2.4.2 A Vortical Thrust Expression for the Actuator Disk 74
2.4.3 The Wake Contraction Thrust 76
2.4.4 Numerical Verification of the Vortical Thrust Expression 77
2.5 Summary of the Achievements of This Chapter 80

3 Applications: New Methods for New Aircraft **83**
3.1 Drag Breakdown of an Innovative Turboprop Configuration 83
3.1.1 Natural Laminar Flow and Riblets Technologies 85
3.1.2 A Riblets Model for CFD Analysis 86
3.1.3 The Drag Breakdown Method 87
3.1.4 Drag Performance of IRON Turboprop Configuration 88
3.2 Induced Drag of Box Wings in Compressible Flow 99
3.2.1 Box Wing: the Best Wing System 101
3.2.2 Aerodynamic performance of Box Wings 103
3.2.3 Box Wing Vs. Elliptical Wing 119
3.3 Summary of the Achievements of This Chapter 124

Conclusions **127**

A Derivative Moment Transformations **129**

B Thermodynamics estimate on the far field surface **131**

C Summary of Aerodynamic Force Formulae **133**
C.1 Aerodynamic Thrust 133
C.2 Aerodynamic Force 133

D Accuracy Analysis of Box-wing Numerical Results **135**
D.1 Box Wing with $\mathcal{AR} = 6$ and $\mathbb{V} = 0.2$ 135
D.2 Box Wing with $\mathcal{AR} = 6$ and $\mathbb{V} = 0.4$ 139
D.3 Elliptical Wing with $\mathcal{AR} = 6$ 140

References **152**

List of Author's Publications **153**

Nomenclature

$\underline{a}$	=	particle fluid acceleration
$\mathcal{AR}$	=	wing aspect ratio
B	=	solid body
b	=	wingspan
c	=	wing-section chord
$\bar{c}$	=	standard mean chord
C_x	=	non-dimensional coefficient of the quantity x
D	=	total drag
$\underline{e}$	=	unit vector
E	=	aerodynamic efficiency
$\underline{F}$	=	aerodynamic force
$\underline{F}_\ell$	=	vortex force
$\underline{F}_{\text{irr}}$, $\underline{F}_{\text{rev}}$	=	irreversible and reversible aerodynamic force definitions
$\underline{F}_\rho$	=	compressible generation term of aerodynamic force
$\underline{F}_\Sigma$	=	Lamb vector surface integral contribution to aerodynamic force
$\underline{g}$	=	arbritary vector field
h	=	static enthalpy
H	=	total enthalpy
$\mathcal{H}$	=	lenght of the box-wing joint
$\underline{\underline{I}}$	=	identity matrix
k	=	space dimension minus one
$\underline{\ell}$	=	$\underline{\zeta} \times \underline{V}$ (Lamb vector)
L	=	lift

m	=	body mass
$\dot{m}$	=	mass flow rate
M_∞	=	freestream Mach number
$\underline{n}$	=	unit normal vector
p	=	static pressure
p_d	=	dynamic pressure
p_T	=	total pressure
r	=	position vector
R	=	tip fin radius
Re_∞	=	freestream Reynolds number
s	=	entropy
S	=	surface
t	=	time
T	=	thrust
T_∞	=	freestream static temperature
$\underline{V}$	=	velocity vector
$\mathcal{V}$	=	fluid domain
$\mathbb{V}$	=	vertical aspect ratio
w	=	induced axial velocity
$\mathcal{W}$	=	far field wake plane
y^+	=	non-dimensional wall distance
S_B	=	body surface
α	=	angle of attack
γ	=	load distribution
Γ	=	circulation
$\underline{\underline{\Delta}}_\mu$	=	viscosity containing term of aerodynamic force
ε	=	aerodynamic efficiency ratio
φ	=	induced rotational velocity
λ	=	sensor
μ	=	dynamic viscosity
$\underline{\underline{\tau}}$	=	stress tensor
$\underline{\underline{\tau}}_v$	=	viscous stress tensor
τ_w	=	viscous wall stress
ρ	=	fluid density

Σ = far field surface

$\underline{\zeta}$ = fluid vorticity vector

χ = generic potential function

Subscripts

B = referred to body

ent. = referred to entropy

far = referred to far field

H = referred to horizontal wing

imp = referred to impulse

m = referred to material volume

mom = referred to momentum

nac = referred to nacelle

near = referred to near field

o = referred to overall net thrust

opt = referred to optimal conditions

pre = referred to pre-entry thrust

S = referred to surface

sp = referred to spurious drag

t = referred to time

v = referred to viscous drag

V = referred to vertical wing

$\mathcal{V}$ = referred to volume

v = referred to viscous and wave drag

w = referred to wave drag

Superscripts

DV = referred to Van Der Vooren & Destarac formula

L = referred to lower wing

nf = referred to near field method

M = referred to Maskell's formula

O = referred to Oswatitsch's formula

ref = referred to the optimal conditions of the cantilevered wing

U = referred to upper wing

vf = referred to vortical method

WS = referred to generic wing system

List of figures

1.1.1 The *falling apple*: sketch of the material volume for aerodynamic force computation. 2

1.3.1 Hart K-1442 experimental set. Comparison between wing-section drag computed by Betz's and Jones' methods changing the wake plane position in fraction of chord $r_{\mathcal{W}}/c$. Jones (—⊖—), Betz (- ⊟ -). Extracted from [13]. 8

1.4.1 Drag bar chart. Wing-body large transport aircraft at $M_\infty = 0.85, Re_\infty = 8 \times 10^6$ and $C_L \approx 0.5$. RANS computations with $k-l$ turbulence model and 3.8 million cells. Extracted from [23]. 13

1.4.2 Drag polars. DLR-ALVAST aircraft in power-off (WB) and power-on (WBPN) configurations at $M_\infty = 0.75, Re_\infty = 4.3 \times 10^6$ and $C_L \approx 0.5$. RANS computations with $k - \zeta$ turbulence model and 1.5 million cells for WB and 4.0 million cells for WBPN. Extracted from [23]. . . . 14

1.4.3 Regions selected for far field drag analysis. DLR-ALVAST aircraft in power-off (WB) and power-on (WBPN) configurations at $M_\infty = 0.75, Re_\infty = 4.3 \times 10^6$ and $C_L \approx 0.5$. RANS computations with $k - \zeta$ turbulence model and 1.5 million cells for WB and 4.0 million cells for WBPN. Extracted from [23]. 14

1.4.4 Grid convergence analysis on a NACA0012 airfoil at $M_\infty = 0.7, Re_\infty = 49 \times 10^6$ and $C_L = 0.24$. RANS computations with 163 thousand cells for $h = 1$ grid level. Extracted from [25]. 17

1.4.5 Drag polars of DLR-ALVAST wing-body at $M_\infty = 0.75, Re_\infty = 4.3 \times 10^6$. RANS computations with 1.5 million cells. Extracted from [25]. . . 17

1.4.6 IDEA grid set for NASA Common Research Model. Extracted from [28]. 19

1.4.7 Drag breakdown of the NASA CRM at $M_\infty = 0.75$, $Re_\infty = 5 \times 10^6$. Extracted from [28]. 19
1.5.1 Oscillating cylinder in incompressible flow. Comparison of lift coefficient C_L obtained with: near-field (——), Impulse Equation (—○—), Momentum Equation (—●—). Extracted from [33]. 22
1.5.2 Oscillating cylinder in incompressible flow. Comparison of lift coefficient C_L obtained with: near-field (——), Momentum Equation (— ○ —), Flux Equation (—●—). Extracted from [33]. 22
1.5.3 Drag polars of an elliptical wing with $\mathcal{AR} = 7$, $M_\infty = 0.01$ and $Re_\infty = 3\times10^6$. Near field (—□—), F (—△—), F_ℓ (—◇—), Maskell's formula(—○—), $C_L^2/(\pi\mathcal{AR})$ (- - -). Extracted from [42]. 26
1.5.4 Drag polars of an elliptical wing with $\mathcal{AR} = 7$ at $Re_\infty = 3 \times 10^6$ and different Mach numbers. Near field (—△—), F (—□—), F_ℓ (— ∗ —),$F_{\Sigma-S_B}$ (— ◇ —),$C_L^2/(\pi\mathcal{AR})$ (—). Extracted from [46]. 28
1.5.5 NASA CRM at $Re_\infty = 5 \times 10^6$. Computed lift-drag polars. Near field (—△—), F (—□—), vortical induced drag (— ○ —), vortical wave drag (—◇—), vortical viscous drag (— ∗ —), $C_L^2/(\pi\mathcal{AR})$ (—). Extracted from [47]. 29
1.5.6 NASA CRM at $Re_\infty = 5 \times 10^6$, $M_\infty = 0.85$ and $C_L \approx 0.5$. Selected boundary-layer a) and shock-wave b) regions. Extracted from [46]. . . . 29
1.5.7 Pitching flat plate, $\bar{a} = 30°$, $k = 0.05$, $Re_\infty = 300$. Comparison between lift and drag coefficients computed by near field formula (—), inertial formula (· · ·) and mixed inertial-non inertial formula (- - -). Extracted from [47]. 30

2.1.1 Sketch of fluid domain considered for the aerodynamic force analysis. . 34
2.2.1 NACA 0012 airfoil, $Re_\infty = 6 \times 10^6$, $M_\infty = 0.75$, $a = 2°$. C_p and C_f distributions over the airfoil. 45
2.2.2 Elliptical wing with $\mathcal{AR} = 7$, $Re_\infty = 3 \times 10^6$, $M_\infty = 0.5$, $a = 4°$. C_p and C_f distributions over the wing. 46
2.2.3 NACA 0012 airfoil, $Re_\infty = 6 \times 10^6$, $M_\infty = 0.75$, $a = 2°$. Computed drag breakdown against position of the wake plane: comparison between vortex force theory and thermodynamic methods. D_i (—✶—), D_i^M (—✶—), D_{vw}^{DV} (—⊗—), $D_{\mathcal{W}}$ (—⊟—), D_{nf} (- - -). 48

2.2.4 Elliptical wing with $\mathcal{AR} = 7, Re_\infty = 3\times10^6, M_\infty = 0.5, \alpha = 4°$. Computed drag breakdown against position of the wake plane: comparison between vortex force theory and thermodynamic methods. D_i (—✳—), D_i^M (—✳—), $C_L^2/\pi\mathcal{AR}$ (·····), D_{vw}^{DV} (—⊗—), $D_\mathcal{W}$ (—⊟—), D_{nf} (- - -). 49
2.3.1 Sketch of the integration domain for an effectively inviscid flow. 49
2.3.2 Finite volume domain used for deriving Eq. (2.66). 52
2.3.3 NACA 0012 airfoil, $\alpha = 4°$, weak Euler solution. Contours of vorticity at ζ a) $M_\infty = 0.3$ and b) $M_\infty = 0.7$. 55
2.3.4 Elliptic wing, $M_\infty = 0.1, \alpha = 4°$, weak Euler solution. Contours of x-vorticity modulus $|\ \zeta_x\ |$ in the wake and pressure coefficient C_p on the wing. 55
2.3.5 NACA 0012 airfoil, $\alpha = 4°$, effectively inviscid flow. Breakdown of lift a) and drag b) coefficients at different Mach numbers. F_ℓ (—✳—), F_ρ (—⊗—), F_{vf} (—⊟—), F_{nf} (-⊖-). 59
2.3.6 Elliptic wing, $\alpha = 4°$, effectively inviscid flow, subsonic regime. Breakdown of lift a) and drag b) coefficients for different Mach numbers. F_ℓ (—✳—), F_ρ (—⊗—), F_{vf} (—⊟—), $CD_i = CL^2/\pi\mathcal{AR}$ (3.9), F_{nf} (-⊖-). 60
2.3.7 NACA 0012 airfoil, $M_\infty = 0.8, \alpha = 2°$, effectively inviscid flow, transonic regime. Breakdown of lift a) and drag b) coefficients changing the distance r_Σ of the far field surface Σ from the body. F_ℓ (—✳—), F_ρ (—⊗—), F_Σ (—△—), F_{vf} (—⊟—), F_{nf} (-⊖-). 62
2.3.8 NACA 0012 airfoil, $M_\infty = 0.3, \alpha = 2°, Re_\infty = 10^3$. Effect of wake plane position $r_\mathcal{W}$ on lift and drag coefficients. Breakdown of F_{vf} and comparison with F_{nf}. F_{rev} (—◇—), F_{irr} (—△—), F_{vf} (—⊟—), F_{nf} (-⊖-). . . . 66
2.3.9 NACA 0012 airfoil, $M_\infty = 0.3, \alpha = 2°, Re_\infty = 10^6$. Effect of wake plane position $r_\mathcal{W}$ on lift and drag coefficients. Breakdown of F_{vf} and comparison with F_{nf}. F_{rev} (—◇—), F_{irr} (—△—), F_{vf} (—⊟—), F_{nf} (-⊖-). . . . 67
2.3.10 NACA 0012 airfoil, $M_\infty = 0.3, \alpha = 2°, Re_\infty = 10^7$. Effect of wake plane position $r_\mathcal{W}$ on lift and drag coefficients. Breakdown of F_{vf} and comparison with F_{nf}. F_{rev} (—◇—), F_{irr} (—△—), F_{vf} (—⊟—), F_{nf} (-⊖-). . . . 68
2.3.11 NACA 0012 airfoil, $M_\infty = 0.3, \alpha = 2°$. Effect of Reynolds number on $r_\mathcal{W}$ for drag-breakdown convergence. 69
2.3.12 NACA 0012 airfoil, $M_\infty = 0.3, \alpha = 2°$. Effect of Reynolds number on lift and drag breakdown. F_{rev} (—◇—), F_{irr} (—△—), F_{vf} (—⊟—), F_{nf} (-⊖-). 69

2.3.13 NACA 0012 airfoil, $Re_\infty = 10^3, M_\infty = 0.3, a = 2°$. Contours of $-\ell_x$. 70
2.4.1 Main results of Actuator Disk Theory. Simple Momentum Theory (–); General Momentum Theory (–). 71
2.4.2 Reference fluid domain for the derivation of the vortical thrust formula. 74
2.4.3 Discrete model of the wake in inviscid flow. 76
2.4.4 2D Actuator disk: $Re_\infty = 6 \times 10^3, M_\infty = 0, a = 0.5$. Pressure jump and axial interference factor along z. 77
2.4.5 2D Actuator disk: $Re_\infty = 6 \times 10^3, M_\infty = 0, a = 0.5$. Top Figure: contour of axial velocity component; bottom figure: Near field vs vortical thrust coefficients changing the wake plane position $z_\mathcal{W}$. T_ℓ (–✶–), $T_\mathcal{W}$ (–△–), T_{vf} (–⊟–), T_{nf} (-⊙-). 78
2.4.6 3D actuator disk with hub. 79
2.4.7 3D actuator disk with hub: $Re_\infty = 6 \times 10^3, M_\infty = 0, a = 0.05$, $v_\theta/V_\infty = 0.069$. Top figure: contour of axial velocity component. Bottom figure: near field vs vortical thrust coefficients changing the wake plane position $z_\mathcal{W}$. T_ℓ (–✶–), $T_\mathcal{W}$ (–△–), T_s (–○–),T_{vf} (–⊟–), T_{nf} (-⊙-). 80

3.1.1 IRON innovative turboprop wing-body configuration. 84
3.1.2 NACA 0012 airfoil, $M_\infty = 0.7, Re_\infty = 9 \times 10^6, a = 3.25°$. Example of flow domain division in boundary-layer region $\mathcal{V}_v$, shock region $\mathcal{V}_w$ and spurious region $\mathcal{V}_{sp}$. 88
3.1.3 IRON wing-body configuration at $Re_\infty = 18.2 \times 10^6, M_\infty = 0.64$, $a = 0°$. Wing section pressure coefficients and transition points. 89
3.1.4 IRON wing-body configuration at $Re_\infty = 18.2 \times 10^6, M_\infty = 0.64$, $a = 0°$. Laminar (blue) and turbulent (red) flow regions. 90
3.1.5 IRON wing-body configuration at $M_\infty = 0.64, Re_\infty = 18.2 \times 10^6$, fully turbulent flow. Grid convergence analysis with (right figure) and without (left figure) riblets. LVL4 (–■–), LVL2 (–●–), LVL1 (–▲–). . 91
3.1.6 IRON wing-body configuration at $M_\infty = 0.64, Re_\infty = 18.2 \times 10^6$ and $a = 0°$, fully turbulent flow. Computed Drag reduction due to riblets against grid level (optimum height distribution on wing and fuselage). Total drag reduction (–■–); friction drag reduction (–◆–); zero mesh size extrapolation (- - -). 92

3.1.7 IRON wing-body configuration at $M_\infty = 0.64$, $Re_\infty = 18.2 \times 10^6$. Polar curves with and without drag reduction systems installed. Clean configuration (-*-); riblets only (—o—); NLF only (—⊗—); combined NLF+riblets (—●—). 92

3.1.8 IRON wing-body configuration at $M_\infty = 0.64$, $Re_\infty = 18.2 \times 10^6$ and $\alpha = 0^\circ$ (zero mesh extrapolation). Bookkeeping of drag reduction due to NLF and riblets. 93

3.1.9 IRON wing-body configuration at $M_\infty = 0.64$ and $Re_\infty = 18.2 \times 10^6$. Drag reduction due to riblets vs angle of attack. Total drag reduction (—■—); friction drag reduction (—◆—). Reference value in percentages is smooth condition. 93

3.1.10 IRON wing-body configuration without NLF control at $M_\infty = 0.64$ and $Re_\infty = 18.2 \times 10^6$. Grid convergence analysis of far-field drag and near-field drag with (right figure) and without (left figure) riblets installed. Far-field drag (—⊟—); near-field drag (-⊖-). 94

3.1.11 IRON wing-body configuration without NLF control and riblets at $M_\infty = 0.64$ and $Re_\infty = 18.2 \times 10^6$: drag breakdown. Far-field drag without spurious contribution (—⊟—); near-field drag (-⊖-); viscous drag (—⊖—); wave drag (—●—); induced drag (—◇—). 95

3.1.12 IRON wing-body configuration without NLF control and with riblets at $M_\infty = 0.64$ and $Re_\infty = 18.2 \times 10^6$: drag breakdown. Far-field drag without spurious contribution (—⊟—); near-field drag (-⊖-); viscous drag (—⊖—); wave drag (—●—); induced drag (—◇—). 96

3.1.13 IRON wing-body configuration at $M_\infty = 0.64$ and $Re_\infty = 18.2 \times 10^6$: viscous drag breakdown without (left figure) and with riblets (right figure). Viscous drag (—⊖—); friction drag (—⊗—); form drag (—×—). . . . 96

3.1.14 IRON wing-body configuration with NLF control and without riblets at $M_\infty = 0.64$ and $Re_\infty = 18.2 \times 10^6$: drag breakdown. Far-field drag without spurious contribution (—⊟—); near-field drag (-⊖-); viscous drag (—⊖—); wave drag (—●—); induced drag (—◇—). 97

3.1.15 IRON wing-body configuration with NLF control and riblets at $M_\infty = 0.64$ and $Re_\infty = 18.2 \times 10^6$: drag breakdown. Far-field drag without spurious contribution (—⊟—); near-field drag (-⊖-); viscous drag (—⊖—); wave drag (—●—); induced drag (—◇—). 98

3.1.16 IRON wing-body configuration with NFL control at $M_\infty = 0.64$ and $Re_\infty = 18.2 \times 10^6$: viscous drag breakdown without (left figure) and with riblets (right figure). Viscous drag (—⊖—); friction drag (—⊗—); form drag (—×—). 98

3.2.1 Geometry of the Box Wing with $\mathcal{AR} = 6$ and $\mathbb{V} = 0.2$. 101

3.2.2 Box Wing with $\mathcal{AR} = 6$ and $\mathbb{V} = 0.2$ at $Re_\infty = 10^7$. Detail of the grid LVL1 on the symmetry plane and wing. 104

3.2.3 Box Wing with $\mathcal{AR} = 6$ and $\mathbb{V} = 0.2$ at $C_L = 0.5017$. Comparison between the load distribution obtained in present analysis at $Re_\infty = 10^7$ (——), the reference one given by [103] in inviscid flow (- - -) and the theoretical minimum induced drag load distribution (·····). 105

3.2.4 Box Wing with $\mathcal{AR} = 6$ and $\mathbb{V} = 0.2$ at $Re_\infty = 10^7$, $M_\infty = 0.3$ and $\alpha = 0°$. Decay of vorticity in the body wake. 105

3.2.5 Box Wing with $\mathcal{AR} = 6$ and $\mathbb{V} = 0.2$ at $Re_\infty = 10^7$, $\alpha = 4°$ and different Mach numbers. C_p distributions over the wing sections at $\eta_H = 0.5$. Upper wing (——), lower wing (- - -). 106

3.2.6 Box Wing with $\mathcal{AR} = 6$ and $\mathbb{V} = 0.2$ at $Re_\infty = 10^7$, $\alpha = 4°$ and different Mach numbers. C_f distributions over the wing sections at $\eta_H = 0.5$. Upper wing (——), lower wing (- - -). 107

3.2.7 Box Wing with $\mathcal{AR} = 6$ and $\mathbb{V} = 0.2$ at $Re_\infty = 10^7$ and $M_\infty = 0$. $C_L(\alpha)$ and $C_L(C_D)$ curves and their breakdown in incompressible flow. Reference near field (-⊖-), F_{vf} (—⊟—), F_{rev} (—◇—), F_{irr} (—△—), $C_L^2/(\pi\mathcal{AR}\varepsilon)$ with $\varepsilon = 1.46$ (·····). 108

3.2.8 Box Wing with $\mathcal{AR} = 6$ and $\mathbb{V} = 0.2$ at $Re_\infty = 10^7$ and $M_\infty = 0.3$. $C_L(\alpha)$ and $C_L(C_D)$ and breakdown in subsonic flow. Reference near field (-⊖-), F_{vf} (—⊟—), F_{rev} (—◇—), F_{irr} (—△—), $C_L^2/(\pi\mathcal{AR}\varepsilon)$ with $\varepsilon = 1.46$ (·····). 109

3.2.9 Box Wing with $\mathcal{AR} = 6$ and $\mathbb{V} = 0.2$ at $Re_\infty = 10^7$ and $M_\infty = 0.7$. $C_L(\alpha)$ and $C_L(C_D)$ and their breakdown in low transonic flow. Reference near field (-⊖-), F_{vf} (—⊟—), F_{rev} (—◇—), F_{irr} (—△—), $C_L^2/(\pi\mathcal{AR}\varepsilon)$ with $\varepsilon = 1.46$ (·····). 109

3.2.10 Box Wing with $\mathcal{AR} = 6$ and $\mathbb{V} = 0.2$ at $Re_\infty = 10^7$ and $M_\infty = 0.9$. $C_L(\alpha)$ and $C_L(C_D)$ and their breakdown in high transonic flow. Reference near field (-⊖-), F_{vf} (-⊟-), F_{rev} (-◇-), F_{irr} (-△-), $C_L^2/(\pi\mathcal{AR}\varepsilon)$ with $\varepsilon = 1.46$ (·····). 110

3.2.11 Box Wing with $\mathcal{AR} = 6$ and $\mathbb{V} = 0.2$ at $Re_\infty = 10^7$ and $\alpha = 6°$; left ($M_\infty = 0.7$), right ($M_\infty = 0.9$). Shock wave region identified by Eq. (3.3) and contour of Mach number over the wingspan. 111

3.2.12 Box Wing with $\mathcal{AR} = 6$ and $\mathbb{V} = 0.2$ at $Re_\infty = 10^7$. Breakdown of F_{rev} in vortex force and compressible generation term at different Mach numbers. Reference near field (-⊖-), F_{rev} (-◇-), vortex force (-✳-), compressible generation term (-⊗-), $C_L^2/(\pi\mathcal{AR}\varepsilon)$ with $\varepsilon = 1.46$ (·····). 113

3.2.13 Box Wing with $\mathcal{AR} = 6$ and $\mathbb{V} = 0.2$ at $Re_\infty = 10^7$ and $M_\infty = 0$. Effect of angle of attack on load distribution. $\alpha = 0$ $C_L = 0$ (——), $\alpha = 2$ $C_L = 0.1676$ (——), $\alpha = 4$ $C_L = 0.3351$ (——), $\alpha = 6$ $C_L = 0.5017$ (——); present study (solid lines), theoretical minimum induced drag load distributions (dotted lines). 114

3.2.14 Box Wing with $\mathcal{AR} = 6$ and $\mathbb{V} = 0.2$ at $Re_\infty = 10^7$ and $\alpha = 4°$. Effect of Mach number on load distribution. $M_\infty = 0$ $C_L = 0.3351$ (——), $M_\infty = 0.3$ $C_L = 0.3471$ (——), $M_\infty = 0.7$ $C_L = 0.4150$ (——), $M_\infty = 0.9$ $C_L = 0.3322$ (——); present study (solid lines), theoretical minimum induced drag load distributions (dotted lines). 114

3.2.15 Box Wing with $\mathcal{AR} = 6$ and $\mathbb{V} = 0.4$ at $Re_\infty = 10^7$ and $M_\infty = 0$. $C_L(\alpha)$ and $C_L(C_D)$ in incompressible flow and breakdown in F_{rev} and F_{irr}. Reference near field (-⊖-), F_{vf} (-⊟-), F_{rev} (-◇-), F_{irr} (-△-), $C_L^2/(\pi\mathcal{AR}\varepsilon)$ with $\varepsilon = 1.82$ (·····). 116

3.2.16 Box Wing with $\mathcal{AR} = 6$ and $\mathbb{V} = 0.4$ at $Re_\infty = 10^7$ and $M_\infty = 0.3$. $C_L(\alpha)$ and $C_L(C_D)$ in incompressible flow and breakdown in F_{rev} and F_{irr}. Reference near field (-⊖-), F_{vf} (-⊟-), F_{rev} (-◇-), F_{irr} (-△-), $C_L^2/(\pi\mathcal{AR}\varepsilon)$ with $\varepsilon = 1.82$ (·····). 116

3.2.17 Box Wing with $\mathcal{AR} = 6$ and $\mathbb{V} = 0.4$ at $Re_\infty = 10^7$ and $M_\infty = 0.7$. $C_L(\alpha)$ and $C_L(C_D)$ in incompressible flow and breakdown in F_{rev} and F_{irr}. Reference near field (-⊖-), F_{vf} (-⊟-), F_{rev} (-◇-), F_{irr} (-△-), $C_L^2/(\pi\mathcal{AR}\varepsilon)$ with $\varepsilon = 1.82$ (·····). 117

3.2.18 Box Wing with $\mathcal{AR} = 6$ and $\mathbb{V} = 0.4$ at $Re_\infty = 10^7$ and $M_\infty = 0.9$. $C_L(\alpha)$ and $C_L(C_D)$ in incompressible flow and breakdown in F_{rev} and F_{irr}. Reference near field (-⊖-), F_{vf} (—⊟—), F_{rev} (—◇—), F_{irr} (—△—), $C_L^2/(\pi\mathcal{AR}\varepsilon)$ with $\varepsilon = 1.82$ (·····). 117

3.2.19 Box Wings with $\mathcal{AR} = 6$ at $Re_\infty = 10^7$, $M_\infty = 0$ and $\alpha = 4°$. Comparison between the load distributions obtained for the Box Wing with $\mathbb{V} = 0.2$ (—△—) and the one with $\mathbb{V} = 0.4$ (—⊟—). The lift coefficient for $\mathbb{V} = 0.2$ is $C_L = 0.3351$; the lift coefficient for $\mathbb{V} = 0.4$ is $C_L = 0.3570$. 118

3.2.20 Box Wings with same aspect ratio $\mathcal{AR} = 6$ and different $\mathbb{V}$ at $Re_\infty = 10^7$, $M_\infty = 0.9$ and $\alpha = 0°$. Front view of wing configuration and contour of Mach number in the symmetry plane (black line $M_\infty = 1$). 119

3.2.21 Elliptical Wing with $\mathcal{AR} = 6$ at $Re_\infty = 10^7$, $M_\infty = 0.7$ and $\alpha = 4°$. Isosurface of $|\omega_x|$ in the wake and contour of Mach number over the wingspan. 120

3.2.22 Elliptical Wing with $\mathcal{AR} = 6$ at $Re_\infty = 10^7$ and $M_\infty = 0$. Effect of angle of attack on load distribution. $\alpha = 0°$ $C_L = 0$ (——), $\alpha = 2°$ $C_L = 0.1498$ (——), $\alpha = 4°$ $C_L = 0.3051$ (——), $\alpha = 6°$ $C_L = 0.457$ (——); present study (solid lines), elliptical load distributions (dotted lines). 121

3.2.23 Elliptical Wing with $\mathcal{AR} = 6$ at $Re_\infty = 10^7$ and $\alpha = 4°$. Effect of Mach number on load distribution. $M_\infty = 0$ $C_L = 0.3051$ (——), $M_\infty = 0.3$ $C_L = 0.3146$ (——), $M_\infty = 0.7$ $C_L = 0.3823$ (——); present study (solid lines), elliptical load distributions (dotted lines). 121

3.2.24 Elliptical Wing with $\mathcal{AR} = 6$ at $Re_\infty = 10^7$ and $M_\infty = 0$. $C_L(\alpha)$ and $C_L(C_D)$ in incompressible flow and breakdown in F_{rev} and F_{irr}. Reference near field (-⊖-), F_{vf} (—⊟—), F_{rev} (—◇—), F_{irr} (—△—), $C_L^2/(\pi\mathcal{AR})$ (·····). 122

3.2.25 Elliptical Wing with $\mathcal{AR} = 6$ at $Re_\infty = 10^7$ and $M_\infty = 0.3$. $C_L(\alpha)$ and $C_L(C_D)$ in incompressible flow and breakdown in F_{rev} and F_{irr}. Reference near field (-⊖-), F_{vf} (—⊟—), F_{rev} (—◇—), F_{irr} (—△—), $C_L^2/(\pi\mathcal{AR})$ (·····). 122

3.2.26 Elliptical Wing with $\mathcal{AR} = 6$ at $Re_\infty = 10^7$ and $M_\infty = 0.7$. $C_L(\alpha)$ and $C_L(C_D)$ in incompressible flow and breakdown in F_{rev} and F_{irr}. Reference near field (-⊖-), F_{vf} (—⊟—), F_{rev} (—◇—), F_{irr} (—△—), $C_L^2/(\pi\mathcal{AR})$ (·····). 123

3.2.27 Comparison of polar curves obtained at $Re_\infty = 10^7$ for the equivalent Elliptical Wing with $\mathcal{AR} = 6$ (—o—), the Box Wing with $\mathbb{V} = 0.2$ (—△—) and the Box Wing with $\mathbb{V} = 0.4$ (—□—). 124

D.1.1 Box Wing with $\mathcal{AR} = 6$ and $\mathbb{V} = 0.2$ at $Re_\infty = 10^7$, $M_\infty = 0.3$ and $\alpha = 4°$. Grid convergence analysis in terms of *near-field* F_{nf} and *far-field* F_{vf} lift (C_L) and drag (C_D) coefficients and their breakdown. F_{nf} (-o-), F_{vf} (—□—), F_{rev} (—◇—), F_{irr} (—△—), induced drag of an optimally loaded Box Wing with $\varepsilon = 1.46$ (··*··). 136

D.1.2 Box Wing with $\mathcal{AR} = 6$ and $\mathbb{V} = 0.2$ at $Re_\infty = 10^7$, $M_\infty = 0.3$ and $\alpha = 4°$. Effect of the wake plane position $r_{\mathcal{W}}$ on C_L and C_D computed by F_{vf} and breakdown in F_{rev} and F_{irr}. Reference near field (- - -), F_{vf} (—■—), F_{rev} (—•—), F_{irr} (—▲—), induced drag of an optimally loaded Box Wing with $\varepsilon = 1.46$ (·····). 138

D.2.1 Box Wing with $\mathcal{AR} = 6$ and $\mathbb{V} = 0.4$ at $Re_\infty = 10^7$, $M_\infty = 0.3$ and $\alpha = 4°$. Grid convergence analysis in terms of *near field* F_{nf} and *far field* F_{vf} lift (C_L) and drag (C_D) coefficients and their breakdown. F_{nf} (-o-), F_{vf} (—□—), F_{rev} (—◇—), F_{irr} (—△—), induced drag of an optimally loaded Box Wing with $\varepsilon = 1.82$ (··*··). 139

D.3.1 Elliptical Wing with $\mathcal{AR} = 6$ at $Re_\infty = 10^7$, $M_\infty = 0.3$ and $\alpha = 4°$. Grid convergence analysis in terms of *near field* F_{nf} and *far field* F_{vf} lift (C_L) and drag (C_D) coefficients and their breakdown. F_{nf} (-o-), F_{vf} (—□—), F_{rev} (—◇—), F_{irr} (—△—), theoretical induced drag of an Elliptical Wing computed by Eq. (3.6) (··*··). 141

List of tables

2.3.1 NACA 0012 airfoil, weak Euler solution, $\alpha = 4°$. Breakdown of F_{vf} at different Mach numbers and comparison with near field value F_{nf}. . . . 57

2.3.2 Elliptic wing, weak Euler solution, $\alpha = 4°$. Breakdown of F_{vf} at different Mach numbers and comparison with near field value F_{nf}. 58

2.3.3 NACA0012 airfoil, weak Euler solution, $M_\infty = 0.8$, $\alpha = 2°$. Breakdown of F_{vf} and comparison with near field value F_{nf} at $r_\Sigma = 4c$. 63

C.1.1 Vortical thrust formula in incompressible laminar flow. 133

C.2.1 Summary of the aerodynamic force formulae used in different flow conditions. 134

D.1.1 Box Wing with $\mathcal{AR} = 6$ and $\mathbb{V} = 0.2$ at $Re_\infty = 10^7$, $M_\infty = 0.3$ and $\alpha = 4°$. Results of the grid convergence analysis in terms of *near field* F_{nf} and *far field* F_{vf} lift (C_L) and drag (C_D) coefficients and their breakdown in F_{rev} and F_{irr}. 137

D.2.1 Box Wing with $\mathcal{AR} = 6$ and $\mathbb{V} = 0.4$ at $Re_\infty = 10^7$, $M_\infty = 0.3$ and $\alpha = 4°$. Results of the grid convergence analysis in terms of *near field* F_{nf} and *far field* F_{vf} lift (C_L) and drag (C_D) coefficients and their breakdown in F_{rev} and F_{irr}. 140

D.3.1 Elliptical Wing with $\mathcal{AR} = 6$ at $Re_\infty = 10^7$, $M_\infty = 0.3$ and $\alpha = 4°$. Results of the grid convergence analysis in terms of *near field* F_{nf} and *far field* F_{vf} lift (C_L) and drag (C_D) coefficients and their breakdown in F_{rev} and F_{irr}. 141

Introduction

Air travel is one the great privileges of living in our time and the number of air passengers is estimated to double in the next twenty years. Anyway, airplanes run on oil and it is shown that, in general, aircraft have the highest primary energy consumption and the highest carbon dioxide emissions with respect to the other transport systems.

The Directorate General for the Research of the European Commission stated that "the contribution of aircraft exhaust fumes to air pollution was not a negligible quantity" already in early nineties [1] but, since the introduction of the winglets [2], the commercial aircraft architecture remained substantially unchanged.

Aerodynamic drag is the main responsible of the *airplane environmental impact* and aeronautical designers of our time are called to profuse a big effort in drag reduction and aerodynamic optimization. Thanks to new technologies and computational resources, both the experimental and the computational fluid dynamics (CFD) improved in recent years and allowed the aerodynamicists to obtain a large amount of data to deepen the issues of modern aerodynamics; anyway, collecting data seems not enough to solve the problem, as Bushnell & Moore clearly states in *Annual Review of Fluid Mechanics* [3]: "the kernel problem for drag reduction is the genesis and development of new approaches, techniques, insights and understanding".

The key to success in the design of the next-generation aircraft may be a more intense use of the theoretical aerodynamics in order to effectively take advantage of the detailed description capabilities of CFD and advanced experimental tools. With this aim, researchers have been developing unconventional aerodynamic force theories in recent years. Indeed, the standard aerodynamic force computation technique (*near field method*), that is based on the stress integration on the body, suffers the drawback of allowing the decomposition of the aerodynamic drag in friction and pressure contributions only. Moreover, this approach hides the deep connection between the aerodynamic force generation and flow

field phenomena occurring around the body.

On the other hand, *far field methods* clearly connects the characteristics of the flow field to the aerodynamic force allowing for a deep understanding of what, how and why the force is generated. In addition, under a practical perspective, only with these methods is possible to perform two crucial tasks of modern aerodynamics: the breakdown of the total drag in its viscous, wave and lift-induced contributions and the thrust/drag bookkeeping, that consists in the separation of propulsive and drag forces in case of power-on configurations.

Core subject of present dissertation is the analysis of the far-field methods and their application to the numerically obtained flows around innovative aeronautical configurations. The thesis is structured as follows:

- Chapter 1: the theories developed for the aerodynamic force analysis are reviewed and the main differences between the so-called *thermodynamic* and *vortical* methods are highlighted. Pros. and cons. of each technique are described and reference results are reported.

- Chapter 2: the method for the aerodynamic force breakdown based on the *vortex force theory* is deeply analyzed. The analytical derivation of the theory is reported with its extension to turbulent flow; comparisons with other far-field methods are provided and an extension to *effectively inviscid flow* is proposed in order to definitely link the vortex force to the *reversible* aerodynamic force and ascertain the long-waited definition of induced drag in viscous flow. Finally, a vortical thrust/drag bookkeeping method for actuator disk is presented.

- Chapter 3: two drag breakdown analyses are proposed. The aerodynamic force of an innovative wing-body turboprop configuration, with natural laminar flow and riblets installed, is decomposed with an assessed thermodynamic method. The second analysis, performed by the innovative vortical technique analyzed in Chapter 2, is used to study the compressibility effects on box-wing aerodynamic performance with particular attention to its low-induced drag feature.

To every action there is always opposed an equal reaction.

Isaac Newton - 1687

1 The Aerodynamic Force

The fascinating journey in the aerodynamic force computation and its breakdown draws its origin in a sunny day of 1667 when a young Isaac Newton was sitting under an apple tree and was bonked on the head by a falling piece of fruit. The legend tells that this hilarious moment prompted Newton to suddenly come up with his law of gravity which states that every body in the universe is attracted to every other body with a force that is directly proportional to the product of their masses and inversely proportional to the square of the distance between them. Nobody knows if that sunny day the idea of an aerodynamic force opposing the gravitational attraction between the earth and the apple flashed in the young Newton's mind.

1.1 Near Field and Far Field Formulae

Besides the *Universal Gravitation Law*, in 1687 Newton founded the classical mechanics with the laws of motion; the second law states that the acceleration $\underline{a}$ of a body is dependent

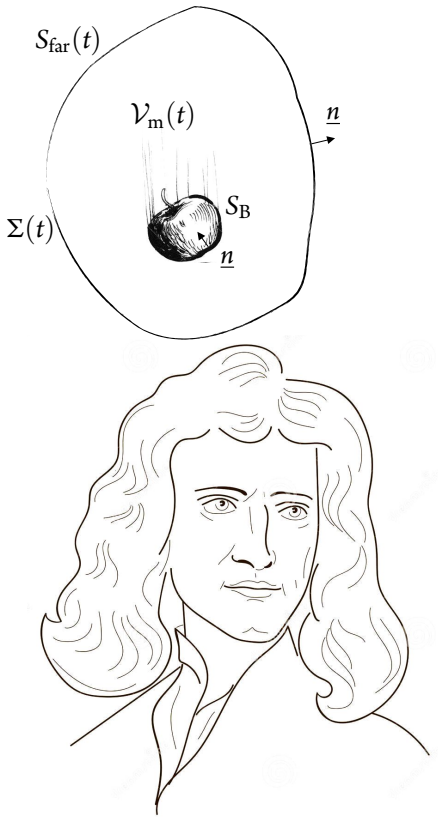


Figure 1.1.1: The *falling apple*: sketch of the material volume for aerodynamic force computation.

upon two variables: the net force acting upon the object and its mass m

$$\underline{F} = m\underline{a}\,. \tag{1.1}$$

The net force $\underline{F}$ is the sum of the external forces acting on the body: the gravity and the fluid force experienced by the *falling apple*. The force exerted by the fluid on the body can be computed by the momentum balance in the fluid itself.

Considering the material fluid volume $\mathcal{V}_m(t)$ enclosed in $\Sigma(t) = S_B \cup S_{far}(t)$ and constituted by a continuum of the fluid particles (see Fig. 1.1.1), for every particle $\underline{F} = \rho\underline{V}\mathrm{d}\mathcal{V}$ (in the continuum hypothesis), where ρ is the particle density, $\underline{V}$ is its velocity and $\underline{F}$ is the

sum of all the forces applied to the fluid particle. For the Newton's third law, all the forces between particles cancel each other and the total force exerted on the material volume $\mathcal{V}_m(t)$ is

$$\underline{F} = \frac{d}{dt}\int_{\mathcal{V}_m(t)} \rho \underline{V}\, d\mathcal{V}\,. \tag{1.2}$$

The external forces applied to the body $\underline{F}$ can be splitted into the *volume forces* $\underline{f}_{\mathcal{V}}$ and the *surface forces* $\underline{f}_S$ [4]:

$$\frac{d}{dt}\int_{\mathcal{V}_m(t)} \rho \underline{V}\, d\mathcal{V} = \int_{\mathcal{V}_m(t)} \underline{f}_V\, d\mathcal{V} - \int_{\Sigma(t)} \underline{f}_S\, dS\,, \tag{1.3}$$

where the *surface forces* of a boundary point can be expressed in terms of the general stress tensor of the fluid $\underline{\underline{\tau}}$ and the unit vector normal to $\Sigma(t)$ in that point: $\underline{f}_S = -\underline{n}\cdot\underline{\underline{\tau}}$. The momentum balance can be written as

$$\frac{d}{dt}\int_{\mathcal{V}_m(t)} \rho \underline{V}\, d\mathcal{V} = \int_{\mathcal{V}_m(t)} \underline{f}_{\mathcal{V}}\, d\mathcal{V} + \int_{\Sigma(t)} \left(\underline{n}\cdot\underline{\underline{\tau}}\right)\, dS\,, \tag{1.4}$$

where the *surface-forces* integral can be further divided in the integral on S_B and the one on $S_{far}(t)$

$$\int_{\Sigma(t)} \left(\underline{n}\cdot\underline{\underline{\tau}}\right)\, dS = \int_{S_{far}(t)} \left(\underline{n}\cdot\underline{\underline{\tau}}\right)\, dS + \int_{S_B} \left(\underline{n}\cdot\underline{\underline{\tau}}\right)\, dS\,. \tag{1.5}$$

The surface integral extended to S_B of Eq. (1.5) is the classical definition of the aerodynamic force: the *near field* formula.

For a Newtonian fluid the stress tensor is given by $\underline{\underline{\tau}} = -p\underline{\underline{I}} + \underline{\underline{\tau}}_\nu$ with $\underline{\underline{I}}$ is the unit normal tensor, $\underline{\underline{\tau}}_\nu = \mu\left[\underline{\underline{\nabla V}} + \underline{\underline{(\nabla V)}}^T\right]$ is the dissipative stress tensor and μ is the molecular viscosity. The *near field* formula allows for the decomposition of the total aerodynamic force into the *pressure* and the *friction* aerodynamic forces:

$$\underline{F} = \int_{S_B} \left(\underline{n}\cdot\underline{\underline{\tau}}\right)\, dS = \int_{S_B} \left[\underline{n}\cdot\left(-p\underline{\underline{I}} + \underline{\underline{\tau}}_\nu\right)\right]\, dS\,, \tag{1.6}$$

and is typically applied in both Computational Fluid Dynamics (CFD) and Experimental Fluid Dynamics (EFD). In CFD the body-surface stresses are directly computed by the flow solver whereas in EFD the pressure and the shear stresses can be obtained by sensors installed on the body.

The integrals of Eq. (1.4) which do not contain the flow variables on the body surface

form the *far field* aerodynamic force expression

$$\underline{F} = -\frac{\mathrm{d}}{\mathrm{d}t}\int_{\mathcal{V}_\mathrm{m}(t)} \rho\underline{V}\,\mathrm{d}\mathcal{V} + \int_{\mathcal{V}_\mathrm{m}(t)} \underline{f}_\mathrm{V}\,\mathrm{d}\mathcal{V} + \int_{S_\mathrm{far}(t)} \left(\underline{n}\cdot\underline{\tau}\right)\,\mathrm{dS}\,. \tag{1.7}$$

Equation 1.7 involves the fluid variables *outside* the body. It is called *far field* formula because in the classical problems of steady aerodynamics the volume integral linked to the time derivative is zero whereas the one linked to the gravitational effects is negligible and only the integral extended to S_far remains.

Dealing with the problem of the aerodynamic-force computation with the material surface $S_\mathrm{m}(t)$, dependent on time, is not trivial; therefore, it is better to rewrite the aerodynamic force formulae for an arbitrary volume coincident with the material volume at the time t^*: $\mathcal{V} = \mathcal{V}_\mathrm{m}(t^*)$ and enclosed by $\Sigma = \Sigma(t^*)$. Applying the Reynolds Transport Theorem[1], Eq. (1.7) becomes:

$$\underline{F} = -\int_{\mathcal{V}} \frac{\partial\left(\rho\underline{V}\right)}{\partial t}\,\mathrm{d}\mathcal{V} - \int_{\Sigma} \left(\underline{n}\cdot\rho\underline{V}\underline{V}\right)\,\mathrm{dS} + \int_{\mathcal{V}} \underline{f}_\mathrm{V}\,\mathrm{d}\mathcal{V} + \int_{S_\mathrm{far}} \left(\underline{n}\cdot\underline{\tau}\right)\,\mathrm{dS}\,, \tag{1.8}$$

that is again a *far field* formula even if it contains a body-surface integral. Introducing the material derivative $\frac{\mathrm{D}}{\mathrm{D}t} = \frac{\partial}{\partial t} + \underline{V}\cdot\underline{\nabla}$, Eq. (1.8) becomes

$$\underline{F} = -\int_{\mathcal{V}} \rho\underline{a}\mathrm{d}\mathcal{V} + \int_{S_\mathrm{far}} \left(\underline{n}\cdot\underline{\tau}\right)\,\mathrm{dS}\,, \tag{1.9}$$

where $\underline{a}$ is the local flow acceleration.

The *far field* aerodynamic force expression has been historically adopted for the development of the theoretical aerodynamics: the demonstration of the Kutta-Joukowskij Theorem [5, 6] uses this approach. *Far field* formula is also applied in experimental sets where it is more convenient to compute the aerodynamic force far from the body. However, one of the most useful recent application of the *far field* approach is the possibility to relate the aerodynamic force to the local flow variables in order to better understand the mechanisms

[1] Suppose $\mathcal{V}(t)$ is a region in Euclidean space with boundary Σ, and let be $\underline{n}$ the outward unit normal to the boundary at time t. Let $\underline{r}(t)$ be the positions of points in the region, $\underline{V}(t)$ the velocity field in the region, and let be $\underline{g}$ a vector field in the region (it may also be a scalar field). The Reynolds Transport Theorem states that:

$$\frac{\mathrm{d}}{\mathrm{d}t}\int_{\mathcal{V}(t)} \underline{g}\,\mathrm{d}\mathcal{V} = \int_{\mathcal{V}(t)} \frac{\partial\underline{g}}{\partial t}\,\mathrm{d}\mathcal{V} + \int_{\partial\mathcal{V}(t)} \left(\underline{V}\cdot\underline{n}\right)\underline{g}\,\mathrm{dS}\,.$$

governing the force generation and decompose the total force in the physical contributions needed by the aerodynamic designers.

1.2 Aerodynamic Force Breakdown

The total aerodynamic force exerted by the fluid on a solid body passing through it is a vector formed, in general, by three components. Named $\underline{V}_\infty$ the freestream velocity vector, the component of $\underline{F}$ normal to $\underline{V}_\infty$ is the *aerodynamic lift*, the component parallel to the freestream is the *aerodynamic drag* whereas the remaining component (present in case of 3D flows) is the *aerodynamic side force*. Among the three aerodynamic force components aircraft designers give particular attention to the aerodynamic drag, since this force components opposes to the movement of the airplane through the fluid flow. As Meredith pointed out in [7]: "a one percent increase in the lift-to-drag ratio (L/D) during takeoff is equivalent to a 2800 lb increase in payload for a generic twin engine subsonic transport airplane on a long-range mission or approximately 200 lb in payload (or 1 passenger) per drag count (1 drag count = 0.0001)" whereas Raj in [8] showed that, in case of a supersonic civil transport aircraft an increase of one drag count augments the takeoff gross weight of 18750 lb. Today, the demand for air travel is increasing with the same rate at which the need of more efficient and eco-friendly aircraft is advancing and the cited examples highlight the high impact of the aerodynamic drag on airplane-transport economy and environmental acceptance.

A correct drag prediction by both CFD and EFD procedures is a crucial point for the design of the next-generation aircraft. Thanks to recent technological advances (sophisticated sensors and high performance computing systems) the aerodynamic force, and in particular the drag, can be calculated more accurately. Anyway, the interest in more and more complex flows pushed the designers to the application of unconventional methods to *purify* the aerodynamic force computation from the error (in case of CFD computation the so-called *spurious drag* is an unphysical drag contribution introduced by the solver) and better understand how and where the aerodynamic force is generated.

In aeronautical application, the aerodynamic drag is firstly linked to the flow viscosity that generates the irreversible processes accounted by the *friction drag* and changes the pressure distribution over the body producing the *form drag*. The sum of friction and form drag is called *viscous drag*. If a lifting body is considered the trailing vortex system related to lift production also affects the pressure distribution over the body generating the *lift-*

induced drag [9, 10]. Finally, in transonic and supersonic flow regimes, when shock waves arises, another drag contribution, the *wave drag*, comes out. Viscous, induced and wave drag contributions are deeply connected to the flow phenomena occurring around the aerodynamic body so that, the decomposition of the total aerodynamic drag in these components allows the aerodynamicists for adopting ad-hoc design solutions with the aim to reduce one or another drag source. This task, not possible by using the standard *near field* aerodynamic force expression, is a crucial point for aerodynamic optimization as stressed by Van Dam; in [11], discussing about the pressure drag, he states: *"note that the total pressure drag is the result of three quite different flow phenomena; (1) boundary-layer displacement effect, (2) trailing vortex system, and (3) shock waves. The design approaches typically followed to reduce/minimize each of these pressure drag components tend to be quite different. For instance, varying the wing span has a dramatic effect on the trailing vortex system and, hence, the induced drag, but, this does not play a significant role in the boundary-layer development and, hence, the form drag."*

The aerodynamic force computation and its breakdown by *far field* approach is the core theme of present dissertation. First, the far-field aerodynamic force analysis techniques will be recalled and discussed in Chapter 1. In Chapter 2 an exact unconventional aerodynamic force formula based on the *vortex force* will be presented. Its theoretical extension to inviscid steady flow is provided and its link with classical thermodynamic methods is analyzed. In Chapter 3 the application of both thermodynamic and vortical methods for the aerodynamic force breakdown applied to CFD solutions of the flow around innovative aeronautical configurations is proposed.

1.3 Far-field Methods

With the term *Far-field Methods* are intended all the techniques for aerodynamic force computation and breakdown based on the flow variables integration far from the body. Even if the *Thermodynamic Methods* and the *Vortical Methods* can be ascribed to the Far-field Methods category it has been chosen to separate them because linked to particular variables of the flow field: the flow entropy and the vorticity field, respectively.

1.3.1 Betz: the Wing-section Drag (1925)

Betz's method [12] is historically the first example of *direct* calculation of a drag component: the *wing-section drag*. Before, it was indirectly obtained by subtracting the induced

drag (computed by Prandtl's theory) from the total drag.

Betz used Ackeret's idea of calculating the drag directly from the energy loss of the air and introduced an experimental technique for computing the wing-section drag in case of both lifting and non-lifting bodies immersed in incompressible and steady flow. If the flow is assumed to be substantially two-dimensional, the wing-section drag can be computed with the impulse law and the total pressure loss:

$$D_{w-s} = \int_{\mathcal{W}} (p_{T\infty} - p_T)\ \mathrm{dS} - \frac{\rho}{2} \int_{\mathcal{W}} \left[\left(u' - u\right) \left(2u_\infty - u' - u\right) \right]\ \mathrm{dS}\,, \qquad (1.10)$$

where $\mathcal{W}$ is a line behind the wing section far enough to have the velocity parallel to the freestream, p_T is the total pressure, u is the velocity component parallel to the freestream and u' is the velocity of the "potential flow" present outside the vortical region. With an order of magnitude analysis Betz showed that the second integral of Eq. (1.10) is 20 times lower than the first one so that an acceptable estimation of the wing-section drag can be obtained by total pressure loss only.

An important advantage of Betz's method is the possibility to determine the wing-section drag for each individual section letting the designers to identify the body parts that mostly affect the aerodynamic performance.

1.3.2 Jones: improved Betz's Method (1936)

Jones improved Betz's technique for the computation of the wing-section drag avoiding the introduction of the potential-flow velocity u' [13]. His method states that the wing-section drag is:

$$D_{ws} = p_{d\infty} \int_{\mathcal{W}} 2\sqrt{p_d^* - p^*} \left(1 - \sqrt{p_d^*}\right)\ \mathrm{dS}, \qquad (1.11)$$

where $p_d = 1/2\rho V^2$ is the dynamic pressure, p is the static pressure whereas the superscript '$*$' indicates a dimensionless pressure with respect to $p_{d\infty}$.

Figure 1.3.1 shows the comparison between the wing-section drag computed by Betz's and Jones' methods in case of Hart K-1442 airplane experimental set. The results clearly differ only when the wake plane position $r_{\mathcal{W}}$ is very near the trailing edge.

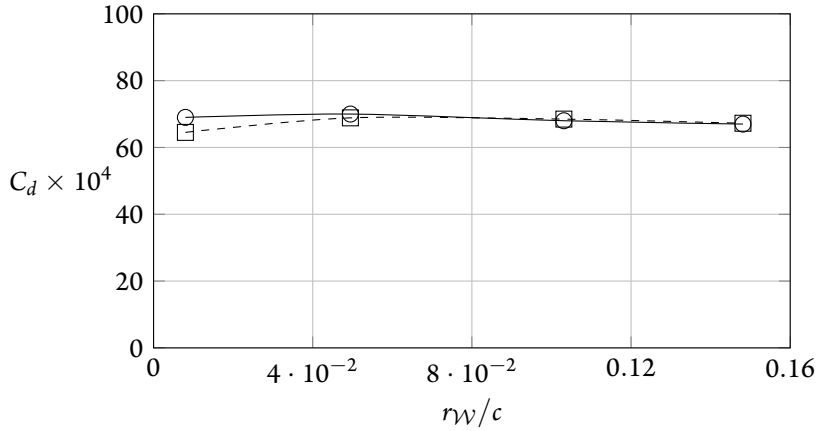


Figure 1.3.1: Hart K-1442 experimental set. Comparison between wing-section drag computed by Betz's and Jones' methods changing the wake plane position in fraction of chord $r_{\mathcal{W}}/c$. Jones (—○—), Betz (- □ -). Extracted from [13].

1.3.3 Maskell: Induced Drag Formula (1972)

Maskell in [14] proposed two aerodynamic force formulae to compute both lift and drag using the flow variables in an ideal plane $\mathcal{W}$ transverse to the freestream and downstream the body, where the variation of u, the velocity component parallel to the freestream, can be assumed negligible; such a plane is called *Trefftz plane*. The formulae are valid in the hypothesis of incompressible and steady flow.

The expression of the total drag contains a corrected version of the Betz's formula for the computation of the wing-section drag that takes into account for the wind tunnel blockage in case of experimental set. The remaining part of the formula corresponds to the induced drag, given by the following expression:

$$D_{\mathrm{i}} = \frac{\rho}{2} \int_{\mathcal{W}} (\psi \zeta_x - \Phi \sigma) \, \mathrm{dS} \,, \tag{1.12}$$

where ρ is the fluid density, ψ is the stream function, ζ_x is the vorticity component in freestream direction, Φ is the flow potential and σ is the source strength given by $\sigma = \frac{\partial v}{\partial y} + \frac{\partial w}{\partial z}$. Generally, the contribution of the term containing σ is negligible respect to the other [15] which means that trailing vorticity should fully account for induced drag, and that the effect of streamwise gradients in the wake should not be significant. Therefore,

the induced drag can be straightforwardly obtained by:

$$D_{\mathrm{i}} \approx \frac{\rho}{2} \int_{\mathcal{W}} \psi \zeta_x \, \mathrm{dS} \,, \tag{1.13}$$

with ψ computed by the integration of the Poisson's equation $\nabla^2 \psi = -\zeta_x$ or using the Green's function method [16].

1.4 Thermodynamic Methods

Thermodynamic Methods have been developed since the introduction of Oswatitsch's entropy drag concept [17]. These methods are based on the separation between the reversible and irreversible flow phenomena, used to realize the drag breakdown by momentum equation. The irreversible drag is identified by selecting the component associated to entropy production. Thermodynamic methods are widely adopted in industrial and research environment [18, 19] and already contributed to the design of last generation of transonic transport aircrafts. Anyway, they are limited to the computation and analysis of the force components of irreversible nature and therefore cannot compute and analyze lift. Lift-induced drag can be derived only in an indirect way by subtracting the irreversible drag to the near-field force.

1.4.1 Oswatitsch: entropy drag concept (1956)

Starting from the thermodynamic entropy definition and both momentum and energy equations Oswatitsch directly linked the profile drag to the product of the freestream temperature T_∞ times the entropy flux through a surface $S_{\text{ent.}}$ enclosing all the entropy changes caused by the presence of the body [17]:

$$D_{\text{ent.}} = \frac{T_\infty}{V_\infty} \int_{S_{\text{ent.}}} \rho u \Delta s \, \mathrm{dS} \,. \tag{1.14}$$

Equation 1.14 clearly links the drag production to the *irreversible* processes occurring in the steady and compressible flow and accounts for the drag rise of compressible shocks; if the shocks are curved, the flow behind them shows temperature variations whose equilibrium also causes an entropy rise but it is small if compared with the one across the shock itself and can be neglected in first approximation.

Lock [20] used Eq. (1.14) for computing the wave drag in inviscid flows in terms of entropy jumps across the shocks.

Kusunose [21] applied the entropy drag concept to experiments and was able to obtain an approximate split of the profile drag into viscous and wave components by wind tunnel wake survey. This decomposition was possible thanks to the introduction of a vorticity magnitude cutoff that enabled the separation of viscous and wave regions.

1.4.2 Van Der Vooren & Destarac (2003-4)

Van der Vooren & Destarac proposed a full aerodynamic drag breakdown in [22] and a drag/thrust bookkeeping for jet-propelled aircraft in [23].

In power-off conditions they derived a far field expression of viscous and wave drag starting from Eq. (1.9) and steady flow hypothesis. It was possible by dividing the flow field in which the body is immersed in the so-called *viscous inner flow* (composed by $\mathcal{V}_v$, containing the boundary layers and the viscous shear layers, and $\mathcal{V}_w$, containing the shock layers) and the *inviscid outer flow*. Assuming the latter volume truly inviscid and without trailing vortices inside, the total drag is given by the viscous drag D_v and the wave drag D_w that can be computed by the streamwise momentum balance at the far-field wake plane $\mathcal{W}$

$$D_v + D_w = -\int_{\mathcal{W}} \rho \Delta u \, (\underline{V} \cdot \underline{n}) \; \mathrm{dS} \,, \tag{1.15}$$

where $\Delta u = u_{\mathrm{irr}} - u_\infty$ is the variation of the streamwise velocity component due to irreversible processes and $\underline{n}$ is the unit vector normal to $\mathcal{W}$. Δu can be expressed in terms of entropy and stagnation enthalpy variations ($\Delta s = s - s_\infty$ and $\Delta H = H - H_\infty$ respectively):

$$u_{irr} = u_\infty \sqrt{1 + \frac{2\Delta H}{u_\infty^2} - \frac{2}{(\gamma - 1) M_\infty^2} \left[e^{\dfrac{(\gamma - 1)\, \Delta s}{\gamma R}} - 1 \right]} \,, \tag{1.16}$$

where R is the gas constant, M_∞ is the freestream Mach number and γ is the heat capacity ratio. Using the Gauss' Theorem Eq. (1.15) becomes

$$D_v + D_w = -\int_{\mathcal{V}_v \cup \mathcal{V}_w} \underline{\nabla} \cdot (\rho \Delta u \underline{V}) \; \mathrm{d}\mathcal{V} \,, \tag{1.17}$$

that, with a proper identification of $\mathcal{V}_v$ and $\mathcal{V}_w$, allows for the following drag breakdown in

viscous and wave drag contributions

$$D_{\mathrm{v}} = -\int_{\mathcal{V}_{\mathrm{v}}} \underline{\nabla} \cdot (\rho \Delta u \underline{V}) \; \mathrm{d}\mathcal{V} \,, \tag{1.18}$$

$$D_{\mathrm{w}} = -\int_{\mathcal{V}_{\mathrm{w}}} \underline{\nabla} \cdot (\rho \Delta u \underline{V}) \; \mathrm{d}\mathcal{V} \,. \tag{1.19}$$

Computing the total drag with the streamwise component of the aerodynamic force $\underline{F} \cdot \underline{e}_x$ by near-field formula Eq. (1.6), the induced drag is obtained by subtracting the viscous and the wave drag components from it

$$D_{\mathrm{i}} = -\int_{\mathcal{V}_{\mathrm{v}} \cup \mathcal{V}_{\mathrm{w}}} \underline{\nabla} \cdot (\rho \Delta u \underline{V}) \, \mathrm{d}\mathcal{V} - \underline{F} \cdot \underline{e}_x \,, \tag{1.20}$$

where $\underline{e}_x$ defines the freestream direction. Assuming the *exact near field/far field drag balance* Eq. (1.9) can be used to compute $\underline{F} \cdot \underline{e}_x$; applying the Gauss' Theorem and the small disturbance theory, Eq. (1.20) returns the Maskell's formula for induced drag computation Eq. (1.13).

The first drawback of this theory is that the drag breakdown is based on a *definition*: Destarac & van der Vooren assume that the irreversible velocity is given by Eq. (1.16); if u_{irr} definition is incorrect an incorrect drag breakdown is realized. The second and the biggest drawback, present generally in all the thermodynamic methods, is the indirect definition of induced drag, consequence of the assumption of an *exact near field/far field drag balance*. This is not assured when dealing with CFD data where the already discussed spurious drag, due to numerical error, is present in the entire flow domain considered for the integration of the far field formula. In particular, a non-negligible production of spurious drag is confined in a small region in the immediate vicinity of the aircraft and is linked to the explicit numerical dissipation introduced by the numerical technique, whereas a second lower production of spurious drag is related to the grid coarsening and happens in a wider flow domain far from the body [24].

Computing D_{v} and D_{w} with Eq. (1.17), and the induced drag with Maskell's formula the second spurious drag contribution can be detected as:

$$D_{\mathrm{sp}} = -\int_{\mathcal{V} - \mathcal{V}_{\mathrm{v}} \cup \mathcal{V}_{\mathrm{w}}} [\underline{\nabla} \cdot (\rho \Delta u \underline{V})] \; \mathrm{d}\mathcal{V} \,, \tag{1.21}$$

and a more precise drag breakdown can be obtained

$$D_{\text{near}} = D_{\text{v}} + D_{\text{w}} + D_{\text{i}} + D_{\text{sp}} \,. \tag{1.22}$$

Repeating the theoretical analysis in case of power-on conditions Destarac & van der Vooren obtained a drag/thrust bookkeeping method defining the total thrust from the momentum balance

$$T = -\int_{S_{\text{in}} \cup S_{\text{out}}} \left[\rho u \left(\underline{V} \cdot \underline{n}\right) + \left(p - p_\infty\right) \underline{e}_x - \left(\underline{\underline{\tau}} \cdot \underline{n}\right)\right] \, \mathrm{dS} \,, \tag{1.23}$$

and further dividing it in the thrust contribution given by the momentum linked to the fuel consumption $\dot{m}u$ and the *pre-entry thrust* T_{pre}. The net thrust given by aircraft engines is obtained by reducing T of the *scrubbing drag* D_{scrub} and the *throughflow drag* D_{tf}.

Thus, the following thrust/drag bookkeeping is proposed

$$D_{\text{v}} + D_{\text{w}} + D_{\text{i}} + D_{\text{tf}} + D_{\text{scrub}} = \overline{T} + \dot{m}u + T_{\text{pre}} \,, \tag{1.24}$$

where $\overline{T} = T - \dot{m}u - T_{\text{pre}}$.

Two applications of the drag breakdown and the drag/thrust bookkeeping proposed by Destarac & van der Vooren are reported. The first one allows the reader to appreciate the accuracy improvements reachable with a far field drag computation instead of the standard near-field technique. In Fig. 1.4.1 the drag computed by numerical analysis is compared with the experimental values in case of wing-body large transport aircraft; removing almost 10 drag counts of spurious contribution from the near field value, the far field gets closer the experimental result.

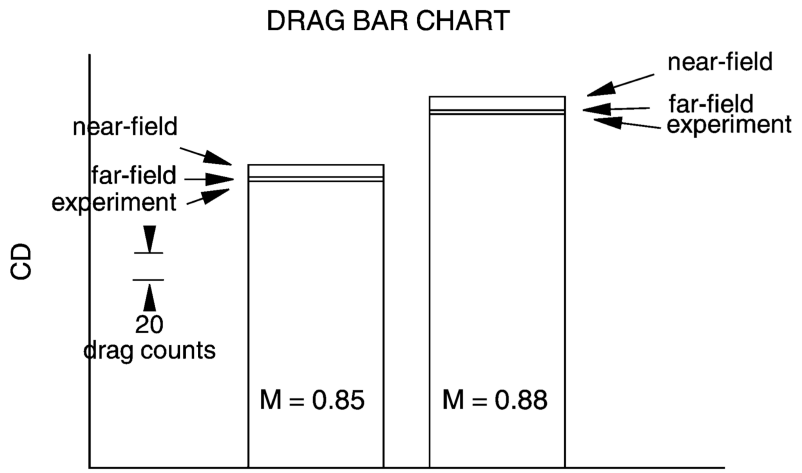


Figure 1.4.1: Drag bar chart. Wing-body large transport aircraft at $M_\infty = 0.85$, $Re_\infty = 8 \times 10^6$ and $C_L \approx 0.5$. RANS computations with $k-l$ turbulence model and 3.8 million cells. Extracted from [23].

In the second application the drag polars of the DLR/ALVAST twin engine transport aircraft configuration has been obtained in both power-off and power-on conditions (see Fig. 1.4.2). A comparison with the experimental data shows that 17 spurious drag counts have been found in wing-body configuration and 30 in wing-body-pylon-nacelle one. The regions used for D_v and D_w computations are shown in Fig. 1.4.3.

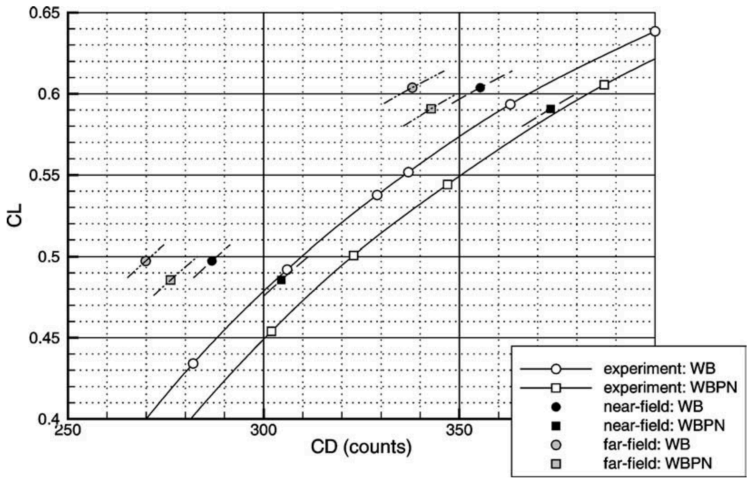


Figure 1.4.2: Drag polars. DLR-ALVAST aircraft in power-off (WB) and power-on (WBPN) configurations at $M_\infty = 0.75$, $Re_\infty = 4.3 \times 10^6$ and $C_L \approx 0.5$. RANS computations with $k-\zeta$ turbulence model and 1.5 million cells for WB and 4.0 million cells for WBPN. Extracted from [23].

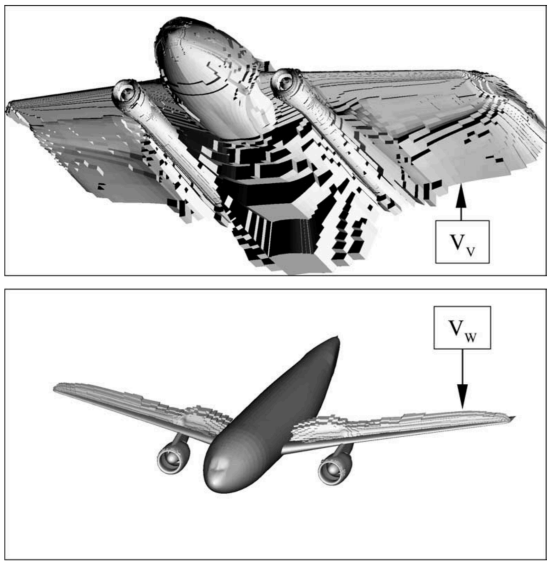


Figure 1.4.3: Regions selected for far field drag analysis. DLR-ALVAST aircraft in power-off (WB) and power-on (WBPN) configurations at $M_\infty = 0.75$, $Re_\infty = 4.3 \times 10^6$ and $C_L \approx 0.5$. RANS computations with $k-\zeta$ turbulence model and 1.5 million cells for WB and 4.0 million cells for WBPN. Extracted from [23].

1.4.3 Paparone & Tognaccini (2003-5)

Paparone & Tognaccini stressed the entropy drag concept to obtain a total drag breakdown for both 2D and 3D flow in power-off conditions. The streamwise integral momentum equation extended on a far-field surface is:

$$D = -\int_{\Sigma - S_B} \left[(p - p_\infty)\, \underline{e}_x + \rho u\, (\underline{V} \cdot \underline{n}) \right] \, \mathrm{dS}\,, \tag{1.25}$$

and gives the total drag. In Eq. (1.25) $\Sigma - S_B$ represents a surface far from the body, $\underline{e}_x$ is the streamwise direction and u is the velocity component parallel to it. The authors first showed that, in case of 2D subsonic flows and in the limit of $\Sigma - S_B \rightarrow S_\infty$, the integral of $(p - p_\infty)\, \underline{e}_x$ gives no contribution D. Thus, Eq. (1.25) becomes:

$$D = -\int_{S_\infty} \rho V\, (\underline{V} \cdot \underline{n}) \, \mathrm{dS}\,, \tag{1.26}$$

where u has been expressed as $V cos\delta$ with $\delta = \arctan(w/v)$ and expanded in Taylor's series. Expressing the velocity module in terms of total enthalpy variations ΔH, entropy variations Δs and static pressure variations Δp and expanding in Taylor's series, Eq. (1.26) is rewritten as follows

$$\begin{aligned} D = &- V_\infty \left\{ \int_{S_\infty} \left[f_{s1} \frac{\Delta s}{R} + f_{s2} \left(\frac{\Delta s}{R} \right)^2 \right] \rho\, (\underline{V} \cdot \underline{n}) \, \mathrm{dS} \right. \\ &+ \int_{S_\infty} \left[f_{H1} \frac{\Delta H}{V_\infty^2} + f_{H2} \left(\frac{\Delta H}{V_\infty^2} \right)^2 \right] \rho\, (\underline{V} \cdot \underline{n}) \, \mathrm{dS} \\ &\left. + \int_{S_\infty} f_{sH2} \frac{\Delta s}{R} \frac{\Delta H}{V_\infty^2} \rho\, (\underline{V} \cdot \underline{n}) \, \mathrm{dS} \right\} \\ &+ \mathcal{O}\left[\left(\frac{\Delta s}{R} \right)^3, \left(\frac{\Delta H}{V_\infty^2} \right)^3, \dots \right], \end{aligned} \tag{1.27}$$

where $f_\otimes$ are the coefficients of the series expansions dependent on γ and M_∞. According to Eq. (1.27), if S_∞ doesn't intersect the boundary layer and no engine is present in the flow, the terms containing ΔH are negligible and the total drag (viscous + wave) can be computed by the terms related to Δs; moreover, if the Taylor's expansion stops at the first order Eq. (1.27) returns the Oswatitsch's entropy drag definition.

In three dimensional lifting flows the pressure integral is no more negligible and Eq. (1.25)

becomes

$$
\begin{aligned}
D = &- V_\infty \left\{ \int_{\Sigma - S_B} \left[f_{s1} \frac{\Delta s}{R} + f_{s2} \left(\frac{\Delta s}{R} \right)^2 \right] \rho \left(\underline{V} \cdot \underline{n} \right) \, \mathrm{dS} \right. \\
&+ \int_{\Sigma - S_B} \left[f_{H1} \frac{\Delta H}{V_\infty^2} + f_{H2} \left(\frac{\Delta H}{V_\infty^2} \right)^2 \right] \rho \left(\underline{V} \cdot \underline{n} \right) \, \mathrm{dS} \\
&+ \int_{\Sigma - S_B} \left[1 + f_{p1} \frac{\Delta p}{p_\infty} + f_{p2} \left(\frac{\Delta p}{p_\infty} \right)^2 \right] \rho \left(\underline{V} \cdot \underline{n} \right) \, \mathrm{dS} \\
&+ \rho V_\infty \frac{1}{\gamma M_\infty^2} \int_{\Sigma - S_B} \frac{\Delta p}{p_\infty} \, \mathrm{dS} \\
&\left. + \int_{\Sigma - S_B} \left(f_{ps2} \frac{\Delta s}{R} \frac{\Delta p}{p_\infty} + f_{sH2} \frac{\Delta s}{R} \frac{\Delta H}{V_\infty^2} \right) \rho \left(\underline{V} \cdot \underline{n} \right) \, \mathrm{dS} \right\} \\
&+ \mathcal{O} \left[\left(\frac{\Delta s}{R} \right)^3, \left(\frac{\Delta H}{V_\infty^2} \right)^3, \left(\frac{\Delta p}{p_\infty} \right)^3, \dots \right] ,
\end{aligned}
\tag{1.28}
$$

where $\Sigma - S_B$ can be placed anywhere in the flow field even if the induced drag can be converted in entropy drag increasing the distance of $\Sigma - S_B$ from the body surface. It is worth noting that Eq. (1.27) and Eq. (1.28) differs only for the presence of the integrands containing $\Delta p / p_\infty$ that can so directly related to the induced drag generation. Moreover, the entropy drag in both 2D and 3D flows can be computed by volume integral and a breakdown in viscous and wave drag is obtained after the identification of boundary layer and shock wave regions. In the remaining part of the flow domain the spurious entropy drag is computed:

$$
D_v = V_\infty \int_{\mathcal{V}_v} \underline{\nabla} \cdot \left(\rho g \underline{V} \right) \, \mathrm{d}\mathcal{V} \, , \tag{1.29}
$$

$$
D_w = V_\infty \int_{\mathcal{V}_w} \underline{\nabla} \cdot \left(\rho g \underline{V} \right) \, \mathrm{d}\mathcal{V} \, , \tag{1.30}
$$

$$
D_{sp} = V_\infty \int_{\mathcal{V}_{sp}} \underline{\nabla} \cdot \left(\rho g \underline{V} \right) \, \mathrm{d}\mathcal{V} \, , \tag{1.31}
$$

where $g \left(\Delta s / R \right) = - f_{s1} \left(\Delta s / R \right) - f_{s2} \left(\Delta s / R \right)^2$. The selection of the flow regions where the drag is generated is provided by ad-hoc flow sensor; in Section 3.1.3 these sensors will be briefly described and applied for the drag breakdown of an innovative turboprop wing-body configuration.

The described drag breakdown method has been successfully applied to both 2D and

3D configurations. In Fig. 1.4.4 the effect of grid size on both near-field and far-field drag computation is analyzed: it is shown that removing the spurious contribution, the value of viscous and drag contributions is independent of the grid size. In Fig. 1.4.5 the drag breakdown on the DLR-ALVAST wing-body configuration, the same analyzed by Destarac & van der Vooren, is presented.

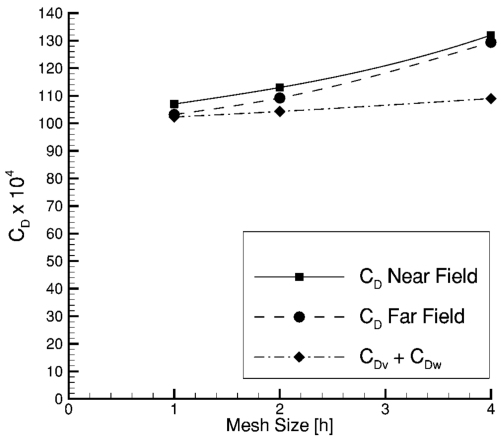


Figure 1.4.4: Grid convergence analysis on a NACA0012 airfoil at $M_\infty = 0.7$, $Re_\infty = 49 \times 10^6$ and $C_L = 0.24$. RANS computations with163 thousand cells for $h = 1$ grid level. Extracted from [25].

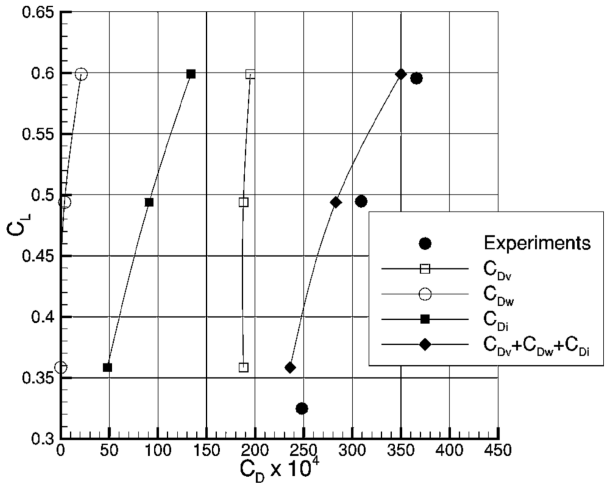


Figure 1.4.5: Drag polars of DLR-ALVAST wing-body at $M_\infty = 0.75$, $Re_\infty = 4.3 \times 10^6$. RANS computations with 1.5 million cells. Extracted from [25].

Tognaccini in [26] proposed a thrust/drag bookkeeping formula for jet propelled configurations. He defined the *modified overall net thrust* $\tilde{T}_o$ as the momentum balance between the capture area and the infinitely downstream interface T_o without the contribution δT_{tb} which is the first order effect introduced by the boundary layer of the exhaust jet

$$\tilde{T}_o = T_o - \delta T_{tb} \,. \tag{1.32}$$

Introducing p_i as the pressure field of an equivalent ideal flow around the same geometry and with the same freestream and engine working conditions, the nacelle drag is defined as follows

$$D_{nac} = \underline{e}_x \cdot \int_{S_{nac}} \left\{ \left[(p - p_i)\, \underline{\underline{I}} - \underline{\underline{\tau}} \right] \cdot \underline{n} \right\} \, \mathrm{dS} \,, \tag{1.33}$$

with S_{nac} given by the external nacelle surface.

Finally, the drag/thrust bookkeeping is:

$$F_x = \tilde{T}_o + D_{nac} \,. \tag{1.34}$$

1.4.4 Gariepy et al. (2011-13)

Starting from the method proposed by Destarac & van der Vooren Section 1.4.2, Gariepy et al. [27] derived a new drag breakdown based on a different definition of the *irreversible velocity* to overcome the problem of a possible negative square root in Eq. (1.16)

$$u_{irr} = u_\infty \sqrt{1 + \frac{2\Delta H}{u_\infty^2} - \frac{2}{(\gamma - 1)\, M_\infty^2} \left[\left(\frac{p}{p_\infty} \right)^{\frac{\gamma - 1}{\gamma}} - 1 \right] - \frac{v^2 + w^2}{u_\infty^2}} \,. \tag{1.35}$$

The irreversible velocity is responsible for D_{irr}, linked to viscous and wave and spurious drag contributions; the induced drag (D_{rev}) is computed ad the counterpart of the streamwise momentum balance equation. In [28] this drag breakdown is applied to the Drag Prediction Workshop (DPW) 5 cases. DPWs are organized by the *American Institute for Aeronautics and Astronautics* in order to give the possibility to companies, universities and research centers to discuss and propose numerical drag computations on common configurations. In Fig. 1.4.6 the *Nasa Common Research Mode* (CRM), a standard wing-body configuration used as a reference for drag prediction in transonic flight, is showed; in Fig. 1.4.7 its drag breakdown at $Re_\infty = 5 \times 10^6, M_\infty = 0.85$ and $C_L \approx 0.5$ is reported.

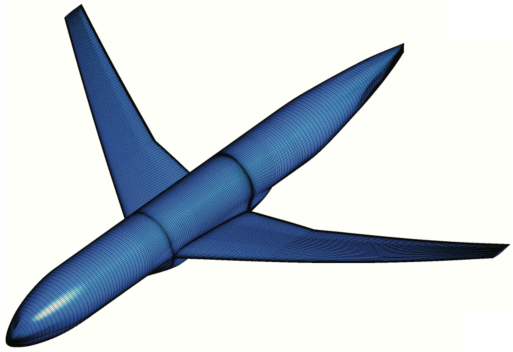
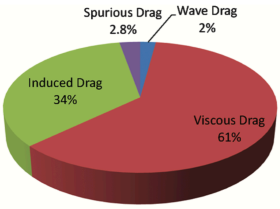


Figure 1.4.6: IDEA grid set for NASA Common Research Model. Extracted from [28].



	Wave	Viscous	Induced	Spurious	Total
Drag Count	5.5	156.0	87.7	7.3	249.2

Figure 1.4.7: Drag breakdown of the NASA CRM at $M_\infty = 0.75$, $Re_\infty = 5 \times 10^6$. Extracted from [28].

1.4.5 Thermodynamic Methods for Unsteady Flow

Thermodynamic methods have been developed also to perform the drag computation and its breakdown in unsteady flows. Gariepy et al. [29] defined a reversible drag (generated without entropy production) caused by the unsteady fluctuations in the flow; it is given by the volume integral of all the time-dependent terms present in the streamwise momentum balance. Similarly, using an inertial reference frame for the momentum balance integration, Toubin & Bailly [30, 31] proposed obtained another drag breakdown in wave, viscous and (unsteady) lift-induced drag.

1.5 Vortical Methods

"Lift is number-one issue in aerodynamics. ...A successful physical theory has to capture its features". With this statements Wu et al. [32] asserted the importance of direct lift (and lift-

induced drag) computation in aerodynamics. Vortical Methods rely on the flow vorticity field and allows for the analysis of the entire aerodynamic force (both lift and drag) using CFD and EFD data. In the following pages the main developments and results obtained by vortical-methods researchers are recalled.

1.5.1 Noca et al. 1999

Noca et al. [33] derived three exact formulae for the computation of the total aerodynamic force in unsteady flows. As in Thermodynamic Methods, the starting point is the integral momentum equation extended to the material volume $\mathcal{V}_m(t)$ (Eq. (1.3)). This equation contains a pressure term that hides the explicit link between the flow structures and the aerodynamic force. To overcome this inconvenience the authors rearranged Eq. (1.3) in a form involving the time derivative of the impulse and the flow-particle position vector $\underline{r}$

$$\begin{aligned}\underline{F} = &-\frac{1}{k}\frac{\mathrm{d}}{\mathrm{d}t}\int_{\mathcal{V}_\infty(t)}\left(\underline{r}\times\underline{\zeta}\right)\,\mathrm{d}\mathcal{V}\\ &+\frac{1}{k}\frac{\mathrm{d}}{\mathrm{d}t}\int_{S_B(t)}\left[\underline{r}\times\left(\underline{n}\times\underline{V}\right)\right]\,\mathrm{dS}\\ &-\int_{S_B(t)}\left[\underline{n}\cdot\left(\underline{V}-\underline{V}_B\right)\underline{V}\right]\,\mathrm{dS}\,,\end{aligned} \tag{1.36}$$

where $k = N - 1$ ($N = 2, 3$ in 2D and 3D flows, respectively), $\underline{\zeta}$ is the fluid vorticity and $\underline{V}_B$ is the body wall velocity, if present. Equation 1.36 has traditionally been known to be valid for infinite fluid regions $\mathcal{V}_\infty$ delimited by kinematic surfaces.

Using Eqs. (1.3) and (1.36) the following formulae are derived:

$$\begin{aligned}\underline{F} = &-\frac{1}{k}\frac{\mathrm{d}}{\mathrm{d}t}\int_{\mathcal{V}_m(t)}\underline{r}\times\underline{\zeta}\,\mathrm{d}\mathcal{V}\\ &+\int_{\Sigma(t)-S_B(t)}\underline{n}\cdot\underline{\underline{\gamma}}_{\mathrm{imp}}\,\mathrm{dS}\\ &+\frac{1}{k}\frac{\mathrm{d}}{\mathrm{d}t}\int_{S_B(t)}\left[\underline{r}\times\left(\underline{n}\times\underline{V}\right)\right]\,\mathrm{dS}\\ &-\int_{S_B(t)}\left[\underline{n}\cdot\left(\underline{V}-\underline{V}_B\right)\right]\underline{V}\,\mathrm{dS}\,,\end{aligned} \tag{Impulse Equation}$$

where

$$\begin{aligned}\underline{\underline{\gamma}}_{\text{imp}} =& \frac{1}{2}V^2\underline{\underline{I}} - \underline{V}\underline{V} - \frac{1}{k}\left(\underline{V}-\underline{V}_{\text{B}}\right)\left(\underline{r}\times\underline{\zeta}\right)\\ &+\frac{1}{k}\underline{\zeta}\left(\underline{r}\times\underline{V}\right)+\frac{1}{k}\left[\underline{r}\cdot\left(\underline{\nabla}\cdot\underline{\underline{\tau}}\right)\underline{\underline{I}}-\underline{r}\left(\underline{\nabla}\cdot\underline{\underline{\tau}}\right)\right]+\underline{\underline{\tau}}\,.\end{aligned} \tag{1.37}$$

$$\begin{aligned}\underline{F} =& -\frac{\mathrm{d}}{\mathrm{d}t}\int_{\mathcal{V}_{\text{m}}(t)}\underline{V}\,\mathrm{d}\mathcal{V}\\ &+\int_{\Sigma(t)-S_{\text{B}}(t)}\underline{n}\cdot\underline{\underline{\gamma}}_{\text{mom}}\,\mathrm{dS}-\int_{S_{\text{B}}(t)}\underline{n}\cdot\left(\underline{V}-\underline{V}_{\text{B}}\right)\underline{V}\,\mathrm{dS}\,,\end{aligned} \tag{Momentum Equation}$$

where

$$\begin{aligned}\underline{\underline{\gamma}}_{\text{mom}} =& \frac{1}{2}V^2\underline{\underline{I}}+\left(\underline{V}_{\text{B}}-\underline{V}\right)\underline{V}-\frac{1}{k}\underline{V}\left(\underline{r}\times\underline{\zeta}\right)\\ &+\frac{1}{k}\underline{\zeta}\left(\underline{r}\times\underline{V}\right)-\frac{1}{k}\left[\left(\underline{r}\cdot\frac{\partial\underline{V}}{\partial t}\right)\underline{\underline{I}}-\underline{r}\frac{\partial\underline{V}}{\partial t}\right]\\ &+\frac{1}{k}\left[\underline{r}\cdot\left(\underline{\nabla}\cdot\underline{\underline{\tau}}\right)\underline{\underline{I}}-\underline{r}\left(\underline{\nabla}\cdot\underline{\underline{\tau}}\right)\right]+\underline{\underline{\tau}}\,.\end{aligned} \tag{1.38}$$

$$\begin{aligned}\underline{F} =& \int_{\Sigma(t)-S_{\text{B}}(t)}\underline{n}\cdot\underline{\underline{\gamma}}_{\text{flux}}\,\mathrm{dS}\\ &-\int_{S_{\text{B}}(t)}\underline{n}\cdot\left(\underline{V}-\underline{V}_{\text{B}}\right)\underline{V}\,\mathrm{dS}-\frac{\mathrm{d}}{\mathrm{d}t}\int_{S_{\text{B}}(t)}\underline{n}\cdot\left(\underline{V}\underline{r}\right)\,\mathrm{dS}\,,\end{aligned} \tag{Flux Equation}$$

where

$$\begin{aligned}\underline{\underline{\gamma}}_{\text{flux}} =& \frac{1}{2}V^2\underline{\underline{I}}-\underline{V}\underline{V}-\frac{1}{k}\underline{V}\left(\underline{r}\times\underline{\zeta}\right)+\frac{1}{k}\underline{\zeta}\left(\underline{r}\times\underline{V}\right)\\ &-\frac{1}{k}\left[\left(\underline{r}\cdot\frac{\partial\underline{V}}{\partial t}\right)\underline{\underline{I}}-\underline{r}\frac{\partial\underline{V}}{\partial t}+k\frac{\partial\underline{V}}{\partial t}\underline{r}\right]\\ &+\frac{1}{k}\left[\underline{r}\cdot\left(\underline{\nabla}\cdot\underline{\underline{\tau}}\right)\underline{\underline{I}}-\underline{r}\left(\underline{\nabla}\cdot\underline{\underline{\tau}}\right)\right]+\underline{\underline{\tau}}\,.\end{aligned} \tag{1.39}$$

With the Impulse Equation the volume integration of Eq. (1.36) can be limited to a finite domain $\mathcal{V}_{\text{m}}(t)$ and thus used in CFD and EFD applications. The Momentum Equation is an equivalent expression of Eq. (1.3) but it doesn't contain the pressure term. The Flux Equation eliminates the volume integrations of previous equations (it is not a trivial task to capture the boundary-layer structures in experimental situations); anyway, its validity is limited to incompressible flows. The three expressions can be used in both experiments and numerical simulations; their application for the computation of the lift of an oscillating cylinder of diameter D immersed in an incompressible viscous flow at freestram velocity U ($Re_\infty = 392$) is shown in Figs. 1.5.1 and 1.5.2.

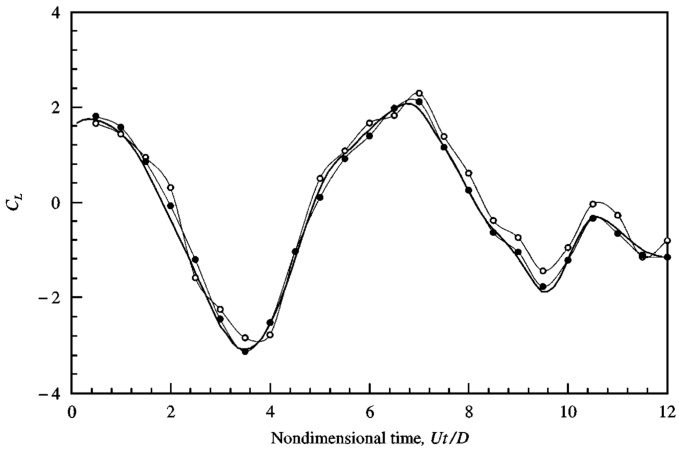


Figure 1.5.1: Oscillating cylinder in incompressible flow. Comparison of lift coefficient C_L obtained with: near-field (——), Impulse Equation (—○—), Momentum Equation (—●—). Extracted from [33].

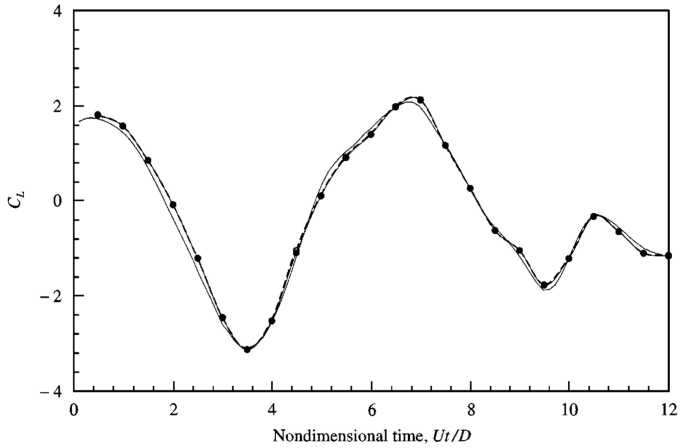


Figure 1.5.2: Oscillating cylinder in incompressible flow. Comparison of lift coefficient C_L obtained with: near-field (——), Momentum Equation (– ○ –), Flux Equation (—●—). Extracted from [33].

1.5.2 Wu et al. (2006-19)

Wu et al. [34] proposed two innovative unconventional exact formulae to compute aerodynamic force in incompressible viscous unsteady flows, based on the local vorticity field $\underline{\zeta}$ and the vector identities known as *Derivative Moment Transformations* (DMT), reported

in appendix A. The first equation is:

$$\underline{F} = -\frac{\mu}{k}\int_{\mathcal{V}} \underline{r} \times \nabla^2 \underline{\zeta}\, \mathrm{d}\mathcal{V} + \underline{F}_{\mathrm{B}} + \underline{\Delta}_{\mu}\,, \qquad \text{(Diffusion Form)}$$

where

$$\begin{aligned} \underline{F}_{\mathrm{SB}} &= \frac{1}{k}\int_{\mathrm{B}} \rho \underline{r} \times (\underline{n} \times \underline{a})\ \mathrm{dS}\,, \\ \underline{\Delta}_{\mu} &= -\frac{\mu}{k}\int_{\Sigma - S_{\mathrm{B}}} \underline{r} \times \left[\underline{n} \times \left(\underline{\nabla} \times \underline{\zeta}\right)\right]\ \mathrm{dS} + \mu \int_{\Sigma - S_{\mathrm{B}}} \underline{\zeta} \times \underline{n}\, \mathrm{dS}\,. \end{aligned} \tag{1.40}$$

The term denoted as $\underline{F}_B$ is caused by the body acceleration $\underline{a}$, which takes into account both body motion and potential body deformations whereas the surface integral $\underline{F}_{\Sigma}$, over the external surface $\Sigma - S_{\mathrm{B}}$ explicitly depends on the local viscous stresses.

Second formula can be derived from the Diffusive Form by means of DMT

$$\underline{F} = -\rho \int_{\mathcal{V}} \left(\frac{\underline{r}}{k} \times \frac{\partial \underline{\zeta}}{\partial t} + \underline{\ell}\right)\ \mathrm{d}\mathcal{V} - \frac{\rho}{k}\int_{\Sigma} \underline{r} \times (\underline{n} \times \underline{\ell})\ \mathrm{dS} + \underline{F}_B + \underline{\Delta}_{\mu}\,, \quad \text{(Advection Form)}$$

where $\underline{\ell} = \underline{\zeta} \times \underline{V}$ is the Lamb vector, defined as the cross product of vorticity and velocity. Lamb vector is unquestionably linked with the aerodynamic force as discussed by Von Karman & Burgers [35] about the lift of 2D airfoils in potential flow given by Kutta-Joukowskij theorem. Saffman [36] related with a theoretical proof the aerodynamic force to the volume integral of the Lamb Vector field and named it *vortex force*. He considered bounded vorticity field and demonstrated that the vortex force contributes to the whole aerodynamic force. Wu [34] extended the vortex force concept to unbounded vorticity fields for dealing with the aerodynamic force computation in case of bodies with wakes convected infinitely downstream.

The formulae reported have been successfully applied to compute the aerodynamic force experienced by a cylinder immersed in incompressible unsteady flow. Yang et al. [37] discussed the application of the Advection Form in steady flow. They showed that, in this condition, both $\underline{F}_{\mathrm{B}}$ and $\partial\underline{\zeta}/\partial t$ are zero and that $\underline{\Delta}_{\mu}$ gives a negligible contribution at high Reynolds numbers (the ones of main aeronautical interest). Thus, the total aerodynamic force in incompressible steady flow is given by the volume integral of the Lamb vector (the vortex force) and its "angular moment" on a surface far from the body. Moreover, being the Lamb vector directly linked to the vorticity field, it is possible to limit the

integration to the vortical regions only: the boundary layer and the body wake. Wu et al. [38] argued that the surface integral in the body wake gives the total pressure deficit on the wake plane equal to the wing-section drag defined by classical far-field methods. The vortex force is thus responsible for the remaining part of the aerodynamic force: the lift, in case of 2D flow, and both lift and induced drag in 3D flows.

Anyway, as in the case of thermodynamic methods, the proposed vortical drag breakdown is affected by the exchange between induced (D_i) and profile (D_p) drag, deeply discussed in [39]. Analyzing the $\mathrm{d}C_{D_\mathrm{i}}/\mathrm{d}r_{\mathcal{W}}$ and $\mathrm{d}C_{D_\mathrm{p}}/\mathrm{d}r_{\mathcal{W}}$ functions (with both C_{D_i} C_{D_p} expressed in wake integral form), the authors concluded that exists an interval of wake plane position $r_{\mathcal{W}}$ in which both the function are nearly zero and a *quasi objective* breakdown is possible. On the other hand, they found a strong impact of flow nature (attached/separated flow) on the breakdown objectiveness. In present dissertation this hot topic has been further investigated in Chapter 2 and numerical examples of *objective drag breakdown* in case of strongly separated flow will be presented in Chapter 3.

An extension of the Advection Form for compressible flows is suggested in [38]

$$\begin{aligned}\underline{F} = &-\int_{\mathcal{V}} \left[\frac{\underline{r}}{k} \times \frac{\partial\left(\rho\underline{\zeta}\right)}{\partial t}\right] \mathrm{d}\mathcal{V} \\ &-\int_{\mathcal{V}} \left(\rho\underline{\ell} - \frac{1}{2}V^2\underline{\nabla}\rho\right) \mathrm{d}\mathcal{V} \\ &-\int_{\mathcal{V}} \frac{\underline{r}}{k} \times \left[\underline{n} \times \left(\rho\underline{\ell} - \frac{1}{2}\rho V^2\underline{\nabla}\rho\right)\right] \mathrm{dS} + \underline{F}_B + \underline{\Delta}_\mu \,.\end{aligned} \tag{1.41}$$

This extension relies on both the integrals of Lamb vector field and $\underline{\nabla}\rho$; the latter is present also in the flow regions where $\underline{\zeta} = \underline{0}$ and thus eliminates the possibly to identify the flow regions where the aerodynamic force is generated as happened with the Advection Form.

1.5.3 Tognaccini et al. (2010-16)

In order to face with the aerodynamic force breakdown from Reynolds Averaged Navier Stokes (RANS) data, Marongiu and Tognaccini [40] successfully extended Eq. (Advection Form) to turbulent flows by substituting the flow variables with averaged ones. The proof is reported in Section 2.1.2 for the compressible case. Moreover, the authors gave a proof that the term explicitly linked to the molecular viscosity $\underline{\Delta}_\mu$ is negligible in flows where the boundary layer hypothesis can be applied. In a steady, incompressible and high-

Reynolds number flow, the Advection Form Formula, proposed by Wu et al., becomes:

$$\underline{F} = \underline{F}_{\ell} + \underline{F}_{\mathcal{W}} \,, \tag{1.42}$$

where

$$\underline{F}_{\ell} = -\rho \int_{\mathcal{V}} \underline{\ell} \, \mathrm{d}\mathcal{V} \,, \tag{1.43}$$

is the vortex-force, present only in the boundary layer and in the body-wake regions;

$$\underline{F}_{\mathcal{W}} = -\frac{1}{k}\rho \int_{\mathcal{W}} \underline{r}_{\mathcal{W}} \times (\underline{n} \times \underline{\ell}) \; \mathrm{dS} \,, \tag{1.44}$$

is the Lamb-vector angular moment, present only in the wake plane $\mathcal{W}$, downstream the body.

Starting from the proof of the direct link between $\underline{F}_{\mathcal{W}}$ and the *irreversible* profile drag provided in [41] for 2D flows, Marongiu et al. [42] proved the direct link of $\underline{F}_{\ell}$ with the *reversible* lift and lift-induced drag in incompressible conditions: a first step towards the long-waited definition of induced drag in viscous flow [43]. They considered the vector identity

$$\underline{\ell} = \underline{V} \cdot \underline{\nabla V} - \underline{\nabla} \left(\frac{V^2}{2} \right) \,, \tag{1.45}$$

and that in incompressible flow $\underline{\nabla} \cdot \underline{V} = 0 \rightarrow \underline{V} \cdot \underline{\nabla V} = \underline{\nabla} \cdot (\underline{VV})$. Thus, applying Gauss'Theorem to $\underline{F}_{\ell}$, it hods

$$\underline{F}_{\ell} = \rho \int_{\Sigma - S_{\mathrm{B}}} \left[\frac{V^2}{2} \underline{n} - \underline{V} (\underline{V} \cdot \underline{n}) \right] \; \mathrm{dS} \,, \tag{1.46}$$

The obtained $\underline{F}_{\ell}$ expression is exactly the far-field expression of the total aerodynamic force in the limit of inviscid flow (taking into account for Bernoulli's theorem). In Section 2.3 a similar analysis is proposed by the author of present dissertation for compressible flow.

The application of Eq. (1.42) to the case of an elliptical wing with $\mathcal{AR} = 7, M_{\infty} = 0.01$ and $Re_{\infty} = 3 \times 10^6$ is showed in Fig. 1.5.3. The vortex-force contribution is compared with Maskell's formula and Prandtl's formula $\left(C_{D_{\mathrm{i}}} = C_L^2 / (\pi \mathcal{AR}) \right)$ for induced drag computation. The three expressions are always in remarkable agreement.

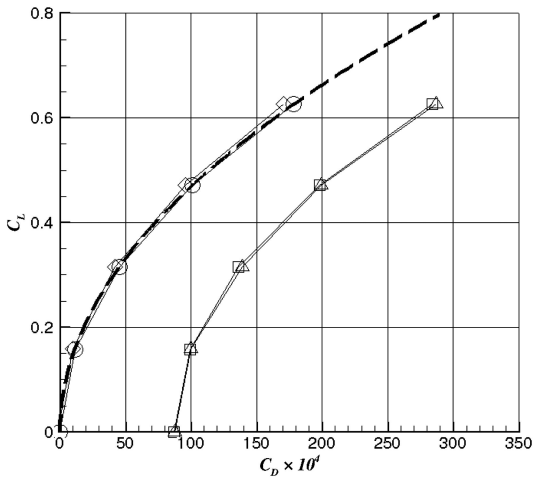


Figure 1.5.3: Drag polars of an elliptical wing with $\mathcal{AR} = 7$, $M_\infty = 0.01$ and $Re_\infty = 3 \times 10^6$. Near field $(-\square-)$, F $(-\triangle-)$, F_ℓ $(-\diamond-)$, Maskell's formula$(-\circ-)$, $C_L^2/(\pi\mathcal{AR})$ (- - -). Extracted from [42].

Recently, Mele & Tognaccini [44] provided a vortical formula for the aerodynamic force breakdown in compressible flow that overcomes the problems of Eq. (1.41). A detailed description of the formula and its analytical derivation are presented in Section 2.1. The main difference with Wu's formula is here discussed.

In Eq. (1.41) the compressibility effects are related to $\underline{\nabla}\rho$, a flow quantity generally present in the entire flow field. To recover one of the main benefit of the drag breakdown based on Lamb-vector theory (the connection between the force generation and the vortical flow regions) the terms containing the density gradient in Eq. (1.41) were transformed using the DMT identities reported in Appendix A. In particular, for a steady, compressible and high-Reynolds number flow a *compressible generation term* $\underline{F}_\rho$ is introduced in Eq. (1.42)

$$\underline{F} = \underline{F}_\ell + \underline{F}_{\Sigma - S_B} + \underline{F}_\rho \,, \tag{1.47}$$

with

$$\underline{F}_\rho = -\frac{1}{k}\int_{\mathcal{V}} \underline{r} \times \left\{ \underline{\nabla} \times \left[\rho \underline{\nabla} \left(\frac{V^2}{2} \right) \right] \right\} \mathrm{d}\mathcal{V} \,. \tag{1.48}$$

Equation 1.41 (in steady and high-Reynolds number hypothesis) and 1.47 are equivalent, but in Eq. (1.47), the integration can be limited to the rotational region only. Indeed, outside the boundary layer and the wakes of both boundary layer and shock waves, a high-Reynolds number flow is, practically, homoenthalpic (i.e., with constant total enthalpy

$H = h + V^2 2$, where h is the specific enthalpy) as well as homoentropic (i.e., with constant entropy). Crocco's relation gives $\underline{\zeta} = \underline{0}$. In addition, applying Gibbs's equation, there is $\underline{\nabla} h = \underline{\nabla} p/\rho$ whence $\rho \underline{\nabla} \left(V^2/2\right) = -\underline{\nabla} p$ with the result that both $\underline{F}_\ell$ and $\underline{F}_\rho$ are zero.

The drag breakdown given by Eq. (1.47) has been widely tested with numerical flow data around 2D and 3D aeronautical configurations [45–47]; the main results obtained are here reported.

The lift and the drag breakdown for an elliptical wing at different Mach numbers is presented in Fig. 1.5.4. The drag breakdown provided shows an *a priori* unexpected result: the induced drag of the elliptical wing predicted by the streamwise component of $\underline{F}_\ell$ is in remarkable agreement with Prandtl's induced-drag formula $\left(C_{D_i} = C_L^2/\left(\pi \mathcal{AR}\right)\right)$ valid in incompressible and inviscid flow.

The aerodynamic force breakdown has been provided also for the Nasa CRM configuration (see Fig. 1.5.5). In this case the profile drag has been further divided in its viscous and wave drag contribution by a proper region selection. The boundary-layer and the shock wave regions used for obtaining the results of Fig. 1.5.5 are showed in Fig. 1.5.6.

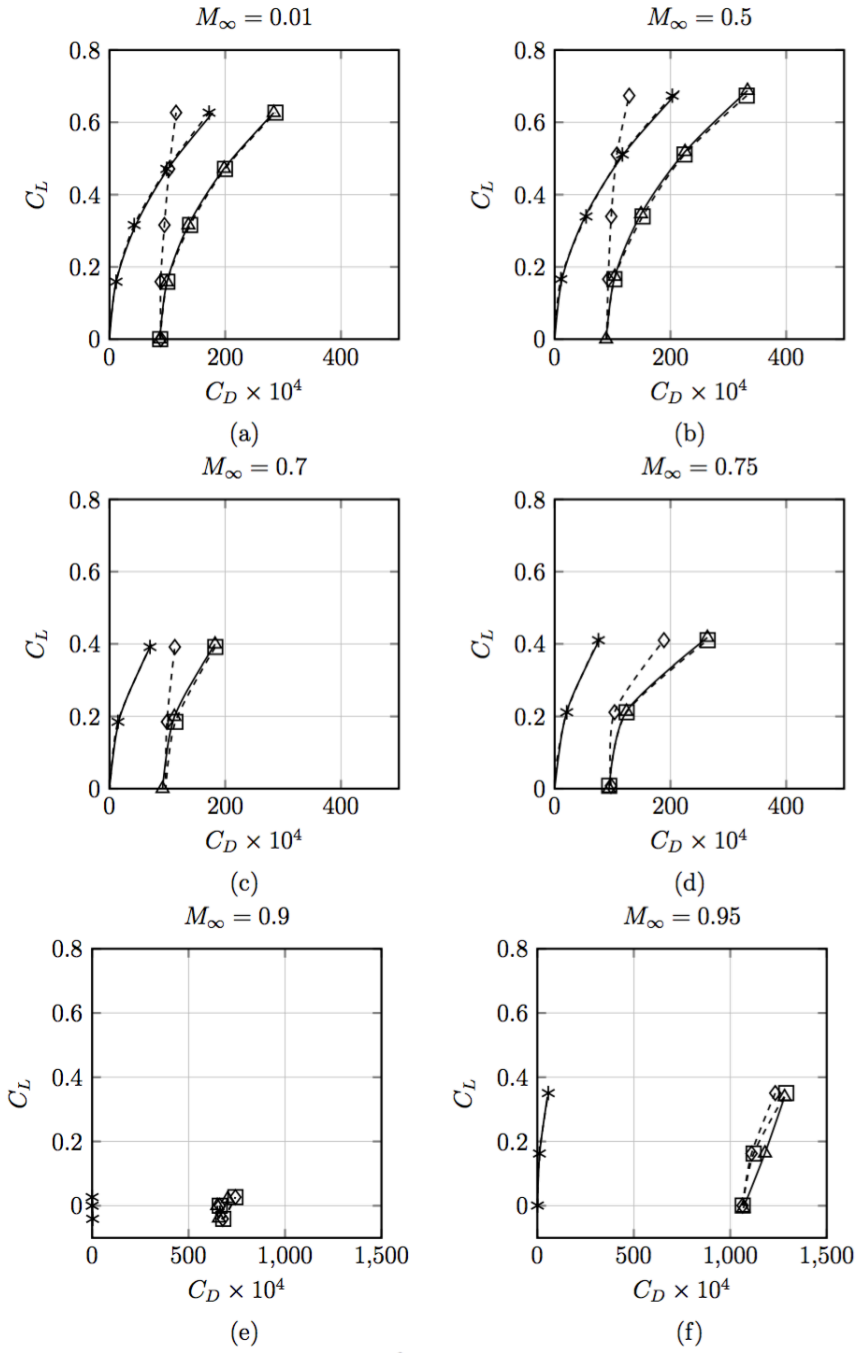


Figure 1.5.4: Drag polars of an elliptical wing with $\mathcal{AR} = 7$ at $Re_\infty = 3 \times 10^6$ and different Mach numbers. Near field $(-\triangle-)$, F $(-\square-)$, F_ℓ $(-*-)$,$F_{\Sigma-S_B}$ $(-\diamond-)$,$C_L^2/(\pi\mathcal{AR})$ (—). Extracted from [46].

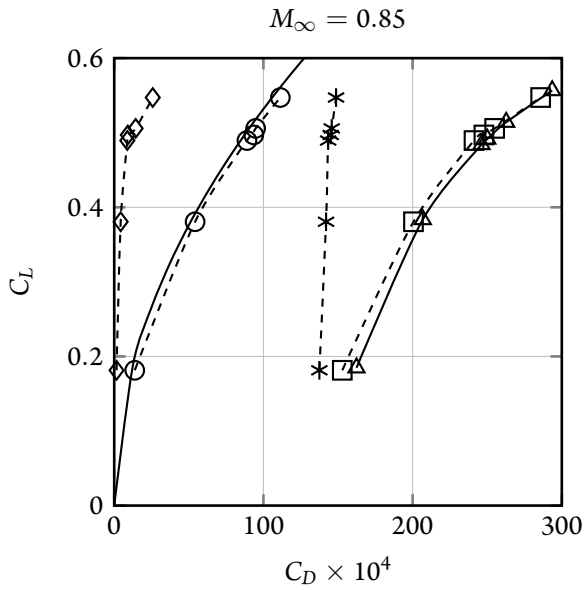


Figure 1.5.5: NASA CRM at $Re_\infty = 5 \times 10^6$. Computed lift-drag polars. Near field $(-\triangle-)$, F $(-\square-)$, vortical induced drag $(-\circ-)$, vortical wave drag $(-\diamond-)$, vortical viscous drag $(-*-)$, $C_L^2/(\pi \mathcal{AR})$ (—). Extracted from [47].

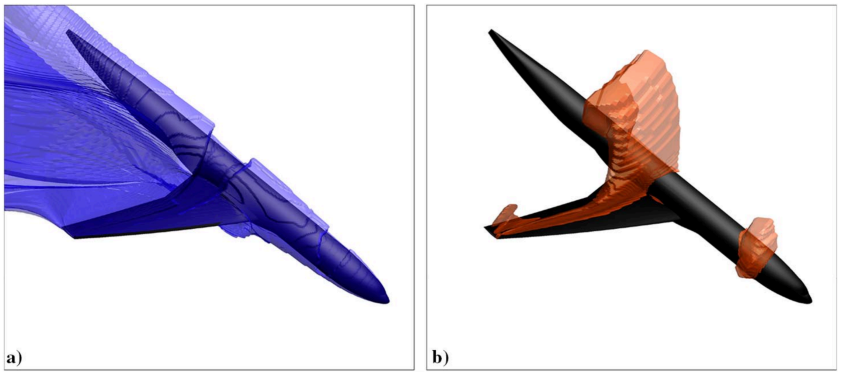


Figure 1.5.6: NASA CRM at $Re_\infty = 5 \times 10^6$, $M_\infty = 0.85$ and $C_L \approx 0.5$. Selected boundary-layer a) and shock-wave b) regions. Extracted from [46].

1.5.4 Vortical Methods for Unsteady Aerodynamics

The methods based on the Lamb-vector theory include the time-derivative terms for the analysis of the aerodynamic force in unsteady conditions. The Advection Form equation has been successfully applied by Wu et al. [34] and Liu et al. [48] in case of 2D low-

Reynolds number flows. An interesting variation of the Advection Form equation has been proposed by Ostieri et al. [49] in which a mixed inertial-non inertial reference frame has been used to better deal with data obtained by moving mesh technique. The authors applied the formula to the case of an oscillating flat plate and correctly computed the aerodynamic force even in case of very complex flow: in Fig. 1.5.7 the results for the pure pitching flat plate in dynamic stall are showed.

The author of present dissertation used the mixed inertial-non inertial formula to compute the thrust produced by a pure plunging NACA0012 airfoil [50] in both viscous and inviscid flow.

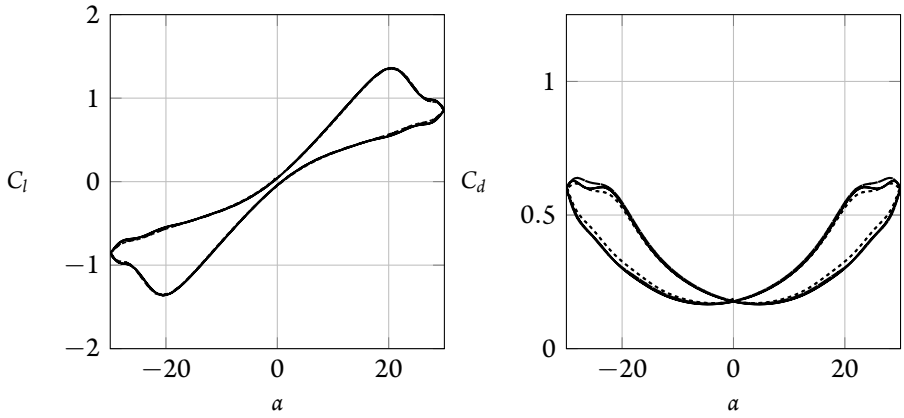


Figure 1.5.7: Pitching flat plate, $\bar{\alpha} = 30°$, $k = 0.05$, $Re_\infty = 300$. Comparison between lift and drag coefficients computed by near field formula (—), inertial formula (···) and mixed inertial-non inertial formula (- - -). Extracted from [47].

1.6 Modern Aerodynamics and Classical Theories

As discussed in previous sections, the far-field approach played a fundamental role in the development of modern aerodynamics. It permitted to better understand the generation of the aerodynamic force, linking it to the flow structures and its property, and allowing for high-level optimization of aerodynamic surface in industry. On the other hand, it was crucial also in the theoretical development of aerodynamics. Just think of the pioneering approach used by Kutta and Joukowskij [6] for the airfoil aerodynamic force (lift) computation in potential flow ($\underline{V} = \underline{\nabla}\Phi$): $\underline{F} = \rho_\infty \underline{V}_\infty \times \underline{\Gamma}_\Phi$, where $\underline{\Gamma}_\Phi$ is the vectorial circulation with the subscript 'Φ' remanding that the circulation is calculated for potential flow.

Afterwards, Filon [51] studied the drag for 2D viscous and incompressible flow and obtaining this exact and universal formula: $D = \rho_\infty V_\infty Q_\psi$, where Q_ψ is the inflow of the vortical part of the velocity $\left(Q_\psi \equiv - \int_{\Sigma - S_B} (\underline{n} \times \underline{\nabla}) \cdot \underline{\psi} \right)$ and ψ is the vector potential of the transverse velocity field.

The Kutta-Joukowskij and Filon theorems have been successfully extended in 3D flows and just a few years ago in compressible and even supersonic flow (Liu et al. [52]).

Thanks to the far-field approach a long-waited and fascinating *unified far-field theory* which defines the aerodynamic force independently from the flow regime considered and represent the bridge between the classical theory and modern aerodynamics has been obtained: the Kutta-Joukowskij-Filon Theorem.

1.6.1 The Kutta-Joukowskij-Filon Theorem

For an N-dimensional steady flow of viscous and compressible fluid over a rigid body, N=2,3, the lift and drag exerted to the body are solely determined by the multi-valueness and/or singularities of the velocity potential Φ in the circulation Γ_Φ and the vortical stream function ψ in the inflow Q_ψ, respectively:

$$\underline{F} = (N-1)\rho_\infty \underline{V}_\infty \times \Gamma_\Phi + \rho_\infty \underline{V}_\infty Q_\psi \,. \tag{1.49}$$

An ambition which will have to wait is a rigorous definition of induced drag in viscous flow.

Philippe Spalart - 2008

2

A Recent Aerodynamic Force Decomposition

In this chapter, a recently developed vortical method for the computation and the decomposition of the aerodynamic force is recalled and its analytical derivation is proposed. The author contributes to the development of the method providing an extension of the theory to the inviscid flow (proposed in [53] and reported in Section 2.3) and investigating its applicability to the Thrust/Drag Bookkeeping problem (see [50] and Section 2.4).

2.1 A Lamb Vector Based Aerodynamic Force Formula

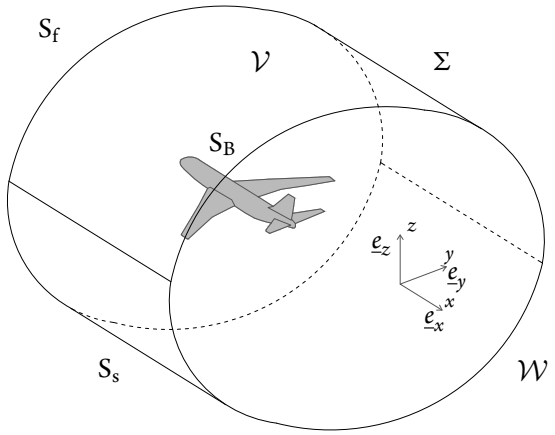


Figure 2.1.1: Sketch of fluid domain considered for the aerodynamic force analysis.

A solid body B immersed in a laminar flow domain $\mathcal{V}$ generates an aerodynamic force that can be computed by the following exact aerodynamic force expression [44]

$$\underline{F}_{\mathrm{vf}} = \underline{F}_{\ell} + \underline{F}_{\rho} + \underline{F}_{\Sigma} + \underline{F}_{\mathrm{t}} + \underline{F}_{\mathrm{t_B}} + \underline{\Delta}_{\mu} \,. \tag{2.1}$$

Each term present in Eq. (2.1) is a volume or a surface integral; the volume integrals are extended to the flow domain $\mathcal{V}$ whereas the surface integrals are referred to the volume boundary surface $\Sigma = S_f \cup S_s \cup \mathcal{W} \cup S_B$, as showed in Fig. 2.1.1.

The *vortex force* is defined as the volume integral of the Lamb vector field $\underline{\ell} = \underline{\zeta} \times \underline{V}$

$$\underline{F}_{\ell} = -\int_{\mathcal{V}} \rho \underline{\ell} \mathrm{d}\mathcal{V} \,, \tag{2.2}$$

with ρ given by the local fluid density. $\underline{F}_{\rho}$ is the so-called *compressible generation term*, present only in case of compressible flow, since it relies on the density gradient

$$\underline{F}_{\rho} = -\frac{1}{k}\int_{\mathcal{V}} \underline{r} \times \left\{ \underline{\nabla} \times \left[\rho \underline{\nabla} \left(\frac{V^2}{2} \right) \right] \right\} \mathrm{d}\mathcal{V} \,, \tag{2.3}$$

with $\underline{r}$ used to indicate the position vector with the origin placed at any point of the fluid domain and $k = N - 1$ with N equal to the space dimension.

The term $\underline{F}_\Sigma$ is a surface integral extended to the flow volume boundaries:

$$\underline{F}_\Sigma = -\frac{1}{k}\int_\Sigma \underline{r}\times(\underline{n}\times\rho\underline{\ell})\,\mathrm{dS}\,, \tag{2.4}$$

where $\underline{n}$ is the unitary vector normal to Σ and pointing outside $\mathcal{V}$; obviously in steady and viscous flow the body surface integral is zero thanks to the no-slip boundary condition and $\underline{F}_\Sigma$ becomes:

$$\underline{F}_\Sigma = -\frac{1}{k}\int_{\Sigma-S_B} \underline{r}\times(\underline{n}\times\rho\underline{\ell})\,\mathrm{dS}\,. \tag{2.5}$$

The term $\underline{F}_{t_B}$ relies on the local flow acceleration $\underline{a}$ on the body surface S_B and is present only in case of inviscid and/or unsteady flow, since the flow acceleration on the body is zero in case of viscous steady flow

$$\underline{F}_{t_B} = \frac{1}{k}\int_{S_B} \underline{r}\times[\underline{n}\times(\rho\underline{a})]\,\mathrm{d}\mathcal{V}\,, \tag{2.6}$$

whereas $\underline{F}_t$ is present only in unsteady flow conditions and given by

$$\underline{F}_t = -\frac{1}{k}\int_{\mathcal{V}} \underline{r}\times\left(\underline{\nabla}\times\frac{\partial\underline{V}}{\partial t}\right)\mathrm{d}\mathcal{V}\,. \tag{2.7}$$

Finally, $\underline{\Delta}_\mu$ explicitly contains the viscous stress tensor $\underline{\underline{\tau}}_\nu = \mu\left[\underline{\underline{\nabla V}} + \underline{\underline{(\nabla V)}}^T\right]$

$$\underline{\Delta}_\mu = \frac{1}{k}\int_{\Sigma-S_B} \underline{x}\times\left(\underline{n}\times\underline{\nabla}\cdot\underline{\underline{\tau}}_\nu\right)\mathrm{dS} + \int_{\Sigma-S_B}\underline{\underline{\tau}}_\nu\cdot\underline{n}\,\mathrm{dS}\,. \tag{2.8}$$

This term is equal to zero in inviscid flow conditions and negligible for viscous flow with Reynolds numbers of aeronautical interests ($Re_\infty \gg 1$) since $\underline{\underline{\tau}} = \mathcal{O}(1/Re_\infty)$, as discussed by Batchelor in [54] and Marongiu & Tognaccini in [40].

2.1.1 Analytical Derivation of Lamb Vector Based Formula

The aerodynamic force expression given by Eq. (2.1) is here derived from the far field momentum equation (Eq. (1.9)) applied to the flow domain showed in Fig. 2.1.1

$$\underline{F} = -\int_{\mathcal{V}}\rho\underline{a}\mathrm{d}\mathcal{V} - \int_{\Sigma-S_B} p\underline{n}\mathrm{dS} + \int_{\Sigma-S_B}\underline{\underline{\tau}}_\nu\cdot\underline{n}\,\mathrm{dS}\,. \tag{2.9}$$

Using the vector identity Eq. (A.1) of Appendix A on the volume integral of $\rho\underline{a}$, there is:

$$\int_{\mathcal{V}} \rho\underline{a}\,\mathrm{d}\mathcal{V} = \frac{1}{k}\int_{\mathcal{V}} \underline{r}\times[\underline{\nabla}\times(\rho\underline{a})]\;\mathrm{d}\mathcal{V} - \frac{1}{k}\int_{\Sigma}\underline{r}\times[\underline{n}\times(\rho\underline{a})]\;\mathrm{dS}\,, \tag{2.10}$$

moreover the fluid acceleration is

$$\underline{a} = \frac{\partial\underline{V}}{\partial t} + \underline{V}\cdot(\underline{\nabla}\underline{V}) = \frac{\partial\underline{V}}{\partial t} + \underline{\nabla}\left(\frac{V^2}{2}\right) + \underline{\ell}\,, \tag{2.11}$$

and Eq. (2.10) can be written as:

$$\begin{aligned}\int_{\mathcal{V}} \rho\underline{a}\,\mathrm{d}\mathcal{V} =& \frac{1}{k}\int_{\mathcal{V}}\underline{r}\times\left[\underline{\nabla}\times\left(\rho\frac{\partial\underline{V}}{\partial t} + \rho\underline{\nabla}\left(\frac{V^2}{2}\right) + \rho\underline{\ell}\right)\right]\;\mathrm{d}\mathcal{V}\\ &- \frac{1}{k}\int_{\Sigma}\underline{r}\times[\underline{n}\times(\rho\underline{a})]\;\mathrm{dS}\,.\end{aligned} \tag{2.12}$$

The surface integral of Eq. (2.12) can be rewritten splitting the integration domain into the body surface S_B and the far field surface $\Sigma - S_B$ and using the momentum balance equation $\rho\underline{a} = -\underline{\nabla}p + \underline{\nabla}\cdot\underline{\underline{\tau}}_{\nu}$

$$\begin{aligned}\int_{\Sigma}\underline{r}\times[\underline{n}\times(\rho\underline{a})]\;\mathrm{dS} =& \int_{S_B}\underline{r}\times[\underline{n}\times(\rho\underline{a})]\;\mathrm{dS}\\ &- \int_{\Sigma-S_B}\underline{r}\times(\underline{n}\times\underline{\nabla}p)\;\mathrm{dS}\\ &+ \int_{\Sigma-S_B}\underline{r}\times\left[\underline{n}\times\left(\underline{\nabla}\cdot\underline{\underline{\tau}}_{\nu}\right)\right]\;\mathrm{dS}\,.\end{aligned} \tag{2.13}$$

At this point Eq. (2.9) can be rewritten as:

$$\begin{aligned}\underline{F} =& -\frac{1}{k}\int_{\mathcal{V}}\underline{r}\times\left[\underline{\nabla}\times\left(\rho\frac{\partial\underline{V}}{\partial t} + \rho\underline{\nabla}\left(\frac{V^2}{2}\right) + \rho\underline{\ell}\right)\right]\;\mathrm{d}\mathcal{V}\\ &+ \frac{1}{k}\int_{S_B}\underline{r}\times[\underline{n}\times(\rho\underline{a})]\;\mathrm{dS}\\ &- \int_{\Sigma-S_B} p\underline{n}\mathrm{dS} - \frac{1}{k}\int_{\Sigma-S_B}\underline{r}\times(\underline{n}\times\underline{\nabla}p)\;\mathrm{dS}\\ &+ \int_{\Sigma-S_B}\underline{\underline{\tau}}_{\nu}\cdot\underline{n}\,\mathrm{dS} + \frac{1}{k}\int_{\Sigma-S_B}\underline{r}\times\left[\underline{n}\times\left(\underline{\nabla}\cdot\underline{\underline{\tau}}_{\nu}\right)\right]\;\mathrm{dS}\,.\end{aligned} \tag{2.14}$$

In order to rearrange the terms of Eq. (2.14) explicitly containing the static pressure p, the solid body B is replaced by a fluid volume with a proper pressure and velocity distribution. In this fashion, a new fluid volume equal to $\mathcal{V} \cup \mathrm{B}$ with a single boundary $(\Sigma - \mathrm{S_B})$ is obtained and Eq. (A.2) of Appendix A can be applied with p as potential function

$$\int_{\Sigma} p\underline{n}\,\mathrm{dS} = -\frac{1}{k}\int_{\Sigma} \underline{r} \times (\underline{n} \times \underline{\nabla} p)\;\mathrm{dS}\,. \tag{2.15}$$

So, Eq. (2.14) becomes

$$\begin{aligned}\underline{F} = &-\frac{1}{k}\int_{\mathcal{V}} \underline{r} \times \left[\underline{\nabla} \times \left(\rho\frac{\partial \underline{V}}{\partial t} + \rho\underline{\nabla}\left(\frac{V^2}{2}\right) + \rho\underline{\ell}\right)\right]\;\mathrm{d}\mathcal{V} \\ &+ \frac{1}{k}\int_{\mathrm{S_B}} \underline{r} \times [\underline{n} \times (\rho\underline{a})]\;\mathrm{dS} \\ &+ \int_{\Sigma} \underline{\underline{\tau}}_{\nu} \cdot \underline{n}\,\mathrm{dS} + \frac{1}{k}\int_{\Sigma} \underline{r} \times \left[\underline{n} \times \left(\underline{\nabla} \cdot \underline{\underline{\tau}}_{\nu}\right)\right]\;\mathrm{dS}\,.\end{aligned} \tag{2.16}$$

Finally, applying Eq. (A.1) of Appendix A to the volume integral of $\underline{r} \times (\underline{\nabla} \times \rho\underline{\ell})$ Eq. (2.1) is obtained the *exact* vortical expression of the aerodynamic force

$$\begin{aligned}
\underline{F}_{\mathrm{vf}} = & \underbrace{-\int_{\mathcal{V}} \rho\underline{\ell}\, \mathrm{d}\mathcal{V}}_{\underline{F}_{\ell}} \\
& \underbrace{-\frac{1}{k}\int_{\mathcal{V}} \underline{r} \times \left\{\underline{\nabla} \times \left[\rho\underline{\nabla}\left(\frac{V^2}{2}\right)\right]\right\} \mathrm{d}\mathcal{V}}_{\underline{F}_{\rho}} \\
& \underbrace{-\frac{1}{k}\int_{\Sigma - \mathrm{S_B}} \underline{r} \times (\underline{n} \times \rho\underline{\ell})\, \mathrm{dS}}_{\underline{F}_{\Sigma}} \\
& \underbrace{-\int_{\mathcal{V}} \underline{r} \times \left(\underline{\nabla} \times \frac{\partial \underline{V}}{\partial t}\right) \mathrm{d}\mathcal{V}}_{\underline{F}_{\mathrm{t}}} \\
& \underbrace{+\frac{1}{k}\int_{\mathrm{S_B}} \underline{r} \times [\underline{n} \times (\rho\underline{a})]\ \mathrm{dS}}_{\underline{F}_{\mathrm{t_B}}} \\
& \underbrace{+\int_{\Sigma} \underline{\underline{\tau}}_{\nu} \cdot \underline{n}\, \mathrm{dS} + \frac{1}{k}\int_{\Sigma} \underline{r} \times \left[\underline{n} \times \left(\underline{\nabla} \cdot \underline{\underline{\tau}}_{\nu}\right)\right]\ \mathrm{dS}}_{\underline{\Delta}_{\mu}} .
\end{aligned} \tag{2.17}$$

2.1.2 Extension of the Lamb Vector Theory to Turbulent Flow

Mele & Tognaccini [44] successfully extended Eq. (2.1) to turbulent flows governed by RANS equations [55] with a Favre averaging of the flow variables. In order to complete the analysis of the aerodynamic force by the Lamb vector theory in steady and viscous flow their procedure is here briefly recalled.

Let be f a random property of the flow field that can be expressed as $f = \bar{f} + f'$ with $\bar{f}$ equal to the ensemble average of f and f' equal to the corresponding fluctuations. The Favre average of f, defined as $\widetilde{f} = \overline{\rho f}/\bar{\rho}$, allows for the following variable decomposition: $f = \widetilde{f} + f''$ with f'' equal to the corresponding fluctuations. As discussed in [40] the following relations define the average of the Lamb vector field

$$\widetilde{\underline{\ell}} = \widetilde{\underline{\zeta}} \times \widetilde{\underline{V}} + \widetilde{\left(\underline{\zeta}'' \times \underline{V}''\right)}, \tag{2.18}$$

$$\bar{\rho}\widetilde{\left(\underline{\zeta}''\times\underline{V}''\right)} = -\underline{\nabla}\cdot\underline{\underline{\tau}}_{\mathrm{R}} - \bar{\rho}\underline{\nabla}\mathcal{K} - \underline{\delta}_{\rho\mathrm{V}}\,, \tag{2.19}$$

where $\underline{\underline{\tau}}_{\mathrm{R}}$ is the Reynolds stress tensor, $\mathcal{K}$ is the turbulent kinetic energy whereas $\underline{\delta}_{\rho\mathrm{V}} = \overline{\underline{V}''\underline{\nabla}\cdot(\rho\underline{V}'')}$.

Thanks to the hypothesis of statistically stationary flow governed by RANS equations the average of the *unsteady* term $\underline{F}_{\mathrm{t}}$ of Eq. (2.1) is zero; similarly $\underline{F}_{\mathrm{t_B}} = 0$ thanks to the no-slip boundary condition on $\mathrm{S_B}$. The average of the *vortex force* is

$$\overline{\underline{F}_{\ell}} = -\int_{\mathcal{V}}\bar{\rho}\left(\widetilde{\underline{\xi}}\times\widetilde{\underline{V}}\right)\,\mathrm{d}\mathcal{V} + \int_{\mathcal{V}}\underline{\nabla}\cdot\underline{\underline{\tau}}_{\mathrm{R}}\,\mathrm{d}\mathcal{V} + \int_{\mathcal{V}}\bar{\rho}\underline{\nabla}\mathcal{K}\,\mathrm{d}\mathcal{V} + \int_{\mathcal{V}}\underline{\delta}_{\rho\mathrm{V}}\,\mathrm{d}\mathcal{V}\,. \tag{2.20}$$

The average of $\underline{F}_{\Sigma}$ is

$$\begin{aligned}\overline{\underline{F}_{\Sigma}} = &-\frac{1}{k}\int_{\Sigma}\underline{r}\times\left[\underline{n}\times\bar{\rho}\left(\widetilde{\underline{\xi}}\times\widetilde{\underline{V}}\right)\right]\,\mathrm{dS} + \frac{1}{k}\int_{\Sigma}\underline{r}\times\underline{n}\times\left(\underline{\nabla}\cdot\underline{\underline{\tau}}_{\mathrm{R}}\right)\,\mathrm{dS}\\ &+\frac{1}{k}\int_{\Sigma}\underline{r}\times\underline{n}\times\left(\bar{\rho}\underline{\nabla}\mathcal{K}\right)\,\mathrm{dS} + \frac{1}{k}\int_{\Sigma}\underline{r}\times\underline{n}\times\underline{\delta}_{\rho\mathrm{V}}\,\mathrm{dS}\,.\end{aligned} \tag{2.21}$$

Since $\widetilde{V^2} = \widetilde{V}^2 + \widetilde{\underline{V}''\cdot\underline{V}''}$, the average of the *compressible generation term* is

$$\begin{aligned}\overline{\underline{F}_{\rho}} = &-\frac{1}{k}\int_{\mathcal{V}}\underline{r}\times\left\{\underline{\nabla}\times\left[\bar{\rho}\underline{\nabla}\left(\frac{\widetilde{V}^2}{2}\right)\right]\right\}\mathrm{d}\mathcal{V}\\ &-\frac{1}{k}\int_{\mathcal{V}}\underline{r}\times\left[\underline{\nabla}\times\left(\bar{\rho}\underline{\nabla}\mathcal{K}\right)\right]\mathrm{d}\mathcal{V}\,.\end{aligned} \tag{2.22}$$

Finally, for Δ_{μ}

$$\overline{\Delta}_{\mu} = \int_{\Sigma}\underline{\underline{\tau}}_{\nu t}\cdot\underline{n}\,\mathrm{dS} + \frac{1}{k}\int_{\Sigma}\underline{r}\times\left[\underline{n}\times\left(\underline{\nabla}\cdot\underline{\underline{\tau}}_{\nu t}\right)\right]\,\mathrm{dS}\,, \tag{2.23}$$

with $\underline{\underline{\tau}}_{\nu t} = \mu\left(\underline{\nabla}\widetilde{\underline{V}} + \underline{\nabla}\widetilde{\underline{V}}^{T}\right)$.

Applying Eq. (A.1) to the vector fields $\underline{\delta}_{\rho\mathrm{V}}$ and $\rho\underline{\nabla}\mathcal{K}$ of Eq. (2.20) and $\underline{\nabla}\cdot\underline{\underline{\tau}}_{\mathrm{R}}$ of Eq. (2.21), summing Eqs. (2.20) to (2.23) and using the Gauss' theorem for

$$\int_{\mathcal{V}}\underline{\nabla}\cdot\underline{\underline{\tau}}_{\mathrm{R}}\mathrm{d}\mathcal{V} = \int_{\Sigma-\mathrm{S_B}}\underline{n}\cdot\underline{\underline{\tau}}_{\mathrm{R}}\mathrm{dS}\,, \tag{2.24}$$

since $\widetilde{V}$ is zero on $\mathrm{S_B}$, the aerodynamic force expression for a flow governed by RANS equa-

tions is obtained

$$\begin{aligned}\overline{\underline{F}_{\mathrm{vf}}} = &-\int_{\mathcal{V}} \bar{\rho}\left(\widetilde{\underline{\zeta}}\times\widetilde{\underline{V}}\right)\,\mathrm{d}\mathcal{V}\\ &-\frac{1}{k}\int_{\mathcal{V}}\underline{r}\times\left\{\underline{\nabla}\times\left[\bar{\rho}\underline{\nabla}\left(\frac{\widetilde{V}^2}{2}\right)\right]\right\}\mathrm{d}\mathcal{V}\\ &-\frac{1}{k}\int_{\Sigma}\underline{r}\times\left[\underline{n}\times\bar{\rho}\left(\widetilde{\underline{\zeta}}\times\widetilde{\underline{V}}\right)\right]\,\mathrm{dS}\\ &+\int_{\Sigma}\underline{\underline{\tau}}^{*}\cdot\underline{n}\,\mathrm{dS}+\frac{1}{k}\int_{\Sigma}\underline{r}\times\left[\underline{n}\times\left(\underline{\nabla}\cdot\underline{\underline{\tau}}^{*}\right)\right]\,\mathrm{dS}+\int_{\Sigma}\underline{r}\times\underline{n}\times\underline{\delta}_{\rho\mathrm{V}}\,\mathrm{dS}\,,\end{aligned} \tag{2.25}$$

where:

$$\underline{F}_{\ell} = -\int_{\mathcal{V}}\bar{\rho}\left(\widetilde{\underline{\zeta}}\times\widetilde{\underline{V}}\right)\,\mathrm{d}\mathcal{V}\,, \tag{2.26}$$

$$\underline{F}_{\rho} = -\frac{1}{k}\int_{\mathcal{V}}\underline{r}\times\left\{\underline{\nabla}\times\left[\bar{\rho}\underline{\nabla}\left(\frac{\widetilde{V}^2}{2}\right)\right]\right\}\mathrm{d}\mathcal{V}\,, \tag{2.27}$$

$$\underline{F}_{\Sigma} = -\frac{1}{k}\int_{\Sigma}\underline{r}\times\left[\underline{n}\times\bar{\rho}\left(\widetilde{\underline{\zeta}}\times\widetilde{\underline{V}}\right)\right]\,\mathrm{dS}\,, \tag{2.28}$$

$$\underline{\Delta}_{\mu} = \int_{\Sigma}\underline{\underline{\tau}}^{*}\cdot\underline{n}\,\mathrm{dS}+\frac{1}{k}\int_{\Sigma}\underline{r}\times\left[\underline{n}\times\left(\underline{\nabla}\cdot\underline{\underline{\tau}}^{*}\right)\right]\,\mathrm{dS}+\int_{\Sigma}\underline{r}\times\underline{n}\times\underline{\delta}_{\rho\mathrm{V}}\,\mathrm{dS}\,. \tag{2.29}$$

In Eq. (2.29) $\underline{\underline{\tau}}^{*} = \underline{\underline{\tau}}_{vt}+\underline{\underline{\tau}}_{\mathrm{R}}$ whereas $\int_{\Sigma}\underline{r}\times\underline{n}\times\underline{\delta}_{\rho\mathrm{V}}\,\mathrm{dS}$ can be neglected thanks to Morkovin hypothesis ([55], page 228).

2.2 Thermodynamic vs. Vortex-force Methods

A comparison between the Vortical and the Thermodynamic methods could be useful to the reader who wants to deepen the pros. and the cons. of each technique. As mentioned before, the vortical methods are characterized by an interesting feature that permits to overcome the greatest limitations of the Thermodynamic methods:

- since these methods are related to the *irreversible* processes occurring in the flow, only drag can be computed;
- lack of a direct definition of the induced drag (it is computed by near-field/far-field

drag balance).

In this section, the formulae derived in Section 2.1 will be rewritten in terms of wake survey integrals of entropy and total enthalpy variations ($\Delta s = s - s_\infty$ and $\Delta H = H - H_\infty$ respectively) in order to compare the drag expression obtained to the classical Thermodynamic ones: the viscous and wave drag definition given by Destarac and Van Der Vooren D_{vw}^{DV} [23], the classical Oswatitsch's entropy drag concept D_{vw}^{O} [17] and the Maskell's formula for the lift-induced drag D_i^M. Note that only the streamwise component of the aerodynamic force can be correctly computed limiting the integration domain to the wake surface only. Indeed, neglecting the term explicitly containing the molecular viscosity in Eq. (2.9) and applying the Gauss'Theorem to the volume integral, the following aerodynamic force expression is obtained:

$$\underline{F} = -\int_{\Sigma - S_B} \left[(p - p_\infty)\,\underline{n} + \rho\,(\underline{V} - \underline{V}_\infty)\,\underline{V}\cdot\underline{n} \right] \mathrm{dS}\,. \tag{2.30}$$

As shown in Fig. 2.1.1 the far field surface $\Sigma - S_B$ consists in the upstream surface S_f, the side surface S_s and the wake plane $\mathcal{W}$. If the upstream velocity is in the plane $\left(\underline{e}_x, \underline{e}_y\right)$ the local velocity can be expressed as:

$$\underline{V} = u\underline{e}_x + \underline{V}_\pi = (V_\infty + u')\underline{e}_x + v\underline{e}_y + w\underline{e}_z\,, \tag{2.31}$$

where the subscript π denotes the velocity components in the plane $\left(\underline{e}_y, \underline{e}_z\right)$. The total drag and lift are:

$$\begin{aligned} D = D_{\mathcal{W}} + D' = &-\int_{\mathcal{W}} \left[(p - p_\infty) + \rho u' u \right] \mathrm{dS} \\ &+ \int_{S_f} \left[(p - p_\infty) + \rho u' u \right] \mathrm{dS} - \int_{S_s} \rho u' v_\theta \,\mathrm{dS}\,, \end{aligned} \tag{2.32}$$

$$\begin{aligned} L = L_{\mathcal{W}} + L' = &-\int_{\mathcal{W}} \rho w u \,\mathrm{dS} + \int_{S_f} \rho w u \,\mathrm{dS} \\ &- \underline{e}_z \cdot \int_{S_s} \left[(p - p_\infty)\,\underline{n} + \rho \underline{v}_\theta v \right] \mathrm{dS}\,, \end{aligned} \tag{2.33}$$

where $D_{\mathcal{W}}$ and $L_{\mathcal{W}}$ are the integrals on $\mathcal{W}$, D' and L' group the integrals on the remaining part of Σ and $v_\theta = vn_y + wn_z$ is the component of $\underline{V}$ normal to the side surface S_s. Assuming S_s and S_f sufficiently far from the body ($r_{S_f \cup S_s} \to \infty$) the the flow can be considered

inviscid and the velocity perturbations satisfy: $\mathcal{O}(u') = \mathcal{O}(v) = \mathcal{O}(w) = \mathcal{O}(r^{-2})$ [56, 57]; L' and D' expressions can be rearranged by using Eq. (B.8) and Eq. (B.9)

$$\begin{aligned} L' &= \int_{S_f} \rho_\infty U_\infty w \, \mathrm{dS} + \int_{S_s} \rho_\infty U_\infty u' \underline{e}_z \cdot \underline{n} \, \mathrm{dS} + \mathcal{O}\left(r^{-2}\right) \\ &\approx \int_{S_f} \rho_\infty U_\infty w \, \mathrm{dS} + \int_{S_s} \rho_\infty U_\infty u' \underline{e}_z \cdot \underline{n} \, \mathrm{dS} \,, \end{aligned} \tag{2.34}$$

$$D' = \int_{S_f \cup S_s} \mathcal{O}(u', v, w)^2 dS = \mathcal{O}\left(r^{-2}\right) \approx 0 \,, \tag{2.35}$$

which show that the drag can be computed by the wake integral only but the lift cannot.

In a steady, compressible and high Reynolds number flow the drag expression given by the Vortex Force Theory is:

$$\underline{F}_{\mathrm{vf}} = \underline{F}_\ell + \underline{F}_\rho + \underline{F}_\Sigma \,. \tag{2.36}$$

In the drag breakdown proposed by Mele et al. [45] the streamwise component of $\underline{F}_\ell + \underline{F}_\rho$ gives the lift-induced drag D_{i} whereas $\underline{F}_\Sigma$ is responsible for the viscous and wave drag D_{vw} and is the only surface integral present in Eq. (2.36); thanks to the no-slip boundary condition on the body and $\underline{\zeta} = 0$ on S_s and S_f the integration domain can be limited to the wake plane only:

$$D_{\mathrm{vw}} = \underline{e}_x \cdot \underline{F}_\Sigma = \underline{e}_x \cdot \underline{F}_{\mathcal{W}} = -\frac{1}{k} \underline{e}_x \cdot \int_{\mathcal{W}} \left[\underline{r} \times (\underline{n} \times \rho \underline{\ell})\right] \mathrm{dS} = -\frac{1}{k} \underline{e}_x \cdot \int_{\mathcal{W}} \underline{r}_\pi \times \rho \underline{\ell} \mathrm{dS} \,, \tag{2.37}$$

where $\underline{r}_\pi$ is the position vector in the wake plane. Using the Crocco's equation for a steady and high-Reynolds number flow ($\underline{\ell} = T\underline{\nabla} s - \underline{\nabla} H$) Eq. (2.37) becomes

$$D_{\mathrm{vw}} = \underline{e}_x \cdot \frac{1}{k} \int_{\mathcal{W}} \underline{r} \times \left[\underline{n} \times (\rho \underline{\nabla} H)\right] \, \mathrm{dS} - \underline{e}_x \cdot \frac{1}{k} \int_{\mathcal{W}} \underline{r} \times \left[\underline{n} \times \left(\frac{p}{R} \underline{\nabla} s\right)\right] \, \mathrm{dS} \,. \tag{2.38}$$

Applying Eqs. (B.6) and (B.7) of Appendix B with second-order approximation, there is:

$$\begin{aligned} D_{\mathrm{vw}} \approx & \int_{\mathcal{W}} \left(p_\infty \frac{\Delta s}{R} - \rho_\infty \Delta H\right) \, \mathrm{dS} \\ & - \int_{\mathcal{W}} \left(\frac{\rho_\infty}{2a_\infty^2} \Delta H^2 + \frac{p_\infty}{2} \frac{\Delta s^2}{R^2} - \rho_\infty \Delta H \frac{\Delta s}{R}\right) \, \mathrm{dS} \\ & + \frac{\rho_\infty V_\infty^2}{k} \int_{\mathcal{W}} \frac{u'}{V_\infty} \underline{r}_\pi \times \underline{\nabla}_\pi \left(\frac{\Delta s}{R} - \frac{\Delta H}{a_\infty^2}\right) \, \mathrm{dS}, \end{aligned} \tag{2.39}$$

where the first order terms are grouped in the first surface integral and $a_\infty = \sqrt{\gamma R T_\infty}$ is the freestream speed of sound.

The thermodynamic method developed by Destarac & Van der Vooren is based on the definition of the *irreversible velocity*

$$V_{\text{irr}} = V_\infty \sqrt{1 + \frac{2\Delta H}{U_\infty^2} - \frac{2}{(\gamma-1)M_\infty^2}\left(e^{\frac{\gamma-1}{\gamma}\frac{\Delta s}{R}} - 1\right)}\,, \tag{2.40}$$

where M_∞ is the freestream Mach number. The wake integral form of the viscous and wave drag proposed by Destarac & Van der Vooren is:

$$D_{\text{vw}}^{\text{DV}} = -\int_{\mathcal{W}} \rho\,(V_{\text{irr}} - V_\infty)\,u\,\mathrm{dS}\,. \tag{2.41}$$

Expressing also in this case the velocity in terms of entropy and total enthalpy variations, with second order approximation D_{vw}^{DV} becomes

$$\begin{aligned} D_{\text{vw}}^{\text{DV}} \approx & \int_{\mathcal{W}} \left(p_\infty \frac{\Delta s}{R} - \rho_\infty \Delta H\right) \mathrm{dS} \\ & - \int_{\mathcal{W}} \left(\frac{\rho_\infty}{a_\infty^2}\Delta H^2 + p_\infty \frac{\Delta s^2}{R^2} - \frac{\gamma+1}{\gamma}\rho_\infty \Delta H \frac{\Delta s}{R}\right) \mathrm{dS} \\ & -\rho_\infty V_\infty^2 \left(1 - \frac{1}{M_\infty^2}\right) \int_{\mathcal{W}} \frac{u'}{V_\infty}\left(\frac{1}{\gamma}\frac{\Delta s}{R} - \frac{\Delta H}{a_\infty^2}\right) \mathrm{dS}\,. \end{aligned} \tag{2.42}$$

$DV_{\text{vw}} = D_{\text{vw}}^{\text{DV}}$ with first-order approximation. According to Oswatitsch's entropy drag concept, the viscous and wave drag can be defined in terms of entropy variation only:

$$D_{\text{vw}}^{\text{O}} = \frac{T_\infty}{V_\infty}\int_{\mathcal{W}} \rho \underline{V}\cdot\underline{n}\Delta s\,\mathrm{dS}\,, \tag{2.43}$$

that, with first-order approximation, becomes

$$D_{\text{vw}}^{\text{O}} \approx \int_{\mathcal{W}} p_\infty \frac{\Delta s}{R}\,\mathrm{dS}\,. \tag{2.44}$$

The enthalpy variation is substantially linked to the thrust production in case of engine-on configurations but it is not strictly equal to zero for engine-off conditions in viscous flow. Nonetheless, the Crocco's solution for the thermal boundary layer assures that $\Delta H = 0$ when the Prandtl number (Pr) is equal to one. In turbulent flows $Pr \approx 1$ and the total

enthalpy variations can be therefore neglected. Thus, viscous and wave drag D_{vw} defined in Eq. (2.39) and D_{vw}^{DV}, expressed in terms of only entropy variation, are equal to the Oswatitsch's entropy drag D_{vw}^{O} with first-order approximation.

The induced drag defined in [45] $\left(D_i = \underline{F}_\ell + \underline{F}_\rho\right)$ can be consistently compared with the classical Maskell's induced drag definition D_i^M expressing the volume integrals present in Eq. (2.36) as one wake-surface integral. To do that the contribution of $\underline{F}_\Sigma$ is subtracted by the far-field expression of the drag $(D_\mathcal{W})$

$$D_i = D_\mathcal{W} - D_{vw} = -\int_\mathcal{W} \left[(p - p_\infty) + \rho u' u\right] \, \mathrm{dS} + \frac{1}{k}\underline{e}_x \cdot \int_\mathcal{W} \underline{r}_\pi \times \rho\underline{\ell} \, \mathrm{dS} \,. \quad (2.45)$$

Using Eq. (A.2) of Appendix A on the integral of the static pressure

$$D_i = \frac{1}{k}\underline{e}_x \cdot \int_\mathcal{W} \underline{r} \times (\underline{n} \times \underline{\nabla} p) \, \mathrm{dS} - \int_\mathcal{W} \rho u' u \, \mathrm{dS} + \frac{1}{k}\underline{e}_x \cdot \int_\mathcal{W} \underline{r}_\pi \times \rho\underline{\ell} \, \mathrm{dS} \,, \quad (2.46)$$

and, from the momentum equation $\underline{\nabla} p = -\rho\underline{\ell} - \rho\underline{\nabla}\left(\frac{V^2}{2}\right)$; thus

$$D_i = -\frac{1}{k}\underline{e}_x \cdot \int_\mathcal{W} \underline{r} \times \left[\underline{n} \times \rho\underline{\nabla}\left(\frac{V^2}{2}\right)\right] \, \mathrm{dS} - \int_\mathcal{W} \rho u' u \, \mathrm{dS} \,. \quad (2.47)$$

Since $\underline{\nabla}\left(\frac{V^2}{2}\right) = \underline{\nabla}\left(\frac{V^2}{2}\right) - \frac{V^2}{2}\underline{\nabla}\rho$, the first integral of Eq. (2.47) can be rearranged and the final expression of D_i can be obtained applying again Eq. (A.2) of Appendix A:

$$D_i = \frac{1}{k}\underline{e}_x \cdot \int_\mathcal{W} \underline{r}_\pi \times \left(\frac{V^2 + {V_\infty}^2}{2}\right) \underline{\nabla}_\pi \rho \, \mathrm{dS} + \int_\mathcal{W} \frac{1}{2}\rho \left({v_\pi}^2 - {u'}^2\right) \, \mathrm{dS} \,. \quad (2.48)$$

Equation 2.48 in case of incompressible flow becomes

$$D_i = \frac{1}{2}\rho \int_\mathcal{W} \left({v_\pi}^2 - {u'}^2\right) \, \mathrm{dS} \,, \quad (2.49)$$

which returns Maskell's expression of lift-induced drag

$$D_i^M = \frac{1}{2}\rho \int_\mathcal{W} {v_\pi}^2 \, \mathrm{dS} \,, \quad (2.50)$$

if the cross flow on $\mathcal{W}$ satisfies $u' = 0$.

2.2.1 Numerical Comparison of Drag Breakdown Methods

The expressions given for the viscous and wave drag (D_{vw}, D_{vw}^{DV} and D_{vw}^{O}) and for the lift-induced drag (D_i and D_i^M) are applied to numerically obtained flow solutions. In particular, two test cases are considered: a NACA 0012 airfoil immersed in a flow with $M_\infty = 0.75$ and $Re_\infty = 6 \times 10^6$ at angle of attach $\alpha = 2^\circ$ and an elliptical wing immersed flow with $M_\infty = 0.5, Re_\infty = 3 \times 10^6$ at $\alpha = 4^\circ$.

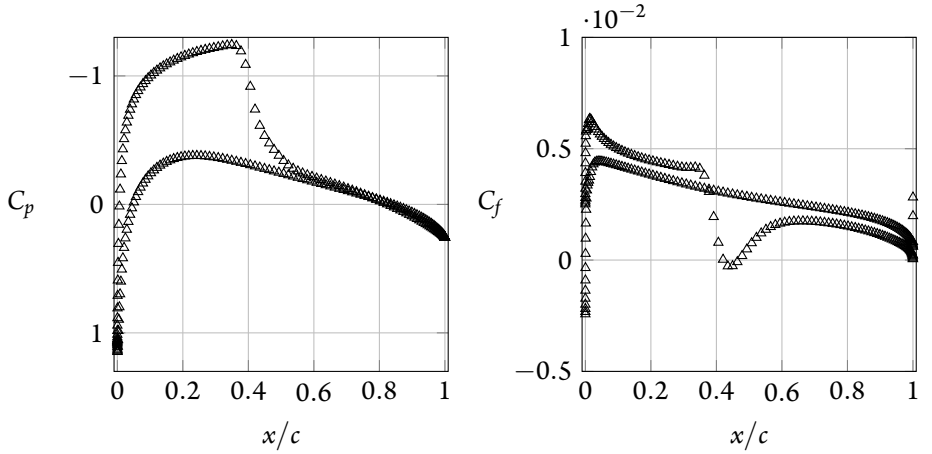


Figure 2.2.1: NACA 0012 airfoil, $Re_\infty = 6 \times 10^6$, $M_\infty = 0.75$, $\alpha = 2^\circ$. C_p and C_f distributions over the airfoil.

CFD data are obtained solving the Reynolds-averaged Navier-Stokes (RANS) equations in FLOWer: a multiblock structured compressible solver developed at DLR (the German Aerospace Center) widely validated and adopted by the scientific and engineering community [58].

For both the simulations a standard second-order scheme with explicit second- and fourth-order artificial dissipation and explicit-pseudo time integration has been adopted. A C-type computational grid with 256 cells on the airfoil and 128 in normal direction has been used for the airfoil; the far-field has been placed 100 airfoil chords distant from the airfoil and $y^+ \approx 0.5$ has been realized all over the body surface.

For the elliptical wing a C-C type grid with the far-field placed at a distance of about 30 root airfoil chords from the body, 384 cells around the wing section, 64 cells along the wing span and 96 cells in normal-to-body direction has been used. Both the simulations reached a satisfactory convergence, with the L2-norm of the residual of the continuity equation

reduced to 10^6 times the initial residual. Some details of the solution obtained in case of 2D flow are shown in Section 2.2.1 where the pressure coefficient distribution $C_p(x/c) = 2\left(p - p_\infty\right)/\rho_\infty V_\infty^2$ and the skin friction coefficient distribution $C_f(x/c) = 2\tau_w/\rho_\infty V_\infty^2$ are displayed and the presence of a shock wave at $x/c \approx 0.4$ is highlighted. The contour of C_p and C_f over the elliptical wing are shown in Section 2.2.1.

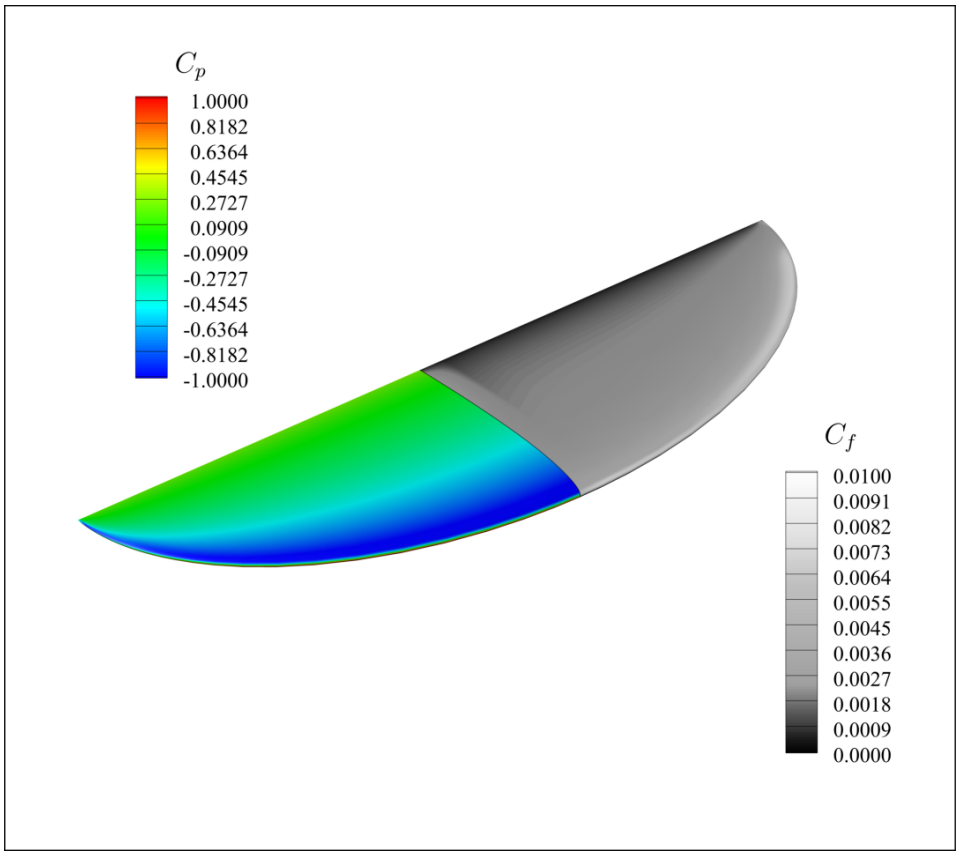


Figure 2.2.2: Elliptical wing with $\mathcal{AR} = 7$, $Re_\infty = 3 \times 10^6$, $M_\infty = 0.5$, $a = 4°$. C_p and C_f distributions over the wing.

In Fig. 2.2.3 the drag computed by the far-field formulae present in Section 2.2 are displayed. The viscous and wave drag D_{vw}, computed by Eq. (2.38), is compared with the one given by Destarac & Van Der Vooren D_{vw}^{DV} [Eq. (2.41)] whereas D_i [Eq. (2.48)] is compared with the Maskell's formula D_i^M [Eq. (2.50)]. The computations are performed changing the wake plane position $r_{\mathcal{W}}$ in streamwise direction $\underline{e}_x$ starting from the body trailing edge. As expected, since induced drag is not present in 2D flows, D_i and D_i^M go

to zero soon after the body and the drag expressions are very stable and agree between themselves for $r_{\mathcal{W}} > 2$ with the discrepancy changing from 8 drag counts ($r_{\mathcal{W}} = 2.3$) to 0 drag count ($r_{\mathcal{W}} = 19$). The D_{vw} and $D_{\text{vw}}^{\text{DV}}$ go to the total drag and the discrepancy between the drag experessions changes from 7 drag counts ($r_{\mathcal{W}} = 2.3$) to 2 drag counts ($r_{\mathcal{W}} = 19$). This analysis shows the numerical robustness of the formulae used in case od 2D flows. Unluckily, in three-dimensional problems, the drag decomposition does not converge moving $r_{\mathcal{W}}$ infinitely downstream. Indeed, as for instance discussed in detail by Liu in [59], the kinetic energy of the free-vortices dissipates in internal energy and the result is that infinitely downstream the whole drag is given by D_{vw}. This behaviour can be easily evidenced by numerical experiments. For instance, Lanzetta et al. [60] already verified it post-processing by D_{i} and Maskell's formula [14] the numerical solution around a high-lift wing body configuration. The Lamb vector field is generated by the body boundary layer where velocity and vorticity are essentially orthogonal. On the contrary, due to Kelvin theorem, the free vorticity in the wake is parallel to the local velocity and the associated Lamb vector is zero. As shown by Mele et al. [45] the vortex force of the body boundary layer and near wake is the main responsible for lift, but it also generates a drag component, the lift-induced drag indeed. However, as the dissipation of kinetic energy of free vortices advances, the vortex force of the far wake provides a thrust force which counterweights the former drag contribution. In the case of elliptical wing analyzed (see Fig. 2.2.4), the computed total drag is independent of $r_{\mathcal{W}}$ and in agreement with the near field value with the maximum drag variation being within 4 drag counts for $r_{\mathcal{W}} > 1$. D_{i} reaches a maximum value for $r_{\mathcal{W}} \approx 1$chord downstream of wing trailing edge approaching the reference value $C_{D_{\text{i}}} = C_L^2/(\pi \mathcal{AR})$, but then starts to decrease. As anticipated, the kinetic energy reduction is compensated by the increase of D_{vw} preserving a computation of the total drag independent of the integration domain. The exchange between D_{i} and D_{vw} as the distance of the wake plane from the body increases is essentially of numerical nature.

This analysis suggests to associate the lift-induced drag to the vortex force generated by the body and very near wake boundary layer, obtained in practice by the maximum value reached by the reversible drag component ($r_{\mathcal{W}} \approx 1$ in present calculations). Indeed, as shown in [45], this value is in remarkable agreement with the Prandtl's expression of lift-induced drag for an elliptical wing even in transonic flow.

The analysis in the limit of effectively inviscid flow ($Re_\infty \to \infty$) can definitely prove that vortex force is generated in the flow regions near the body. Increasing the Reynolds

number, indeed, the body-boundary layer gets closer to the body surface and, in inviscid and subsonic flow conditions, the physical Lamb vector field to be considered is generated only on the body surface; other contributions are numerical artifacts and should not be taken into account. The extension of vortex-force theory in effectively inviscid flow will finally confirm the direct link between the Lamb vector field and the *reversible* part of the aerodynamic force, a fundamental aspect for the comprehension of the aerodynamic force generation process.

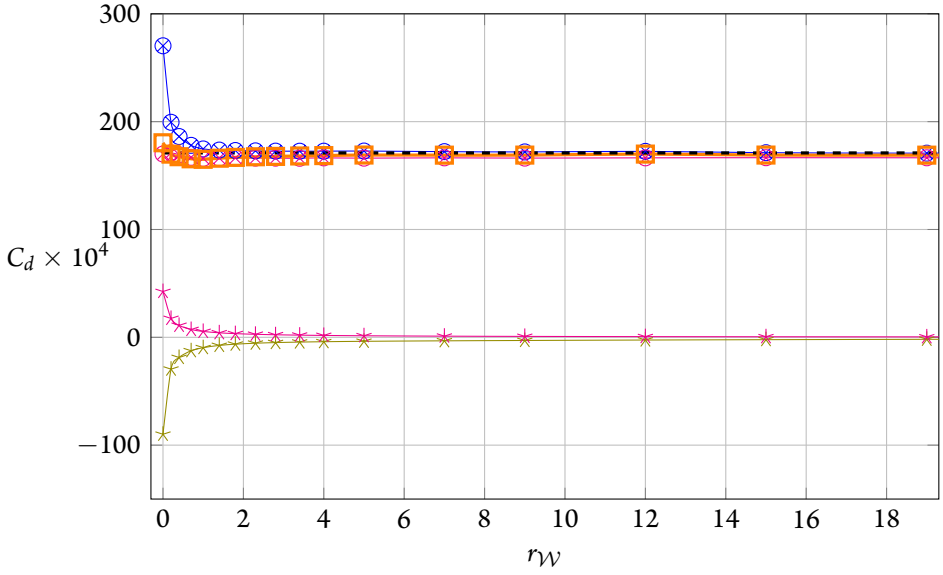


Figure 2.2.3: NACA 0012 airfoil, $Re_\infty = 6 \times 10^6$, $M_\infty = 0.75$, $a = 2°$. Computed drag breakdown against position of the wake plane: comparison between vortex force theory and thermodynamic methods. D_{i} (—✳—), $D_{\mathrm{i}}^{\mathrm{M}}$ (—✳—), $D_{\mathrm{vw}}^{\mathrm{DV}}$ (—⊗—), $D_{\mathcal{W}}$ (—⊟—), D_{nf} (- - -).

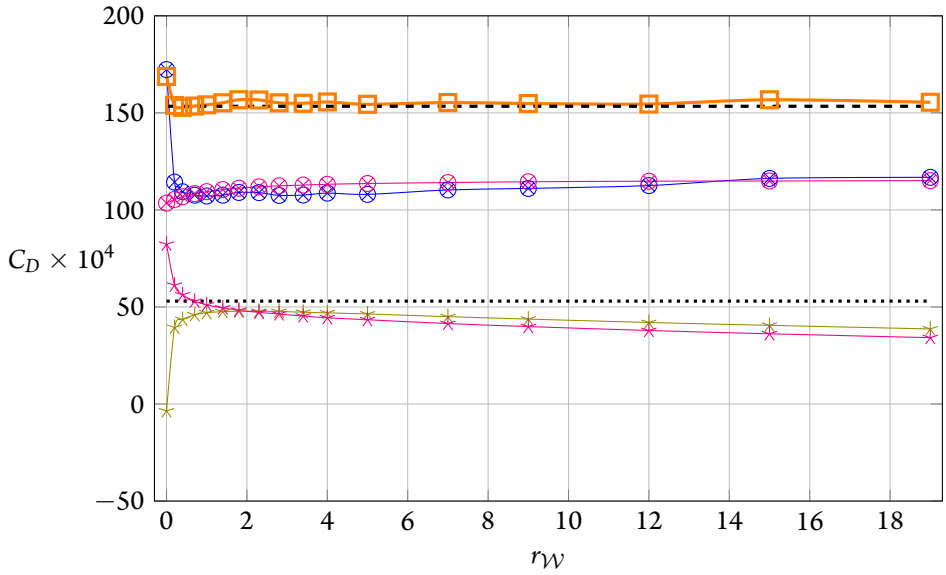


Figure 2.2.4: Elliptical wing with $\mathcal{AR} = 7$, $Re_\infty = 3 \times 10^6$, $M_\infty = 0.5$, $\alpha = 4°$. Computed drag breakdown against position of the wake plane: comparison between vortex force theory and thermodynamic methods. D_i (—✳—), D_i^M (—✳—), $C_L^2/\pi\mathcal{AR}$ (·····), $D_\mathrm{vw}^\mathrm{DV}$ (—⊗—), $D_{\mathcal{W}}$ (—□—), D_nf (- - -).

2.3 Extension of the Lamb Vector Theory to Inviscid Flow

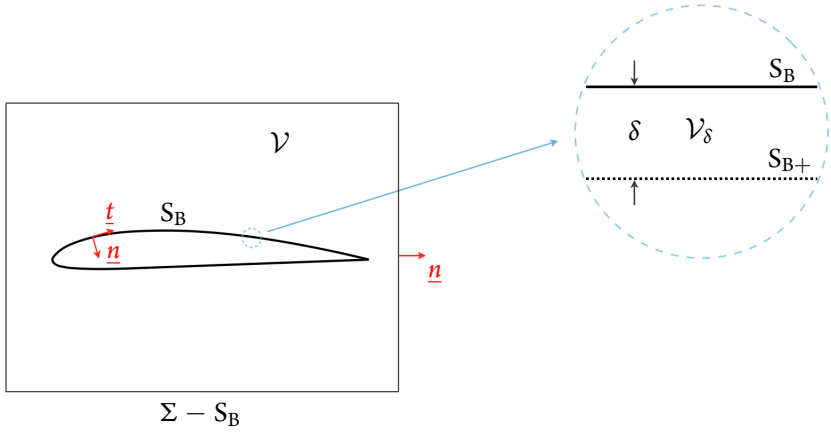


Figure 2.3.1: Sketch of the integration domain for an effectively inviscid flow.

The weak solution of the steady Euler equations governing the flow domain $\mathcal{V}$ around the solid body B is now considered. The extension of the Lamb vector based theory to such a flow is not trivial: for instance, the application of Eq. (2.1) to the case of incompressible flow around a two-dimensional airfoil would lead to the absence of lift since $\underline{\zeta} = 0$ in the flow. Indeed, the vorticity due to the shear stresses in the body boundary layer cannot be generated without the viscosity of a real flow. To take into account for the body boundary layer, a proper vortex sheet on the body surface needs to be added to the solution so that an *effectively inviscid flow* is realized.

For a steady inviscid flow, the near-field expression of the aerodynamic force Eq. (1.6) reduces to

$$\underline{F}_{\mathrm{nf}} = \int_{S_B} p\underline{n}\, \mathrm{dS}\,, \tag{2.51}$$

whereas the momentum equation can be written as:

$$\rho\left(\underline{\zeta} \times \underline{V}\right) + \rho\underline{\nabla}\left(\frac{V^2}{2}\right) = -\underline{\nabla} p\,. \tag{2.52}$$

Integrating Eq. (2.52) in $\mathcal{V}$ bounded by the body surface S_B and the far-field surface Σ and applying the Gauss' theorem,

$$\begin{aligned} \underline{F} = &-\int_{\mathcal{V}} \rho\left(\underline{\zeta} \times \underline{V}\right)\, \mathrm{d}\mathcal{V} + \int_{\mathcal{V}} \frac{V^2}{2}\underline{\nabla}\rho\, \mathrm{d}\mathcal{V} \\ &-\int_{\Sigma - S_B}\left(\rho\frac{V^2}{2} + p\right)\underline{n}\, \mathrm{dS} - \int_{S_B}\rho\frac{V^2}{2}\underline{n}\, \mathrm{dS}\,. \end{aligned} \tag{2.53}$$

Using Eq. (A.1) of Appendix A on the volume integral containing $\underline{\nabla}\rho$ and first Eq. (A.2) and then Eq. (2.52) on the surface integral extended to $\Sigma - S_B$, Eq. (2.53) becomes

$$\begin{aligned} \underline{F} = &-\int_{\mathcal{V}}\left\{\rho\underline{\zeta} \times \underline{V} - \frac{1}{k}\underline{r} \times \left[\underline{\nabla} \times \left(\frac{V^2}{2}\underline{\nabla}\rho\right)\right]\right\}\, \mathrm{d}\mathcal{V} \\ &-\frac{1}{k}\int_{S_B}\underline{r} \times \left(\underline{n} \times \frac{V^2}{2}\underline{\nabla}\rho\right)\, \mathrm{dS} - \int_{S_B}\rho\frac{V^2}{2}\underline{n}\, \mathrm{dS} \\ &-\frac{1}{k}\int_{\Sigma - S_B}\underline{r} \times \left[\underline{n} \times \left(\rho\underline{\zeta} \times \underline{V}\right)\right]\, \mathrm{dS}\,. \end{aligned} \tag{2.54}$$

The aerodynamic force expression based on the vortex-force theory $\underline{F}_{\mathrm{vf}}$ can now be found extending the fluid volume to $\mathcal{V}_+ = \mathcal{V} \cup \mathcal{V}_\delta$, bounded by $\Sigma - S_B$ and S_{B+} (see Fig. 2.3.1).

Imposing $\delta \to 0$ and a no-slip boundary condition on S_{B_+}, a no-thickness vortex sheet is added to the inviscid flow present in $\mathcal{V}$ and an *effectively inviscid flow* is realized. Extending Eq. (2.54) to $\mathcal{V}_+$ it becomes:

$$\begin{aligned}\underline{F}_{vf} = &- \int_{\mathcal{V}_+} \left\{ \rho\underline{\zeta} \times \underline{V} - \frac{1}{k}\underline{r} \times \left[\underline{\nabla} \times \left(\frac{V^2}{2} \underline{\nabla}\rho \right) \right] \right\} \, d\mathcal{V} \\ &- \frac{1}{k} \int_{\Sigma - S_{B+}} \underline{r} \times \left[\underline{n} \times \left(\rho\underline{\zeta} \times \underline{V} \right) \right] \, dS \, .\end{aligned} \tag{2.55}$$

Equation (2.55), valid in both subsonic and transonic regimes, allows for the following aerodynamic force breakdown:

$$\underline{F}_{vf} = \underline{F}_{\ell} + \underline{F}_{\rho} + \underline{F}_{\Sigma} \, , \tag{2.56}$$

with

$$\underline{F}_{\ell} = - \int_{\mathcal{V}_+} \rho \left(\underline{\zeta} \times \underline{V} \right) \, d\mathcal{V} \, , \tag{2.57}$$

$$\underline{F}_{\rho} = \frac{1}{k} \int_{\mathcal{V}_+} \underline{r} \times \left[\underline{\nabla} \times \left(\frac{V^2}{2} \underline{\nabla}\rho \right) \right] \, d\mathcal{V} \, , \tag{2.58}$$

$$\underline{F}_{\Sigma} = -\frac{1}{k} \int_{\Sigma - S_{B+}} \underline{r} \times \left[\underline{n} \times \left(\rho\underline{\zeta} \times \underline{V} \right) \right] \, dS \, . \tag{2.59}$$

In a subsonic effectively inviscid flow Eq. (2.55) can be simplified limiting the integration domain to $\mathcal{V}_\delta$ only. Indeed, if no shock wave is present in $\mathcal{V}$, the vorticity is not zero only in the body wake where $\underline{\zeta} \| \underline{V}$ and $\underline{\ell} = 0$. Therefore, $\underline{F}_{\ell}$ can be limited to $\mathcal{V}_\delta$ whereas $\underline{F}_{\Sigma} = 0$. Moreover, thanks to Gibbs'equation

$$\begin{aligned}\frac{1}{k} \int_{\mathcal{V}} \underline{r} \times \left[\underline{\nabla} \times \left(\frac{V^2}{2} \underline{\nabla}\rho \right) \right] \, d\mathcal{V} &= -\frac{1}{k} \int_{\mathcal{V}} \underline{r} \times \left\{ \underline{\nabla} \times \left[\rho \underline{\nabla} \left(\frac{V^2}{2} \right) \right] \right\} \, d\mathcal{V} \\ &= \frac{1}{k} \int_{\mathcal{V}} \underline{r} \times \left(\underline{\nabla} \times \underline{\nabla} p \right) \, d\mathcal{V} = 0 \, .\end{aligned} \tag{2.60}$$

Thus, Eq. (2.56) in a subsonic flow can be rewritten as:

$$\underline{F}_{vf} = \underline{F}_{\ell} + \underline{F}_{\rho} \, , \tag{2.61}$$

with

$$\underline{F}_\ell = -\int_{\mathcal{V}_\delta} \rho \left(\underline{\zeta} \times \underline{V}\right) \, \mathrm{d}\mathcal{V} \,, \tag{2.62}$$

$$\underline{F}_\rho = \frac{1}{k} \int_{\mathcal{V}_\delta} \underline{r} \times \left[\underline{\nabla} \times \left(\frac{V^2}{2} \underline{\nabla}\rho\right)\right] \, \mathrm{d}\mathcal{V} \,. \tag{2.63}$$

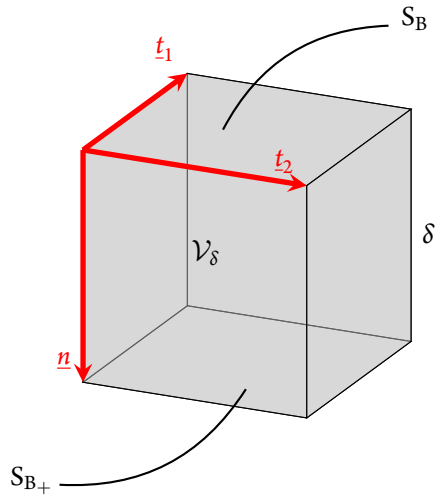


Figure 2.3.2: Finite volume domain used for deriving Eq. (2.66).

Although Eq. (2.61) has a clear physical meaning, it is immeasurable because the body vortex sheet has no thickness. To get a measurable form for Eqs. (2.62) and (2.63) a body vortex sheet of finite thickness δ must be considered. The fluid velocity $\underline{V}$ is imposed to be zero on S_{B_+} and equal to the value given by the weak Euler solution on S_B. Equation 2.62 can be rewritten as:

$$\underline{F}_\ell = \int_{\mathcal{V}_\delta} \rho \underline{\nabla} \left(\frac{V^2}{2}\right) \, \mathrm{d}\mathcal{V} - \int_{\mathcal{V}_\delta} \rho \underline{V} \cdot \underline{\nabla V} \mathrm{d}\mathcal{V} \,, \tag{2.64}$$

where, according to the notation showed in Fig. 2.3.2 $\underline{\nabla}$ can be decomposed in $\underline{\nabla}_t = (\partial/\partial t_1 \, \underline{t}_1, \partial/\partial t_2 \, \underline{t}_2)$ to take into account for the derivatives in the direction tangent to S_B and $\underline{\nabla}_n = \partial/\partial n \, \underline{n}$ for the derivative in the direction normal to S_B. Thus Eq. (2.64)

becomes

$$\begin{aligned}\underline{F}_\ell = &\int_{S_B} dS \int_\delta \rho \underline{\nabla}_n \left(\frac{V^2}{2}\right) dl + \int_{S_B} dS \int_\delta \rho \underline{\nabla}_t \left(\frac{V^2}{2}\right) dl \\ &- \int_{S_B} dS \int_\delta \rho \underline{V} \cdot \underline{\nabla}_t \underline{V} \, dl - \int_{S_B} dS \int_\delta \rho \underline{V} \cdot \underline{\nabla}_n \underline{V} \, dl \,,\end{aligned} \tag{2.65}$$

where the last term is zero because $\underline{V}$ and $\underline{\nabla}_n$ are orthogonal each other. When $\delta \to 0$ the integrals of Eq. (2.65) containing $\underline{\nabla}_t$ go to zero because they are not δ-functions and $\underline{F}_\ell$ reduces to

$$\underline{F}_\ell = -\int_{\mathcal{V}_\delta} \rho \underline{\zeta} \times \underline{V} \, d\mathcal{V} = -\int_{S_B} \rho \frac{V^2}{2} \, dS \,. \tag{2.66}$$

The vortex force expression given by Eq. (2.66) has already been derived by Saffman [36] for an incompressible flow and clearly returns the near-field aerodynamic force formula via the Bernoulli's equation.

The measurable form of the compressible generation term for a subsonic inviscid flow Eq. (2.63) can be easly obtained considering the total aerodynamic force expression $\underline{F}$ as given by Eq. (2.54); since in subsonic conditions $\underline{\zeta} = 0$ in $\mathcal{V}$ the formula becomes

$$\underline{F} = -\int_{S_B} \rho \frac{V^2}{2} \, dS - \frac{1}{k} \int_{S_B} \underline{r} \times \left[\underline{n} \times \left(\frac{V^2}{2} \underline{\nabla} \rho\right)\right] dS \,. \tag{2.67}$$

Subtracting Eq. (2.66) from Eq. (2.67) there is

$$\underline{F}_\rho = -\frac{1}{k} \int_{S_B} \underline{r} \times \left[\underline{n} \times \left(\frac{V^2}{2} \underline{\nabla} \rho\right)\right] dS \,. \tag{2.68}$$

Since both the terms present in Eq. (2.67) consist in surface integrals on the body surface S_B we can conclude that in the limit case of subsonic and effectively inviscid flow the lift-induced drag definition does not depend on the integration domain.

Finally the measurable form of the aerodynamic force expression for a transonic effectively inviscid flow is obtained considering for $\underline{F}_\ell$ and $\underline{F}_\rho$ the explicit part contained in $\mathcal{V}$

$$\underline{F}_{vf} = \underline{F}_\ell + \underline{F}_\rho + \underline{F}_\Sigma \,, \tag{2.69}$$

$$\underline{F}_\ell = -\int_{\mathcal{V}} \rho \underline{\zeta} \times \underline{V} \, d\mathcal{V} - \int_{S_B} \rho \frac{V^2}{2} \, dS \,, \tag{2.70}$$

$$\underline{F}_{\rho} = -\frac{1}{k}\int_{\mathcal{V}} \underline{r} \times \left[\underline{\nabla} \times \left(\frac{V^2}{2}\underline{\nabla}\rho\right)\right] \mathrm{d}\mathcal{V} - \frac{1}{k}\int_{S_B} \underline{r} \times \left[\underline{n} \times \left(\frac{V^2}{2}\underline{\nabla}\rho\right)\right] \mathrm{dS}\,, \quad (2.71)$$

$$\underline{F}_{\Sigma} = -\frac{1}{k}\int_{\Sigma - S_B +} \underline{r} \times \left[\underline{n} \times \rho\left(\underline{\zeta} \times \underline{V}\right)\right] \mathrm{dS}\,. \quad (2.72)$$

2.3.1 Force Breakdown in Inviscid Flow: Numerical Verifications

The formulae for the aerodynamic force computation and breakdown derived in Section 2.3 will be now checked by analyzing CFD solutions of the Euler equations. A NACA 0012 airfoil and an elliptic wing with $\mathcal{AR} = 7$ and the wing sections shaped as the same airfoil at different Mach numbers will be considered. The software used for the computations present in this section is FLOWer. An O-type structured grid with 256×128 cells and the far field placed $40c$ distant from the airfoil has been adopted for the two-dimensional flow.For the elliptic wing a CO-type structured mesh with $192 \times 64 \times 64$ cells and the far field distant $30c$ from the body has been used.The integrations present in Eqs. (2.61) and (2.69) have been performed by a second-order accurate trapezoidal method using nodal values.

It is well known that in a two-dimensional steady, subsonic, and inviscid condition there is no vorticity in the flow, but in weak Euler solutions an unphysical vorticity field due to the numerical viscosity is present; this is clearly visible near the leading edge of the airfoil of Fig. 2.3.3-a where the vorticity field ζ obtained at angle of attack $a = 4^\circ$ and Mach number $M_\infty = 0.3$ is showed. In Fig. 2.3.3-b the vorticity contour at $M_\infty = 0.7$ is displayed to highlight the physical vorticity arising from the curved shock wave. In addition, a strong trailing edge wake is present because of the upper and lower airfoil stagnation pressures with different values. In three-dimensional flows (see Fig. 2.3.4), even if the vorticity of the trailing vortices is explicitly captured, the associated Lamb vector field is still zero because $\underline{\zeta} \parallel \underline{V}$, as discussed in the previous section.

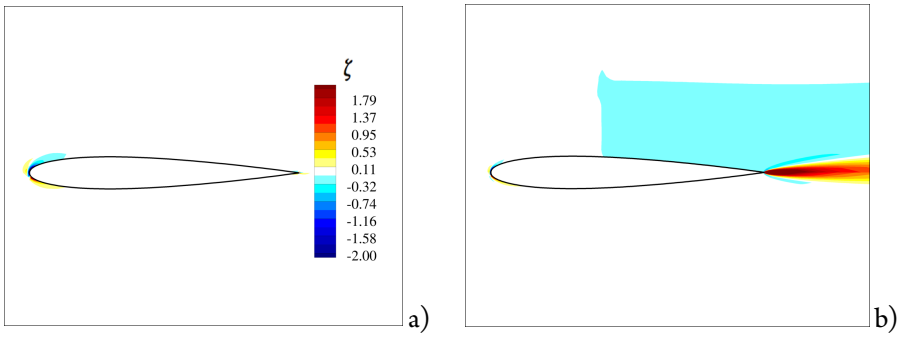


Figure 2.3.3: NACA 0012 airfoil, $\alpha = 4°$, weak Euler solution. Contours of vorticity at ζ a) $M_\infty = 0.3$ and b) $M_\infty = 0.7$.

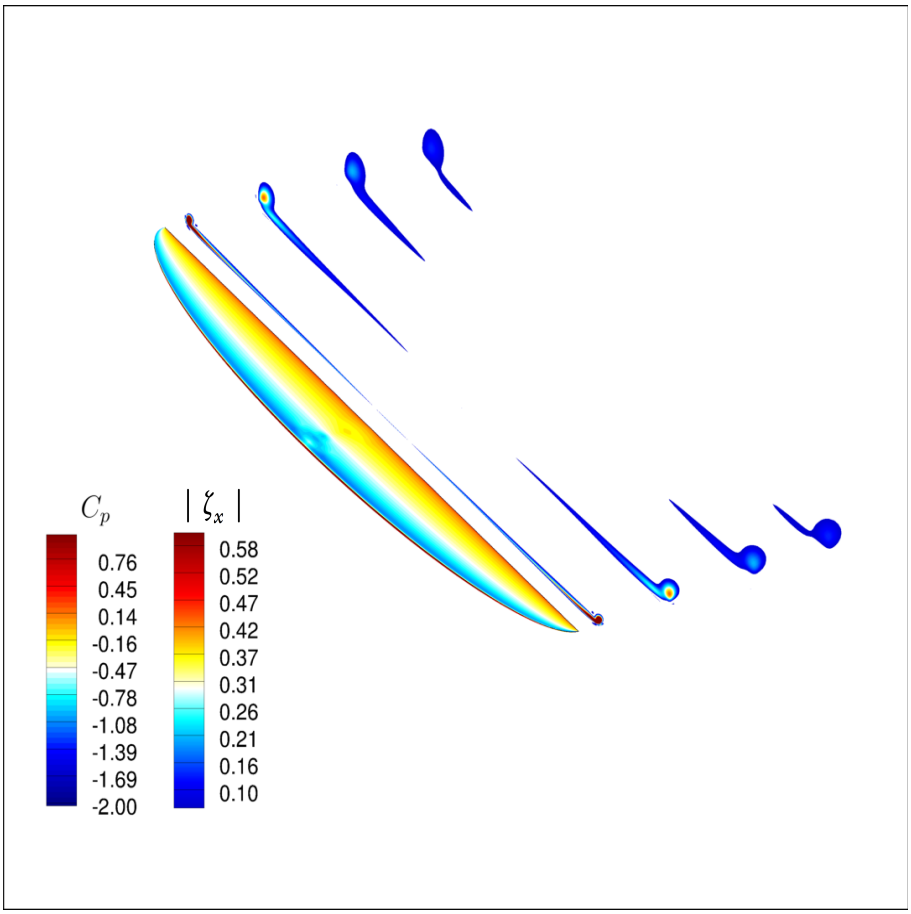


Figure 2.3.4: Elliptic wing, $M_\infty = 0.1$, $\alpha = 4°$, weak Euler solution. Contours of x-vorticity modulus $|\zeta_x|$ in the wake and pressure coefficient C_p on the wing.

To correctly compute the aerodynamic force from the weak Euler solutions the nonzero Lamb vector field due to the unphysical vorticity present in subsonic condition must be considered. Therefore, Eqs. (2.70) to (2.72) have been adopted in both subsonic and transonic calculations. The vortex sheet contribution required the numerical calculation of surface integrals on the body: it has been computed using a simple second-order accurate formula based on the knowledge of velocity and density on the body cell faces. Tables 2.3.1 and 2.3.2 show the lift and drag components calculated in subsonic flow for the NACA 0012 airfoil and elliptic wing at different Mach numbers. $F_{\ell(\mathcal{V})}$, the first term on the right-hand side of Eq. (2.70), and $F_{\ell(S_B)}$, the second term on the right-hand side of Eq. (2.70) represent the vortex force contributed by the distributed vorticity and in the flow field the body vortex sheet, respectively. Even if very small, the unphysical contribution of $F_{\ell(\mathcal{V})}$ improves the agreement with the reference near-field result. In the two-dimensional test it is within the fourth digit for Cl. The computed spurious drag is lower than three drag counts. The three-dimensional test is still satisfactory, although the errors introduced by the more complex grid are larger. The agreement can be better appreciated by the analysis of Fig. 2.3.5, which shows the total aerodynamic force $\underline{F}_{\text{vf}}$ in subsonic conditions for the airfoil case. A comparison with the near-field value Eq. (1.6) in terms of lift and drag coefficients changing the Mach number up to $M_\infty = 0.5$ is presented. The decomposition of the force in $\underline{F}_\ell$ and $\underline{F}_\rho$ is also shown. A reduction of the vortex force term (the total aerodynamic force in incompressible flow) increasing the Mach number has been found for the lift component: as expected, the most of total lift increase with Mach number is due to the compressibility generation term $\underline{F}_\rho$. In terms of drag coefficient, it is shown that the Lamb vector term $\underline{F}_\ell$ is responsible for the drag, while the compressible generation term $\underline{F}_\rho$ provides a thrust.

The same analysis, but obtained for the elliptic wing, is shown in Fig. 2.3.6. The two-dimensional results are confirmed; in particular it is evidenced that the total aerodynamic force, given by $\underline{F}_\ell + \underline{F}_\rho$ in subsonic condition is responsible for both lift and lift-induced drag, the latter also in agreement with the Prandtl's formula $CD_i = CL^2/\pi \mathcal{AR}$.

Table 2.3.1: NACA 0012 airfoil, weak Euler solution, $\alpha = 4^\circ$. Breakdown of F_{vf} at different Mach numbers and comparison with near field value F_{nf}.

C_l

M_∞	$F_{\ell(S_B)}$	$F_{\ell(\mathcal{V})}$	F_ℓ	$F_{\rho(S_B)}$	$F_{\rho(\mathcal{V})}$	F_ρ	F_Σ	F_{vf}	F_{nf}
0.01	0.47974	0.00280	0.48254	0.00003	0.00000	0.00003	0.00001	0.48258	0.48219
0.3	0.47672	0.00095	0.47767	0.03176	0.00006	0.03182	0.00000	0.50949	0.50923
0.5	0.46352	0.00314	0.46666	0.10711	0.00024	0.10735	0.00005	0.57406	0.57433

$C_d \times 10^4$

M_∞	$F_{\ell(S_B)}$	$F_{\ell(\mathcal{V})}$	F_ℓ	$F_{\rho(S_B)}$	$F_{\rho(\mathcal{V})}$	F_ρ	F_Σ	F_{vf}	F_{nf}
0.01	12	-16	-4	3	3	0	1	-3	1
0.3	33	-16	17	-19	1	-18	0	-1	1
0.5	80	-11	69	-71	2	-69	1	1	1

Table 2.3.2: Elliptic wing, weak Euler solution, $\alpha = 4^\circ$. Breakdown of F_{vf} at different Mach numbers and comparison with near field value F_{nf}.

C_L

M_∞	$F_{\ell(S_B)}$	$F_{\ell(\mathcal{V})}$	F_ℓ	$F_{\rho(S_B)}$	$F_{\rho(\mathcal{V})}$	F_ρ	F_Σ	F_{vf}	F_{nf}
0.01	0.34173	0.00074	0.34247	0.00002	-0.00004	-0.00002	-0.00025	0.34220	0.34207
0.3	0.33209	0.00102	0.33311	0.01980	0.00110	0.02090	0.00893	0.36294	0.35426
0.5	0.31331	0.00172	0.31503	0.06710	-0.01437	0.05273	0.00903	0.37679	0.38176

$C_D \times 10^4$

M_∞	$F_{\ell(S_B)}$	$F_{\ell(\mathcal{V})}$	F_ℓ	$F_{\rho(S_B)}$	$F_{\rho(\mathcal{V})}$	F_ρ	F_Σ	F_{vf}	F_{nf}
0.01	52	-3	49	0	0	0	-3	46	55
0.3	62	-1	61	-4	5	1	27	89	61
0.5	88	-2	86	-12	-19	-31	26	81	71

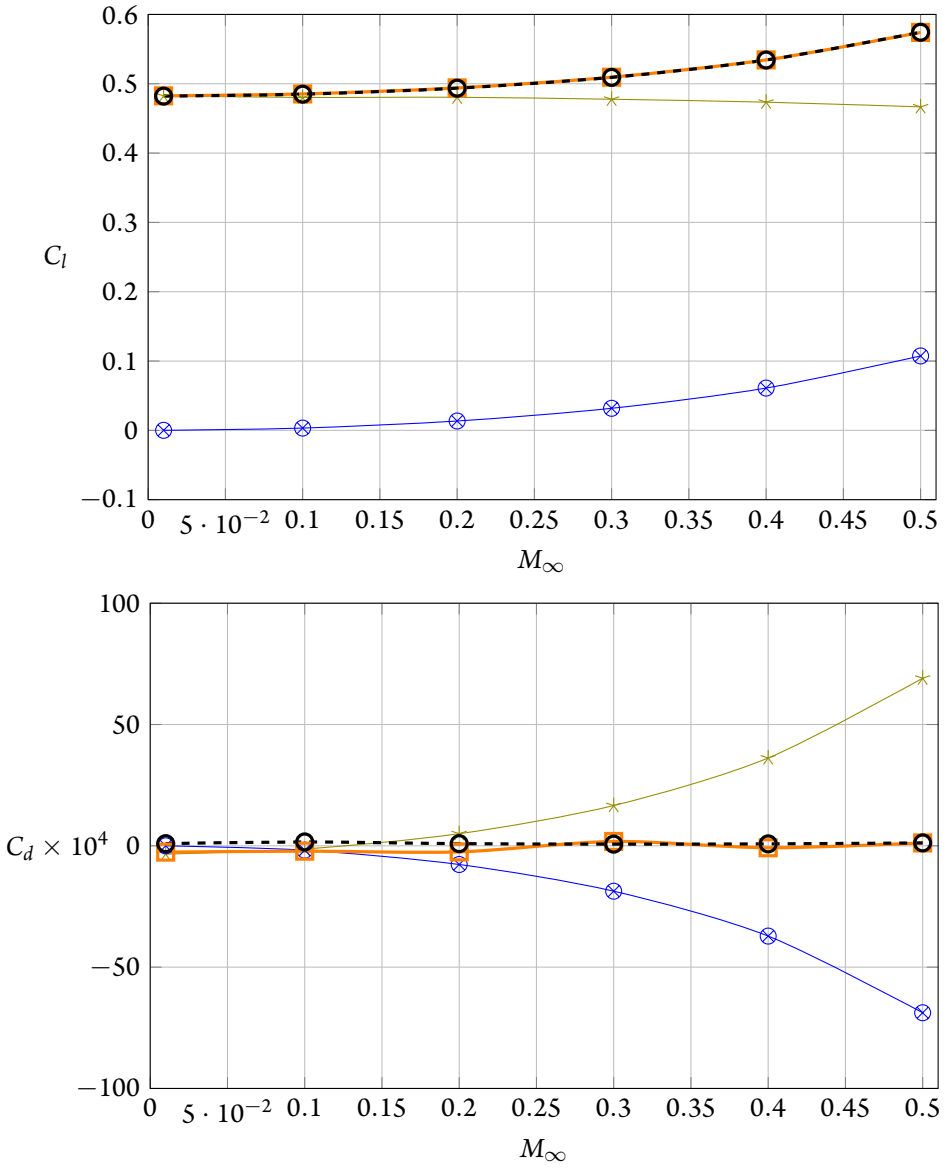


Figure 2.3.5: NACA 0012 airfoil, $\alpha = 4°$, effectively inviscid flow. Breakdown of lift a) and drag b) coefficients at different Mach numbers. F_ℓ (—✶—), F_ρ (—⊗—), F_{vf} (—⊟—), F_{nf} (-⊙-).

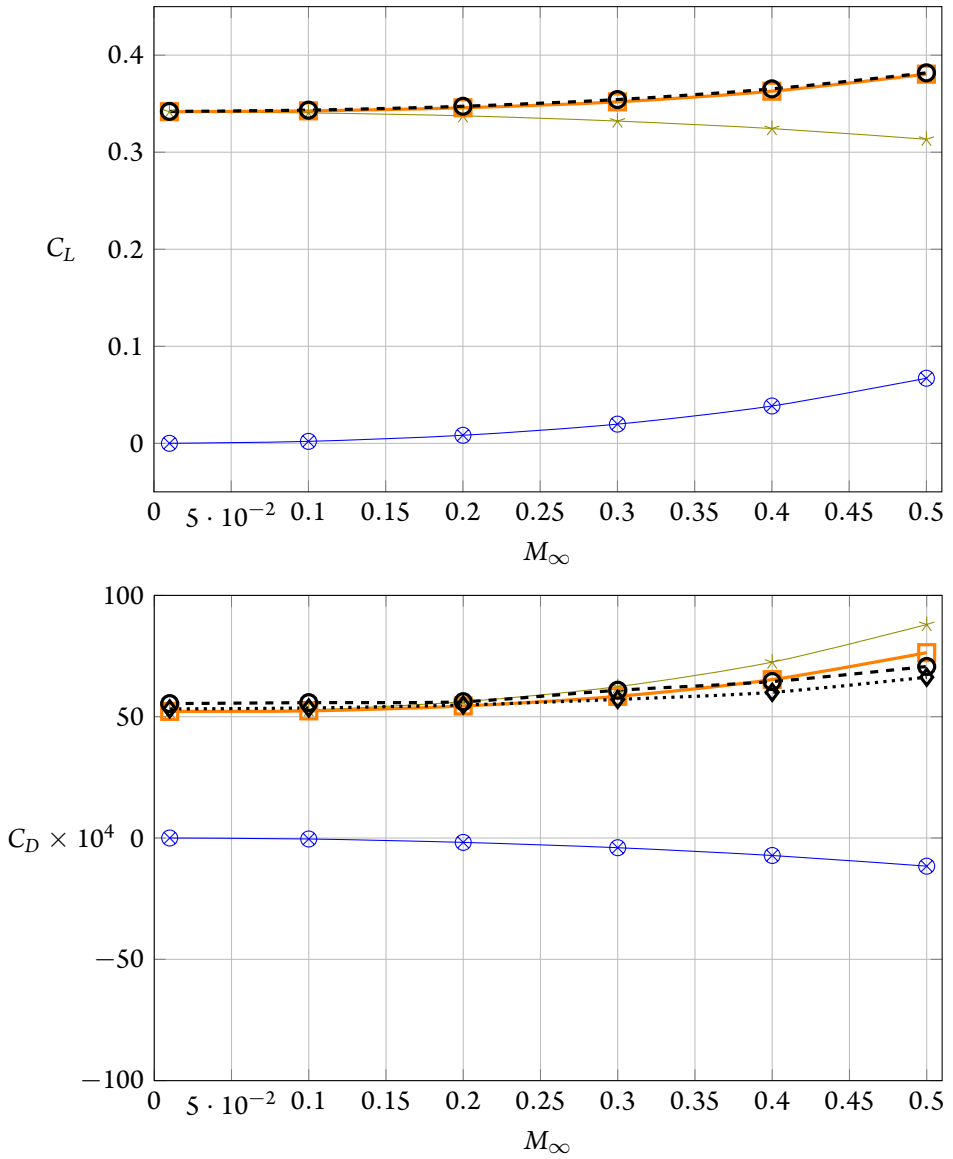


Figure 2.3.6: Elliptic wing, $a = 4°$, effectively inviscid flow, subsonic regime. Breakdown of lift a) and drag b) coefficients for different Mach numbers. F_ℓ (—✶—), F_ρ (—⊗—), F_{vf} (—⊟—), $CD_i = CL^2/\pi\mathcal{R}$ (3.9), F_{nf} (-⊖-).

The computation and breakdown of the aerodynamic force for the NACA 0012 airfoil immersed in inviscid transonic flow has also been performed. Fig. 2.3.7 shows the sensi-

tivity of the results to the choice of the integration region. The agreement improves as the integration domain is enlarged, but it is already very satisfactory when the far field surface Σ is placed at $r_\Sigma = 4c$, with r equal to the modulus of a position vector with the origin in the airfoil leading edge. Obviously, The results are displayed only when the integration domain contains the whole shock wave to guarantee a consistent calculation of the aerodynamic force. As expected, the contribution of F_Σ is negligible in terms of lift (within 1 drag count when $r_\Sigma \geq 4.8c$) while represents the main part of the drag (substantially the wave drag). In Table 2.3.3 the results obtained with $r_\Sigma = 4c$ with the separated contributions of flow field $(F_{\ell(\mathcal{V})}, F_{\rho(\mathcal{V})})$ and vortex sheet $(F_{\ell(S_B)}, F_{\rho(S_B)})$ are reported. As already discussed, in subsonic regime and in the limit of effectively inviscid flow $(Re_\infty \to \infty)$, the force decomposition does not depend on the integration domain but only on the body vortex sheet; in other words, the force generation occurs in the body boundary layer only.

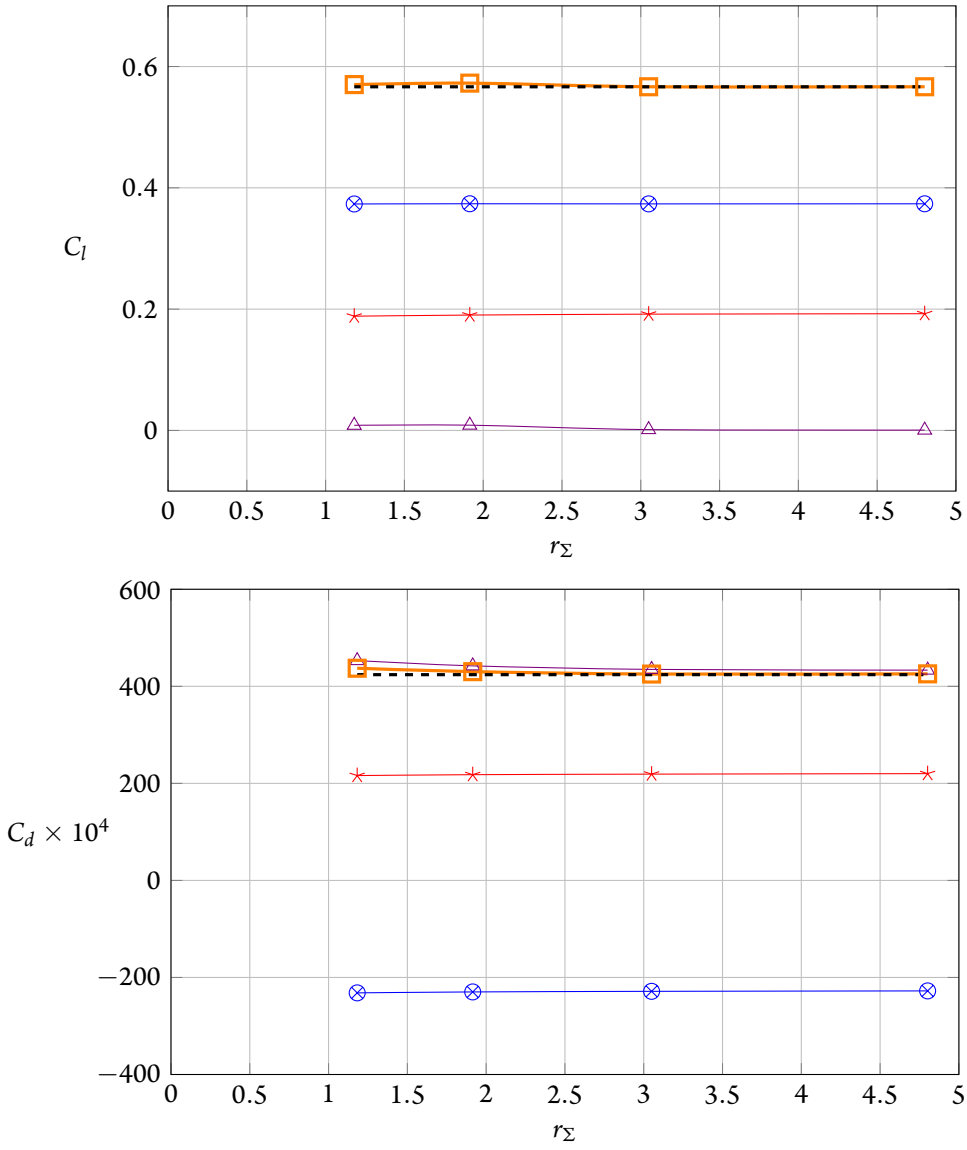


Figure 2.3.7: NACA 0012 airfoil, $M_\infty = 0.8$, $\alpha = 2°$, effectively inviscid flow, transonic regime. Breakdown of lift a) and drag b) coefficients changing the distance r_Σ of the far field surface Σ from the body. F_ℓ (—✶—), F_p (—⊗—), F_Σ (—△—), F_{vf} (—□—), F_{nf} (-⊖-).

Table 2.3.3: NACA0012 airfoil, weak Euler solution, $M_\infty = 0.8$, $\alpha = 2^\circ$. Breakdown of F_{vf} and comparison with near field value F_{nf} at $r_\Sigma = 4c$.

	$F_{\ell(S_B)}$	$F_{\ell(\mathcal{V})}$	F_ℓ	$F_{\rho(S_B)}$	$F_{\rho(\mathcal{V})}$	F_ρ	F_Σ	F_{vf}	F_{nf}
C_l	0.16188	0.02984	0.19173	0.27174	0.10179	0.37353	0.00137	0.56623	0.56657
$C_d \times 10^4$	170	49	219	195	-424	-229	435	425	424

2.3.2 Reversible and Irreversible Aerodynamic Forces

Present extension of the Lamb Vector Theory to inviscid flow gives two important theoretical results for the aerodynamic force decomposition:

1. the aerodynamic force exerted on a body immersed in a subsonic and inviscid flow reduces to lift and lift-induced drag (in case of three-dimensional body) and is generated without entropy production; in other words it is a *reversible force*;

2. in the limit of $Re_\infty \to \infty$ and subsonic flow the aerodynamic force is generated in the "body boundary layer" only.

A new aerodynamic force breakdown valid for both inviscid and viscous flow is here proposed:

$$\underline{F}_{\text{vf}} = \underline{F}_{\text{rev}} + \underline{F}_{\text{irr}} \,. \tag{2.73}$$

According to Eq. (2.73) there is a *reversible force* ($\underline{F}_{\text{rev}}$) that, as already discussed, is not linked to the entropy production, and an *irreversible force* ($\underline{F}_{\text{irr}}$), present only when the entropy is produced in the flow and accounting for the profile drag. $\underline{F}_{\text{rev}}$ is the sum of the vortex force $\underline{F}_\ell$ and the compressible generation term $\underline{F}_\rho$ given by Eqs. (2.70) and (2.71) for inviscid flow, Eqs. (2.2) and (2.3) for viscous laminar flow and Eqs. (2.26) and (2.27) for viscous turbulent flow. $\underline{F}_{\text{irr}}$ is given by $\underline{F}_\Sigma$, expressed by Eq. (2.72) in inviscid flow, and $\underline{F}_\Sigma + \underline{\Delta}_\mu$ in viscous flow. As discussed in Section 2.1, Δ_μ is negligible at the Reynolds numbers of aeronautical interest and, from now on, we will consider $\underline{F}_{\text{irr}} = \underline{F}_\Sigma$ with $\underline{F}_\Sigma$ given by Eq. (2.4) for viscous laminar flow and Eq. (2.28) for viscous turbulent flow. The aerodynamic force decomposition for inviscid, laminar and turbulent flows is summarized in Appendix C.2 of Appendix C.

To deepen the result reported in Item 2 the effect of the integration domain size on the aerodynamic force computation and decomposition in viscous flow is analyzed. Indeed, in Section 2.2 it has been underlined that one of the open issues related to the drag breakdown problem is the choice of the integration domain because of the exchange (due to both numerical and physical phenomena) between the reversible and the irreversible forces. Moreover, it has been suggested that, if no shock is present, a force breakdown could be obtained limiting the integration domain to the body boundary layer and the near wake. This idea has been strengthen in Section 2.3, where the generation of the total aerodynamic force in case of inviscid and subsonic flow has been linked to the "body boundary layer" only. The choice of the integration domain for a correct force breakdown seems

thus guided by the Reynolds number of the problem analyzed. To test the correctness of this statement the aerodynamic-force breakdowns for a NACA 0012 airfoil immersed in a flow at $M_\infty = 0.3$, $\alpha = 2^\circ$ and different Reynolds numbers have been computed. CFD analyses have been performed on C-type grids with512 cells around the airfoil built as described in Section 2.2.1: laminar flow has been assumed for $Re_\infty = 10^3$ while a fully turbulent flow, modeled with $k - \zeta$ SST turbulence model, has been considered for the other Reynolds numbers ($Re_\infty = 10^6$, $Re_\infty = 10^7$). As done in Section 2.2.1, the effect of the integration domain on the force decomposition has been analyzed changing the wake plane position; the results are collected from Fig. 2.3.8 to Fig. 2.3.10 for the different Reynolds numbers. The agreement of $\underline{F}_{\text{vf}}$ with the reference near field force is confirmed for all Reynolds numbers and the lift decomposition is in practice not affected by $r_{\mathcal{W}}$. For the drag is necessary to take into account for a near wake contribution to obtain a converged decomposition between F_{rev} and F_{irr}: the convergence is reached when the reversible and the irreversible forces changes less than 1 drag count respect to their asymptotic value changing $r_{\mathcal{W}}$. It can be noted that, increasing the Reynolds number, the value of $r_{\mathcal{W}}$ at which the convergence to a constant value is reached, reduces. These value are plotted versus Re_∞ in Fig. 2.3.11. The generation of the aerodynamic force is mainly concentrated in the body boundary layer. The necessary contribution of the near wake shrinks as the Reynolds number increases and vanishes for $Re_\infty \to \infty$ as shown in the previous section (the case of effectively inviscid flow). The computed converged force decomposition against Re_∞ is proposed in Fig. 2.3.12. The figures remarks that $\underline{F}_{rev}$ is responsible, as expected, for the lift generation, but it also provides a thrust contribution very large at $Re_\infty = 10^3$. This *vortex force thrust*, although still present, vanishes as the Reynolds number increases. Figure 2.3.13 highlights where the thrust force is generated. It displays the x-wise component of the Lamb vector field for the case $Re_\infty = 10^3$. The blue color evidences that the thrust production is concentrated in the boundary layer around the leading edge: the airfoil suction region. This result, never noted up to now, should not surprise if one considers that the vortex force is responsible for the propulsive force in the case of a flapping foil [50, 61].

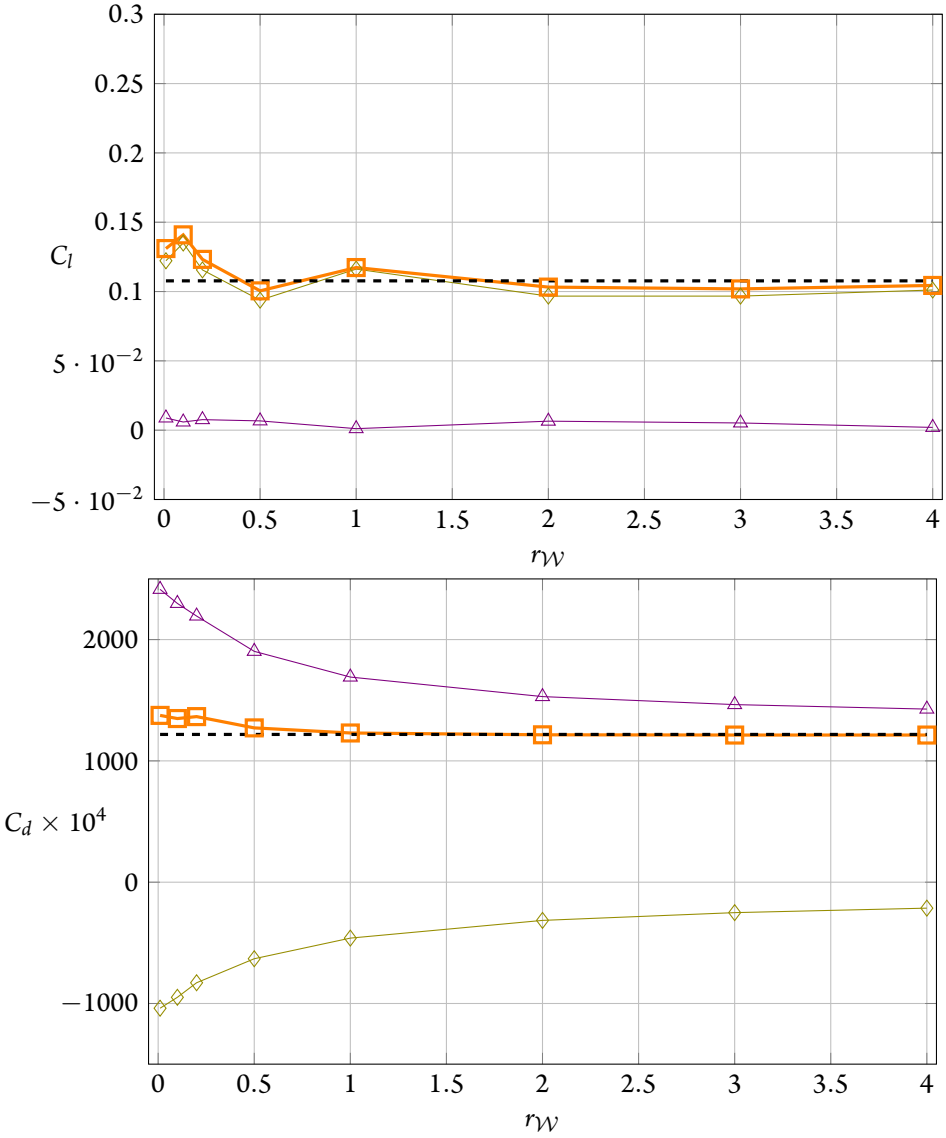


Figure 2.3.8: NACA 0012 airfoil, $M_\infty = 0.3$, $\alpha = 2°$, $Re_\infty = 10^3$. Effect of wake plane position $r_{\mathcal{W}}$ on lift and drag coefficients. Breakdown of F_{vf} and comparison with F_{nf}. F_{rev} (—◇—), F_{irr} (—△—), F_{vf} (—□—), F_{nf} (-⊙-).

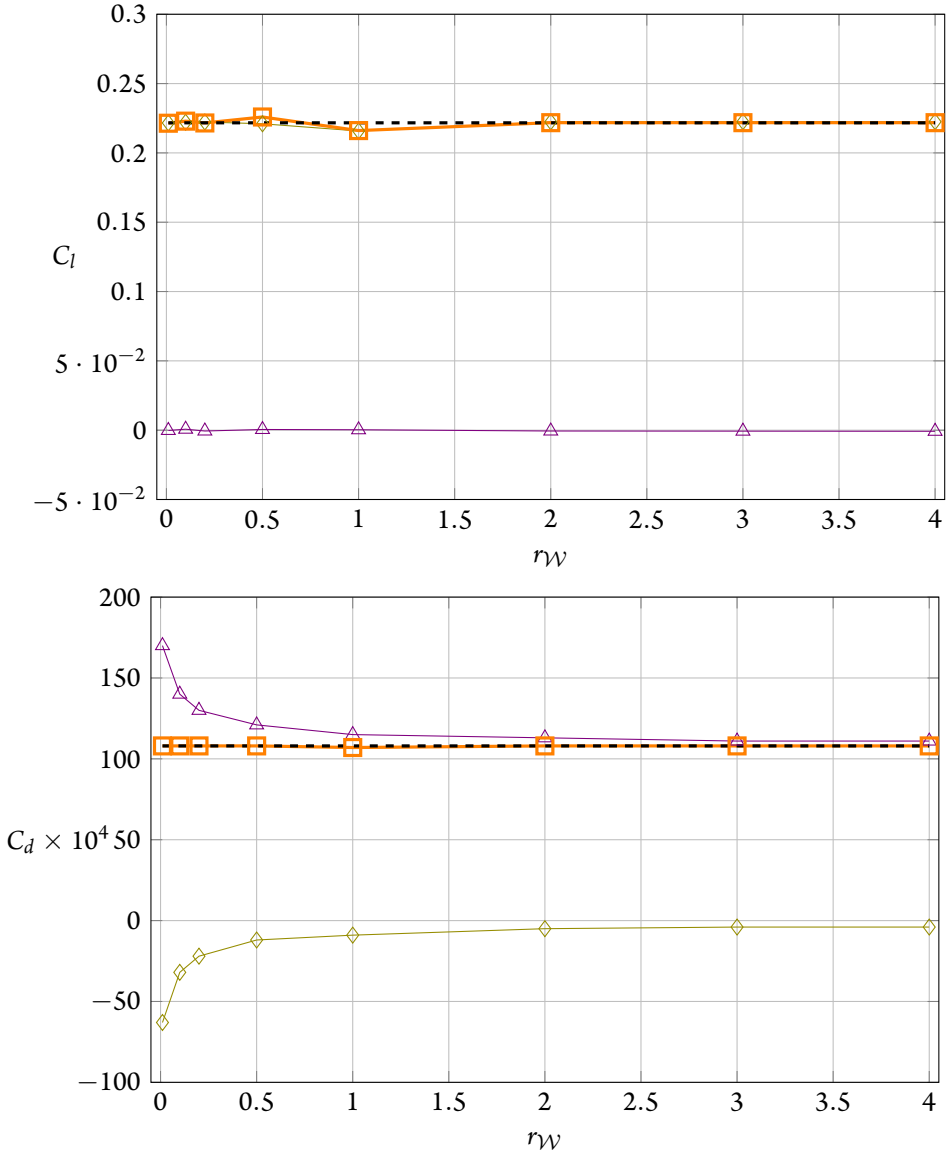


Figure 2.3.9: NACA 0012 airfoil, $M_\infty = 0.3$, $\alpha = 2°$, $Re_\infty = 10^6$. Effect of wake plane position $r_{\mathcal{W}}$ on lift and drag coefficients. Breakdown of F_{vf} and comparison with F_{nf}. F_{rev} (—◇—), F_{irr} (—△—), F_{vf} (—□—), F_{nf} (-⊖-).

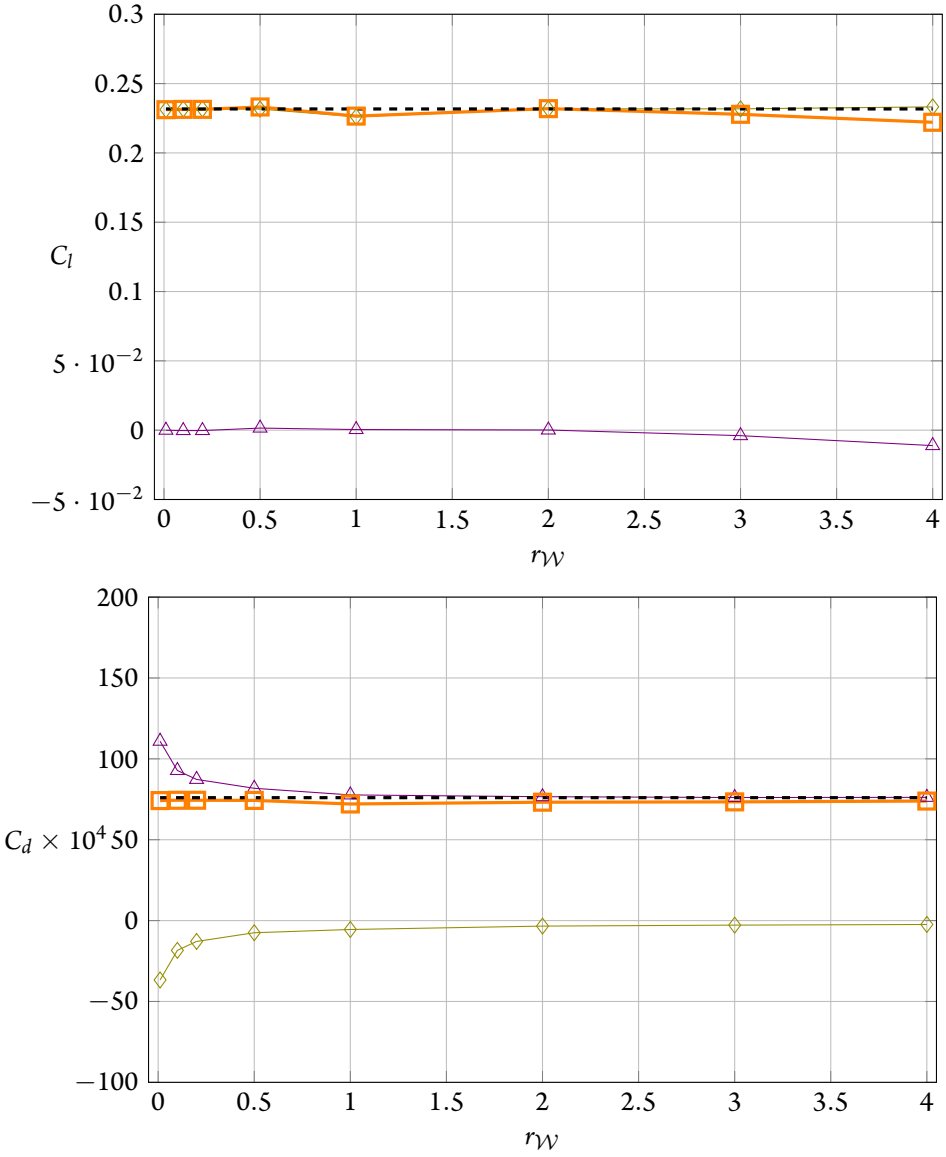


Figure 2.3.10: NACA 0012 airfoil, $M_\infty = 0.3$, $\alpha = 2°$, $Re_\infty = 10^7$. Effect of wake plane position $r_{\mathcal{W}}$ on lift and drag coefficients. Breakdown of F_{vf} and comparison with F_{nf}. F_{rev} (—◇—), F_{irr} (—△—), F_{vf} (—□—), F_{nf} (-⊖-).

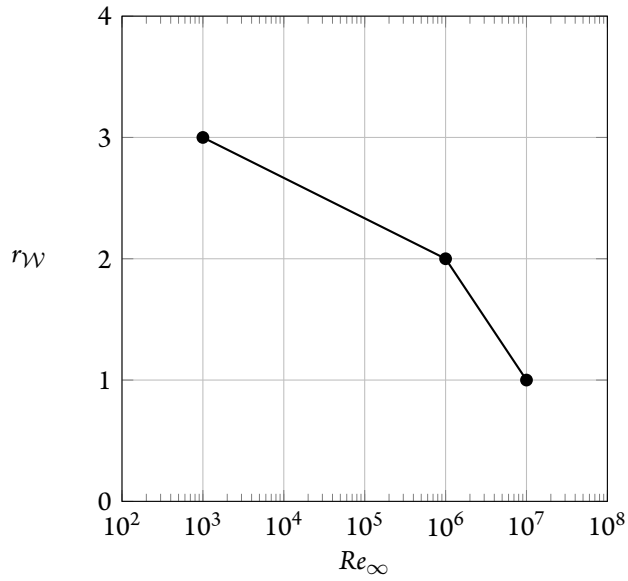


Figure 2.3.11: NACA 0012 airfoil, $M_\infty = 0.3$, $\alpha = 2°$. Effect of Reynolds number on $r_{\mathcal{W}}$ for drag-breakdown convergence.

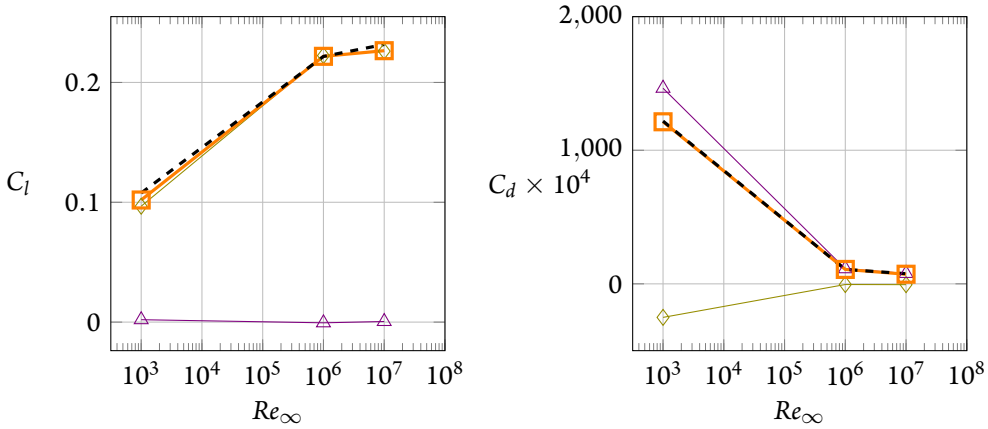


Figure 2.3.12: NACA 0012 airfoil, $M_\infty = 0.3$, $\alpha = 2°$. Effect of Reynolds number on lift and drag breakdown. F_{rev} (—◇—), F_{irr} (—△—), F_{vf} (—□—), F_{nf} (-○-).

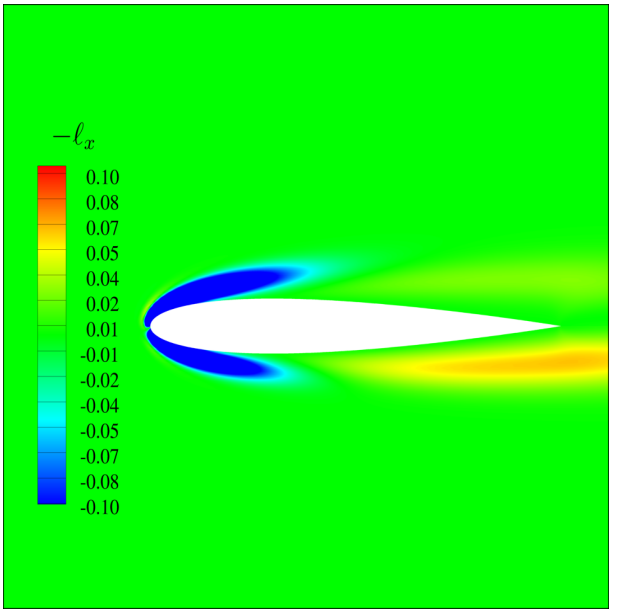


Figure 2.3.13: NACA 0012 airfoil, $Re_\infty = 10^3$, $M_\infty = 0.3$, $a = 2°$. Contours of $-\ell_x$.

2.4 Towards a Vortical Thrust/Drag Bookkeeping

2.4.1 The Actuator Disk Model

The effect of a propeller on the fluid flow in which an aircraft is immersed is commonly studied by means the *actuator disk model* [62]. The propeller is assumed to have a large number of blades, becoming effectively a circular disk, and it is further assumed that the thrust is uniformly distributed over it. The rotation of the slipstream due to the action of the torque can be ignored (simple momentum theory), so that the velocity of the fluid remains continuous in passing through the disk, or included (general momentum theory) [63]. The pressure p of the fluid receives a sudden increment Δp equal to the thrust on unit area of the disk.

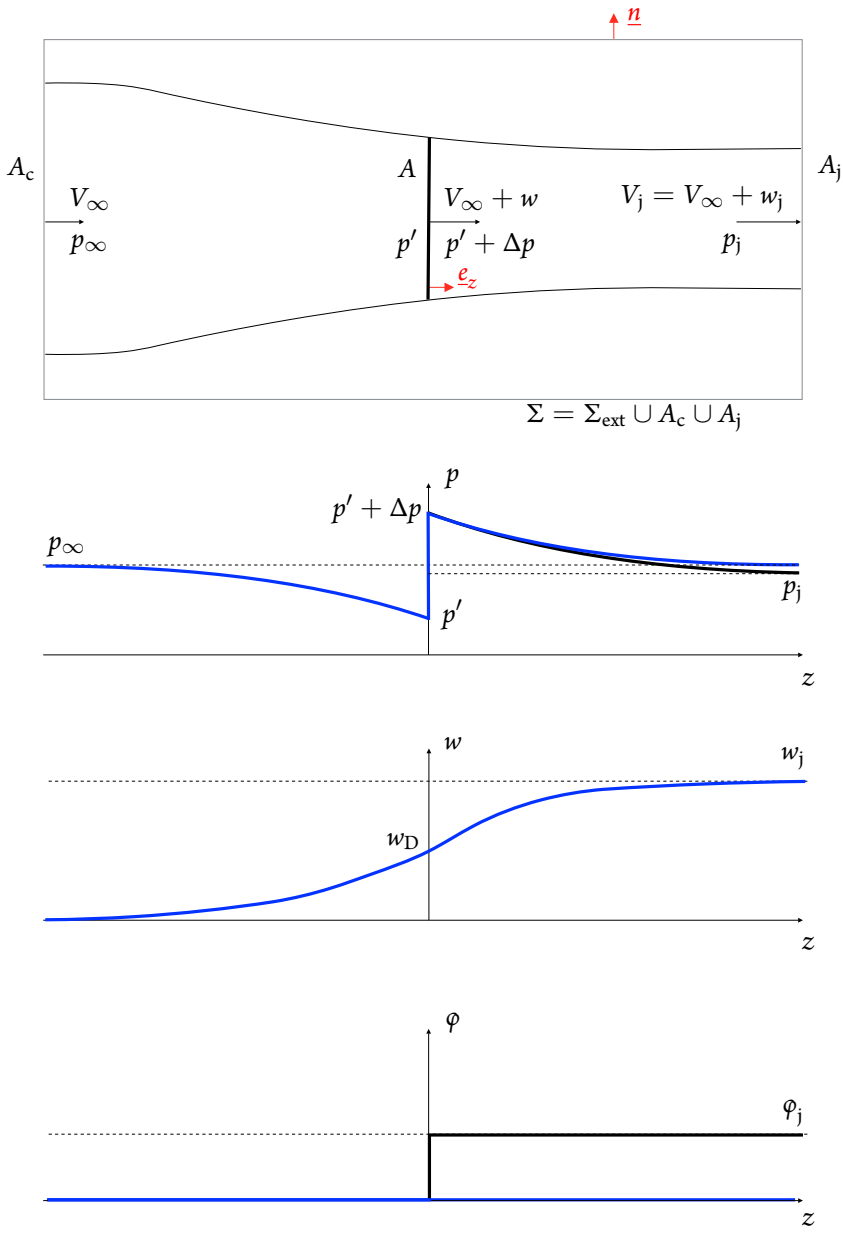


Figure 2.4.1: Main results of Actuator Disk Theory. Simple Momentum Theory (–); General Momentum Theory (–).

This simple model allows for obtaining a number of interesting results starting from the momentum balance equation in incompressible and inviscid flow.

$$T = \Delta p A = \underline{e}_z \cdot \int_{\Sigma} \left[\left(p\underline{\underline{U}} + \rho \underline{VV} \right) \cdot \underline{n} \right] \, \mathrm{dS} \,, \tag{2.74}$$

with $\underline{n}$ pointing outside from the far field surface Σ and A equal to the disk area. According to the sketch of the flow domain in Fig. 2.4.1 the mass flow passing through the disk is:

$$\dot{m} = \rho_\infty \left(V_\infty + w\mathrm{D} \right) A = \rho_\infty V_\infty A_\mathrm{c} = \rho_\infty \left(V_\infty + w_\mathrm{j} \right) A_\mathrm{j} \,, \tag{2.75}$$

where A_c is the stream tube section infinitely upstream the disk whereas A_j is the section infinitely downstream. Thus

$$\begin{aligned} T = \Delta p A = \underline{e}_z \cdot \int_{\Sigma_\mathrm{ext}} \left[\left(p - p_\infty \right) \underline{n} + \rho_\infty \underline{VV} \cdot \underline{n} \right] \, \mathrm{dS} \\ + \dot{m} \left(V_\mathrm{j} - V_\infty \right) + \left(p_\mathrm{j} - p_\infty \right) A_\mathrm{j} \,. \end{aligned} \tag{2.76}$$

Choosing Σ_ext as a *stream surface* the momentum flux through it is zero whereas the integral of $\left(p - p_\infty \right) = \mathcal{O}\left(1/{r_\Sigma}^2 \right)$, negligible when $r_\Sigma \to \infty$. The thrust expression finally becomes:

$$T = \Delta p A = \dot{m} \left(V_\mathrm{j} - V_\infty \right) + \left(p_\mathrm{j} - p_\infty \right) A_\mathrm{j} \,. \tag{2.77}$$

The Simple Momentum Theory states that the velocity of the fluid remains continuous in passing through the disk so that no rotation is imposed to the stream tube $\varphi = 0$ and $p_\mathrm{j} - p_\infty = 0$. Equation 2.77 can be rearranged and Δp can be expressed in terms of the fluid velocity

$$\Delta p = \rho_\infty \left(V_\infty + w\mathrm{D} \right) w_\mathrm{j} \,, \tag{2.78}$$

where w is the axial induced velocity at the disk whereas w_j is that infinitely downstream. Applying the Bernoulli's Theorem to the stream tubes upstream and downstream the disk showed in Fig. 2.4.1 another Δp expression can be obtained:

$$\Delta p = \rho_\infty w_\mathrm{j} \left(V_\infty + \frac{1}{2} w_\mathrm{j} \right) \,. \tag{2.79}$$

Equations 2.78 and 2.79 give the first result of the actuator disk model: the induced axial

velocity infinitely downstream w_j doubles the one at the disk w_D

$$w_D = \frac{1}{2} w_j \,. \tag{2.80}$$

Introducing the axial interference factor $a = w/V_\infty$ the actuator disk thrust is:

$$T = 2\rho_\infty A V_\infty^2 \,(1 + a)\, a \,. \tag{2.81}$$

The General Momentum Theory upgrades the Simple Momentum Theory introducing the swirl velocity φ_j: the angular velocity of the fluid particles respect to the axis of the actuator disk. The rotational interface factor $a' = \varphi_j / (2\zeta)$, with ζ equal to the rotational velocity of the propeller, is defined. Applying the integral angular momentum balance equation to a stream tube enclosed between two stream surfaces it is possible to show that:

$$\frac{\partial\left(\varphi_j r^2\right)}{\partial z} = 0 \tag{2.82}$$

so that, at any radial station r, $\varphi_j(z)$ is constant.

Moreover, if the actuator disk induces a swirl velocity, the term containing the pressure difference infinitely downstream in Eq. (2.77) is no more zero: integrating the momentum balance equation in intrinsic coordinates it is shown that $p_\infty - p_j = \mathcal{O}\left(\varphi_j^2\right)$, negligible for $a' \ll 1$.

2.4.2 A Vortical Thrust Expression for the Actuator Disk

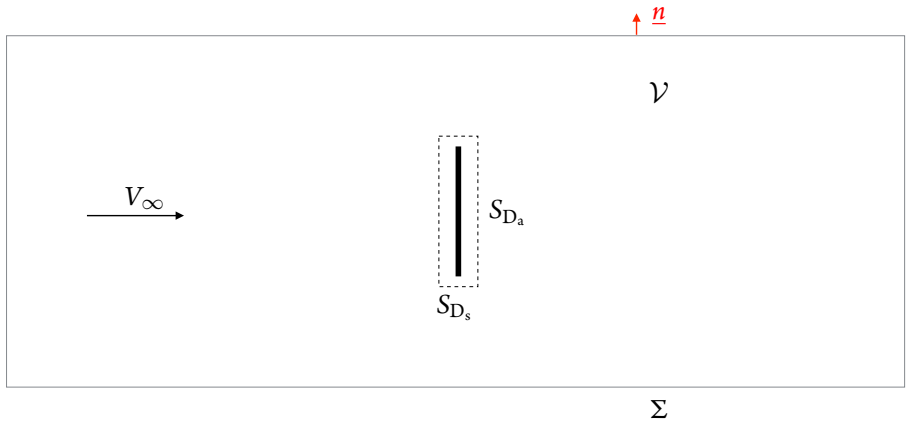


Figure 2.4.2: Reference fluid domain for the derivation of the vortical thrust formula.

Let's consider an actuator disk immersed in a steady, viscous and incompressible axial flow domain $\mathcal{V}$ bounded by $\partial\mathcal{V} = \Sigma \cup S_D$ with Σ, the far field surface, and $S_D = S_{D_s} \cup S_{D_a}$, the surface enclosing the actuator disk (see Fig. 2.4.2). The integral momentum balance equation in this case is:

$$\int_{S_D} \left(p\underline{n} - \underline{\underline{\tau}}_\nu \cdot \underline{n}\right) \, \mathrm{d}S = -\rho \int_{\mathcal{V}} \underline{a} \, \mathrm{d}\mathcal{V} - \int_{\Sigma} \left(p\underline{n} - \underline{\underline{\tau}}_\nu \cdot \underline{n}\right) \, \mathrm{d}S \,, \tag{2.83}$$

with $\underline{n}$ pointing outside $\mathcal{V}$ and the left hand side of Eq. (2.83) which gives the near field thrust expression $\underline{T}_{nf}$. Take into account that $\rho\underline{a} = -\underline{\nabla}p + \underline{\nabla}\cdot\underline{\underline{\tau}}_\nu$ the volume integral of the fluid acceleration $\underline{a}$ present in Eq. (2.83) can be rearranged using Eq. (A.1) of Appendix A

$$\begin{aligned} -\rho \int_{\mathcal{V}} \underline{a} \, \mathrm{d}\mathcal{V} &= -\frac{1}{k}\rho \int_{\mathcal{V}} \underline{r} \times (\underline{\nabla} \times \underline{a}) \, \mathrm{d}\mathcal{V} + \frac{1}{k} \int_{\partial\mathcal{V}} \underline{r} \times (\underline{n} \times \rho\underline{a}) \, \mathrm{d}S \\ &= -\frac{1}{k}\rho \int_{\mathcal{V}} \underline{r} \times (\underline{\nabla} \times \underline{a}) \, \mathrm{d}\mathcal{V} + \frac{1}{k}\rho \int_{S_D} \underline{r} \times (\underline{n} \times \underline{a}) \, \mathrm{d}S \\ &\quad - \frac{1}{k} \int_{\Sigma} \underline{r} \times (\underline{n} \times \underline{\nabla}p) \, \mathrm{d}S + \frac{1}{k} \int_{\Sigma} \underline{r} \times \left[\underline{n} \times \left(\underline{\nabla} \cdot \underline{\underline{\tau}}_\nu\right)\right] \, \mathrm{d}S \,. \end{aligned} \tag{2.84}$$

With a proper choice of the fluid domain $\mathcal{V}$ the application of Eq. (A.2) (Appendix A) to the far field surface integral containing the static pressure p in Eq. (2.84) can be rewritten

as:

$$-\frac{1}{k}\int_{\Sigma}\underline{r}\times(\underline{n}\times\underline{\nabla}p)\ \mathrm{dS}=\int_{\Sigma}p\underline{n}\,\mathrm{dS}\,, \tag{2.85}$$

and cancelled with its opposite present in Eq. (2.83) whereas the terms containing $\underline{\underline{\tau}}_{\nu}$ can be grouped in $\underline{\Delta}_{\mu}$.

Since $\underline{a}=\underline{\ell}+\underline{\nabla}\left(V^2/2\right)$ the volume integral present in Eq. (2.84) can be rearranged by Eq. (A.1) of Appendix A

$$\begin{aligned}-\frac{1}{k}\rho\int_{\mathcal{V}}\underline{r}\times(\underline{\nabla}\times\underline{a})\ \mathrm{d}\mathcal{V}&=-\frac{1}{k}\rho\int_{\mathcal{V}}\underline{r}\times(\underline{\nabla}\times\underline{\ell})\ \mathrm{d}\mathcal{V}\\&=-\rho\int_{\mathcal{V}}\underline{\ell}\,\mathrm{d}\mathcal{V}-\frac{1}{k}\int_{\partial\mathcal{V}}\underline{r}\,(\underline{n}\times\underline{\ell})\ \mathrm{dS}\,.\end{aligned} \tag{2.86}$$

Finally, splitting the surface integral of Eq. (2.86) in the integrals on S_{D} and Σ the following *vortical thrust formula* is obtained:

$$T_{\mathrm{vf}}=T_{\ell}+T_{\mathcal{W}}+T_{\mathrm{s}}+\Delta_{\mu}\,. \tag{2.87}$$

where

$$T_{\ell}=\underline{e}_z\cdot\left(-\rho\int_{\mathcal{V}}\underline{\ell}\,\mathrm{d}\mathcal{V}\right)\,, \tag{2.88}$$

is the same of the vortex force found in case of a solid body immersed in a viscous flow (Eq. (2.2)). This term accounts for the *wake contraction thrust* as shown in Section 2.4.3.

$$T_{\mathcal{W}}=\underline{e}_z\cdot\left[-\frac{1}{k}\rho\int_{\mathcal{W}}\underline{r}\times(\underline{n}\times\underline{\ell})\ \mathrm{dS}\right]\,, \tag{2.89}$$

has the same expression of the far field surface integral Eq. (2.5) and can be limited to the wake plane (the only one where the Lamb vector is present). It accounts for the wake velocity increase.

$$T_{\mathrm{s}}=\underline{e}_z\cdot\left\{\frac{1}{k}\rho\int_{S_{\mathrm{D}}}\underline{r}\times\left[\underline{n}\times\underline{\nabla}\left(\frac{V^2}{2}\right)\right]\ \mathrm{dS}\right\}\,, \tag{2.90}$$

is a new term due to the presence of a discontinuity surface S_{D} instead of a solid body in the flow and is tightly connected to the swirl induced by the actuator disk. Indeed, when $S_{\mathrm{D_s}}\to 0$, T_{s} can give a finite value only if the integrand is a δ-function; this happens only when $\varphi\neq 0$ because both the axial and the radial velocity components are continuous

passing through the actuator disk. T_s accounts for the pressure defect in the actuator disk wake that, as shown in the description of the actuator disk model, is of $\mathcal{O}\left(\varphi_j^2\right)$, negligible for $a' \ll 1$.

Finally $\underline{\Delta}_\mu$ is exactly the same of Eq. (2.8) and, as previously discussed, can be neglected in high-Reynolds number flows.

2.4.3 The Wake Contraction Thrust

A first straightforward verification of equation Eq. (2.87) can be obtained considering a cylindrical duct of constant area with an actuator disk in inviscid flow and no swirl. In this case there is no contraction of the wake and due to the symmetries of the flow the application of equation Eq. (2.87) is particularly simple. Assuming a constant pressure jump across the disk of radius R with induced axial velocity w_{ext} at the exit section of the duct, a discrete model of the wake is obtained considering a finite small thickness δ of the vortex sheet at the disk tip, see Fig. 2.4.3.

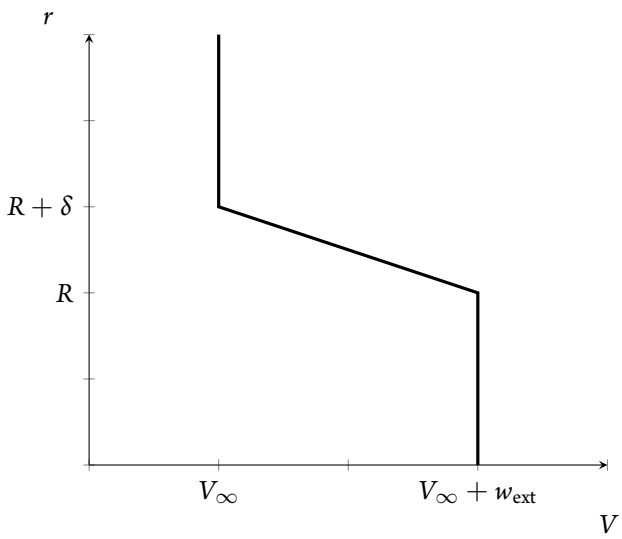


Figure 2.4.3: Discrete model of the wake in inviscid flow.

Vorticity and Lamb vector fields are different than zero in the vortex sheet only. Specifying with $\underline{e}_z$, $\underline{e}_r$ and $\underline{e}_\theta$ the unit vectors in axial, radial and swirl directions respectively,

vorticity and Lamb vector fields in the vortex sheet are:

$$\underline{\zeta}(R) = -\frac{w_{\text{ext}}}{\delta}\underline{e}_\theta\,, \qquad \underline{\ell}(R) = -\left(V_\infty + w_{\text{ext}}\right)\frac{w_{\text{ext}}}{\delta}\underline{e}_r\,. \tag{2.91}$$

Taking into account the symmetries of the wake, the vortex force contribution T_ℓ is zero. In case of no axial flow or contracted disk wake the symmetries would be lost and non zero vortex force contribution realized.

Without swirl and viscosity in the flow Eq. (2.87) reduces to $T_{\mathcal{W}}$ only:

$$\begin{aligned} T_{\text{vf}} = T_{\mathcal{W}} &= \underline{e}_z \cdot \left\{ \lim_{\delta\to 0}\left[-\rho \int_R^{R+\delta}\int_0^{2\pi} \frac{r^2}{2}\underline{e}_r \times \left(\underline{e}_z \times \underline{\ell}\right) \mathrm{d}\theta\mathrm{d}r \right] \right\} \\ &= -\rho\pi R^2 \left(V_\infty + w_{\text{ext}}\right) w_{\text{ext}}\,, \end{aligned} \tag{2.92}$$

which is exactly the thrust expression Eq. (2.81) obtained by a direct application of propeller momentum theory, being $w_j = w_{\text{ext}}$ in case of ducted actuator disk.

2.4.4 Numerical Verification of the Vortical Thrust Expression

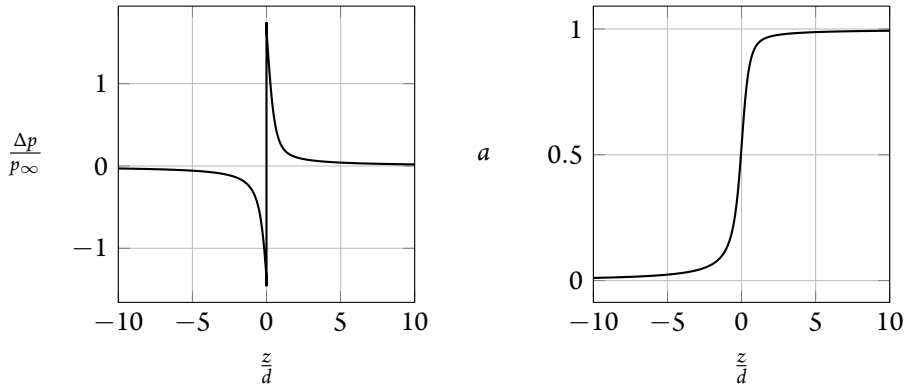


Figure 2.4.4: 2D Actuator disk: $Re_\infty = 6\times 10^3$, $M_\infty = 0$, $a = 0.5$. Pressure jump and axial interference factor along z.

In order to numerically prove the validity of the thrust expression proposed in Eq. (2.87), CFD simulations of a free actuator disk immersed in viscous flow have been performed.

As first example a two-dimensional case has been considered. The incompressible and laminar flow around an *actuator line* with Reynolds number $Re_\infty = 6\times 10^3$ based on the reference length d, has been analyzed. The incompressible flow solver module of ANSYS

Fluent has been used with the Green-Gauss cell based method for gradients and second order upwind scheme for spatial discretization. Calculations were performed on a cartesian grid with the far field distant $100d$ from the actuator line in the axial direction and $50d$ in the side direction. 128 grid cells have been distributed along the actuator line and the axial direction whereas 64 cells have been placed from the line to the far field in the side direction. The actuator line was modeled by imposing a constant non dimensional pressure jump of $\Delta p/p_\infty = 3.00$ and an axial interference factor $a = 0.5$. As shown in Fig. 2.4.4, the numerical results are in perfect agreement with the simple momentum theory; in particular the axial induced velocity in the far wake achieves the expected value $w_j = 2w_D$.

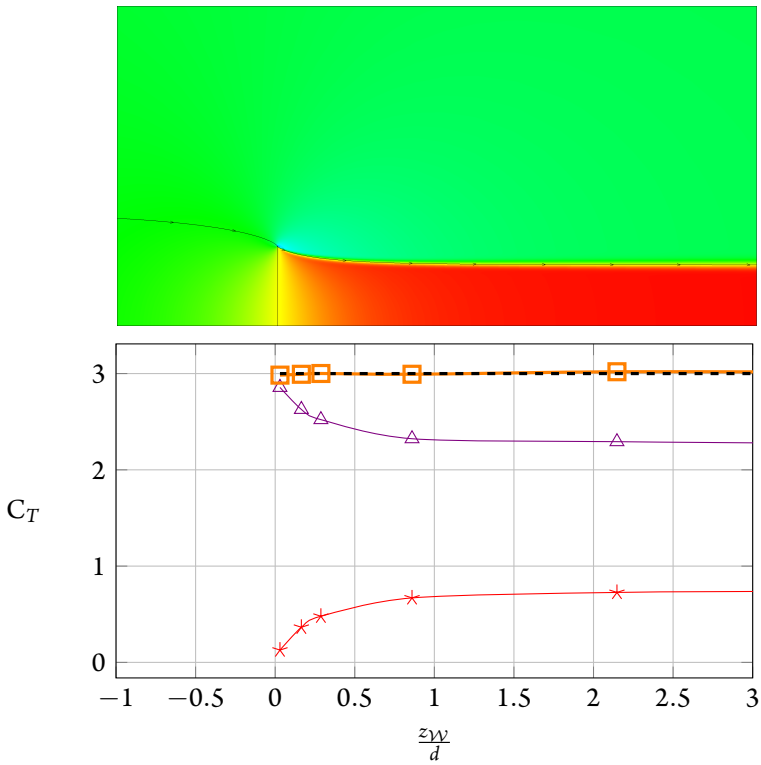


Figure 2.4.5: 2D Actuator disk: $Re_\infty = 6\times10^3$, $M_\infty = 0$, $a = 0.5$. Top Figure: contour of axial velocity component; bottom figure: Near field vs vortical thrust coefficients changing the wake plane position z_W. T_ℓ (—✶—), T_W (—△—), T_{vf} (—□—), T_{nf} (-⊙-).

The near field and the vortical thrust coefficients $\left(C_T = 2T/\rho_\infty V_\infty^2 d\right)$ (the latter changing the wake plane position) are compared in Fig. 2.4.5. The near field thrust was evaluated

by integrating the pressure over the cell layers surrounding the disk, while the far field was computed by using formula (2.87). T_s is exactly 0 because there is no swirl and the flow is axial; Δ_μ resulted negligible. T_{vf}, formed by T_ℓ and $T_{\mathcal{W}}$ only, is in exceptional agreement with the reference value independently of the wake plane position $z_{\mathcal{W}}$. The wake contraction term grows as long as the wake contraction is completed, while $T_{\mathcal{W}}$ reduces so that the total thrust remains unaffected by the integration domain chosen.

A three-dimensional CFD simulation around an actuator disk with swirl has also been performed. The analyzed geometry contains a central hub with a spherical ogive. A viscous wake has been considered as in previous test ($Re_\infty = 6 \times 10^3$), but a slip boundary condition has been imposed on the hub wall in order to neglect the body boundary layer. The far field of the grid, in the axial direction, is distant 15 diameters upstream and 30 downstream the disk; in the radial direction, it is 15 diameters far from the body. A grid with 64 grid cells in the axial direction and 64 in the radial direction was used; 32 cells were set on the disk radius (see Fig. 2.4.6) $a = 0.05$ and $\Delta p/p_\infty = 0.21$ were imposed through the disk. A constant swirl angular velocity has been adopted and a tangential tip velocity $v_\theta/V_\infty = 0.069$ has been realized. A perfect agreement with the momentum theory was again found (not shown), in particular for the swirl, constant in the wake.

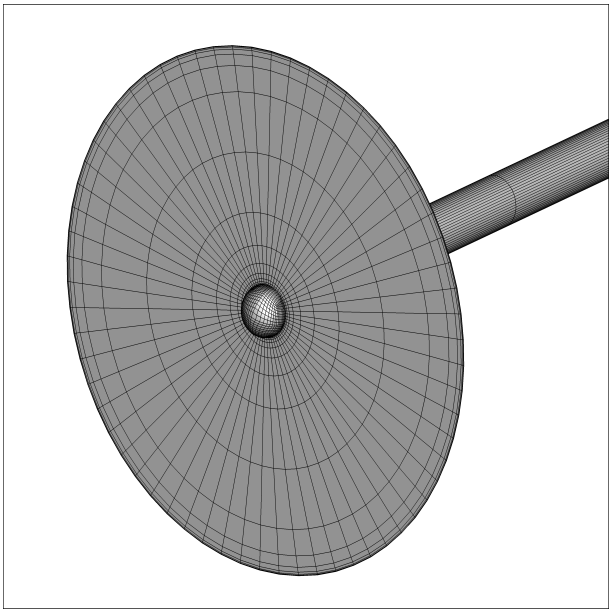


Figure 2.4.6: 3D actuator disk with hub.

The comparison between the thrust given by Eq. (2.87) and the near field value is proposed in Fig. 2.4.7. The obtained results are comparable to the two-dimensional test. It can be noted that some discrepancies are appearing for $z_{\mathcal{W}}/d > 0.5$; this is clearly due to loss of grid resolution downstream in the wake. A negligible contribution of T_s is found as could be expected because of the small swirl velocity imposed.

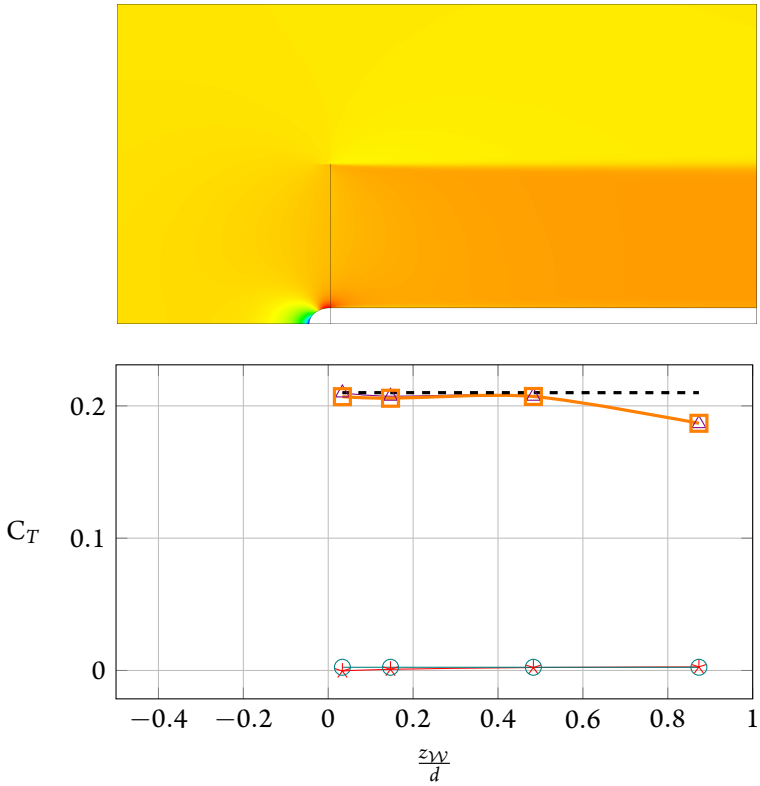


Figure 2.4.7: 3D actuator disk with hub: $Re_\infty = 6 \times 10^3$, $M_\infty = 0$, $a = 0.05$, $v_\theta/V_\infty = 0.069$. Top figure: contour of axial velocity component. Bottom figure: near field vs vortical thrust coefficients changing the wake plane position $z_{\mathcal{W}}$. T_ℓ (—✶—), $T_{\mathcal{W}}$ (—△—), T_s (—○—),T_{vf} (—⊟—), T_{nf} (-⊖-).

2.5 Summary of the Achievements of This Chapter

The aerodynamic force computation and its breakdown based on the vortex-force theory has been discussed. Different aspects of the theory have been analyzed with particular attention to its applicability to CFD flow field. The main results obtained are collected in what follows:

- an analytical proof of the exact *vortical expression* of the aerodynamic force and its extension to turbulent flow have been recalled;
- the *objectiveness* of the drag breakdown in induced and profile drag components has been studied with comparisons and links with classical thermodynamic drag definitions;
- an extension of the vortex-force theory to *effectively inviscid flow* has been proposed giving an unquestionable proof that the vortex force has *reversible* nature and is generated in the body-boundary layer;
- a vortical thrust formula for dealing with incompressible actuator disk model has been proposed verified with numerical tests.

It has been noted that transportation is fundamentally 0% efficient as it involves moving mass from rest at one point to rest at another point, so that the energy of the system is unchanged.

Ilan Kroo - 2001

3

Applications: New Methods for New Aircraft

In this chapter, the aerodynamic force formulae discussed in Chapters 1 and 2 are applied to two innovative aircraft concepts. The aerodynamic performance of a wing-body turboprop with riblets and natural laminar flow (NLF) are analyzed with the Thermodynamic drag breakdown method described in Section 1.4.3 (Section 3.1); the vortical method recalled in Chapter 2 is used to investigate the compressibility effects on the induced drag of Box Wings (Section 3.2). The application of the force breakdown methods allowed to compare the impact of these drag reduction technologies on the overall aerodynamic performance of *future airplanes*. The results reported in the following pages are an original contribution of the author collected in [64] for the turboprop configuration and [65] for the box-wing system.

3.1 Drag Breakdown of an Innovative Turboprop Configuration

Regional aircraft is a core market for today's commercial aviation: by the end of 2015 the regional aviation world fleet comprised of about 9000 units (4350 turboprop and 4650 regional jet) representing more than 33% of the worldwide commercial fleet and performing

over 40% of total commercial flights (and 25% of total flight hours). In the recent past the annual worldwide traffic served by regional aviation exceeded 700 billion ASK (Available Seat Kilometres). Only in Europe were regional carriers able to offer more than 120 billion ASKs to passengers, with an average distance of 320 NM (about 600 km) and more than 200 million people flew on regional aircraft within the European network [66].

The integration of innovative and affordable technologies in future aircraft platforms is a key success factor for manufacturers and motivated the *Innovative turbopROp configuratioN (IRON) project* which complies with the European Union topic JTI-CS2-2015-CPW02-REG-01-03 (Green and cost efficient Conceptual Aircraft Design including Innovative Turbo-Propeller Power-plant) as part of the Clean Sky 2 program for Horizon 2020. IRON project has Leonardo as topic leader and CIRA (the Italian Aerospace Research Center) as coordinator. The University of Naples is a core partner of the project with the main activities concerning the aerodynamic assessment and the performance evaluation of the aircraft model. In particular, the assessment of the effect of NLF control and riblets installation over the turbulent part of wing and fuselage of an innovative low wing and rear-mounted engines aircraft (see Fig. 3.1.1) has been planned. In this frame the bookkeeping of drag reduction due to the combined effect of NLF control and riblets is a relevant topic. In particular, the effect of riblets on the different drag components (friction, form and lift induced drag) is worth of investigation. For this purpose, a drag breakdown, available only by far-field methods in three-dimensional flows, is required.

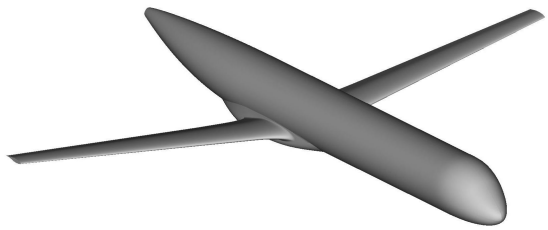


Figure 3.1.1: IRON innovative turboprop wing-body configuration.

3.1.1 Natural Laminar Flow and Riblets Technologies

There has been continuous and focussed activity around the globe concerning development of new techniques for skin friction drag reduction and attempts have progressed broadly in two directions: methods for delaying laminar-turbulent boundary layer transition and methods for altering or modifying the turbulent structure of a turbulent boundary layer.

In the first group of drag reduction technologies there is the Natural Laminar Flow (NLF), based on the particular design of wing sections. NLF airfoils were widely studied since the forties, when NACA developed the well known 6-series airfoil family, characterized by high performance in controlled wind tunnel experiments [67] but also the loss of laminar flow due to leading-edge contamination; the success of the NACA 6-series family was more related to the good high-speed performance rather than to the laminar capabilities. More recently, NASA has designed advanced NLF airfoils such as the NLF(1)-0215F airfoils [68] and the NLF(1)-0414F airfoils [69] that achieve low drag but are intended for low-speed applications: they exhibit large nose-down pitching moments and low drag-divergence Mach numbers. NLF airfoils adapt for high-speed applications are discussed in [70, 71]. Nonetheless, the successful cases of NLF have been limited to the unswept wing configurations, because of the well known cross-flow instability.

In the second group there are the riblets: streamwise grooved surfaces able to reduce friction drag in turbulent flow. Wind tunnel experiments over flat plates showed a drag reduction of the order of 10% due to riblets [72], but riblets effectiveness in pressure gradient flow is still a controversial aspect linked to this drag reduction technology. Walsh [73] found that riblets performance improved under adverse pressure gradients but mentioned contradictory results by other authors; Coustols & Savil [74], summarized the results of previous investigations concluding that the favorable or adverse pressure gradient has a second order effect on riblets performance whereas Debisschop & Nieuwstadt tested riblets in adverse pressure gradient flow an order of magnitude larger than those considered by Walsh [73] and found a maximum drag reduction of 13% instead of 7% due to riblets. The report on the flight tests of an Airbus 320 with riblets over 70% of its surface showed an overall 2% drag reduction based on the flue savings obtained [75]; the work of Lee & Jang [76] and Viswanath [77] confirm that riblets can successfully be applied to reduce the overall drag of airfoils and aircraft with an optimum riblets spacing of order of 30-70 μm.

3.1.2 A Riblets Model for CFD Analysis

Due to riblets dimensions their drag reduction mechanism could be numerically captured only with *Direct Numerical Simulation* (DNS) or *Large Eddy Simulation* (LES) but, these types of computations are still unfeasible for complex aeronautical configurations. In order to overcome this problem, some numerical models for riblets effect simulation for high Reynolds number flows have been recently developed.

Aupoix et al. [78] modified the equation of the Spalart-Allmaras turbulence model to take into account the effect of riblets. Following a different approach, Mele & Tognaccini [79] proposed a boundary condition for the $k\omega$ turbulence models that turned out to be an efficient method for the numerical simulation of riblets, able to calculate riblet performance in complex aeronautical configurations [80]. Koepplin et al. [81] modified the model of Aupoix et al. to analyze the effect of misalignment of riblets in pressure gradient flows. Each cited model has been developed to mimic the effect of riblets in the flow field without inserting riblets geometry in the computational domain: the walls where riblets are adopted are smooth. Very recently, Mele & Tognaccini [82] contributed to clarify the debated issue on the effectiveness of riblets in pressure gradient flow developing a new model based on the slip-length concept. They found that riblets have a secondary but significant effect on form drag and provided also a quantitative analyses by the classical matched asymptotic expansion theory that showed that riblets reduce the displacement thickness leading to a reduction of the form drag. This mechanism was also measured in an experiment of flat plate in adverse pressure-gradient flow [83].

The numerical model adopted to simulate the presence of riblets surface on the IRON turboprop configuration is described in details in [80]. The model replicates the shift of the origin of the velocity profile (i.e. a shift of the constant of the log law) induced by riblets and shown in [84, 85]. To do that a modification to the Saffman's boundary condition [86] for the $k-\omega$ turbulence model families is used:

$$\omega = \frac{\rho u_\tau^2}{\mu} \qquad S_R = \frac{\tau_w}{\mu} S_R(k_s^+)\,, \tag{3.1}$$

where ρ is the density, $u_\tau = \sqrt{\tau_w/\rho}$ is the friction velocity (τ_w is the wall shear stress) and μ is the dynamic viscosity. S_R is an *unknown* function that depends on the nature of the wall and, as shown in [55], its value (and thus the value of ω at the wall) determines

the value of the constant in the log law. The S_R expression for riblets effect simulation is

$$S_R = \frac{C_1}{(l_g^+ - C_2)^{2n} + C_3} \,. \tag{3.2}$$

Equation (3.2) is written as a function of $l_g^+ = \sqrt{A_g^+}$, where A_g^+ is the riblets non dimensional cross section area that can be used to simulate the effects of an arbitrary riblets family. The coefficients have been obtained by numerical experiments matching the experimental data reported in [87]: $C_1 = 2.5 \cdot 10^8$; $C_2 = 10.5$; $C_3 = 1$.

The described boundary condition has been widely validated in flat plate and airfoil flows comparing numerical computation with available experiments as shown in [79, 80].

3.1.3 The Drag Breakdown Method

The aerodynamic drag breakdown has been performed using the method proposed by Paparone & Tognaccini in [25]. As discussed in Section 1.4.3, this drag breakdown method relies on a proper division of the flow domain $\mathcal{V}$ into three regions (see Fig. 3.1.2): the viscous region $\mathcal{V}_v$, containing the body-boundary layer and the body wake, which accounts for the viscous drag D_v, the shock wave region $\mathcal{V}_w$ that corresponds to where the *wave drag* arises and the remaining part of the flow domain $\mathcal{V}_{sp}$ that contains the unphysical drag contribution, the *spurious drag* D_{sp}, due to the numerical dissipation linked to the scheme adopted for the CFD simulations. Removing D_{sp} from the total drag D, a more accurate drag prediction is obtained even if the numerical error could affect also $\mathcal{V}_v$ and $\mathcal{V}_w$, the flow regions needed for the physical drag computation.

The division of the flow domain is provided by a zone selection algorithm: given a numerical RANS solution, the problem is to establish whether a grid cell, belongs to the boundary layer, to the shock wave, or to the remaining part of the flow domain. As described in [25, 60] this operation is possible thanks the introduction of ad hoc shock and boundary-layer sensors. The shock sensor is

$$\lambda_w = \frac{\underline{V} \cdot \underline{\nabla} p}{a \nabla p} \,, \tag{3.3}$$

where a is the local speed of sound. In order to detect both the laminar and turbulent boundary-layer zones a boundary-layer sensor based on the dissipation of the turbulent

kinetic energy is used

$$\lambda_v = \rho\varepsilon\,. \tag{3.4}$$

In the shock/boundary-layer interaction region, a distinction between viscous and shock wave cells becomes ambiguous. In the present method a hierarchy has been chosen in the selection criteria: first the shock wave region test is performed; if not satisfied, the viscous region test follows; if not satisfied, the cell is assumed belonging to the spurious region.

The induced drag has been computed by Maskell's formula (discussed in Section 1.3.3) applied on wake planes $\mathcal{W}$ normal to the direction of the free stream.

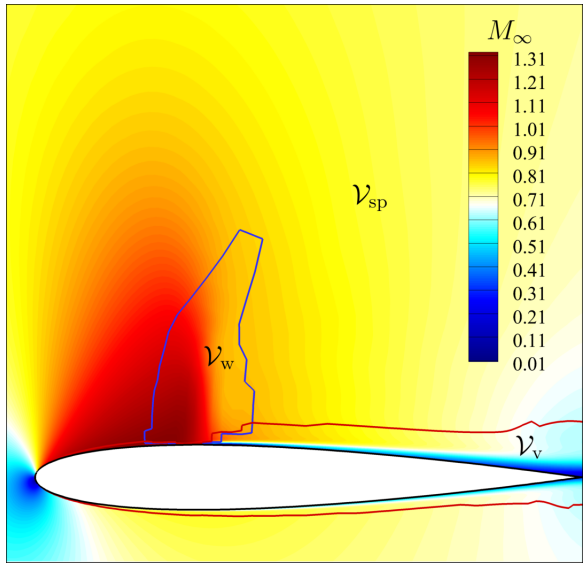


Figure 3.1.2: NACA 0012 airfoil, $M_\infty = 0.7$, $Re_\infty = 9 \times 10^6$, $a = 3.25°$. Example of flow domain division in boundary-layer region $\mathcal{V}_v$, shock region $\mathcal{V}_w$ and spurious region $\mathcal{V}_{sp}$.

3.1.4 Drag Performance of IRON Turboprop Configuration

Compressible RANS simulations at $Re_\infty = 18.2 \times 10^6$, $M_\infty = 0.64$ and $a = -2°, 0°, 2°$ have been performed on the IRON wing-body configuration with the flow solver FLOWer modified for riblets simulations. The numerical setting described in Section 2.2.1 and the $k-\omega$ SST LR turbulence model [88] have been adopted; simulations have been performed with and without riblets in both fully turbulent and mixed laminar-turbulent flow: the laminar condition has been obtained by switching off the turbulence production [89].

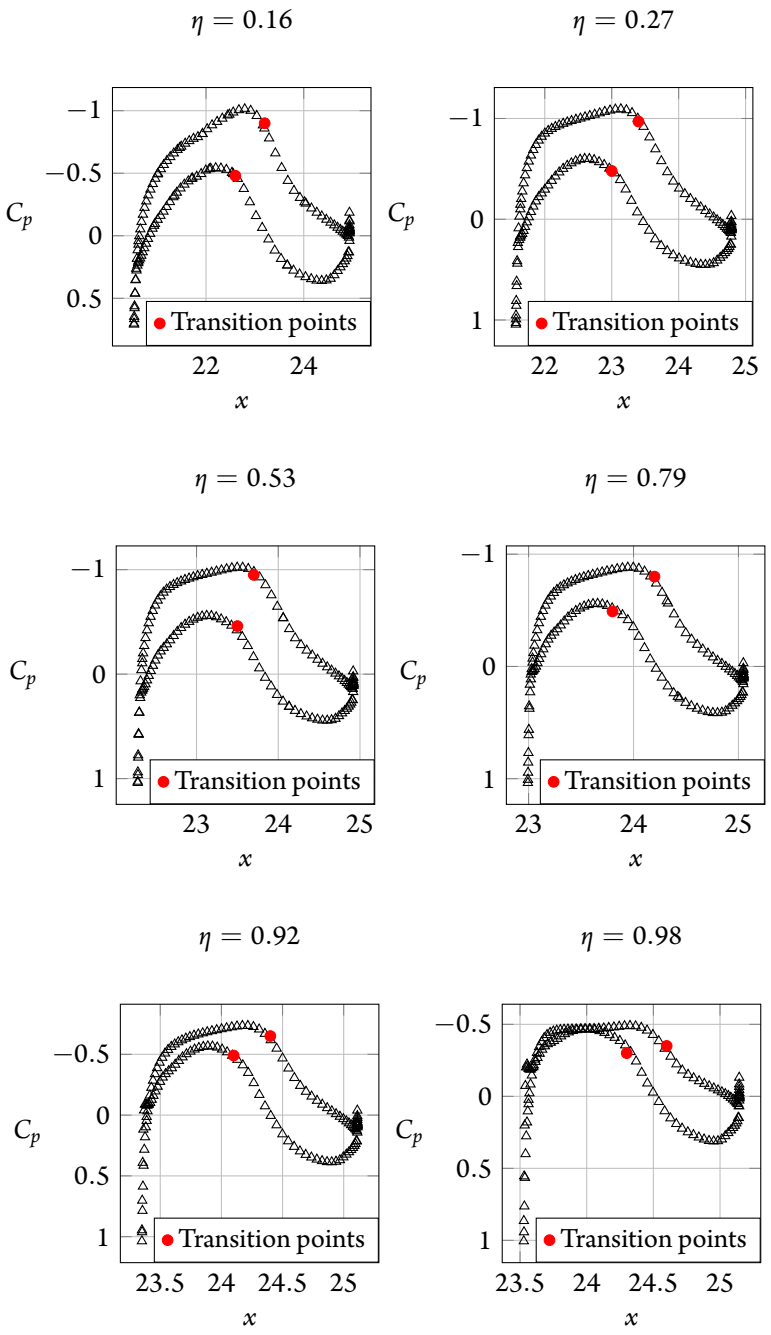


Figure 3.1.3: IRON wing-body configuration at $Re_\infty = 18.2 \times 10^6$, $M_\infty = 0.64$, $\alpha = 0°$. Wing section pressure coefficients and transition points.

Since the wing sweep angle is small, the laminar zone on the wing has been estimated performing a two-dimensional stability analysis by an e^n method on six wing sections; then, a linear interpolation has been adopted. In Fig. 3.1.3 the computed pressure coefficients in fully turbulent flow at $\alpha = 0^\circ$ on the six wing sections considered for stability analysis are shown. It is worth noting that the transition points are correctly placed in the adverse pressure gradient zones. In Fig. 3.1.4 the laminar and turbulent regions identified on the wing-body configuration are displayed.

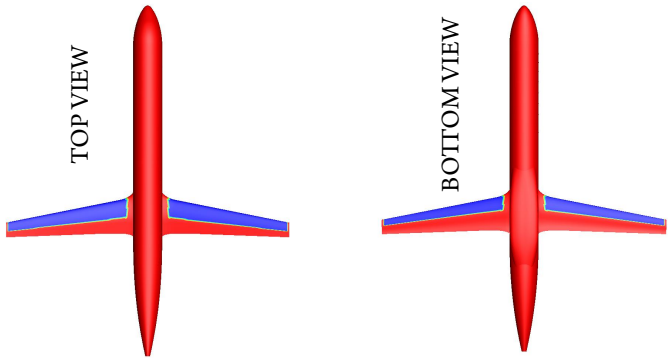


Figure 3.1.4: IRON wing-body configuration at $Re_\infty = 18.2 \times 10^6$, $M_\infty = 0.64$, $\alpha = 0^\circ$. Laminar (blue) and turbulent (red) flow regions.

Riblets have been installed on the entire fuselage and the turbulent part of the wing. A standard riblets geometry with a symmetric V-grooved section with $s^+ = h^+ = \sqrt{2} l_g^+$ and $l_g^+ = 10.5$ has been chosen; in this way an optimal height distribution has been guaranteed over the body surface: one of the advantages of the adopted riblets model is that the optimal riblets height can be retrieved as a result of the numerical simulations even if, as highlighted in [80] the drag reduction obtainable with optimal and constant riblets height distribution is almost the same.

Computations have been performed using a structured mesh with 147 blocks and 40 million cells in the finest grid level (LVL1). The accuracy of the riblets model adopted has been tested comparing the grid convergence analyses on three grid levels with and without riblets in fully turbulent flow Fig. 3.1.5. The results are substantially the same with and without riblets and show that the medium grid level (LVL2) returns a good accuracy and will be used in all the simulations; on this grid level an y^+ distribution well below the unity almost everywhere on the wing-body surface has been guaranteed. The accuracy reached

on LVL2 grid is also confirmed by Fig. 3.1.6 where the drag reduction due to riblets ΔC_D is plotted against the mesh size. ΔC_D differs less than 2 drag counts between LVL1 and LVL2 and the *zero mesh size extrapolation* varies less than 1 drag count respect to LVL1 grid.

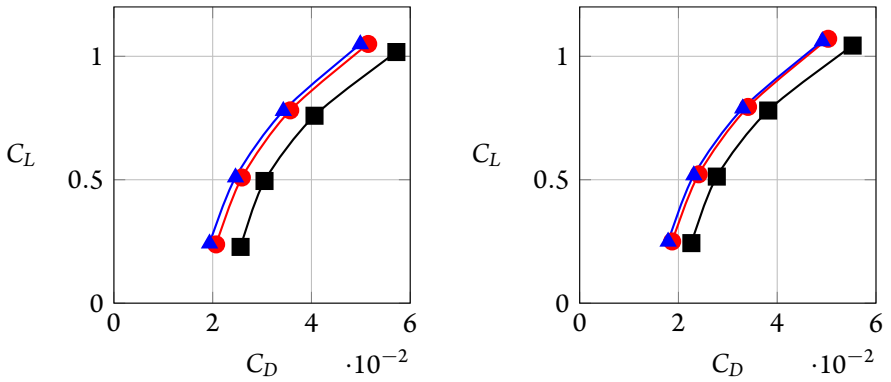


Figure 3.1.5: IRON wing-body configuration at $M_\infty = 0.64$, $Re_\infty = 18.2 \times 10^6$, fully turbulent flow. Grid convergence analysis with (right figure) and without (left figure) riblets. LVL4 (—■—), LVL2 (—●—), LVL1 (—▲—).

The drag reduction due to the combination of riblets and NLF technologies is shown in Fig. 3.1.7 that displays the drag polars of the wing-body configuration with and without drag reduction systems and in Fig. 3.1.8 where the bookkeeping of the drag reduction due to each system is shown for $\alpha = 0°$ and zero mesh extrapolation.

The variation of drag reduction with the angle of attack is shown in Fig. 3.1.9. It is worth noting that, while the friction drag reduction is substantially constant while varying the angle of attack, the total drag reduction decreases. This effect is linked to the increase of the induced drag while increasing the angle of attack: the net effect of riblets should be appreciated just by the friction drag reduction.

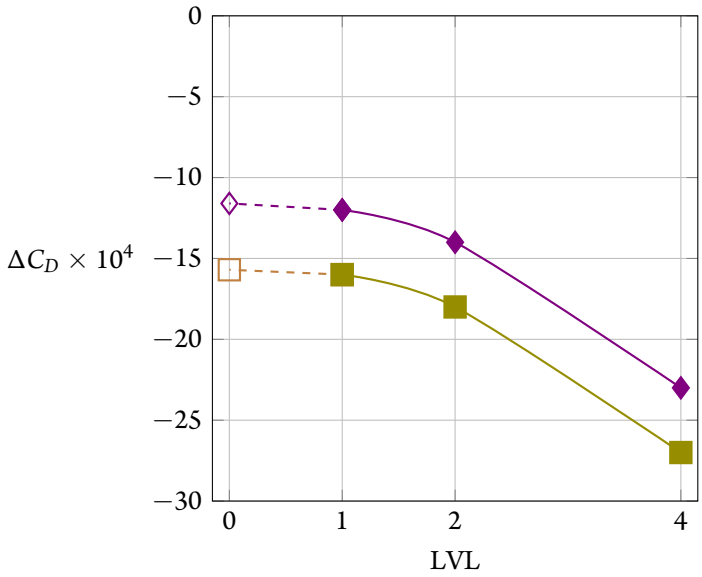


Figure 3.1.6: IRON wing-body configuration at $M_\infty = 0.64$, $Re_\infty = 18.2 \times 10^6$ and $\alpha = 0°$, fully turbulent flow. Computed Drag reduction due to riblets against grid level (optimum height distribution on wing and fuselage). Total drag reduction (—■—); friction drag reduction (—◆—); zero mesh size extrapolation (- - -).

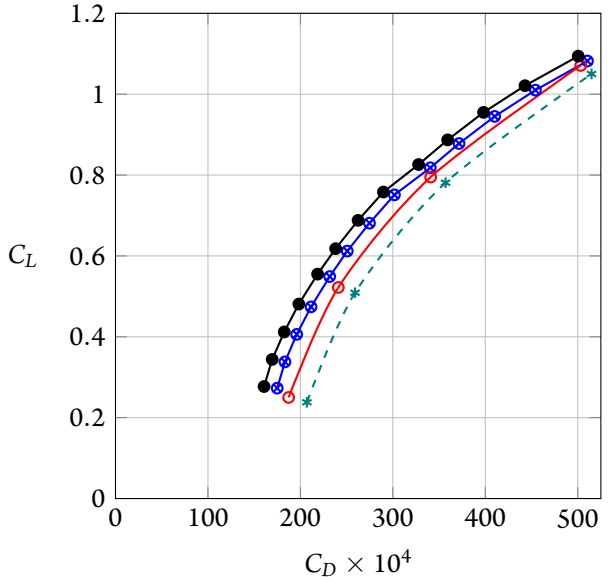


Figure 3.1.7: IRON wing-body configuration at $M_\infty = 0.64$, $Re_\infty = 18.2 \times 10^6$. Polar curves with and without drag reduction systems installed. Clean configuration (- ✱ -); riblets only (—○—); NLF only (—⊗—); combined NLF+riblets (—●—).

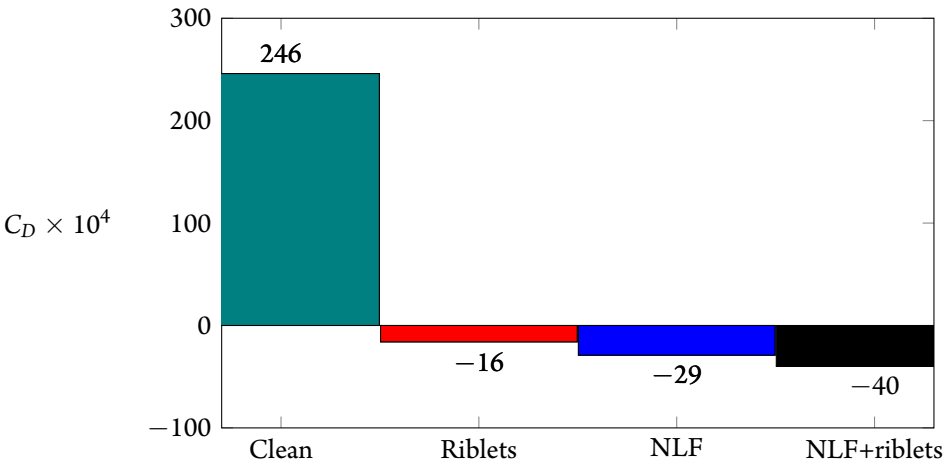


Figure 3.1.8: IRON wing-body configuration at $M_\infty = 0.64$, $Re_\infty = 18.2 \times 10^6$ and $\alpha = 0°$ (zero mesh extrapolation). Bookkeeping of drag reduction due to NLF and riblets.

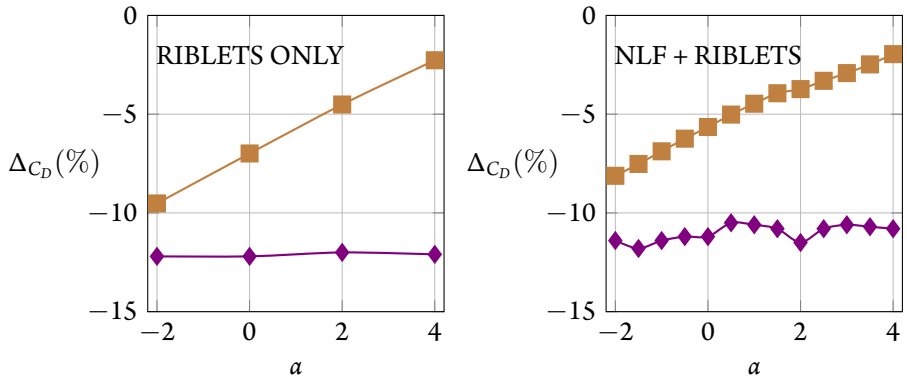


Figure 3.1.9: IRON wing-body configuration at $M_\infty = 0.64$ and $Re_\infty = 18.2 \times 10^6$. Drag reduction due to riblets vs angle of attack. Total drag reduction (—■—); friction drag reduction (—◆—). Reference value in percentages is smooth condition.

The results obtained applying the drag breakdown method of Section 3.1.3 are shown from Fig. 3.1.10 to Fig. 3.1.16. The grid convergence analysis in terms of *near-field* and *far-field* drag (equal to the entropy drag without the spurious drag) is shown in Fig. 3.1.10 for the cruise condition with and without riblets installed and fully turbulent flow (no NLF system). As already seen in Fig. 3.1.5 for the near-field lift and drag values, also the far-field drag provides converged results with the LVL2 grid but, properly removing the spurious

drag contribution it is possible to obtain satisfactory results even using the LVL4 grid. The drag breakdowns showed in Fig. 3.1.11 for the clean configuration and Fig. 3.1.12 for the aircraft with riblets installed are referred to LVL2 grid in which 8 drag counts of spurious drag have been detected in both the cases: this results let us to confirm that the model for riblets simulation does not introduce further artificial dissipation. Moreover, the induced drag computation by Maskell's formula allows to conclude that riblets substantially act only on the viscous drag, since, at the same lift the same induced drag is obtained with and without riblets installed. Finally, at the highest value of lift coefficient the drag rise due to the presence of shock waves in the flow is captured. In Fig. 3.1.13 the viscous drag decomposition is reported and the effect of riblets on form drag can be appreciated. There is an evident reduction of form drag due to riblets except at $C_L = 1.08$ where form drag slightly increases. This is due to the flow separation induced by the shock wave that reduces riblets effectiveness.

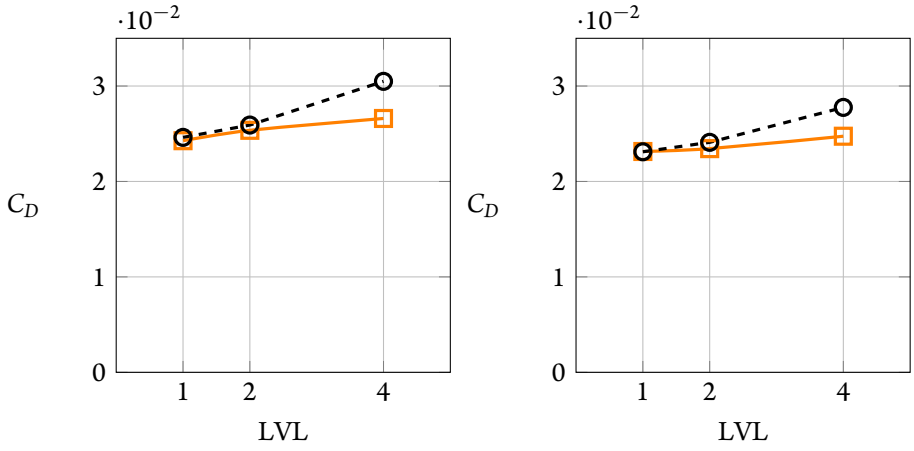


Figure 3.1.10: IRON wing-body configuration without NLF control at $M_\infty = 0.64$ and $Re_\infty = 18.2 \times 10^6$. Grid convergence analysis of far-field drag and near-field drag with (right figure) and without (left figure) riblets installed. Far-field drag (-□-); near-field drag (-○-).

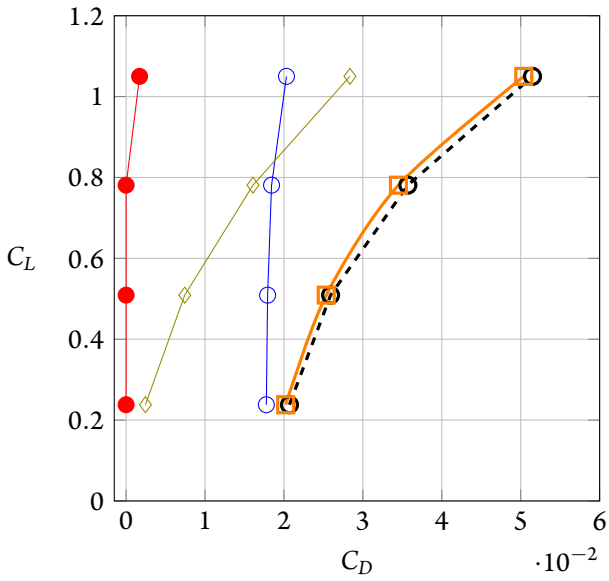


Figure 3.1.11: IRON wing-body configuration without NLF control and riblets at $M_\infty = 0.64$ and $Re_\infty = 18.2 \times 10^6$: drag breakdown. Far-field drag without spurious contribution (—□—); near-field drag (-⊖-); viscous drag (—○—); wave drag (—●—); induced drag (—◇—).

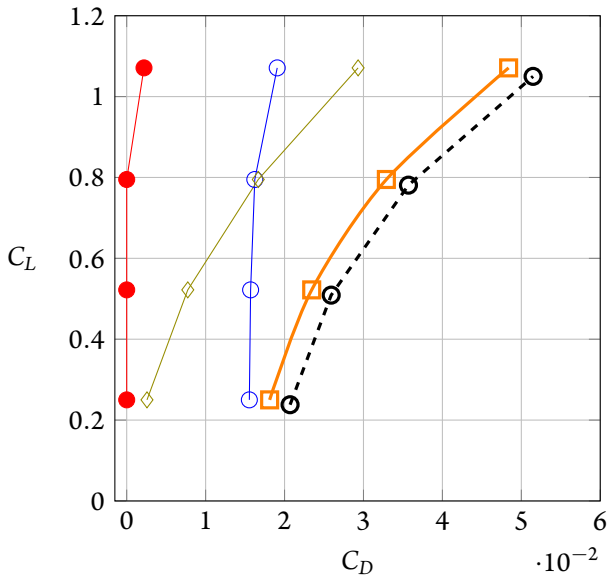


Figure 3.1.12: IRON wing-body configuration without NLF control and with riblets at $M_\infty = 0.64$ and $Re_\infty = 18.2 \times 10^6$: drag breakdown. Far-field drag without spurious contribution (—□—); near-field drag (-⊙-); viscous drag (—⊙—); wave drag (—●—); induced drag (—◇—).

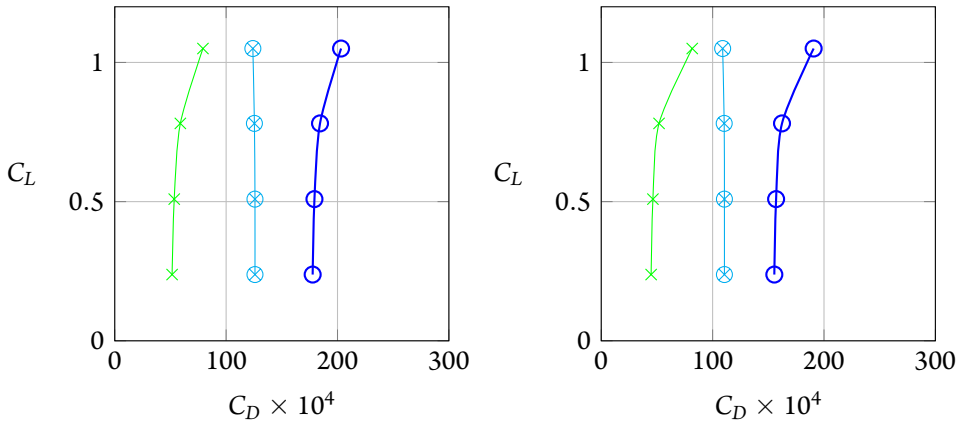


Figure 3.1.13: IRON wing-body configuration at $M_\infty = 0.64$ and $Re_\infty = 18.2 \times 10^6$: viscous drag breakdown without (left figure) and with riblets (right figure). Viscous drag (—⊙—); friction drag (—⊗—); form drag (—×—).

The drag decomposition in the case of NLF control is discussed in what follows. Figures 3.1.14 and 3.1.15 report the drag breakdown without and with riblets; also in these

two conditions 8 drag counts of spurious drag have been detected. The drag decomposition shows that, also in the case of NLF control, a wave drag component is correctly detected at $\alpha = 4^\circ$ where supersonic regions appear. However, differently from the case of fully turbulent flow, in this case the presence of riblets does not influence the wave drag because the shock wave occurs in the laminar zone. The computed wave drag, with only NLF control adopted (21 drag counts) is substantially the same computed in the case of fully turbulent flow and riblets installed (22 drag counts): riblets and NLF systems have similar effect on wave drag.

The decomposition of viscous drag in friction and form drag is shown in Fig. 3.1.16. The reduction of form drag, evident also in this case, is lower with respect to the fully turbulent case: the form drag reduction due to riblets in cruise condition is 13% without NLF control and 7% with NLF control.

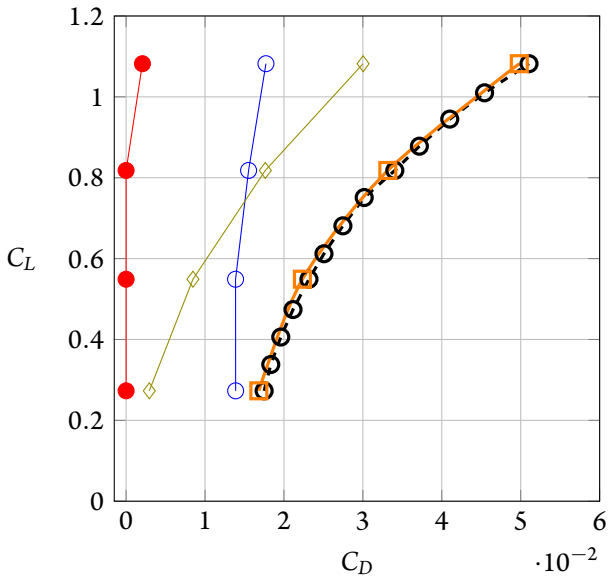


Figure 3.1.14: IRON wing-body configuration with NLF control and without riblets at $M_\infty = 0.64$ and $Re_\infty = 18.2 \times 10^6$: drag breakdown. Far-field drag without spurious contribution (—□—); near-field drag (-○-); viscous drag (—○—); wave drag (—●—); induced drag (—◇—).

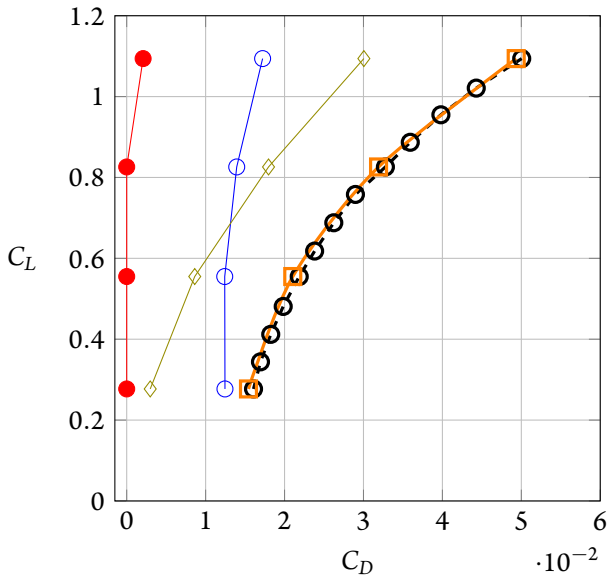


Figure 3.1.15: IRON wing-body configuration with NLF control and riblets at $M_\infty = 0.64$ and $Re_\infty = 18.2 \times 10^6$: drag breakdown. Far-field drag without spurious contribution (—□—); near-field drag (-⊙-); viscous drag (—○—); wave drag (—●—); induced drag (—◇—).

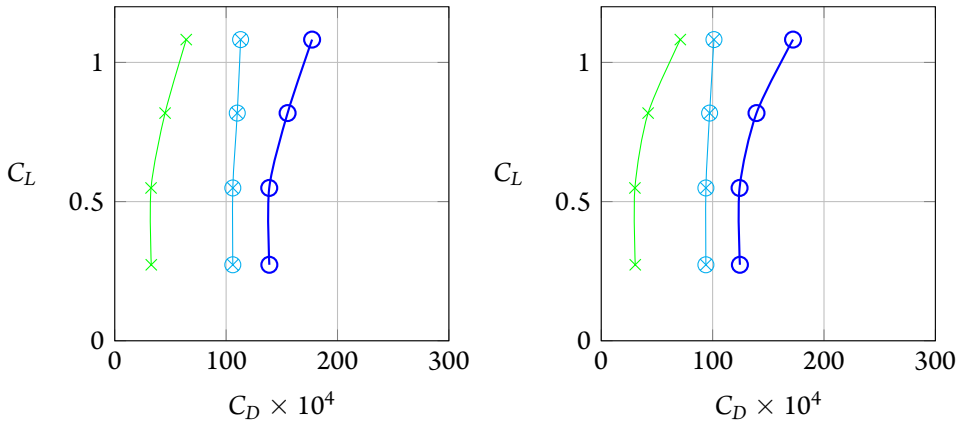


Figure 3.1.16: IRON wing-body configuration with NFL control at $M_\infty = 0.64$ and $Re_\infty = 18.2 \times 10^6$: viscous drag breakdown without (left figure) and with riblets (right figure). Viscous drag (—○—); friction drag (—⊗—); form drag (—×—).

Concluding, the analyses performed have showed that:

- a combined NLF + riblets technology can reduce the total IRON wing-body con-

figuration drag up to 16%;

- also in the case of mixed laminar-turbulent flows, the adoption of riblets on the fuselage and turbulent part of the wing provides an important contribution to drag reduction;
- NLF and riblets drag reduction systems do not affect the induced drag performance;
- in transonic conditions, both NLF and riblets slightly increases the wave drag enlarging the supersonic region.

3.2 Induced Drag of Box Wings in Compressible Flow

Today, the demand for air travel is increasing with the same rate at which the need of more efficient and eco-friendly aircraft is advancing. Although a high technology level has been reached in the last decades thanks to the adoption of sophisticated computational models and experimental campaigns, the aerodynamic design of civil aircraft is substantially unchanged since the introduction in the fifties of the transonic jet configuration. It remains a commonly held view that actual air-frame configuration will be not suitable for the next-generation air transport [90, 91].

Joined Wings are interconnected multi-planar wing systems that could represent a valid solution for aviation's future, providing a substantial increase of the design space and allowing more options in terms of aerodynamics, flight mechanics, engine integration, and aeroelasticity. The first documented and organic examination of joined-wing layout was given by Ludwig Prandtl [92] that introduced the Box Wing, a non-planar wing system with a rectangular path when seen from a frontal view. He named this configuration the *Best Wing System* thanks to the very low level of induced drag for a given lift and span obtainable with this configuration. The box-wing concept has been widely investigated in recent years (see [93–95]) and different aspects of this wing system have been analyzed: Samuels [96] compared the structural weight of the Joined Wing with respect to a reference conventional wing-plus-horizontal tail, Demasi et al. [97–99], deepened the problem of the optimum circulation distribution showing that, although the uniqueness [100] of the minimum induced drag of a Box Wing, there is an infinite number of aerodynamic loads achieving the optimum; Kroo [101, 102] compared the aerodynamic efficiency of various optimally loaded nonplanar wings of fixed span and vertical extent and found that the box-wing performance was superior to that of all other arrangements; Gagnon & Zingg [103]

performed an aerodynamic optimization of this wing system in inviscid flow whereas Andrews & Perez [104] studied the benefits of Box Wings for regional aircraft missions.

The wide literature existing on the Box Wing confirms the interest for this unconventional wing configuration but its most attractive aerodynamic feature (the low induced drag) has been mainly derived in incompressible inviscid flow. However, especially for large airplane applications, flight in the compressible and even transonic regimes may represent the dominant physical aspect in regards of the aerodynamic efficiency and in particular drag performance.

Induced drag evaluation in compressible flow at $M_\infty = 0.5$ was performed in [103], where the optimal shape of Box Wing was presented and Euler equations numerically solved. In [105] the investigation was further refined by performing an aerodynamic shape optimization of a Box-Wing system for regional aircraft applications. Compressibility effects were included at $M_\infty = 0.78$ and Reynolds-averaged Navier-Stokes equations were considered. Goal of the optimization was to maximize the lift-to-drag ratio with a trim constraint. The result indicated that the increase of vertical aspect ratio was preferred by the optimizer, a property found also in [97] for the incompressible inviscid case. Thus, the study [105] was an indirect proof that induced drag is one of the key aspects of the Box Wing for flight conditions well beyond the original ones adopted by Prandtl in 1924, when he first introduced this concept.

As discussed in Section 1.5.3, Mele et al. [45, 46] have recently showed that the induced drag performance of an elliptical wing, predicted by inviscid and incompressible Prandtl's formula, is preserved also in compressible and even transonic flows. This unexpected result, strengthened by the recently developed unified force theory proposing a single force expression valid in steady viscous subsonic, transonic and supersonic flow (Kutta-Jukowskij-Filon Theorem Section 1.6.1), inspired the present investigation: *does the Best Wing System provide the minimum induced drag also in transonic viscous flow?*

Using the vortical force breakdown in *reversible* and *irreversible* aerodynamic forces described in Section 2.3.2 the relative importance of the different drag components (induced, viscous and wave drag) is precisely assessed and goes even forward to demonstrate that the theoretical predictions made in [97] for incompressible and inviscid flow can actually be directly applied to the most general compressible and even transonic regimes. These results are an original contribution of the author and are collected in [65].

3.2.1 Box Wing: the Best Wing System

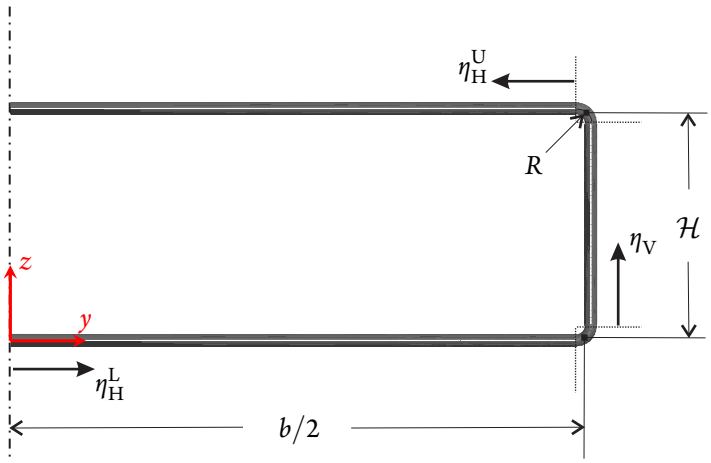


Figure 3.2.1: Geometry of the Box Wing with $\mathcal{AR} = 6$ and $\mathbb{V} = 0.2$.

In the hypothesis of potential flow the optimal load distribution for a *classical* cantilevered planar wing is elliptical [106, 107] and the corresponding minimum induced drag is:

$$D_i^{ref} = \frac{2L^2}{\pi \rho_\infty V_\infty^2 b^2}, \tag{3.5}$$

where L is the lift, ρ_∞ and V_∞ are respectively the freestrem density and velocity of the flow and b is the wingspan. The well known link between lift and induced drag coefficients for the optimum wing can be derived from Eq. (3.5):

$$C_{D_i}^{ref} = \frac{C_L^2}{\pi \mathcal{AR}}, \tag{3.6}$$

with the aspect ratio $\mathcal{AR} = b^2/S$.

For a given wing, the *optimal aerodynamic efficiency ratio* ε physically represents the ratio between its aerodynamic efficiency (defined as $E = L/D$ with $D = D_i$ in inviscid case) and the corresponding efficiency of a reference cantilevered wing with the same wingspan and total lift when both efficiencies are evaluated under their respective optimal conditions [108]:

$$\varepsilon = \frac{E}{E^{ref}} = \frac{2L^2}{\pi \rho_\infty V_\infty^2 b^2 D_i}. \tag{3.7}$$

In other words ε is a measure of the relative performance of an optimum generic wing system with respect to the optimum cantilevered wing; therefore, the induced drag coefficient of a generic wing system $C_{D_i}^{ws}$ can be computed as follow:

$$C_{D_i}^{ws} = \frac{C_L^2}{\pi \mathcal{AR} \varepsilon}. \tag{3.8}$$

More than one hundred years ago Prandtl [92] proposed, without giving any explanation, an approximated formula for evaluating the optimal aerodynamic efficiency ratio of a Box Wing as function of its vertical aspect ratio $\mathbb{V} = \mathcal{H}/b$ [109]:

$$\frac{1}{\varepsilon} \approx \frac{1 + 0.45\mathbb{V}}{1.04 + 2.81\mathbb{V}} \qquad 0 \leqslant \frac{1}{\mathbb{V}} \leqslant \frac{1}{2}, \tag{3.9}$$

where $\mathcal{H}$ is the length of the joint between the horizontal wings (see Fig. 3.2.1). The approximation given by Eq. (3.9) is not satisfactory for $\mathbb{V}$ approaching to zero because it doesn't reproduce the expected unitary value of the optimum cantilevered wing. Very recently, Demasi et al. [99] obtained a two-coefficient equation that will be used as reference in the present study:

$$\frac{1}{\varepsilon} \approx \frac{1}{1 + 1.7433\mathbb{V}^{0.8230}} \qquad 0 \leqslant \frac{1}{\mathbb{V}} \leqslant \frac{1}{2}. \tag{3.10}$$

Facing up to the problem from a mathematical point of view, Demasi et al. [97, 98] also found an analytical expression to approximate the optimal circulation distribution on the horizontal wings Γ_{opt}^{H} and the vertical joints Γ_{opt}^{V}:

$$\Gamma_{opt}^{H} \simeq \frac{2bV_\infty}{E^{ref}} \left[0.166 + \sqrt{1 - \eta_H^2} \left(0.292 - 0.0129\eta_H^2 \right) \right], \tag{3.11}$$

$$\Gamma_{opt}^{V} \simeq \frac{2bV_\infty}{E^{ref}} \left[0.787 \left(2\mathbb{V}\eta_V - \mathbb{V} \right) + 3.829 \left(2\mathbb{V}\eta_V - \mathbb{V} \right)^3 \right], \tag{3.12}$$

where $\eta_H = 2y/b$ and $\eta_V = z/\mathcal{H}$ (see Fig. 3.2.1); they showed that, in the limit of $\mathbb{V} \to \infty$, the minimum induced drag of the Box Wing tends to zero. In this condition, the aerodynamic load $\gamma_{opt} = \Gamma_{opt}/\left(V_\infty b\right)$ on the upper and lower wings is a constant and not given by the superposition of a constant and an elliptical functions [92, 110]. However, this superposition remains an acceptable approximation for low values of $\mathbb{V}$, which are of aeronautical interest.

3.2.2 Aerodynamic performance of Box Wings

The aerodynamic force breakdown proposed in Section 2.3.2 is here applied to numerical flow solutions obtained by CFD analyses.

A simple Box Wing with $\mathcal{AR} = 6$ and $\mathbb{V} = 0.2$ is considered for this investigation. The wing configuration replicates the starting wing used by Gagnon & Zigg in [103] for an aerodynamic optimization study in transonic inviscid flow: the horizontal wings, the joint and the tip fin are generated from a sharp NACA 0012 airfoil, which is rotated of 90° at the wing extremities to close the system (Fig. 3.2.1). The wing-section chord c is equal to 1, the tip fin radius $R = 0.15c$ whereas the wingspan $b = 12c$; the reference area is defined as $S = 2bc$ and is equal to $24c^2$.

Numerical computations in both incompressible and compressible flows at the same freestream Reynolds number $Re_\infty = 10^7$ and different angles of attack a have been performed using the CFD solver ANSYS Fluent. *Reynolds Averaged Navier Stokes* (RANS) simulations have been performed using the Green-Gauss cell based method for gradients and second order upwind scheme for spatial discretization. The $k - \omega$ SST turbulence model has been applied considering a fully turbulent flow. Computations have been performed at different Mach numbers: Fluent compressible flow solver has been used for $M_\infty > 0$ whereas the incompressible flow solver has been chosen for $M_\infty = 0$.

The results here presented have been obtained using a C-C type grid with more than 14 million cells (LVL1 - 256 cells along the wing section, 64 along both the horizontal semi-wingspans and the vertical wingspan and 128 in each direction normal to the body - see Fig. 3.2.2); the far field has been placed $100c$ distant from the wing and $y^+ \approx 1$ has been maintained in the first grid point layer all over the body. The accuracy of the aerodynamic force calculation by both *near field* and *vortical* formulae has been checked by the grid convergence analysis reported in Appendix D.1 where the analysis of the integration domain influence on the aerodynamic force breakdown is also shown.

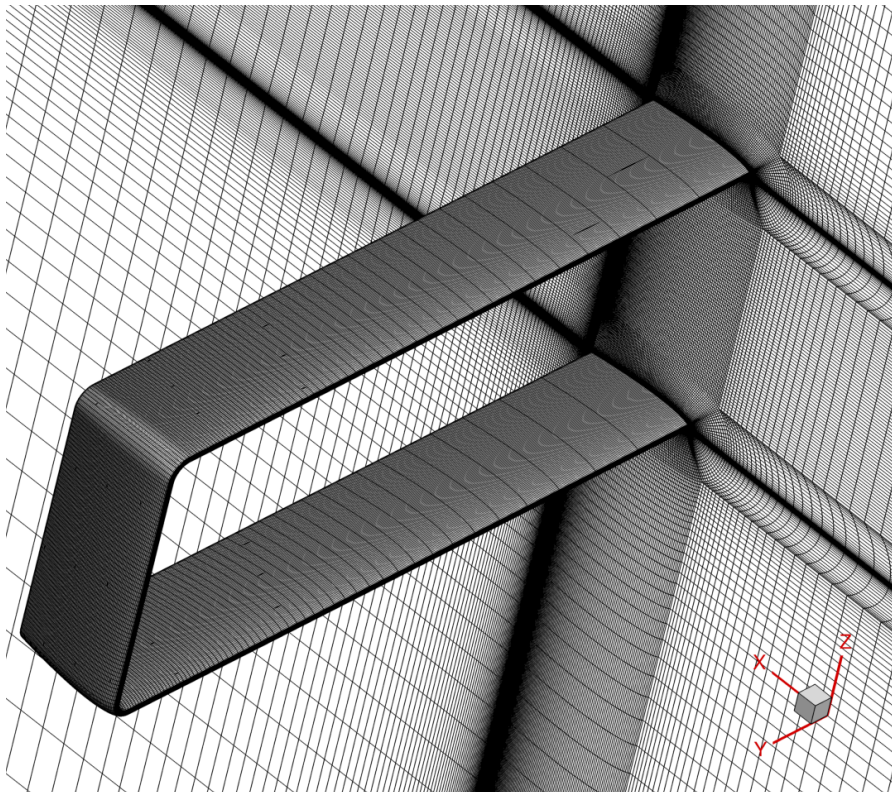


Figure 3.2.2: Box Wing with $\mathcal{AR} = 6$ and $\mathbb{V} = 0.2$ at $Re_\infty = 10^7$. Detail of the grid LVL1 on the symmetry plane and wing.

The load distribution obtained by present calculations and defined as $\gamma_H = cC_l/2b$ on the horizontal wings and $\gamma_V = cC_y/2b$ on the vertical joint has been compared with the reference one obtained by Gagnon & Zingg in [103]. In Fig. 3.2.3 this comparison is showed for $C_L \approx 0.5$; the optimum load distribution $\gamma_{opt} = \Gamma_{opt}/V_\infty b$, with Γ_{opt} computed by Eq. (3.11) and Eq. (3.12) is also showed. The viscous effects are negligible; indeed a substantial agreement has been found between the present and the numerical computation of [103], performed in inviscid flow. As expected, the simple box-wing geometry adopted doesn't realize the optimum load distribution especially on the lower wing and the vertical joint.

The numerically obtained axial vorticity field in the body wake at $M_\infty = 0.3$ and $\alpha = 0°$ is displayed in Fig. 3.2.4: the presence of the vertical joint dramatically reduces the intensity of the tip vortex, hardly recognizable in the figure.

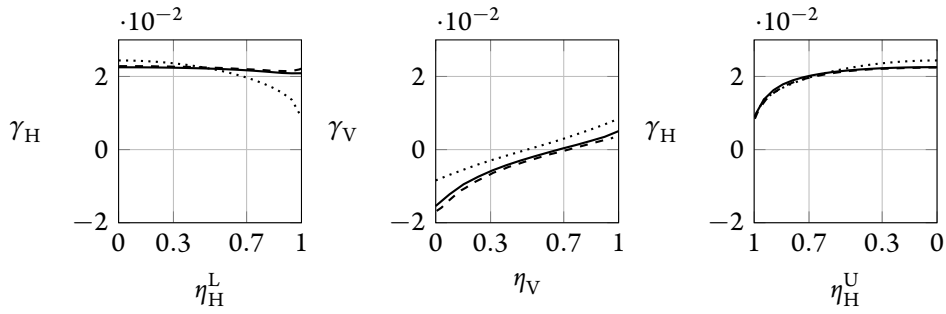


Figure 3.2.3: Box Wing with $\mathcal{AR} = 6$ and $\mathbb{V} = 0.2$ at $C_L = 0.5017$. Comparison between the load distribution obtained in present analysis at $Re_\infty = 10^7$ (——), the reference one given by [103] in inviscid flow (- - -) and the theoretical minimum induced drag load distribution (·····).

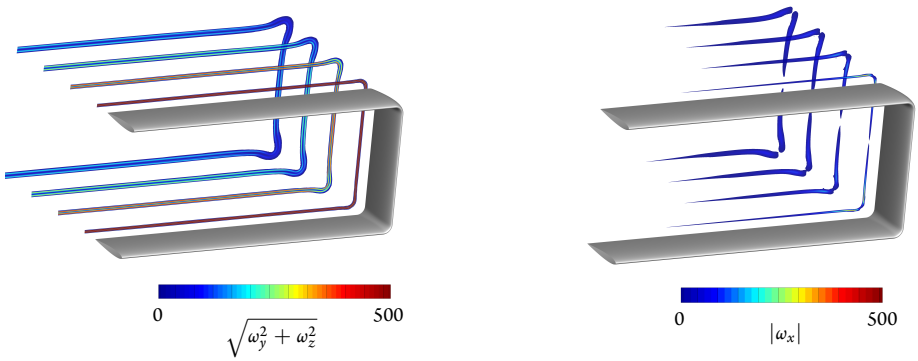


Figure 3.2.4: Box Wing with $\mathcal{AR} = 6$ and $\mathbb{V} = 0.2$ at $Re_\infty = 10^7$, $M_\infty = 0.3$ and $\alpha = 0°$. Decay of vorticity in the body wake.

Four different Mach numbers have been considered for the aerodynamic force analysis: $M_\infty = 0$ (incompressible case), $M_\infty = 0.3$ (subsonic case), $M_\infty = 0.7$ (low-transonic case) and $M_\infty = 0.9$ (high-transonic case): see Figs. 3.2.5 and 3.2.6 where the obtained pressure and skin friction coefficients distributions ($C_p = 2(p - p_\infty)/\rho_\infty V_\infty^2$, $C_f = 2\tau_w/\rho_\infty V_\infty^2$) over the upper and the lower wing sections at $\eta_H = 0.5$ are respectively displayed. As prevoiusly discussed, $\underline{F}_\Sigma$ can be computed limiting the integration to the wake plane $\mathcal{W}$, the only surface crossed by a rotational region and $\underline{\Delta}_\mu$ gives a negligible contribution and will not be reported.

The integrations have been performed by a second-order accurate trapezoidal method

using nodal values. The effect of the adopted integration domain used has been analyzed for each case. A very low effect of the wake plane position $x_{\mathcal{W}}$ on the computed aerodynamic force breakdown has been found with the values almost constant $1c$ downstream the wing trailing edge (see Appendix D.1 where the complete analysis is reported).

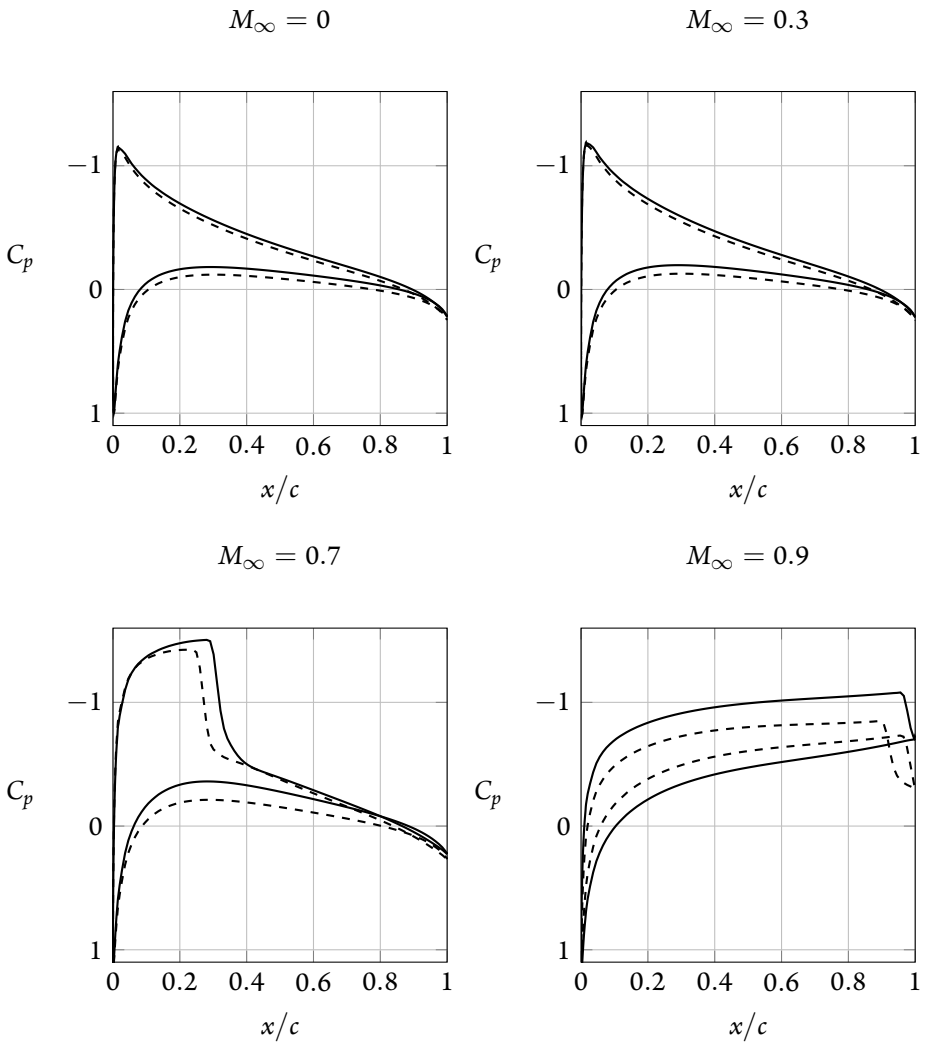


Figure 3.2.5: Box Wing with $\mathcal{AR} = 6$ and $\mathbb{V} = 0.2$ at $Re_\infty = 10^7$, $a = 4^\circ$ and different Mach numbers. C_p distributions over the wing sections at $\eta_{\text{H}} = 0.5$. Upper wing (——), lower wing (- - -).

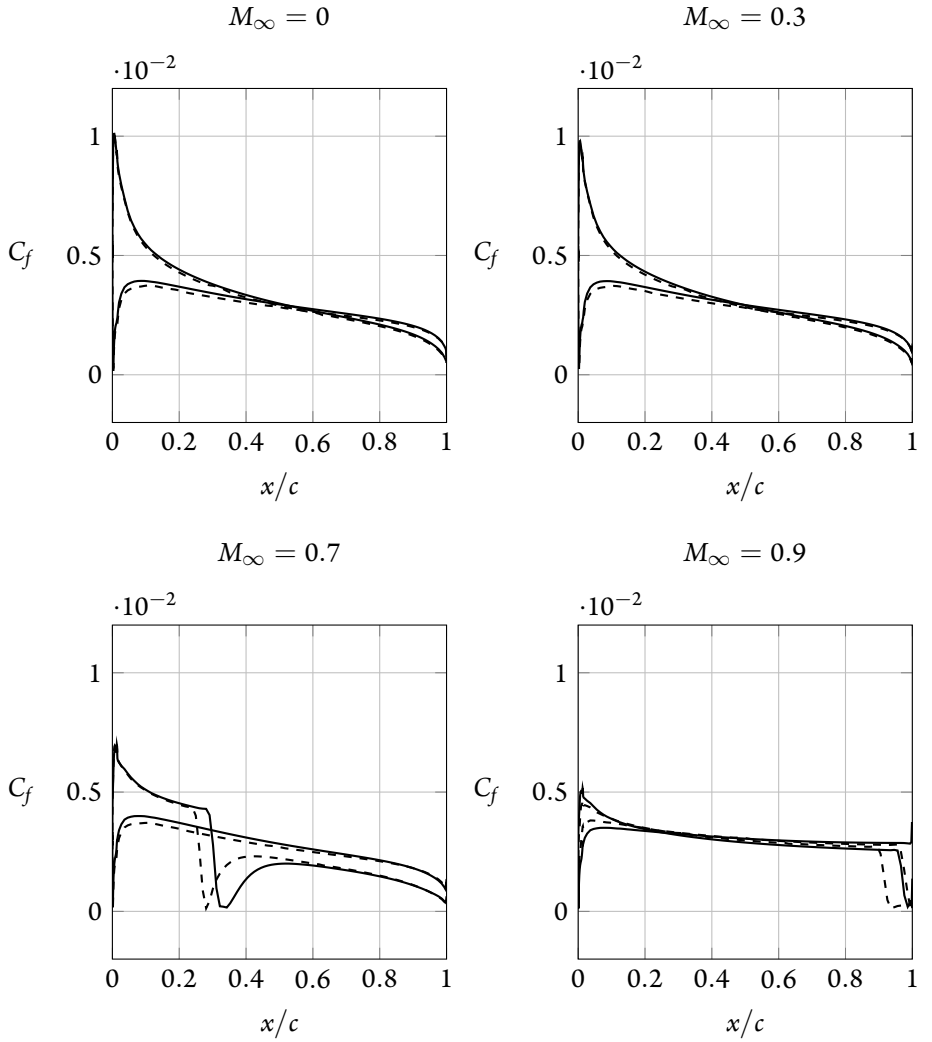


Figure 3.2.6: Box Wing with $\mathcal{AR} = 6$ and $\mathbb{V} = 0.2$ at $Re_\infty = 10^7$, $a = 4°$ and different Mach numbers. C_f distributions over the wing sections at $\eta_H = 0.5$. Upper wing (——), lower wing (- - -).

The lift curves, the lift-drag polar curves and their breakdown in $\underline{F}_{\text{rev}}$ and $\underline{F}_{\text{irr}}$ at different Mach numbers are showed in Figs. 3.2.7 to 3.2.10.

In Fig. 3.2.7 the breakdown for the incompressible case is showed: the total lift and drag computed by $\underline{F}_{\text{vf}}$ are in satisfactory agreement with the near field values. As expected, the lift is almost given by $\underline{F}_{\text{rev}}$ only, whereas the contribution of $\underline{F}_{\text{irr}}$ is practically zero in

terms of lift and nearly constant in terms of drag: it accounts for the viscous drag. The drag contribution given by $\underline{F}_{\text{rev}}$ is in agreement with the induced drag values predicted by Eq. (3.8) using $\varepsilon = 1.46$ (value predicted by Eq. (3.10) with $\mathbb{V} = 0.2$). This is a first unexpected result: a very simple straight box-wing configuration already provides, in practice, the optimum span efficiency predicted by Prandtl's theory of the best wing system.

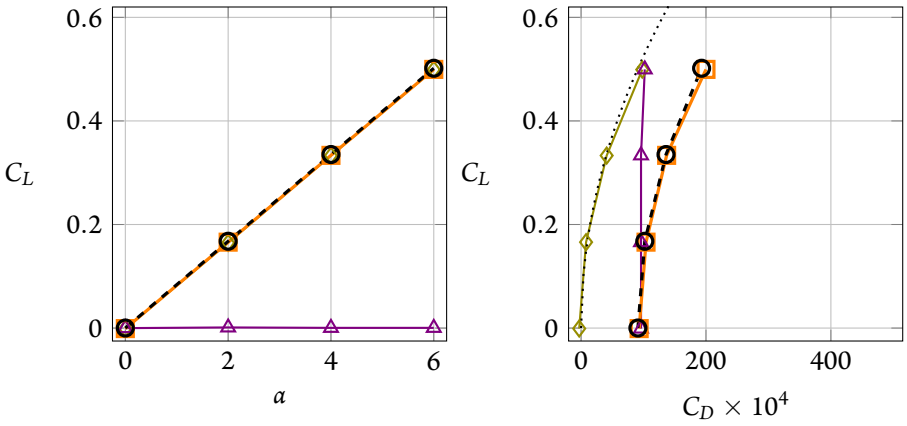


Figure 3.2.7: Box Wing with $\mathcal{AR} = 6$ and $\mathbb{V} = 0.2$ at $Re_\infty = 10^7$ and $M_\infty = 0$. $C_L(\alpha)$ and $C_L(C_D)$ curves and their breakdown in incompressible flow. Reference near field (-⊖-), F_{vf} (—□—), F_{rev} (—◇—), F_{irr} (—△—), $C_L^2/(\pi\mathcal{AR}\varepsilon)$ with $\varepsilon = 1.46$ (·····).

In Fig. 3.2.8 the breakdown in subsonic condition ($M_\infty = 0.3$) is showed and confirms the previous results; the lift, given by $\underline{F}_{\text{rev}}$, is linear and slightly increased respect to the incompressible condition thanks to the low compressibility effects whereas $\underline{F}_{\text{irr}}$ practically equal to the previous case. The reversible contribution superimposed the theoretical induced drag curve, again.

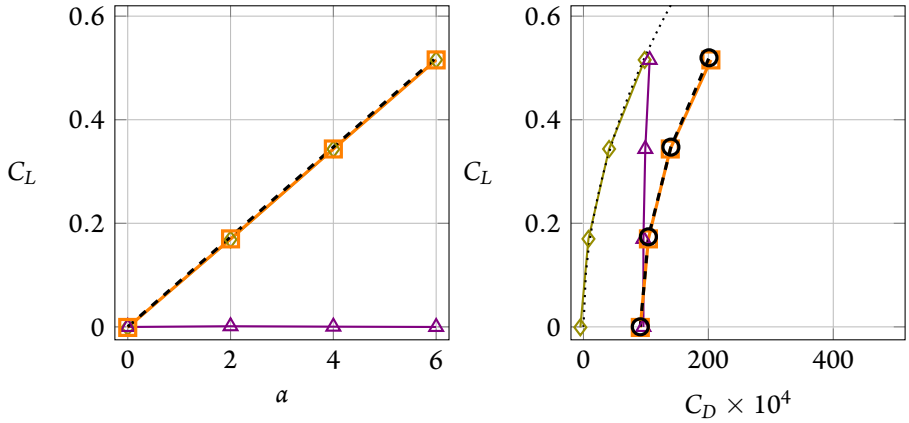


Figure 3.2.8: Box Wing with $\mathcal{AR} = 6$ and $\mathbb{V} = 0.2$ at $Re_\infty = 10^7$ and $M_\infty = 0.3$. $C_L(\alpha)$ and $C_L(C_D)$ and breakdown in subsonic flow. Reference near field (-⊖-), F_{vf} (—⊟—), F_{rev} (—◇—), F_{irr} (—△—), $C_L^2/(\pi\mathcal{AR}\varepsilon)$ with $\varepsilon = 1.46$ (·····).

The results obtained at $M_\infty = 0.7$ are collected in Fig. 3.2.9. In this condition and $\alpha = 0°$ the flow is still subsonic and the $\underline{F}_{\text{irr}}$ computes a value of viscous drag similar to the previous cases; at higher angle of attack the streamwise irreversible part of the aerodynamic force captures the drag rise due to the presence of shock waves in the flow. The reversible part correctly computes the induced drag and the lift also in this case and even when the flow is partially separated after the strong shock wave at $\alpha = 6°$.

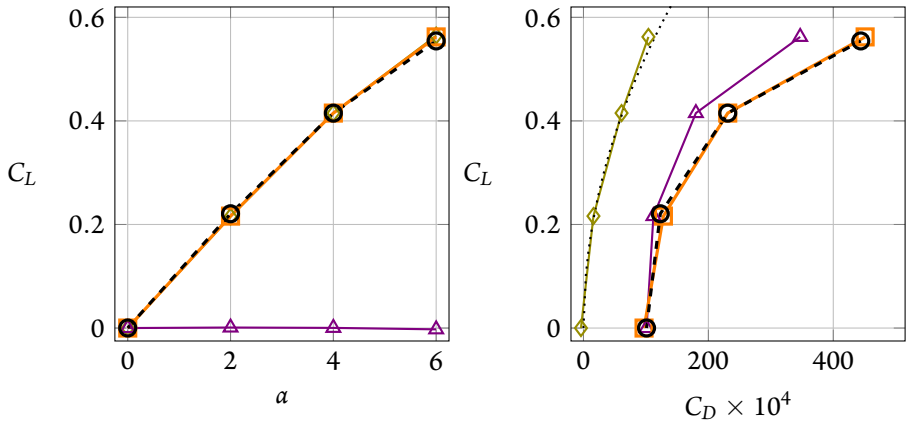


Figure 3.2.9: Box Wing with $\mathcal{AR} = 6$ and $\mathbb{V} = 0.2$ at $Re_\infty = 10^7$ and $M_\infty = 0.7$. $C_L(\alpha)$ and $C_L(C_D)$ and their breakdown in low transonic flow. Reference near field (-⊖-), F_{vf} (—⊟—), F_{rev} (—◇—), F_{irr} (—△—), $C_L^2/(\pi\mathcal{AR}\varepsilon)$ with $\varepsilon = 1.46$ (·····).

The breakdown in high transonic flow ($M_\infty = 0.9$) is displayed if Fig. 3.2.10: in this case the total drag is extremely high ($C_D \approx 0.15$) and more than 95% of the total drag is given by $\underline{F}_{\text{irr}}$ since the region delimited by the wing is choked and a strong shock appears also along the vertical joint (see Fig. 3.2.11). The reversible force is again responsible for the total lift and the lift-induced drag even if the induced drag contribution is less than 5% of the total drag at this Mach number.

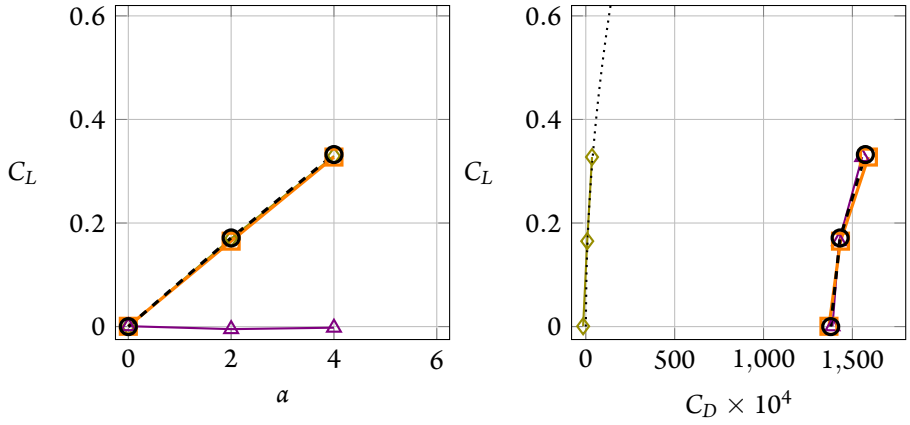


Figure 3.2.10: Box Wing with $\mathcal{AR} = 6$ and $\mathbb{V} = 0.2$ at $Re_\infty = 10^7$ and $M_\infty = 0.9$. $C_L(\alpha)$ and $C_L(C_D)$ and their breakdown in high transonic flow. Reference near field (-⊖-), F_{vf} (—□—), F_{rev} (—◇—), F_{irr} (—△—), $C_L^2/(\pi\mathcal{AR}\varepsilon)$ with $\varepsilon = 1.46$ (·····).

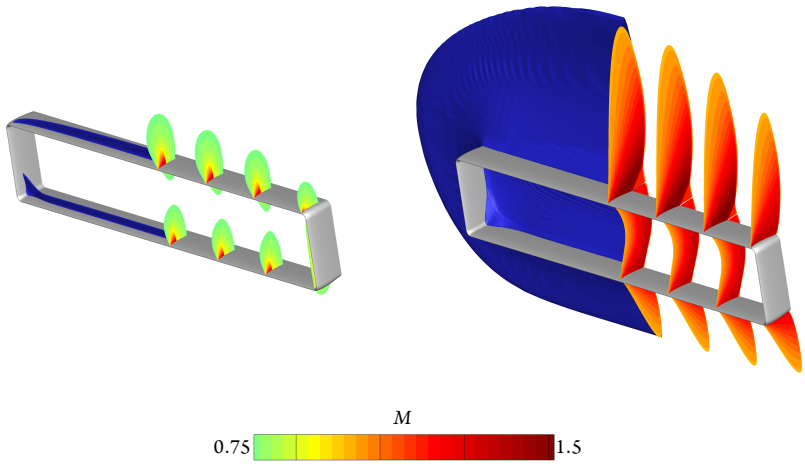


Figure 3.2.11: Box Wing with $\mathcal{AR} = 6$ and $\mathbb{V} = 0.2$ at $Re_\infty = 10^7$ and $\alpha = 6°$; left ($M_\infty = 0.7$), right ($M_\infty = 0.9$). Shock wave region identified by Eq. (3.3) and contour of Mach number over the wingspan.

Summarizing, in each condition $\underline{F}_{\text{vf}}$ correctly predicts the total lift and drag coefficients. C_L is substantially given by the reversible part of the aerodynamic force. The reversible force $\underline{F}_{rev}$ is in extremely good agreement with the induced drag coefficient C_{D_i}, computed by Eq. (3.8) using $\varepsilon = 1.46$ even in presence of strong shock waves, as evidenced in Figs. 3.2.5 and 3.2.6. These results show that the lift-induced drag performance of the tested box-wing are unaffected by compressibility; its span efficiency is practically coincident with the optimum low speed value even at $M_\infty = 0.9$. The very high wave drag obtained clearly requires the introduction of sweep angle and supercritical airfoils, but the Box Wing seems a configuration suitable to be adopted in transonic flow too.

Increasing C_L, $\underline{F}_{\text{irr}}$ computes an almost constant value of the profile drag for the incompressible and the subsonic cases whereas captures the drag rise due to shock waves in transonic conditions. The compressibility effects on the computed induced drag are better analyzed in Fig. 3.2.12 where the reversible force $\underline{F}_{\text{rev}}$ is further decomposed in the *vortex force* $\underline{F}_\ell$ and the *compressible generation term* $\underline{F}_\rho$. The contribution of $\underline{F}_\rho$ increases with the Mach number for lift and reduces for drag: it is responsible for a thrust force not much affected by the angle of attack. The vortex force, that is the entire $\underline{F}_{\text{rev}}$ in incompressible flow and decreases as the Mach number grows.

Figures 3.2.13 and 3.2.14 highlight the differences of the numerically obtained load dis-

tributions changing the angle of attack and the Mach number with the optimal ones computed using Eqs. (3.11) and (3.12) ($M_\infty = 0$). At $\alpha = 0^\circ$ the load on the horizontal wings is almost zero along the wingspan and becomes positive on the lower wing and negative on the upper one. Increasing α both the horizontal loads moves upwards and slightly changes their shapes. On the vertical joint the higher is the angle of attack the more similar to the theoretical load is the shape of the numerical one. Figure 3.2.14 highlights that the shock waves are stronger in the tip regions, as expected.

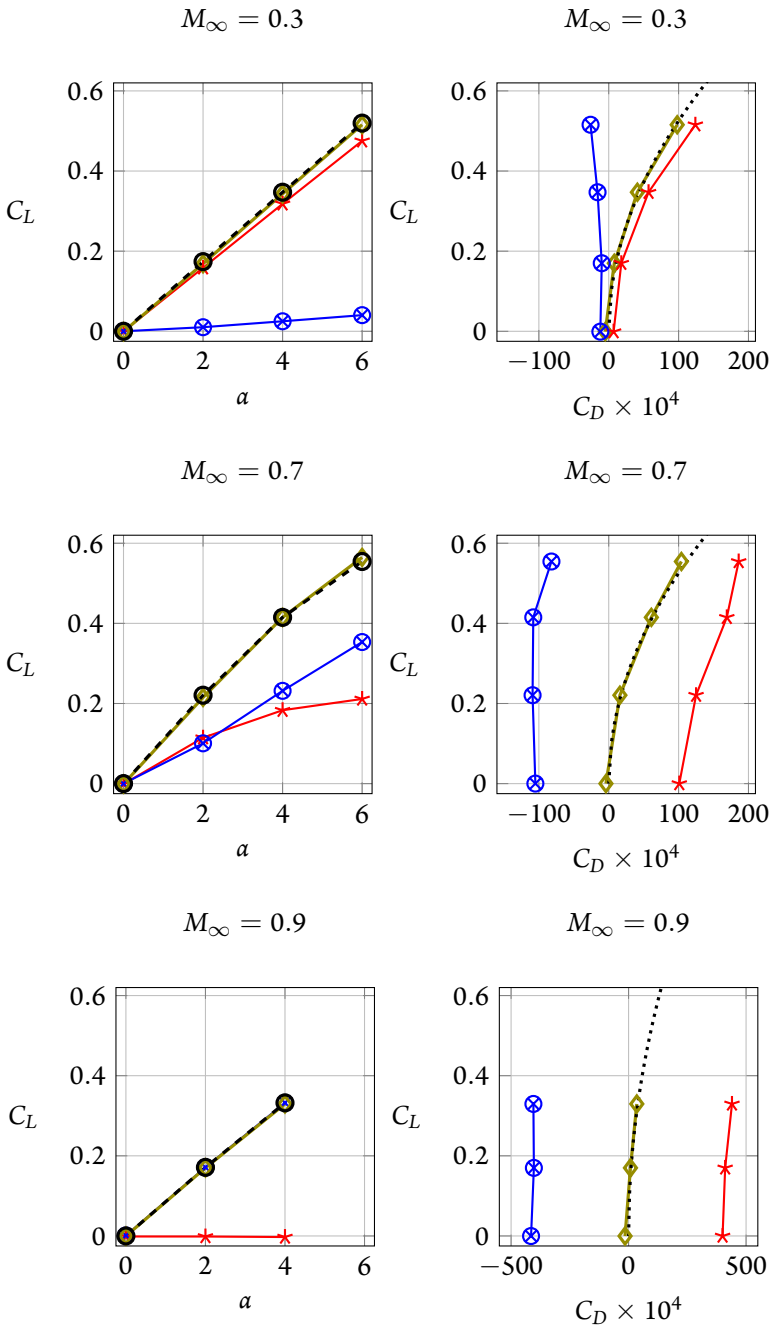


Figure 3.2.12: Box Wing with $\mathcal{AR} = 6$ and $\mathbb{V} = 0.2$ at $Re_\infty = 10^7$. Breakdown of F_{rev} in vortex force and compressible generation term at different Mach numbers. Reference near field (-⊙-), F_{rev} (—◇—), vortex force (—✶—), compressible generation term (—⊗—), $C_L^2/(\pi \mathcal{AR} \varepsilon)$ with $\varepsilon = 1.46$ (·····).

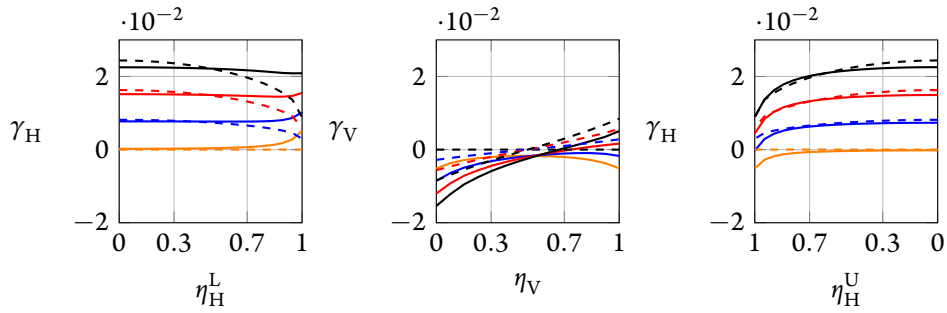


Figure 3.2.13: Box Wing with $\mathcal{AR} = 6$ and $\mathbb{V} = 0.2$ at $Re_\infty = 10^7$ and $M_\infty = 0$. Effect of angle of attack on load distribution. $\alpha = 0$ $C_L = 0$ (——), $\alpha = 2$ $C_L = 0.1676$ (——), $\alpha = 4$ $C_L = 0.3351$ (——), $\alpha = 6$ $C_L = 0.5017$ (——); present study (solid lines), theoretical minimum induced drag load distributions (dotted lines).

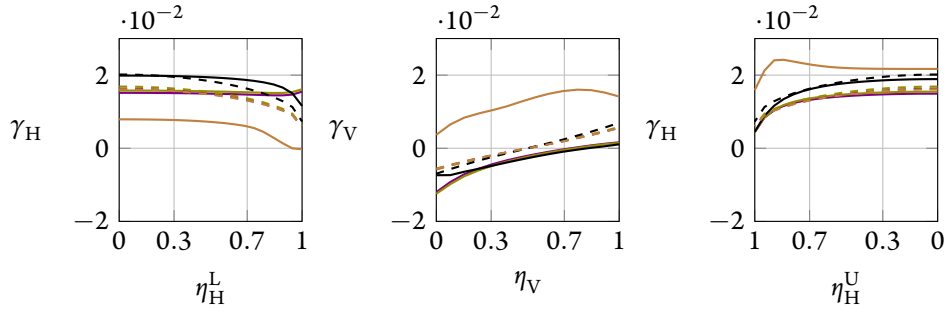


Figure 3.2.14: Box Wing with $\mathcal{AR} = 6$ and $\mathbb{V} = 0.2$ at $Re_\infty = 10^7$ and $\alpha = 4°$. Effect of Mach number on load distribution. $M_\infty = 0$ $C_L = 0.3351$ (——), $M_\infty = 0.3$ $C_L = 0.3471$ (——), $M_\infty = 0.7$ $C_L = 0.4150$ (——), $M_\infty = 0.9$ $C_L = 0.3322$ (——); present study (solid lines), theoretical minimum induced drag load distributions (dotted lines).

The agreement found between the induced drag given by $\underline{F}_{\text{rev}}$ and the one predicted by Eq. (3.8), even when the load distribution is relatively far from the optimum, is an a-priori unexpected result. The theoretically predicted minimum induced drag level for Box Wings immersed in inviscid and incompressible flow can practically be reached in compressible viscous flow just by adopting a constant chord and a rigidly applied angle of attack to the entire configuration (no twist), as presented in this work. This is an indirect indication that there are several off-optimum aerodynamic loads which provide, from a practical engineering perspective, the same optimum level of induced drag. This property appears to hold far beyond the assumptions adopted to formulate the minimum induced drag prob-

lem [97, 98].

Moreover, the optimum span efficiency also obtained in transonic flow conditions suggests that it is possible to adopt an aerodynamic optimization with the only aim of wave-drag reduction in transonic flow with low penalty of induced drag. We do not have a formal proof on this statement, but the study presented here seems indicating that the procedures presented in [97, 98] (and perhaps in general for other configurations) can be applied also in transonic regimes, leaving to the engineer the option to decouple the drag minimization problem into two separate technical parts, where in the first one the configuration is optimized to reduce the induced drag (evaluated using incompressible and inviscid assumption) and the second part focuses on the wave drag reduction in transonic flows.

Effect of Vertical Aspect Ratio

The analysis of the aerodynamic force provided for the Box Wing with $\mathbb{V} = 0.2$ has been repeated for a similar Box Wing with the same $\mathcal{AR} = 6$ and different $\mathbb{V} = 0.4$. The results here showed refer to the C-C type LVL1 grid (see Fig. D.2.1 and Table D.2.1 of Appendix D.2 for the grid convergence analysis). In Figs. 3.2.15 to 3.2.18 the results obtained in terms of lift and drag coefficients for different Mach numbers are showed. The results confirm what obtained for the first configuration: the agreement between $\underline{F}_{\text{rev}}$ and the induced drag of an optimally loaded Box Wing with $\varepsilon = 1.82$. The viscous drag is increased of about 10% respect to the Box Wing with $\mathbb{V} = 0.2$ because of the more extended wet surface of the longer vertical joint. As expected, fixing the angle of attack, this Box-Wing generates an enhanced lift compared to the Box Wing with $\mathbb{V} = 0.2$[1], as evidenced in Fig. 3.2.19 where the comparison between the load distributions obtained for the two Box Wings is showed. Also for this configuration the flow through the Box Wing is chocked at $M_\infty = 0.9$ and the obtained wave drag is higher than the one of the previous configuration. Indeed, even if the shock waves are stronger at $\mathbb{V} = 0.2$ rather than $\mathbb{V} = 0.4$ (see Fig. 3.2.20), the shock extension is higher when the vertical joint is longer.

[1] As for classical biplanes the higher is the distance between the wings the higher is the lift [111]

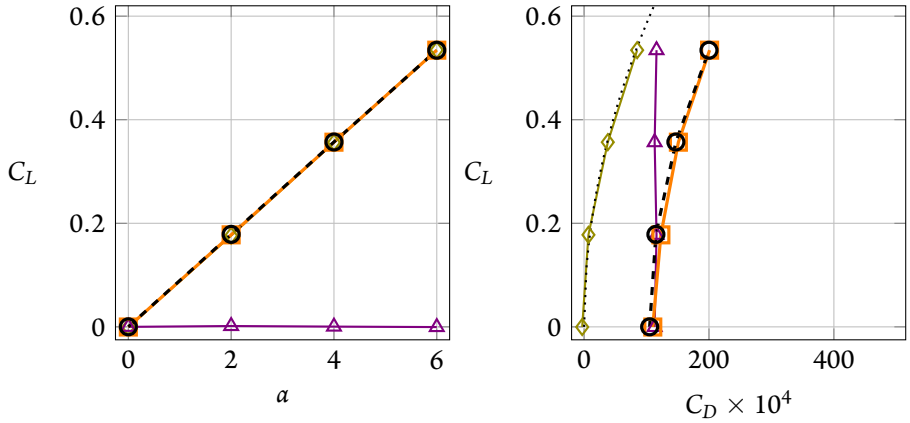


Figure 3.2.15: Box Wing with $\mathcal{AR} = 6$ and $\mathbb{V} = 0.4$ at $Re_\infty = 10^7$ and $M_\infty = 0$. $C_L(\alpha)$ and $C_L(C_D)$ in incompressible flow and breakdown in F_{rev} and F_{irr}. Reference near field (-⊖-), F_{vf} (—⊟—), F_{rev} (—◇—), F_{irr} (—△—), $C_L^2/(\pi\mathcal{AR}\varepsilon)$ with $\varepsilon = 1.82$ (·····).

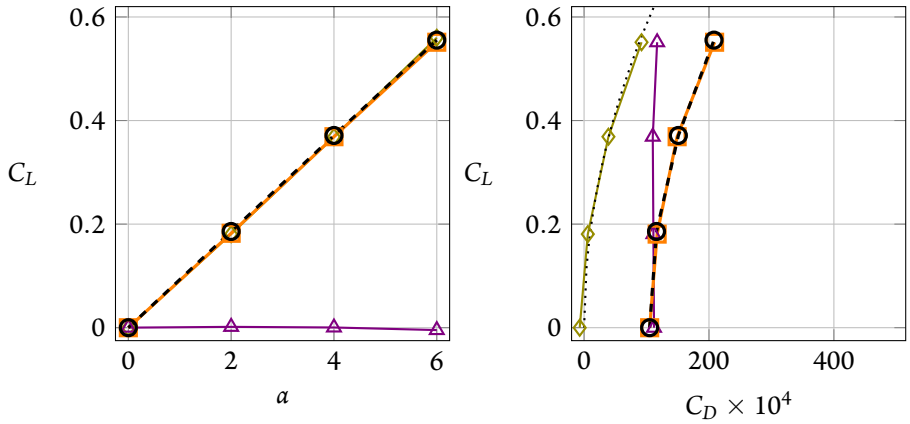


Figure 3.2.16: Box Wing with $\mathcal{AR} = 6$ and $\mathbb{V} = 0.4$ at $Re_\infty = 10^7$ and $M_\infty = 0.3$. $C_L(\alpha)$ and $C_L(C_D)$ in incompressible flow and breakdown in F_{rev} and F_{irr}. Reference near field (-⊖-), F_{vf} (—⊟—), F_{rev} (—◇—), F_{irr} (—△—), $C_L^2/(\pi\mathcal{AR}\varepsilon)$ with $\varepsilon = 1.82$ (·····).

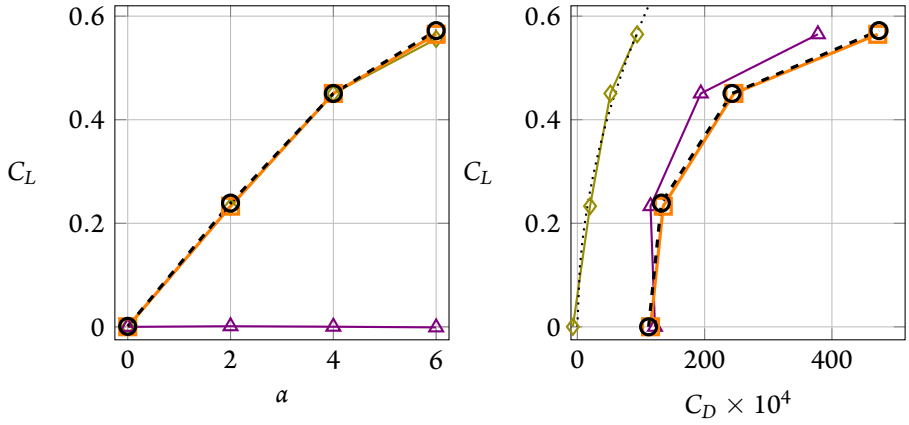


Figure 3.2.17: Box Wing with $\mathcal{AR} = 6$ and $\mathbb{V} = 0.4$ at $Re_\infty = 10^7$ and $M_\infty = 0.7$. $C_L(\alpha)$ and $C_L(C_D)$ in incompressible flow and breakdown in F_{rev} and F_{irr}. Reference near field (-⊙-), F_{vf} (—□—), F_{rev} (—◇—), F_{irr} (—△—), $C_L^2/(\pi\mathcal{AR}\varepsilon)$ with $\varepsilon = 1.82$ (·····).

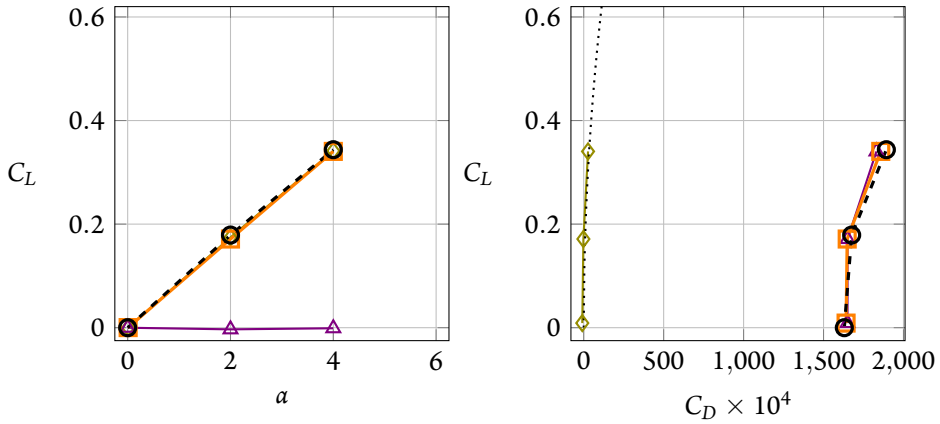


Figure 3.2.18: Box Wing with $\mathcal{AR} = 6$ and $\mathbb{V} = 0.4$ at $Re_\infty = 10^7$ and $M_\infty = 0.9$. $C_L(\alpha)$ and $C_L(C_D)$ in incompressible flow and breakdown in F_{rev} and F_{irr}. Reference near field (-⊙-), F_{vf} (—□—), F_{rev} (—◇—), F_{irr} (—△—), $C_L^2/(\pi\mathcal{AR}\varepsilon)$ with $\varepsilon = 1.82$ (·····).

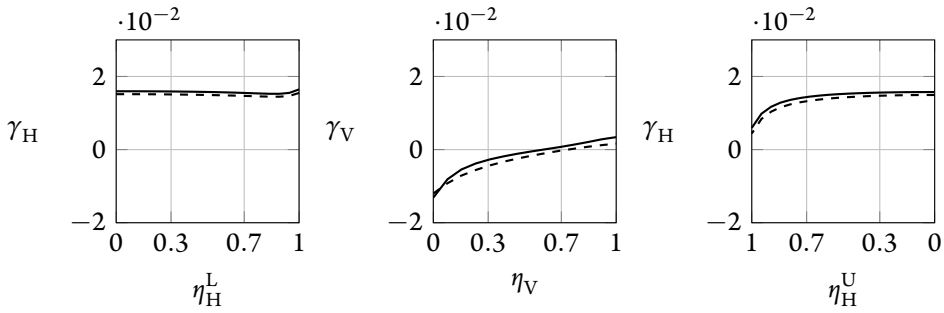


Figure 3.2.19: Box Wings with $\mathcal{AR} = 6$ at $Re_\infty = 10^7$, $M_\infty = 0$ and $\alpha = 4°$. Comparison between the load distributions obtained for the Box Wing with $\mathbb{V} = 0.2$ (—△—) and the one with $\mathbb{V} = 0.4$ (—□—). The lift coefficient for $\mathbb{V} = 0.2$ is $C_L = 0.3351$; the lift coefficient for $\mathbb{V} = 0.4$ is $C_L = 0.3570$.

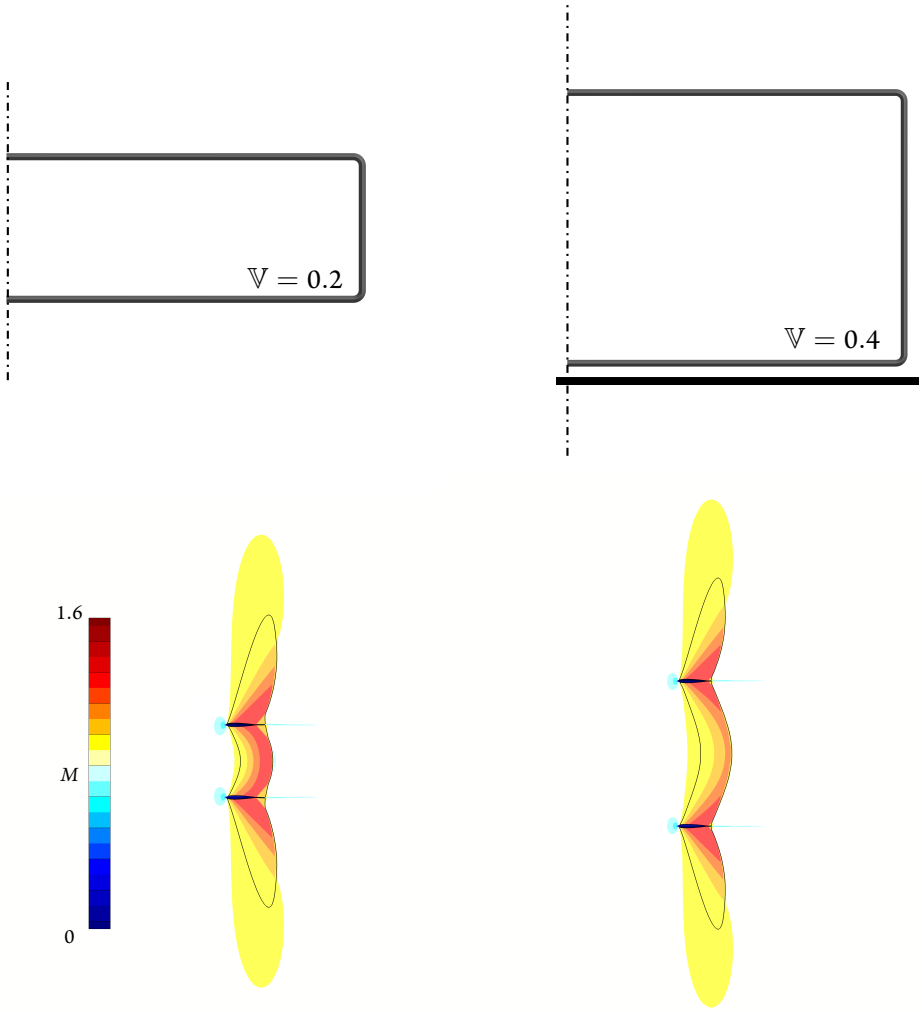


Figure 3.2.20: Box Wings with same aspect ratio $\mathcal{AR} = 6$ and different $\mathbb{V}$ at $Re_\infty = 10^7$, $M_\infty = 0.9$ and $\alpha = 0°$. Front view of wing configuration and contour of Mach number in the symmetry plane (black line $M_\infty = 1$).

3.2.3 Box Wing Vs. Elliptical Wing

An Elliptical Wing with a constant wing section shaped by a sharp NACA 0012 airfoil, no twist, standard mean chord $\bar{c} = 2c$ and wingspan $b = 12c$ has been considered as reference optimum cantilevered wing (see Fig. 3.2.21). Using these geometric characteristics an aspect ratio $\mathcal{AR} = 6$ and a reference area $S = b\bar{c} = 24c^2$ equal to the ones obtained

for the Box Wings of Section 3.2.1 are realized. A C-C type grid with the far field placed $100c$ distant from the body and 17 million cells (512 along the wing section, 128 along the sami-wingspan and on each direction normal to the body - LVL$^1/_2$) has been built up keeping $y^+ \approx 1$ all over the wing; the results of the grid convergence analysis performed for this configuration are collected in Fig. D.3.1 and Table D.3.1 of Appendix D.3.

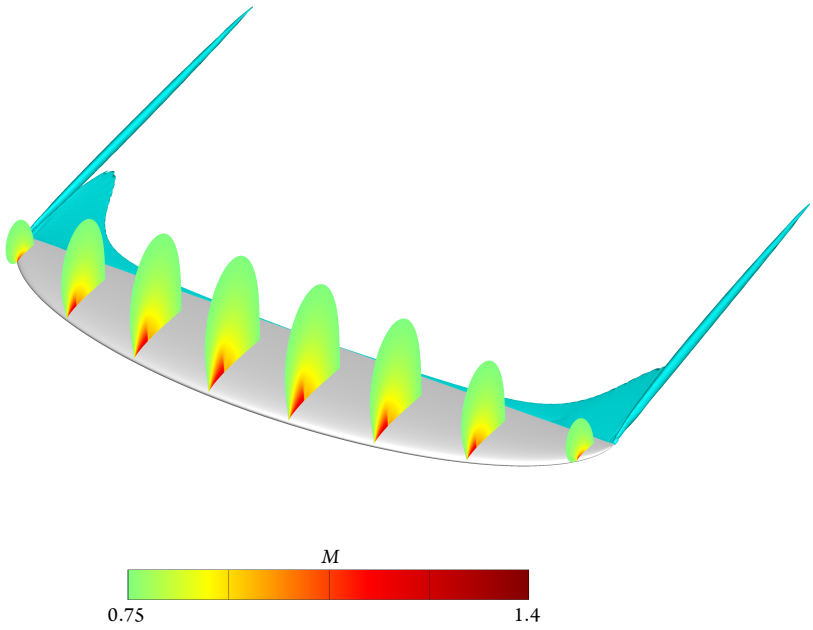


Figure 3.2.21: Elliptical Wing with $\mathcal{AR} = 6$ at $Re_\infty = 10^7$, $M_\infty = 0.7$ and $\alpha = 4°$. Iso-surface of $|\omega_x|$ in the wake and contour of Mach number over the wingspan.

CFD simulations at $Re_\infty = 10^7$ and different Mach numbers have been carried out as described in Section 3.2.1. In Fig. 3.2.22 a comparison between numerically obtained load distribution and the elliptical one for $M_\infty = 0$ and different angles of attack is showed: the curves overlap up to $\eta_H = 0.97$ with just a small discrepancy in the tip region. The same result is obtained fixing α and changing the Mach number (see Fig. 3.2.23) even in presence of shock waves, as evidenced in Fig. 3.2.21 where the Mach number contour over the wing at $M_\infty = 0.7$ and $\alpha = 4°$ is displayed.

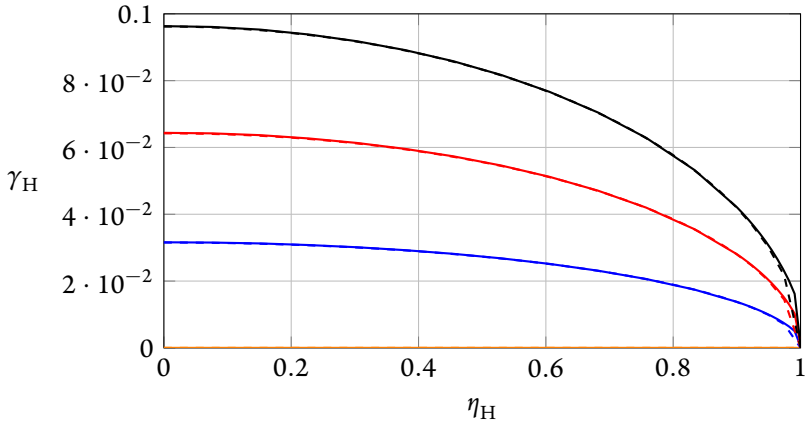


Figure 3.2.22: Elliptical Wing with $\mathcal{AR} = 6$ at $Re_\infty = 10^7$ and $M_\infty = 0$. Effect of angle of attack on load distribution. $\alpha = 0°$ $C_L = 0$ (——), $\alpha = 2°$ $C_L = 0.1498$ (——), $\alpha = 4°$ $C_L = 0.3051$ (——), $\alpha = 6°$ $C_L = 0.457$ (——); present study (solid lines), elliptical load distributions (dotted lines).

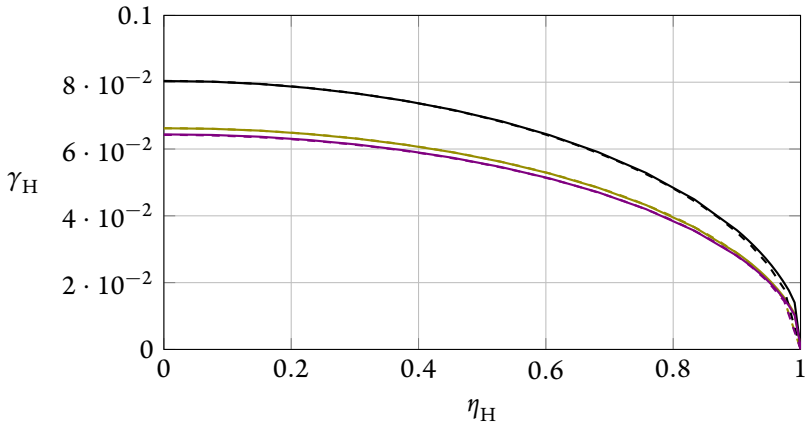


Figure 3.2.23: Elliptical Wing with $\mathcal{AR} = 6$ at $Re_\infty = 10^7$ and $\alpha = 4°$. Effect of Mach number on load distribution. $M_\infty = 0$ $C_L = 0.3051$ (——), $M_\infty = 0.3$ $C_L = 0.3146$ (——), $M_\infty = 0.7$ $C_L = 0.3823$ (——); present study (solid lines), elliptical load distributions (dotted lines).

The aerodynamic force breakdown has been computed for $M_\infty = 0$, 0.3 and 0.7; a shock stall comes out at $M_\infty = 0.9$ as already showed by Mele et al. in [46] for an Elliptical Wing with $\mathcal{AR} = 7$. In the other cases the results, displayed in Figs. 3.2.24 to 3.2.26, confirm the possibility to correctly predict the induced drag of an Elliptical Wing using the well known Prandtl's formula derived for incompressible and inviscid flow (Eq. (3.6))

also in viscous, compressible and even transonic flow conditions. Moreover, $\underline{F}_{\text{vf}}$ accurately computes the total lift and drag forces whereas $\underline{F}_{\text{irr}}$ captures the drag rise due to the presence of shock waves in transonic conditions.

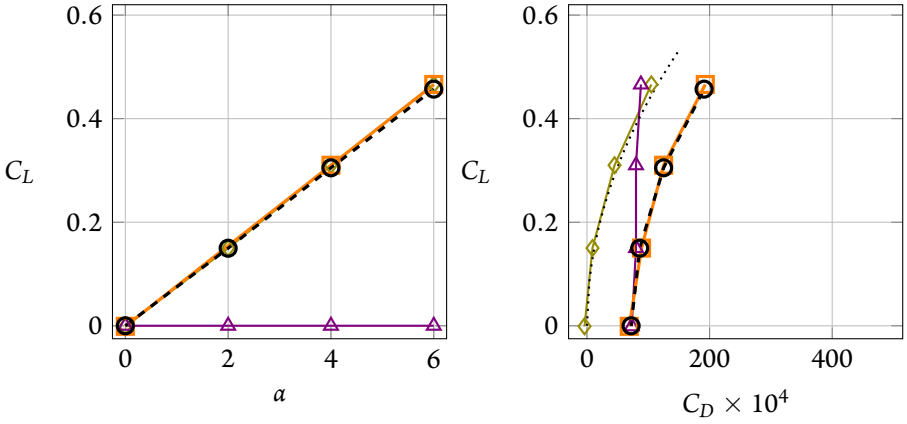


Figure 3.2.24: Elliptical Wing with $\mathcal{AR} = 6$ at $Re_\infty = 10^7$ and $M_\infty = 0$. $C_L(\alpha)$ and $C_L(C_D)$ in incompressible flow and breakdown in F_{rev} and F_{irr}. Reference near field (-⊖-), F_{vf} (—⊟—), F_{rev} (—◇—), F_{irr} (—△—), $C_L^2/(\pi\mathcal{AR})$ (·····).

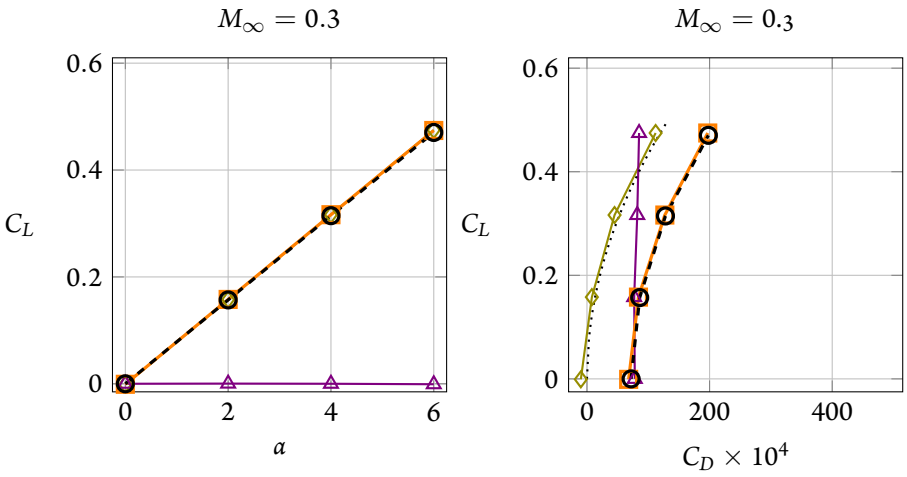


Figure 3.2.25: Elliptical Wing with $\mathcal{AR} = 6$ at $Re_\infty = 10^7$ and $M_\infty = 0.3$. $C_L(\alpha)$ and $C_L(C_D)$ in incompressible flow and breakdown in F_{rev} and F_{irr}. Reference near field (-⊖-), F_{vf} (—⊟—), F_{rev} (—◇—), F_{irr} (—△—), $C_L^2/(\pi\mathcal{AR})$ (·····).

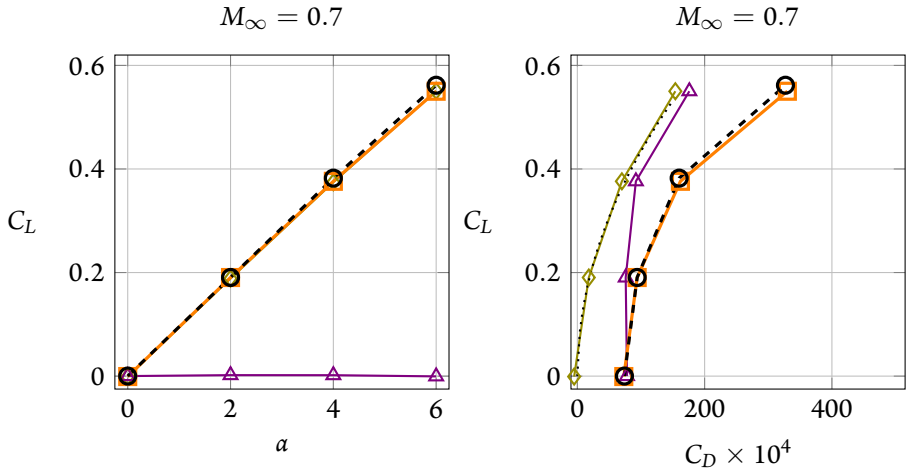


Figure 3.2.26: Elliptical Wing with $\mathcal{AR} = 6$ at $Re_\infty = 10^7$ and $M_\infty = 0.7$. $C_L(\alpha)$ and $C_L(C_D)$ in incompressible flow and breakdown in F_{rev} and F_{irr}. Reference near field (-⊙-), F_{vf} (—□—), F_{rev} (—◇—), F_{irr} (—△—), $C_L^2/(\pi\mathcal{AR})$ (·····).

It is interesting to compare the total drag performance of the box wings analyzed with the elliptical wing. Even if the three configurations have the same reference platform, given by the extension of the horizontal wings, the wet area changes for the presence of the vertical joint. Therefore, in incompressible and subsonic conditions the viscous drag contribution increases of 23% for the Box Wing with $\mathbb{V} = 0.2$ and 45% when $\mathbb{V} = 0.4$ respect to the elliptical wing. On the other hand, the induced drag decreases of 46% when $\mathbb{V} = 0.2$ and 82% when $\mathbb{V} = 0.4$. Since the viscous drag substantially does not change with the lift whereas the induced drag is proportional to C_L^2 the combination of these two effects (augmented viscous drag and lower induced drag) returns a lower total drag for the Box Wings when $C_L > 0.38$, as Fig. 3.2.27 shows.

In transonic flow, even if the shock waves have similar intensity for the three configurations, the extension of the shock region increases for the Box Wings and the *irreversible* drag cancel the induced-drag benefit. These results show that a simple Box Wing can realize a better drag performance respect to the optimum cantilevered wing in subsonic flow but a wave-drag optimization is necessary to obtain the same result in transonic regime.

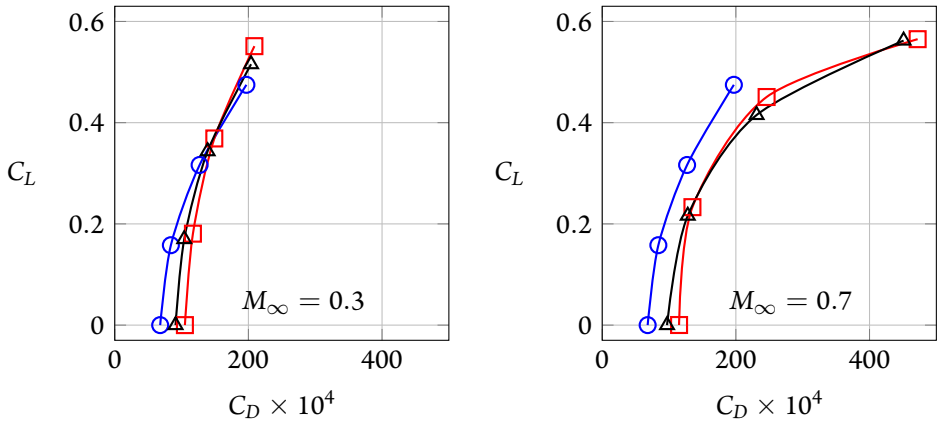


Figure 3.2.27: Comparison of polar curves obtained at $Re_\infty = 10^7$ for the equivalent Elliptical Wing with $\mathcal{AR} = 6$ (—○—), the Box Wing with $\mathbb{V} = 0.2$ (—△—) and the Box Wing with $\mathbb{V} = 0.4$ (—□—).

3.3 Summary of the Achievements of This Chapter

The analysis of the aerodynamic performance of an innovative turboprop wing-body configuration has been performed using the thermodynamic method described in Section 1.4.3. The main results are:

- the drag reduction due to two different passive systems (NLF and Riblets) has been computed and their effect on different parts of drag has been evaluated;
- it has been confirmed that riblets do not affect the induced drag performance;
- an enhanced wave drag has been found in case of drag reduction systems installed.

The analysis of the aerodynamic force generated by two Box Wings and an equivalent Elliptical Wing has been performed with the vortical method presented in Chapter 2. The breakdown of the total force in its reversible (lift and lift-induced drag) and irreversible part (viscous and wave drag) even in presence of strong shocks and separated flow has been provided and the following results obtained:

- the induced drag of Box Wings immersed in viscous and compressible flow is equal to the one predicted by inviscid and incompressible theories even in presence of shock waves;

- the low induced drag performance of Box Wings has been found with different load distributions proving the robustness of the theoretically predicted minimum induced drag optimum load distribution. This result, under an engineering point of view, paves the way for adopting an aerodynamic optimization process in transonic flow with the only aim of wave-drag reduction;
- the comparison of the results with an equivalent cantilevered wing allowed for the estimation of the price to pay in terms of viscous drag if a Box Wing is adopted: fixing the lift coefficient, the viscous drag of a Box Wing with $\mathbb{V} = 0.2$ is 26% higher than the one of the Elliptical Wing; on the other hand a gain of 46% in terms of induced drag is earned.
- in subsonic regime, the total drag performance of the Box Wings analyzed is superior than the one of the Elliptical Wing when $C_L > 0.38$ confirming that the Box Wing is a very efficient wing system even without the adoption of a viscous-drag optimization;
- in transonic regime, the total drag of the equivalent Elliptical Wing is always lower than the one of the Box Wings analyzed: a wave-drag optimization is necessary to obtain competitive drag performance.

We perceive a danger of overconfidence and under-competence in CFD.

Spalart et al. 2016

Conclusions

An innovative method for the aerodynamic force analysis and breakdown has been studied, theoretical developments have been provided and the method has been applied to numerical data of the flow around innovative aeronautical configurations.

THEORETICAL DEVELOPMENTS

- The *objectiviness* of the vorticity-based drag breakdown between induced and profile drag components has been investigated: a wake integral form for the induced drag has been proposed and relations with the classical *irreversible* drag definitions have been provided.
- The extension of the Lamb-vector theory to inviscid and compressible flow has been derived and its *measurable* form has been introduced for facing the aerodynamic force computation in case of CFD data.
- A drag breakdown in *reversible* and *irreversible* force components has been proposed; the leading-edge suction thrust has been identified and its behavior with the Reynolds number has been investigated.
- First steps towards a vortical thrust/drag bookkeeping for propelled aircraft with actuator disk model and incompressible flows have been moved.

APPLICATIONS TO INNOVATE AIRCRAFT CONFIGURATIONS

- The drag breakdown for an innovative turboprop aircraft configuration has been computed. The impact of two drag reduction systems (Natural Laminar Flow and Riblets) on the overall aerodynamic performance have been investigated. The drag decomposition allowed for identifying and understanding the principal mechanisms which generate drag reduction for each system.

- The induced drag of Box Wing has been studied in viscous and compressible flow. It has been found a remarkable agreement between the *reversible drag* predicted by the vortical far-field method and the theoretical induced drag predicted for optimum Box Wing in inviscid and incompressible flow. The analyses permitted to conclude that both compressibility effects and changes from the optimal load distribution have really low impact on box-wing aerodynamic performance. The comparison with an equivalent elliptical wing highlighted a great potential benefit of Box Wings respect standard cantilevered configurations: Box Wings seems to be an advantageous configuration even in transonic flow if a conventional wave drag optimization (supercritical airfoil and swept wing) is adopted.

Present dissertation collects the studies and the results obtained by the author and the research group in which he worked in the last years. Analyzing the aerodynamic force from both theoretical and applied perspectives gave to the author the possibility to deepen countless aspects of classical and modern aerodynamics; he enhanced his knowledge on the physical mechanisms behind the aerodynamic force generation and learned how to make the most of the technological resources of our time. He realized that the understanding of the results obtained is much more important than obtaining results themselves and that CFD is as power as dangerous device to be used with attention and consciousness. The author thinks that his personal growth as CFD/aerodynamic specialist is doubtless the main result achieved during his PhD.

A

Derivative Moment Transformations

Let $\mathcal{V}$ be a subset of R^N with $N = 2, 3$ and $k = N - 1$ bounded by the surface $\partial\mathcal{V}$; for any piecewise differentiable vector field $\underline{g}$ and potential function χ defined in $\mathcal{V}$, there is (see Wu et al. [38]):

$$\int_{\mathcal{V}} \underline{g}\, \mathrm{d}\mathcal{V} = \frac{1}{k}\int_{\mathcal{V}} \underline{r} \times \left(\underline{\nabla} \times \underline{g}\right)\, \mathrm{d}\mathcal{V} - \frac{1}{k}\int_{\partial\mathcal{V}} \underline{r} \times \left(\underline{n} \times \underline{g}\right)\, \mathrm{dS}\,, \tag{A.1}$$

$$\int_{\partial\mathcal{V}} \chi \underline{n}\, \mathrm{dS} = -\frac{1}{k}\int_{\partial\mathcal{V}} \underline{r} \times (\underline{n} \times \underline{\nabla}\chi)\, \mathrm{dS}\,, \tag{A.2}$$

where $\underline{n}$ is the unitary vector normal to $\partial\mathcal{V}$ and pointing outside $\mathcal{V}$ and $\underline{r}$ is the position vector with the origin placed at any point of the fuid domain.

Note that these identities are independent of the origin O of the position vector $\underline{r}$, as can be checked by the fact if the operation '$\underline{r}\times$' is removed, then their left-hand sides vanish and right-hand sides are just the Gauss theorem. Thus, all the new force formulae obtained using the Derivative Moment Transformations must also be O-independent, although some individual terms therein may depend on the choice of the pole.

B

Thermodynamics estimate on the far field surface

Let's consider the energy equation for an adiabatic flow with uniform upstream asymptotic condition

$$h + \frac{q^2}{2} = h_\infty + \frac{U_\infty^2}{2} + \Delta H\,, \tag{B.1}$$

where $h = C_p T = a^2/(\gamma - 1)$ is the specific enthalpy and $a = \sqrt{\gamma R T}$ is the speed of sound (T is the absolute temperature). ΔH denotes the change in total enthalpy due, mainly, to the work down by the engines. $\Delta H > 0$ in the exhaust regions whereas $\Delta H = 0$ in the case of inviscid flow and if the Prandtl number is equal to one (Crocco's solution of the thermal adiabatic boundary layer).

Eq. (B.1) can be written as:

$$\frac{T}{T_\infty} = 1 + \frac{\gamma - 1}{2} M_\infty^2 \left(1 - \frac{q^2}{U_\infty^2} + 2\frac{\Delta H}{U_\infty^2}\right). \tag{B.2}$$

In a perfect gas, the entropy variation can be related to the fluid density ρ, the static pressure

p and the temperature T

$$\frac{\Delta s}{R} \equiv \frac{s - s_\infty}{R} = \frac{1}{\gamma - 1} \ln \frac{T}{T_\infty} - \ln \frac{\rho}{\rho_\infty} , \tag{B.3}$$

so that:

$$\frac{\rho}{\rho_\infty} = e^{-\frac{\Delta s}{R}} \left(\frac{T}{T_\infty} \right)^{\frac{1}{\gamma - 1}} , \tag{B.4}$$

and

$$\frac{p}{p_\infty} = e^{-\frac{\Delta s}{R}} \left(\frac{T}{T_\infty} \right)^{\frac{\gamma}{\gamma - 1}} . \tag{B.5}$$

Substituting Eq. (B.2) into Eq. (B.4) and Eq. Eq. (B.5), with second-order approximation,

$$\begin{aligned} \rho \approx \rho_\infty e^{-\frac{\Delta s}{R}} \Bigg[& 1 - M_\infty^2 \left(\frac{u'}{U_\infty} - \frac{\Delta H}{U_\infty^2} \right) - \frac{M_\infty^2}{2} \left(\frac{u'^2 + v_\pi^2}{U_\infty^2} \right) \\ & + \left(1 - \frac{\gamma}{2} \right) M_\infty^4 \left(\frac{u'^2}{U_\infty^2} + \frac{\Delta H^2}{U_\infty^4} - 2 \frac{\Delta H u'}{U_\infty^3} \right) \Bigg] , \end{aligned} \tag{B.6}$$

$$\begin{aligned} p \approx p_\infty e^{-\frac{\Delta s}{R}} \Bigg[& 1 - \gamma M_\infty^2 \left(\frac{u'}{U_\infty} - \frac{\Delta H}{U_\infty^2} \right) - \frac{\gamma M_\infty^2}{2} \left(\frac{u'^2 + v_\pi^2}{U_\infty^2} \right) \\ & + \frac{\gamma M_\infty^4}{2} \left(\frac{u'^2}{U_\infty^2} + \frac{\Delta H^2}{U_\infty^4} - 2 \frac{\Delta H u'}{U_\infty^3} \right) \Bigg] . \end{aligned} \tag{B.7}$$

Finally, under the inviscid flow approximation,

$$\rho \approx \rho_\infty \left[1 - M_\infty^2 \frac{u'}{U_\infty} - \frac{M_\infty^2}{2} \left(\frac{u'^2 + v_\pi^2}{U_\infty^2} \right) + \left(1 - \frac{\gamma}{2} \right) M_\infty^4 \frac{u'^2}{U_\infty^2} \right] , \tag{B.8}$$

$$p \approx p_\infty \left[1 - \gamma M_\infty^2 \frac{u'}{U_\infty} - \frac{\gamma M_\infty^2}{2} \left(\frac{u'^2 + v_\pi^2}{U_\infty^2} \right) + \frac{\gamma M_\infty^4}{2} \frac{u'^2}{U_\infty^2} \right] . \tag{B.9}$$

C

Summary of Aerodynamic Force Formulae

C.1 Aerodynamic Thrust

Table C.1.1: Vortical thrust formula in incompressible laminar flow.

$$\underline{T} = \underline{T}_\ell + \underline{T}_\mathcal{W} + \underline{T}_\mathrm{s}$$

$$\underline{T}_\ell = -\rho \int_\mathcal{V} \underline{\ell}\, \mathrm{d}\mathcal{V}$$

$$\underline{T}_\mathcal{W} = -\tfrac{1}{k}\rho \int_\mathcal{W} \underline{r} \times (\underline{n} \times \underline{\ell})\ \mathrm{dS}$$

$$\underline{T}_\mathrm{s} = \tfrac{1}{k}\rho \int_{S_D} \underline{r} \times \left[\underline{n} \times \underline{\nabla}\left(\tfrac{V^2}{2}\right)\right]\ \mathrm{dS}$$

C.2 Aerodynamic Force

Table C.2.1: Summary of the aerodynamic force formulae used in different flow conditions.

$$\underline{F}_{\mathrm{vf}} = \underline{F}_{\mathrm{rev}} + \underline{F}_{\mathrm{irr}} \qquad ^{a}$$

	Inviscid	Viscous laminar	Viscous turbulent
Incompressible			
$\underline{F}_{\mathrm{rev}} = \underline{F}_{\ell}$ $\underline{F}_{\mathrm{irr}} = \underline{F}_{\Sigma}$	$\underline{F}_{\ell} = -\rho \int_{S_B} \frac{V^2}{2}\, \mathrm{dS}$ $\underline{F}_{\Sigma} = 0$	$\underline{F}_{\ell} = -\rho \int_{\mathcal{V}} \underline{\ell}\, \mathrm{d}\mathcal{V}$ $\underline{F}_{\Sigma} = -\frac{\rho}{k} \int_{\Sigma} \underline{r} \times (\underline{n} \times \underline{\ell})\, \mathrm{dS}$	$\underline{F}_{\ell} = -\rho \int_{\mathcal{V}} \left(\widetilde{\underline{\zeta}} \times \widetilde{\underline{V}}\right)\, \mathrm{d}\mathcal{V}$ $\underline{F}_{\Sigma} = -\frac{\rho}{k} \int_{\Sigma} \underline{r} \times \left[\underline{n} \times \left(\widetilde{\underline{\zeta}} \times \widetilde{\underline{V}}\right)\right]\, \mathrm{dS}$
Compressible			
$\underline{F}_{\mathrm{rev}} = \underline{F}_{\ell} + \underline{F}_{\rho}$ $\underline{F}_{\mathrm{irr}} = \underline{F}_{\Sigma}$	$\underline{F}_{\ell} = -\int_{\mathcal{V}} \rho \underline{\zeta} \times \underline{V}\, \mathrm{d}\mathcal{V} - \int_{S_B} \rho \frac{V^2}{2}\, \mathrm{dS}$ $\underline{F}_{\rho} = -\frac{1}{k} \int_{\mathcal{V}} \underline{r} \times \left[\underline{\nabla} \times \left(\frac{V^2}{2} \underline{\nabla} \rho\right)\right]\, \mathrm{d}\mathcal{V}$ $-\frac{1}{k} \int_{S_B} \underline{r} \times \left[\underline{n} \times \left(\frac{V^2}{2} \underline{\nabla} \rho\right)\right]\, \mathrm{dS}$ $\underline{F}_{\Sigma} = -\frac{1}{k} \int_{\Sigma} \underline{r} \times \left[\underline{n} \times \left(\underline{\zeta} \times \underline{V}\right)\right]\, \mathrm{dS}$	$\underline{F}_{\ell} = -\int_{\mathcal{V}} \rho \underline{\ell}\, \mathrm{d}\mathcal{V}$ $\underline{F}_{\rho} = -\frac{1}{k} \int_{\mathcal{V}} \underline{r} \times \left\{\underline{\nabla} \times \left[\rho \underline{\nabla} \left(\frac{V^2}{2}\right)\right]\right\}\, \mathrm{d}\mathcal{V}$ $\underline{F}_{\Sigma} = -\frac{1}{k} \int_{\Sigma} \underline{r} \times (\underline{n} \times \rho \underline{\ell})\, \mathrm{dS}$	$\underline{F}_{\ell} = -\int_{\mathcal{V}} \bar{\rho} \left(\widetilde{\underline{\zeta}} \times \widetilde{\underline{V}}\right)\, \mathrm{d}\mathcal{V}$ $\underline{F}_{\rho} = -\frac{1}{k} \int_{\mathcal{V}} \underline{r} \times \left\{\underline{\nabla} \times \left[\bar{\rho} \underline{\nabla} \left(\frac{\widetilde{V}^2}{2}\right)\right]\right\}\, \mathrm{d}\mathcal{V}$ $\underline{F}_{\Sigma} = -\frac{1}{k} \int_{\Sigma} \underline{r} \times \left[\underline{n} \times \bar{\rho} \left(\widetilde{\underline{\zeta}} \times \widetilde{\underline{V}}\right)\right]\, \mathrm{dS}$

[a] Molecular viscosity term Δ_{μ} zero or negligible.

D

Accuracy Analysis of Box-wing Numerical Results

In the following pages the grid convergence analyses performed for the investigations on the Box-wings aerodynamic performances are reported. Both *near field* and *far field* formulae have been tested for each case study including the analysis of the effect of the integration domain on the force breakdown computation, reported only for the Box Wing with $\mathcal{AR} = 6$ and $\mathbb{V} = 0.2$ Appendix D.1. The analysis for the Box Wing with $\mathbb{V} = 0.4$ is reported in Appendix D.2 whereas the analysis for the elliptical wing is presented in Appendix D.3.

D.1 Box Wing with $\mathcal{AR} = 6$ and $\mathbb{V} = 0.2$

For the Box Wing analyzed in Section 3.2.2 the finest grid level (LVL1), with 14 million cells, 256 cells along the wing section, 64 along both the horizontal semi-wingspans and the vertical wingspan and 128 in each direction normal to the body, has been scaled two and four times obtaining respectively a medium (LVL2) and a coarse grid level (LVL4).

The lift C_L and drag C_D coefficients computed by $\underline{F}_{\text{nf}}$ and $\underline{F}_{\text{vf}}$ and their breakdown in reversible ($\underline{F}_{\text{rev}}$) and irreversible ($\underline{F}_{\text{irr}}$) forces changing the grid size (LVL) are reported

in Fig. D.1.1 and summarized in Table D.1.1. Both *near field* and *far field* values converge to constant values increasing the grid size. On the finest grid level (LVL1), that has been used for all the computations, the difference between the aerodynamic force computed by $\underline{F}_{\text{nf}}$ and $\underline{F}_{\text{vf}}$ is of 1% in terms of lift coefficient whereas the drag coefficient differences are lower than one count. Moreover, comparing the induced drag of an optimally loaded Box Wing, computed by Eq. (3.8) with $\varepsilon = 1.46$, and $\underline{F}_{\text{rev}}$ a difference of 2% has been obtained.

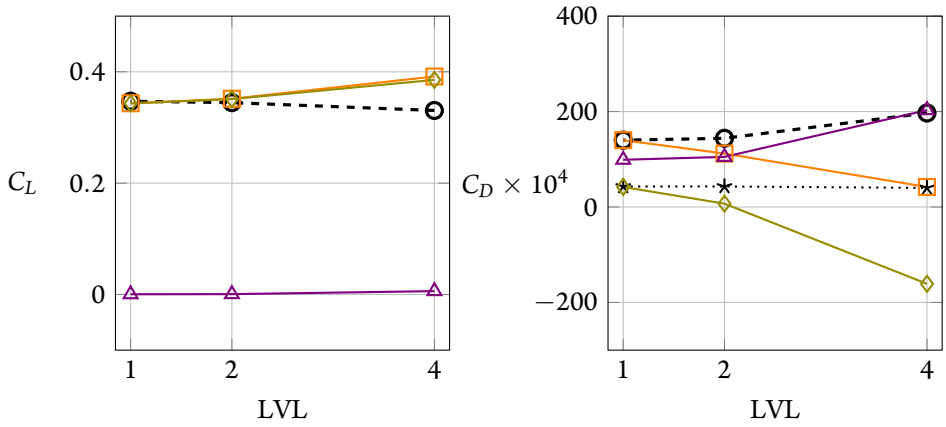


Figure D.1.1: Box Wing with $\mathcal{AR} = 6$ and $\mathbb{V} = 0.2$ at $Re_\infty = 10^7$, $M_\infty = 0.3$ and $\alpha = 4°$. Grid convergence analysis in terms of *near-field* F_{nf} and *far-field* F_{vf} lift (C_L) and drag (C_D) coefficients and their breakdown. F_{nf} (-⊖-), F_{vf} (—□—), F_{rev} (—◇—), F_{irr} (—△—), induced drag of an optimally loaded Box Wing with $\varepsilon = 1.46$ (··✶··).

Table D.1.1: Box Wing with $\mathcal{AR} = 6$ and $\mathbb{V} = 0.2$ at $Re_\infty = 10^7$, $M_\infty = 0.3$ and $\alpha = 4°$. Results of the grid convergence analysis in terms of *near field* F_{nf} and *far field* F_{vf} lift (C_L) and drag (C_D) coefficients and their breakdown in F_{rev} and F_{irr}.

C_L

LVL	F_{irr}	F_{rev}	F_{vf}	F_{nf}
4	-0.0060	0.3855	0.3915	0.3305
2	0.0006	0.3510	0.3516	0.3446
1	0.0004	0.3431	0.3435	0.3471

$C_D \times 10^4$

LVL	F_{irr}	F_{rev}	$C_{D_{\text{i}}}$	F_{vf}	F_{nf}
4	203	-161	40	42	197
2	105	7	43	112	144
1	99	42	43	140	140

The effect of the integration domain on the aerodynamic force computation and its breakdown by *vortical* method has been investigated on each grid level to analyze the *quasi-objective* separation between induced and profile drag discussed in Section 2.2.1. In each computation an integration domain shaped as a box is used. The lateral and the front sides of the integration domain are fixed $20c$ far from the body so that they do not intersect any vortical region; on the other hand, the influence of the rear side of the integration domain on the *far-field* computations has been tested in each case analyzed changing its position from the wing trailing edge ($r_{\mathcal{W}} = 1$) to 19 chords downstream the body. The values reported in Table D.1.1 are the ones obtained when $\underline{F}_{\text{vf}}(r_{\mathcal{W}})$, $\underline{F}_{\text{rev}}(r_{\mathcal{W}})$ and $\underline{F}_{\text{irr}}(r_{\mathcal{W}})$ reach a nearly constant value: $r_{\mathcal{W}} = 18$ for LVL4 and LVL2 grids, $r_{\mathcal{W}} = 4$ for the finest grid level (LVL1); a very low effect of the wake plane position $r_{\mathcal{W}}$ on the aerodynamic force breakdown has been found on this grid level, with values almost constant (drag variation within 3 counts) $1c$ downstream the wing trailing edge as shown in Fig. D.1.2.

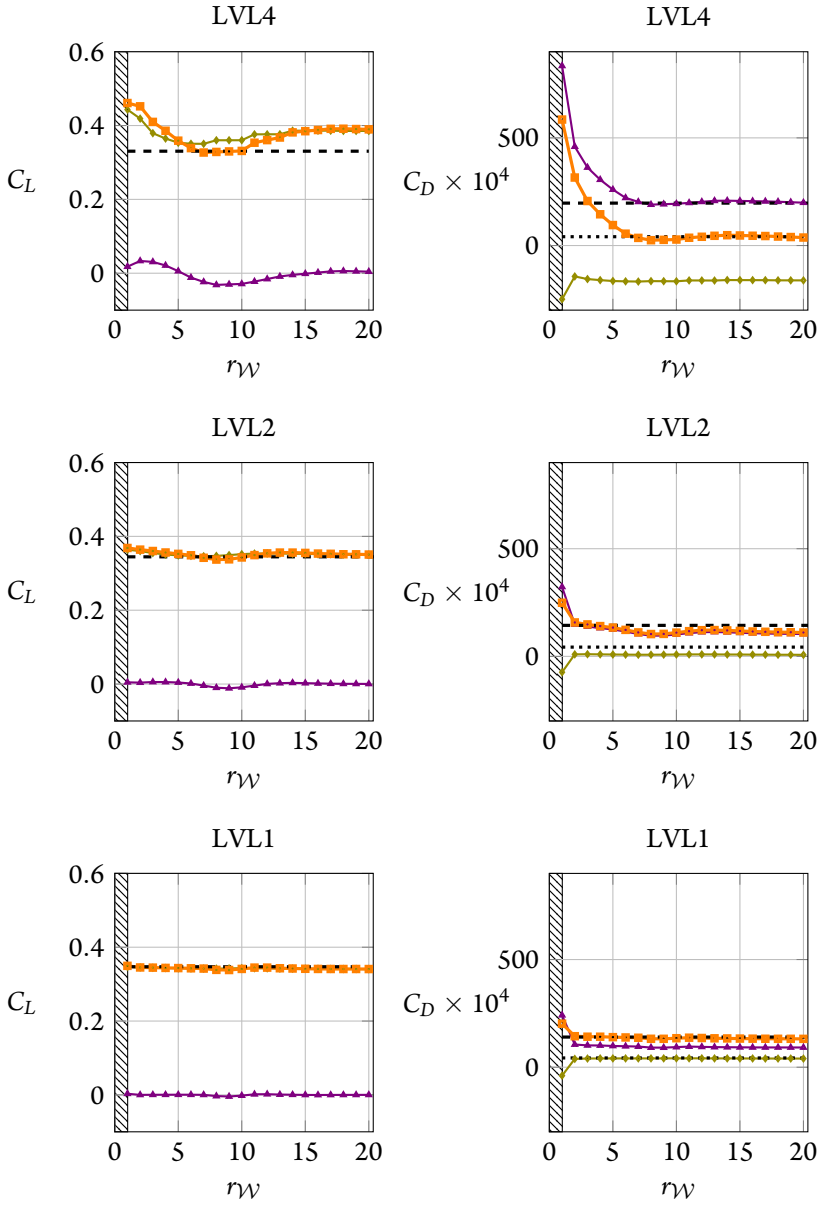


Figure D.1.2: Box Wing with $\mathcal{AR} = 6$ and $\mathbb{V} = 0.2$ at $Re_\infty = 10^7$, $M_\infty = 0.3$ and $a = 4°$. Effect of the wake plane position $r_{\mathcal{W}}$ on C_L and C_D computed by F_{vf} and breakdown in F_{rev} and F_{irr}. Reference near field (- - -), F_{vf} (—■—), F_{rev} (—◆—), F_{irr} (—▲—), induced drag of an optimally loaded Box Wing with $\varepsilon = 1.46$ (·····).

D.2 Box Wing with $\mathcal{AR} = 6$ and $\mathbb{V} = 0.4$

The results of the grid convergence analysis performed for the Box Wing with $\mathbb{V} = 0.4$ analyzed in Section 3.2.1 are shown in Fig. D.2.1 and summarized in Table D.2.1. A computational grid built up similarly to the case of $\mathbb{V} = 0.2$ has been tested on three levels and confirmed the results obtained previously: using the LVL1 grid and an integration domain with $x_{\mathcal{W}} = 4$, $\underline{F}_{\text{vf}}$ is in satisfactory agreement with $\underline{F}_{\text{nf}}$ in both lift and drag coefficients whereas $\underline{F}_{\text{rev}}$ differs from the induced drag computed by Eq. (3.8) with $\varepsilon = 1.82$ less than 3%.

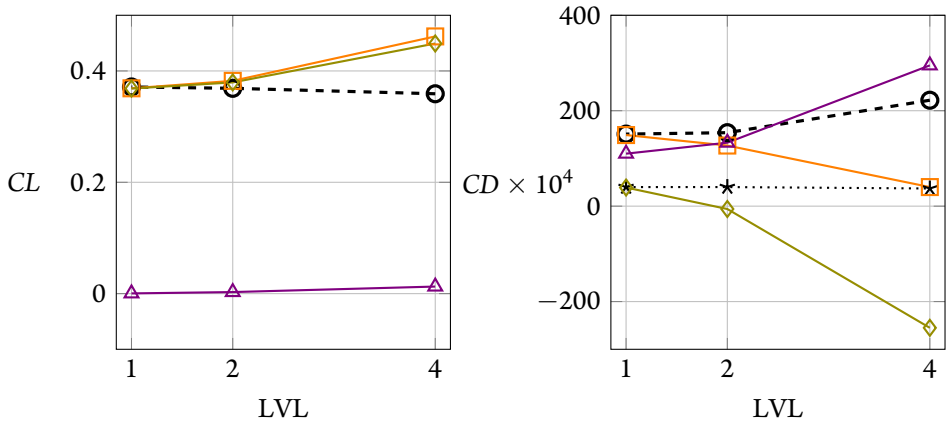


Figure D.2.1: Box Wing with $\mathcal{AR} = 6$ and $\mathbb{V} = 0.4$ at $Re_\infty = 10^7$, $M_\infty = 0.3$ and $\alpha = 4°$. Grid convergence analysis in terms of *near field* F_{nf} and *far field* F_{vf} lift (C_L) and drag (C_D) coefficients and their breakdown. F_{nf} (-⊖-), F_{vf} (—□—), F_{rev} (—◇—), F_{irr} (—△—), induced drag of an optimally loaded Box Wing with $\varepsilon = 1.82$ (··✶··).

Table D.2.1: Box Wing with $\mathcal{AR} = 6$ and $\mathbb{V} = 0.4$ at $Re_\infty = 10^7$, $M_\infty = 0.3$ and $\alpha = 4°$. Results of the grid convergence analysis in terms of *near field* F_{nf} and *far field* F_{vf} lift (C_L) and drag (C_D) coefficients and their breakdown in F_{rev} and F_{irr}.

C_L

LVL	F_{irr}	F_{rev}	F_{vf}	F_{nf}
4	0.0127	0.4493	0.462	0.359
2	0.0028	0.3794	0.3822	0.3688
1	0.0004	0.3684	0.3688	0.3712

$C_D \times 10^4$

LVL	F_{irr}	F_{rev}	F_{vf}	F_{nf}	
4	295	-255	37	40	222
2	133	-6	40	127	154
1	110	39	40	149	151

D.3 Elliptical Wing with $\mathcal{AR} = 6$

The grid used for the computations performed for the Elliptical Wing and present in Section 3.2.3 counts almost 17 million cells: 512 along the wing section and 128 along the semi-wingspan, the wake and each other direction normal to the body. This grid level (LVL$^1/_2$) has been scaled 2 (LVL1) and 4 (LVL2) times to perform the grid convergence analysis reported in Fig. D.3.1 and Table D.3.1. The effect of the integration domain on the computation of $\underline{F}_{\text{rev}}$ has been studied as in the case of the Box Wings with similar results: also for the elliptical wing an almost constant *far field* force and breakdown is obtained with $x_{\mathcal{W}} \geq 4$ on the finest grid level.

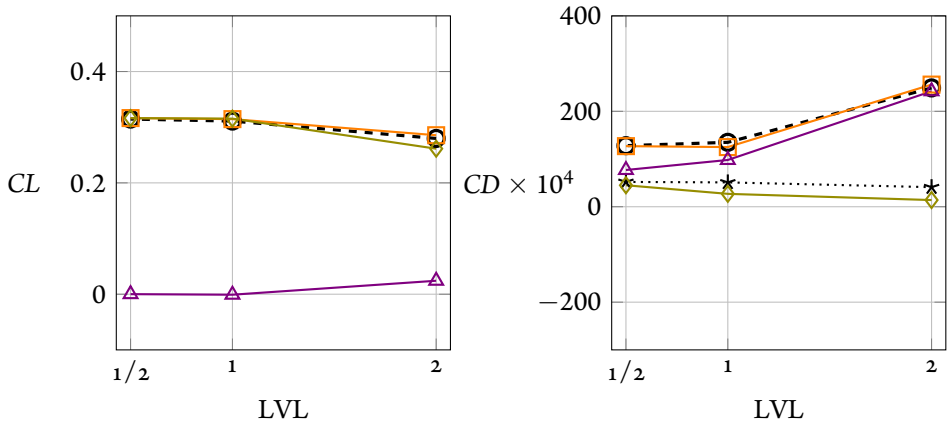


Figure D.3.1: Elliptical Wing with $\mathcal{AR} = 6$ at $Re_\infty = 10^7$, $M_\infty = 0.3$ and $\alpha = 4°$. Grid convergence analysis in terms of *near field* F_{nf} and *far field* F_{vf} lift (C_L) and drag (C_D) coefficients and their breakdown. F_{nf} (-⊖-), F_{vf} (—□—), F_{rev} (—◇—), F_{irr} (—△—), theoretical induced drag of an Elliptical Wing computed by Eq. (3.6) (··✶··).

Table D.3.1: Elliptical Wing with $\mathcal{AR} = 6$ at $Re_\infty = 10^7$, $M_\infty = 0.3$ and $\alpha = 4°$. Results of the grid convergence analysis in terms of *near field* F_{nf} and *far field* F_{vf} lift (C_L) and drag (C_D) coefficients and their breakdown in F_{rev} and F_{irr}.

C_L

LVL	F_{irr}	F_{rev}	F_{vf}	F_{nf}
2	0.0242	0.2614	0.2856	0.2798
1	-0.0009	0.3154	0.3145	0.3110
1/2	0.0001	0.3163	0.3164	0.3146

$C_D \times 10^4$

LVL	F_{irr}	F_{rev}	C_{D_i}	F_{vf}	F_{nf}
2	242	14	41	256	249
1	98	27	51	125	135
1/2	77	45	52	127	128

References

[1] Directorate General for Research (European Parliament). Air traffic and the environment, May 1998.

[2] S. G. Flechner, P. F. Jacobs, and R. T. Whitcomb. A high subsonic speed wind tunnel investigation of winglets on a representative second-generation jet transport wing. Technical Report NASA-TN-D-8264, NASA, July 1976.

[3] D. M. Bushnell and K. J. Moore. Drag reduction in nature. *Annual Review of Fluid Mechanics*, 23(1):65–79, 1991. doi: 10.1146/annurev.fl.23.010191.000433. URL https://doi.org/10.1146/annurev.fl.23.010191.000433.

[4] F. M. White. *Fluid Mechanics*. WCB/McGraw-Hill, 1999.

[5] W. Kutta, M. Auftriebskräfte in stroömenden flüssigkeiten. *Illustrierte Aero- nautische Mitteilungen*, 6:133, 1902.

[6] N. E. Joukowskij. Sur les tourbillons adjoints. *Traraux de la Section Physique de la Societe Imperiale des Amis des Sciences Naturales*, 13(2), 1906.

[7] P. T. Meredith. Viscous phenomena affecting high-lift systems and suggestions for future cfd development. Technical report, High-Lift Systems Aerodynamics, AGARD CP 315, September 1993.

[8] P. Raj. Aircraft design in the 21st century - implications for design methods. In *29th AIAA, Fluid Dynamics Conference*. AIAA, 1998. doi: 10.2514/6.1998-2895. URL https://arc.aiaa.org/doi/abs/10.2514/6.1998-2895.

[9] L. Prandtl. Tragflügeltheorie. i. mitteilung. *Nachrichten von der Gesellschaft der Wissenschaften zu Göttingen, Mathematisch-Physikalische Klasse*, pages 451–477, 1918. URL http://eudml.org/doc/59036.

[10] L. Prandtl. Application of modern hydrodynamics to aeronautics in two parts. Technical Report 116, NACA, 1921.

[11] C.P. van Dam. Recent experience with different methods of drag prediction. *Progress in Aerospace Sciences*, 35(8):751 – 798, 1999. ISSN 0376-0421.

doi: https://doi.org/10.1016/S0376-0421(99)00009-3. URL http://www.sciencedirect.com/science/article/pii/S0376042199000093.

[12] A. Betz. A method for the direct determination of wing-section drag. Technical Report 337, NACA, 1925.

[13] B. Jones. Measurement of profile drag by the pitot-transverse method. Technical Report 1688, British ARC R&M, 1936.

[14] E. C. Maskell. Progress towards a method for the measurement of the components of the drag of a wing of finite span. Technical report, Procurement Executive, Ministry of Defence, Royal Aircraft Establishment, RAE Farnborough, 1972.

[15] J. C. Wu, J. Hackett, and D. Lilley. A generalized wake-integral approach for drag determination in three-dimensional flows. In *17th Aerospace Sciences Meeting*, 1979. doi: 10.2514/6.1979-279. URL https://arc.aiaa.org/doi/abs/10.2514/6.1979-279.

[16] K. Kusunose. Drag prediction based on a wake-integral method. In *16th AIAA Applied Aerodynamics Conference*, 1998. doi: 10.2514/6.1998-2723. URL https://arc.aiaa.org/doi/abs/10.2514/6.1998-2723.

[17] K. Oswatitsch. *Gas Dynamics*. Academic Press, 1956.

[18] D. Hue and S. Esquieu. Computational drag prediction of the dpw4 configuration using the far-field approach. *Journal of Aircraft*, 48(5):1658–1670, 2011.

[19] M. Ueno, K. Yamamoto, K. Tanaka, M. Murayama, and R. Tognaccini. Far-field drag analysis of nasa common research model simulation. *Journal of Aircraft*, 50 (2):388–397, 2013.

[20] R. C. Lock. The prediction of the drag of aerofoils and wings at high subsonic speeds. *The Aeronautical Journal (1968)*, 90(896):207–226, 1986. doi: 10.1017/S000192400001575X.

[21] K. Kusunose. A wake integration method for airplane drag prediction. *The 21st Century COE Program International COE of Flow Dynamics Lecture Series*, 2005.

[22] D. Destarac. *Far-Field / Near-Field drag balance and applications of drag extraction in CFD*. Von Karman Institute Lecture Series, 2003.

[23] D. Destarac and J. Van Der Vooren. Drag/thrust analysis of jet-propelled transonic transport aircraft; definition of physical drag components. *Aerospace Science and Technology*, 8(6):545–556, 2004.

[24] V. Schmitt and D. Destarac. Recent progress in drag prediction and reduction for civil transport aircraft at onera. In *36th AIAA Aerospace Sciences Meeting and Exhibit*, 1998. doi: 10.2514/6.1998-137. URL https://arc.aiaa.org/doi/abs/10.2514/6.1998-137.

[25] L. Paparone and R. Tognaccini. Computational fluid dynamics-based drag prediction and decomposition. *AIAA Journal*, 41(9):1647–1657, 2003. doi: 10.2514/2.7300. URL https://doi.org/10.2514/2.7300.

[26] R. Tognaccini. *Methods for drag gecomposition, Thrust-drag bookkeeping from CFD calculations*. Von Karman Institute Lecture Series, 2003.

[27] M. Gariépy, J. Y. Trépanier, and C. Masson. Convergence criterion for a far-field drag prediction and decomposition method. *AIAA Journal*, 49(12):2814–2818, 2011. doi: 10.2514/1.J050865. URL https://doi.org/10.2514/1.J050865.

[28] M. Gariépy, B. Malouin, J. Y. Trépanier, and E. Laurendeau. Far-field drag decomposition applied to the drag prediction workshop 5 cases. *Journal of Aircraft*, 50(6):1822–1831, 2013. doi: 10.2514/1.C032204. URL https://doi.org/10.2514/1.C032204.

[29] M. Gariepy, J.Y. Trepanier, and B. Malouin. Generalization of the far-field drag decomposition method to unsteady flows. *AIAA Journal*, 51(6):1309–1319, 2013. doi: 10.2514/1.J051609. URL https://doi.org/10.2514/1.J051609.

[30] H. Toubin and D. Bailly. Development and application of a new unsteady far-field drag decomposition method. *AIAA Journal*, 53(11):3414–3429, 2015. doi: 10.2514/1.J054002. URL https://doi.org/10.2514/1.J054002.

[31] H. Toubin, D. Bailly, and M. Costes. Improved unsteady far-field drag breakdown method and application to complex cases. *AIAA Journal*, 54(6):1907–1921, 2016. doi: 10.2514/1.J054756. URL https://doi.org/10.2514/1.J054756.

[32] J.-Z Wu, L. Liu, and T. Liu. Fundamental theories of aerodynamic force in viscous and compressible complex flows. *Progress in Aerospace Sciences*, 99:27 – 63, 2018. ISSN 0376-0421. doi: https://doi.org/10.1016/j.paerosci.2018.04.002. URL http://www.sciencedirect.com/science/article/pii/S0376042117301355.

[33] F. Noca, D. Shiels, and D. Jeon. A comparison of methods for evaluating time-dependent fluid dynamic forces on bodies, using only velocity fields and their derivatives. *Journal of Fluids and Structures*, 13(5):551 – 578, 1999. ISSN 0889-9746. doi: https://doi.org/10.1006/jfls.1999.0219. URL http://www.sciencedirect.com/science/article/pii/S0889974699902190.

[34] J.-Z. Wu, X.-Y. Lu, and L.-X. Zhuang. Integral force acting on a body due to local flow structures. *Journal of Fluid Mechanics*, 576:265–286, 2007. doi: 10.1017/S0022112006004551.

[35] T. Von Karman and J. Burgers. *General Aerodynamic Theory*, chapter Prefect Fluids. Springer Berlin Heidelberg, 1935.

[36] P. G. Saffman. *Vortex Dynamics*. Cambridge Monographs on Mechanics. Cambridge University Press, 1993. doi: 10.1017/CBO9780511624063.

[37] Y. T. Yang, R. K. Zhang, Y. R. An, and J.-Z. Wu. Steady vortex force theory and slender-wing flow diagnosis. *Acta Mechanica Sinica*, 23(6):609–619, Dec 2007. ISSN 1614-3116. doi: 10.1007/s10409-007-0107-0. URL https://doi.org/10.1007/s10409-007-0107-0.

[38] J.-Z. Wu, H.-Y. Ma, and M.-D. Zhou. *Vorticity and Vortex Dynamics*. Springer US, 2006.

[39] S.-F. Zou, J.-Z. Wu, A.-K. Gao, L. Liu, L. Kang, and Y. Shi. On the concept and theory of induced drag for viscous and incompressible steady flow. *Physics of Fluids*, 31(6):065106, 2019. doi: 10.1063/1.5090165. URL https://doi.org/10.1063/1.5090165.

[40] C. Marongiu and R. Tognaccini. Far-field analysis of the aerodynamic force by lamb vector integrals. *AIAA Journal*, 48(11):2543–2555, 2019/04/17 2010. doi: 10.2514/1.J050326. URL https://doi.org/10.2514/1.J050326.

[41] J. C. Wu. Theory for aerodynamic force and moment in viscous flows. *AIAA Journal*, 19(4):432–441, 1981. doi: 10.2514/3.50966. URL https://doi.org/10.2514/3.50966.

[42] C. Marongiu, R. Tognaccini, and M. Ueno. Lift and lift-induced drag computation by lamb vector integration. *AIAA Journal*, 51(6):1420–1430, 2013. doi: 10.2514/1.J052104. URL https://doi.org/10.2514/1.J052104.

[43] P. R. Spalart. On the far wake and induced drag of aircraft. *Journal of Fluid Mechanics*, 603:413–430, 2008. doi: 10.1017/S0022112008001146.

[44] B. Mele and R. Tognaccini. Aerodynamic force by lamb vector integrals in compressible flow. *Physics of Fluids*, 26(5):056104, 2014. doi: 10.1063/1.4875015. URL https://doi.org/10.1063/1.4875015.

[45] B. Mele, M. Ostieri, and R. Tognaccini. Vorticity based breakdown of the aerodynamic force in three-dimensional compressible flows. *AIAA Journal*, 54(4):1198–1208, 2016. doi: 10.2514/1.J054363. URL https://doi.org/10.2514/1.J054363.

[46] B. Mele, M. Ostieri, and R. Tognaccini. Aircraft lift and drag decomposition in transonic flows. *Journal of Aircraft*, 54(5):1933–1944, 2017. doi: 10.2514/1.C034288. URL https://doi.org/10.2514/1.C034288.

[47] M. Ostieri. *Aerodynamic lift and drag breakdown in steady and unsteady flows*. PhD thesis, University of Naples Federico II, 2017.

[48] T. Liu, S. Wang, X. Zhang, and G. He. Unsteady thin-airfoil theory revisited: Application of a simple lift formula. *AIAA Journal*, 53(6):1492–1502, 2015. doi: 10.2514/1.J053439. URL https://doi.org/10.2514/1.J053439.

[49] M. Ostieri, B. Mele, and R. Tognaccini. Linear and nonlinear decomposition of aerodynamic force acting on an oscillating plate. *AIAA Journal*, 56(2):594–608, 2018. doi: 10.2514/1.J056129. URL https://doi.org/10.2514/1.J056129.

[50] L. Russo, M. Ostieri, and R. Tognaccini. Thrust extraction from vorticity fields in steady and unsteady flows. In *2018 AIAA AVIATION Forum*, page 3967, 2018. doi: 10.2514/6.2018-3967.

[51] L. N. G. Filon. The forces on a cylinder in a stream of viscous fluid. *Proceedings of the Royal Society of London. Series A, Containing Papers of a Mathematical and Physical Character*, 113(763):7–27, 1926. doi: 10.1098/rspa.1926.0136. URL https://royalsocietypublishing.org/doi/abs/10.1098/rspa.1926.0136.

[52] L. Q. Liu, J.-Z. Wu, W. D. Su, and L. L. Kang. Lift and drag in three-dimensional steady viscous and compressible flow. *Physics of Fluids*, 29(11):116105, 2017. doi: 10.1063/1.4989747. URL https://doi.org/10.1063/1.4989747.

[53] L. Kang, L. Russo, R. Tognaccini, J.-Z. Wu, and W. Su. Aerodynamic force breakdown based on vortex force theory. In *AIAA Scitech 2019 Forum*, 2019. doi: 10.2514/6.2019-2122. URL https://arc.aiaa.org/doi/abs/10.2514/6.2019-2122.

[54] G. K. Batchelor. *An Introduction to Fluid Dynamics*. Cambridge Mathematical Library. Cambridge University Press, 2000. doi: 10.1017/CBO9780511800955.

[55] D. Wilcox. *Turbulence Modeling for CFD*. DCW Industries, Incorporated, 1994.

[56] J.-Z. Wu, H.-Y. Ma, and M.-D. Zhou. *Vortical Flow*. Springer-Verlag Berlin Heidelberg, 2016. doi: 10.1017/CBO9780511624063.

[57] S. Schmitz. Drag decomposition using partial-pressure fields in the compressible navier-stokes equations. *AIAA Journal*, 57(5), 2018.

[58] J. Raddatz and J. K. Fassbender. Block structured navier-stokes solver flower. In *MEGAFLOW-Numerical Flow Simulation for Aircraft Design*, pages 27–44. Springer, 2005.

[59] L.-Q. Liu. *Far-Field Force Theory of Steady Flow*, pages 59–110. Springer Singapore, Singapore, 2018. ISBN 978-981-10-6223-0. doi: 10.1007/978-981-10-6223-0_3. URL https://doi.org/10.1007/978-981-10-6223-0_3.

[60] M. Lanzetta, B. Mele, and R. Tognaccini. Advances in aerodynamic drag extraction by far field methods. *Journal of Aircraft*, 52(6), 2015. doi: 10.2514/1.C033095.

[61] J. Li and Z. N. Wu. Vortex force map method for viscous flows of general airfoils. *Journal of Fluid Mechanics*, 836:145–166, 2018. doi: 10.1017/jfm.2017.783.

[62] H. Glauert. *The Airscrew: Momentum Theory*, pages 199–207. Cambridge Science Classics. Cambridge University Press, 1983. doi: 10.1017/CBO9780511574481.018.

[63] A. Betz. Development of the inflow theory of the propeller. Technical report, NACA, 1920.

[64] B. Mele, L. Russo, and R. Tognaccini. Drag bookkeeping on an aircraft with riblets and nlf control. *Aerospace Science and Technology*, 98:105714, 2020. ISSN 1270-9638. doi: https://doi.org/10.1016/j.ast.2020.105714.

[65] L. Russo, R. Tognaccini, and L. Demasi. Box wing and induced drag: Compressibility effects in subsonic and transonic regimes. *AIAA Journal*, 2020 (article in advance). doi: 10.2514/1.J059080.

[66] Clean Sky. https://www.cleansky.eu/regional-aircraft.

[67] I. H. Abbott, A. E. Von Doenhoff, and L. S. Stivers. Summary of airfoil data. NACA Report 824, NACA, 1945.

[68] D. M. Somers. *Subsonic Natural-Laminar-Flow Airfoils*, pages 143–176. Springer-Verlag New York, 1992.

[69] R. J. Mcghee, J. K. Viken, W. Pfenninger, W. D. Beasley, and W. D. Harvey. Experimental results for a flapped natural-laminar-flow airfoil with high lift/drag ratio. Technical Report NASA-TM-85788, NAS 1.15:85788, NASA, May 1984.

[70] M. S. Selig, M. D. Maughmer, and D. M. Somers. Natural-laminar-flow airfoil for general-aviation applications. *Journal of Aircraft*, 32(4):710–715, 1995. doi: 10.2514/3.46781. URL https://doi.org/10.2514/3.46781.

[71] U. Cella, D. Quagliarella, R. Donelli, and B. Imperatore. Design and test of the uw-5006 transonic natural-laminar-flow wing. *Journal of Aircraft*, 47(3):783–795, 2010. doi: 10.2514/1.40932. URL https://doi.org/10.2514/1.40932.

[72] M. Walsh and A. Lindemann. Optimization and application of riblets for turbulent drag reduction. In *22nd Aerospace Sciences Meeting*. AIAA, 1984. doi: 10.2514/6.1984-347. URL https://arc.aiaa.org/doi/abs/10.2514/6.1984-347.

[73] M. Walsh. *Riblets*, pages 203–261. Viscous Drag Reduction in Viscous Boundary Layer, 1990. doi: 10.2514/5.9781600865978.0000.0000. URL https://arc.aiaa.org/doi/abs/10.2514/5.9781600865978.0000.0000.

[74] E. Coustols and A. M. Savill. Turbulent skin-friction drag reduction by active and passive means. AGARD Report 786, AGARD, 1992.

[75] J. Szodruch. Viscous drag reduction on transport aircraft. In *29th Aerospace Sciences Meeting*, 1991. doi: 10.2514/6.1991-685. URL https://arc.aiaa.org/doi/abs/10.2514/6.1991-685.

[76] S.-J. Lee and Y.-G. Jang. Control of flow around a naca 0012 airfoil with a micro-riblet film. *Journal of Fluids and Structures*, 20(5):659 – 672, 2005. ISSN 0889-9746. doi: https://doi.org/10.1016/j.jfluidstructs.2005.03.003. URL http://www.sciencedirect.com/science/article/pii/S0889974605000460.

[77] P.R Viswanath. Aircraft viscous drag reduction using riblets. *Progress in Aerospace Sciences*, 38(6):571 – 600, 2002. ISSN 0376-0421. doi: https://doi.org/10.1016/S0376-0421(02)00048-9. URL http://www.sciencedirect.com/science/article/pii/S0376042102000489.

[78] B. Aupoix, G. Pailhas, and R. Houdeville. Towards a general strategy to model riblet effects. *AIAA Journal*, 50:708–716, 2012.

[79] B. Mele and R. Tognaccini. Numerical simulation of riblets on airfoils and wings. In *50th AIAA Aerospace Sciences Meeting Including the New Horizons Forum and Aerospace Exposition*, AIAA 2012-0861, 2012.

[80] B. Mele, R. Tognaccini, and P. Catalano. Performance assessment of a transonic wing-body configuration with riblets installed. *Journal of Aircraft*, 53(1):129–140, 2016. doi: http://arc.aiaa.org/doi/abs/10.2514/1.C033220.

[81] V. Koepplin, F. Herbst, and J. R. Seume. Correlation-based riblet model for turbomachinery applications. *Journal of turbomachinery*, 139(7):1–10, 2017.

[82] B. Mele and R. Tognaccini. Slip length based boundary condition for modeling drag reduction devices. *AIAA Journal*, 56(9):3478–3490, 2018. doi: 10.2514/1.J056589.

[83] J.R. Debisschop and F.T.M. Nieuwstadt. Turbulent boundary layer in an adverse pressure gradient: Effectiveness of riblets. *AIAA Journal*, 34(5):932–937, 1996.

[84] P. Luchini, F. Manzo, and A. Pozzi. Resistance of grooved surface to parallel flow and cross-flow. *Journal of Fluid Mechanics*, 228:87–109, 1991.

[85] D.W. Bechert, M. Bruse, W. Hage, J.G.T. van der Hoeven, and G. Hoppe. Experiments on drag-reducing surfaces and their optimization with an adjustable geometry. *Journal of Fluid Mechanics*, 338:59–87, 1997.

[86] P.G. Saffman. A model for inhomogeneous turbulent flow. *Proc. R. Soc. Lond.*, A 317:417–433, 1970.

[87] R. García-Mayoral and J. Jiménez. Hydrodynamic stability and breakdown of the viscous regime over riblets. *Journal of Fluid Mechanics*, 678:317–347, 2011.

[88] P. Catalano and R. Tognaccini. Turbulence modelling for low Reynolds number flows. *AIAA Journal*, 48:1673–1685, 2010.

[89] P. Catalano, B. Mele, and R. Tognaccini. On the implementation of a turbulence model for low Reynolds number flows. *Computers and Fluids*, 109:67–71, March 2015.

[90] Flightpath 2050: Europe's vision for aviation. Technical report, European Commission, 2011.

[91] A. Bows. Aviation and climate change: confronting the challenge. *The Aeronautical Journal (1968)*, 114(1158):459–468, 2010. doi: 10.1017/S000192400000395X.

[92] L. Prandtl. Induced drag of multiplanes. Technical report, NACA, 1924.

[93] J. J. Wolkovitch. The joined wing - an overview. *Journal of Aircraft*, 23(3):161–178, 1986. doi: 10.2514/3.45285. URL `https://doi.org/10.2514/3.45285`.

[94] A. Frediani, V. Cipolla, and E. Rizzo. The prandtlplane configuration: Overview on possible applications to civil aviation. In Giuseppe Buttazzo and Aldo Frediani, editors, *Variational Analysis and Aerospace Engineering: Mathematical Challenges for Aerospace Design*, pages 179–210, Boston, MA, 2012. Springer US. ISBN 978-1-4614-2435-2.

[95] R. Cavallaro and L. Demasi. Challenges, ideas and innovations of joined-wing configurations: A concept from the past, an opportunity for the future. *Progress in Aerospace Sciences*, 87:1–94, November 2016.

[96] M. F. Samuels. Structural weight comparison of a joined wing and a conventional wing. *Journal of Aircraft*, 19(6):485–491, 1982. doi: 10.2514/3.57418. URL https://arc.aiaa.org/doi/abs/10.2514/3.57418.

[97] L. Demasi, G. Monegato, E. Rizzo, R. Cavallaro, and A. Dipace. Minimum induced drag theorems for joined wings, closed systems, and generic biwings: Applications. *Journal of Optimization Theory and Applications*, 169(1):236–261, apr 2015.

[98] L. Demasi, G. Monegato, A. Dipace, and R. Cavallaro. Minimum induced drag theorems for joined wings, closed systems, and generic biwings: Theory. *Journal of Optimization Theory and Applications*, 169(1):200–235, Apr 2016. ISSN 1573-2878. doi: 10.1007/s10957-015-0849-y. URL https://doi.org/10.1007/s10957-015-0849-y.

[99] L. Demasi, G. Monegato, R. Cavallaro, and R. Rybarczyk. Minimum induced drag conditions for truss-braced wings. *AIAA Journal*, 56(12):4669–4684, 2018.

[100] P. Junghanns, G. Monegato, and L. Demasi. Properties and numerical solution of an integral equation system to minimize airplane drag for a multiwing system. *submitted for pubblication*, 2019.

[101] I. Kroo. Drag due to lift: Concepts for prediction and reduction. *Annual Review of Fluid Mechanics*, 33(1):587–617, 2001. doi: 10.1146/annurev.fluid.33.1.587. URL https://doi.org/10.1146/annurev.fluid.33.1.587.

[102] I. Kroo. Nonplanar wing concepts for increased aircraft efficiency. In *VKI lecture series on Innovative Configurations and Advanced Concepts for Future Civil Aircraft*, 2005.

[103] H. Gagnon and D. W. Zingg. Aerodynamic optimization trade study of a box-wing aircraft configuration. *Journal of Aircraft*, 53(4):971–981, 2016.

[104] S. Andrews and R. Perez. Comparison of box-wing and conventional aircraft mission performance using multidisciplinary analysis and optimization. *Aerospace Science and Technology*, 79:336 – 351, 2018. ISSN 1270-9638. doi: https://doi.org/10.1016/j.ast.2018.05.060. URL http://www.sciencedirect.com/science/article/pii/S1270963818304516.

[105] T. Chau and D. W. Zingg. Aerodynamic shape optimization of a box-wing regional aircraft based on the reynolds-averaged navier-stokes equations. In *35th AIAA Applied Aerodynamics Conference*, 2017. doi: 10.2514/6.2017-3258. URL https://arc.aiaa.org/doi/abs/10.2514/6.2017-3258.

[106] M. Munk. The minimum induced drag of aerofoils. Technical report, NACA, 1923.

[107] J. D. Anderson. *Fundamentals of Aerodynamics*. McGraw-Hill, 2001.

[108] L. Demasi, A. Dipace, G. Monegato, and R. Cavallaro. Invariant formulation for the minimum induced drag conditions of nonplanar wing systems. *AIAA Journal*, 52(10):2223–2240, 2014. doi: 10.2514/1.J052837. URL https://doi.org/10.2514/1.J052837.

[109] L. Demasi, G. Monegato, and R. Cavallaro. Minimum induced drag theorems for multiwing systems. *AIAA Journal*, 55(10):3266–3287, 2017. doi: 10.2514/1.J055652. URL https://doi.org/10.2514/1.J055652.

[110] A. Frediani and G. Montanari. Best wing system: an exact solution of the prandtl's problem. In *Variational Analysis and Aerospace Engineering*, pages 183–211, New York, NY, 2009. Springer New York. ISBN 978-0-387-95857-6.

[111] M. Munk. General biplane theory. Technical Report 151, NACA, 1923.

List of Author's Publications

JOURNAL ARTICLES

- L. L. Kang, L. Russo, R. Tognaccini, J. Z. Wu and W. D. Su. Aerodynamic Force Breakdown in Reversible and Irreversible Components by Vortex Force Theory. *AIAA Journal,* 57(11) 4623–4638, 2019. doi: 10.2514/1.J058379.

- L. Russo, R. Tognaccini and L. Demasi. Box Wing and Induced Drag: Compressibility Effects in Subsonic and Transonic Regimes. *AIAA Journal* 2020 (article in advance). doi: 10.2514/1.J059080.

- B. Mele, L. Russo and R. Tognaccini. Drag bookeeping on an aircraft with riblets and NLF control. *Aerospace Science and Technology*, 98, 2020. doi: 10.1016/j.ast.2020.105714.

CONFERENCE PAPERS[1]

- L. Russo, R. Tognaccini and L. Demasi. Box Wing and Induced Drag: Compressibility Effects in Subsonic and Transonic Regimes. *AIAA Scitech 2020 Forum,* Orlando (USA), 2020.

- L. L. Kang, L. Russo, R. Tognaccini, J. Z. Wu and W. D. Su. Aerodynamic Force Breakdown Based on Vortex Force Theory. *AIAA Scitech 2019 Forum,* San Diego (USA), 2019.

- L. Russo, M. Ostieri and R. Tognaccini. Thrust Extraction from Vorticity Fields in Steady and Unsteady Flows. *2018 AIAA AVIATION Forum,* Atlanta (USA), 2018.

- L. Russo, M. Ostieri and R. Tognaccini. Link between Thrust and Vorticity in Steady and Unsteady Flows. *23rd Conference of the Italian Association of Theoretical and Applied Mechanics, AIMETA 2017,* Salerno (Italy), 2017.

[1] Speaker.

CONFERENCE (BOOK OF ABSTRACTS ONLY)

- L. Russo and R. Tognaccini, Thrust and Drag of a Plunging Foil. *12th European Fluid Mechanics Conference,* Vienna (Austria), 2018.

Colophon

This thesis was typeset using LaTeX, originally developed by Leslie Lamport and based on Donald Knuth's TeX. The body text is set in 11 point Arno Pro, designed by Robert Slimbach in the style of book types from the Aldine Press in Venice, and issued by Adobe in 2007. A template, which can be used to format a PhD thesis with this look and feel, has been released under the permissive MIT (X11) license, and can be found online at github.com/suchow/ or from the author at suchow@post.harvard.edu.